Electromagnetic Design, Implementation and Test of a Superconducting Undulator with a Transverse Gradient Field Amplitude

Zur Erlangung des akademischen Grades eines

DOKTOR-INGENIEURS

von der Fakultät für
Elektrotechnik und Informationstechnik
des Karlsruher Instituts für Technologie (KIT)

genehmigte

DISSERTATION

von

M. Sc. Verónica Afonso Rodríguez

geb. in: Las Palmas de Gran Canaria

Tag der münlichen Prüfung: 25. November 2015

Hauptreferent: Prof. Dr. rer. nat. Marc Weber
Korreferent: Prof. Dr.-Ing. Mathias Noe

ABSTRACT

This thesis describes the development of a novel superconducting transversal gradient undulator (TGU) designed to form a compact, highly brilliant laser-wakefield accelerator-driven radiation source.

Undulators provide monochromatic radiation with high spectral intensity. The working principle of undulators requires a small relative energy spread of the electron beam in the order of $\Delta E/E_0 \sim 0.1\,\%$, where E_0 is the reference electron energy. This is a typical value in for example storage rings. A laser-wakefield accelerator (LWFA) accelerates electrons to up to several 100 MeV within a few millimeters acceleration length. However, the energy spread of a LWFA is relatively large ($\Delta E/E_0 \gtrsim 1\,\%$), spoiling the monochromaticity and the intensity of the undulator radiation.

A TGU in combination with a dispersive beam transport line can be employed to produce undulator radiation with natural bandwidth despite the large energy spread of the LWFA. The flux density amplitude of the TGU varies with the transverse position and is matched to the spatial dispersion of the electrons in such a way that particles with different energies oscillate at the same amplitude and frequency. In this thesis, a TGU with an acceptance for electron energies of $\Delta E/E_0 = \pm 10\,\%$ is presented.

The transverse flux density gradient can be achieved by monotonically increasing the gap width of the undulator. Two possible TGU geometries are described and an undulator with a cylindrical form is chosen. Then a design optimization is performed to identify the optimal parameters of this undulator. With a superconducting cylindrical undulator the highest transverse field gradient is achievable.

In addition, the technical design and construction details such as shape, material and winding coil technique are discussed. Special features of this TGU include a short period length of about 1 cm and iron-free superconducting coils, which are wound by using NbTi wires. To test these concepts, a first short model of the magnet was built and characterized. Based on the results a full-scale TGU has been realized.

Magnetic measurements and quench tests were performed with the undulator within a liquid-Helium bath cryostat. The transversal gradient field measured showed an excellent agreement with the simulations. The operating current of the full-scale TGU will be at 83.5 % of the measured quench current ($\approx$ 890 A), providing a sufficient safety margin. This thesis documents the construction, first tests and characterization, both of the short model and the full-scale TGU.

ZUSAMMENFASSUNG

Diese Dissertation beschreibt die Entwicklung eines neuartigen supraleitenden Undulators mit transversalen Feldgradienten (TGU) mit dem Ziel, eine kompakte, hochbrillante Strahlungsquelle an einem Laser-Wakefield-Beschleuniger zu realisieren.

Undulatoren produzieren monochromatische Strahlung mit hoher spektraler Intensität. Das Arbeitsprinzip von Undulatoren erfordert eine kleine relative Energiebreite des Elektronenstrahls in der Größenordnung von $\Delta E/E_0 \sim 0.1\,\%$, wobei E_0 ist die Referenzelektronenergie. Dies ist ein typischer Wert, wie er zum Beispiel in Speicherringen vorkommt. Ein Laser-Wakefield-Beschleuniger (LWFA) beschleunigt Elektronen auf Energien bis zu mehreren 100 MeV innerhalb von wenigen Millimetern Beschleunigungsstrecke. Allerdings ist die Energiebandbreite LWFA-beschleunigter Elektronen relativ groß ($\Delta E/E_0 \gtrsim 1\,\%$) und beeinträchtigt die Monochromatizität und die Intensität der Undulatorstrahlung.

Ein TGU in Kombination mit einer dispersiven Strahltransportlinie kann eingesetzt werden, um trotz der großen Energiebandbreite der Elektronen Undulatorstrahlung mit einer natürlichen Bandbreite zu erzeugen. Die Flußdichte-Amplitude des TGU, variiert mit der transversalen Position und ist in die räumlichen Dispersion der Elektronen in einer Weise angepasst, dass die Teilchen mit verschiedenen Energien mit der gleichen Amplitude und Frequenz schwingen. In Rahmen dieser Arbeit wird ein TGU mit einer Akzeptanz für Elektronenenergien von $\Delta E/E_0 = \pm 10\,\%$ vorgestellt.

Die transversalen Flußdichtegradienten sind durch monoton zunehmende Breite des Undulatorsgap realisierbar. Zuerst werden zwei mögliche TGU Geometrien beschrieben und die Auswahl der zylindrischen Geometrie begründet. Daraufhin wird eine Designoptimierung durchgeführt, um die optimalen Parameter dieses Undulators zu bestimmen. Mit einem supraleitenden zylindrischen Undulator ist der höchste transversale Feldgradient erreichbar, was für eine große Energieakzeptanz wünschenswert ist.

Nachfolgend wird die technischen Konzeption und die Bau-Details wie die Form, das Material und die Wicklungstechnik der Spulen diskutiert. Zu den Besonderheiten dieses TGU gehören eine kurze Periodenlänge von etwa 1 cm und eisenfreie supraleitende Spulen, die durch die Verwendung NbTi Drähte gewickelt sind. Um diese Konzepte zu testen, wurde ein erstes kurzes Modell des Magneten gebaut und charakterisiert. Auf Basis dieser Ergebnisse wurde der vollständige TGU realisiert.

Magnetische Messungen und Quench-Tests wurden mit dem Undulator in einem Flüssig-Helium Bad Kryostaten durchgeführt. Das gemessene transversale Gradient-Feld zeigte eine sehr gute Übereinstimmung mit den Simulationen. Der Betriebsstrom des Full-Scale-TGU wird bei 83.5 % des gemessenen Quenchstroms ($\approx$ 890 A) sein, was eine ausreichende Sicherheitsmarge bietet. Diese Dissertation dokumentiert die Konstruktion, Prüfung und Charakterisierung, sowohl des kurzen Modells als auch des vollständigen TGU.

ACKNOWLEDGEMENTS

This thesis was carried out during the years 2011-2015 at the Laboratory for Applications of Synchrotron Radiation (LAS) at KIT, headed by Prof. Dr. rer. nat. Tilo Baumbach.

First and foremost, I would like to thank Dr. Axel Bernhard, my supervisor and group leader at LAS, for his unremitting support. The possibility to always come asking when being stuck, his constructive comments and the scientific discussions with him were invaluable. I thank him specially for proof-reading this thesis and for offering me his experience with simulation and magnetic measurements.

Particular thanks goes to Prof. Dr. Marc Weber, my main doctoral supervisor, for his valuable support, advices, comments and feedback for my thesis. I also want to thank Prof. Dr.-Ing. Mathias Noe who co-supervised my work for his support.

I want to thank to all member of the LAS group for the pleasant working atmosphere. Special thanks to the students, which collaborated in this work, through undulator simulations or helping by the magnetic measurements: Nils Braun, Julian Gethmann, Vivien Karcher, Alexander Keilmann, Melissa Morcrette, Christoph Plusczyk, Walter Werner, Christina Widmann and Andreas Will.

I am very glad for all the technical support that I received from Michael Fischer during the winding of the undulator coils and the preparation of the magnetic measurements. I very much enjoyed our discussions about electronics and life. I thank Dr. Peter Peiffer for helping me with the magnetic simulations of the correction coils and the magnetic test of the first short model undulators. I want to thank Dr. Andreas Grau and Dr. Stefan Gerstl for their good collaboration and support in all the undulator tests performed at ANKA-KIT. Special thanks goes to Steffen Schott for helping with the design and construction of the undulator and supports, including mechanical simulations, technical drawings and professional advices. I thank Dr. Robert Rossmanith for providing his experience about undulators.

I thank Prof. Dr. Malte C. Kaluza and Maria Leier from the Friedrich-Schiller University in Jena for their support during this thesis and their collaboration in setting up the proof-of-principle experiment with the full-scale undulator at the laser wakefield accelerator in Jena.

And on a personal level I would like to thank my family and friends from Spain and Germany for their support and encouragement during my studies. Thanks to my friend Marga Deck for her motivation, positive spirit and German classes.

My friend Dr.-Ing. Lourdes Ferre Llin deserves an acknowledgment for changing my destiny when we met at CERN. Thanks to her for making this long-distance friendship work. Her insightful comments on the English language helped me improve this thesis.

Finally, I would like to thank Markus May for his love, believe, patience and support during my thesis. You know how important you have been in my life in the last seven years. Markus's family has provided me with a home away from home. Thanks to Ulrike, Thomas, Katrin and Lukas.

Contents

Appendices

1. Introduction

1.1 Synchrotron radiation

Synchrotron radiation (SR) is the name given to the electromagnetic radiation or light generated by an ultra-relativistic electron beam traveling through a magnetic field. It was discovered in 1946 in a General Electric synchrotron accelerator [1]. Synchrotron radiation sources (SRS) are employed by scientists around the world in the study of matter. The high intensity of X-rays produced in these sources are used for experiments in many areas such as physics, materials science, chemistry and medicine [2].

Electromagnetic waves can be described by the wavelength, the photon energy or the frequency. X-rays are electromagnetic waves, like visible light but situated at the short wavelength end of the electromagnetic spectrum, between ultraviolet light and gamma rays. Figure 1.1 shows the electromagnetic radiation spectrum with its corresponding wavelength, photon energy and frequency.

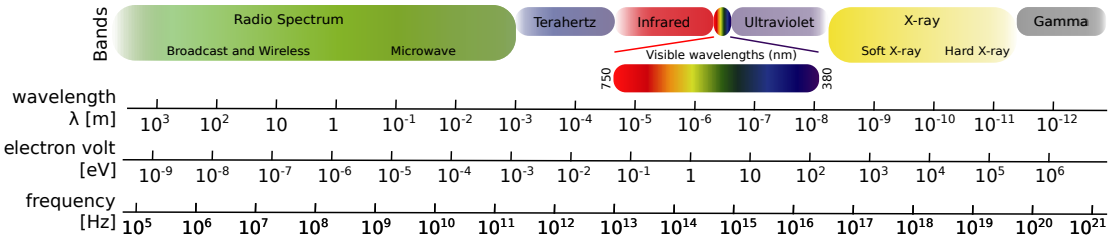

Figure 1.1: The electromagnetic radiation spectrum.

SR sources are often classified in four different generations [3], which are listed next:

- The first generation included storage rings partly dedicated as radiation sources such as the accelerators DORIS in Germany and SPEAR in USA. These storage rings were designed and used originally for high energy physics research and were not optimized for maximum photon beam brightness.

- The second generation was developed in the late 1970s. These sources were built using bending magnets (see Section 1.1.1) and were fully dedicated to SR research such as BESSY I in Germany and MAX I in Sweden.
- The third generation are characterized to produce brilliant X-rays by insertion devices (see Section 1.1.2). Some of X-Ray sources in operation are: SPring-8 in Japan, ESRF in France, APS in USA and DESY's PETRA III in Germany.
- The fourth generation sources are rather under development all over the world. This generation will be more focused on linear accelerators than on storage rings. It will produce greater brightness than the third generation sources and it will be include the free-electron lasers (FELs) as well as the energy recovery linacs (ERLs). Some X-ray laser facilities are: LCLS in USA, SACLA in Japan and the European XFEL in Germany.

The technology of storage ring light sources around the world is developed further to design the so-called "ultimate" storage rings, pushing the brightness of third generation SR several orders of magnitude further [4]. There is nowadays intensive Research and Development (R&D) on low-emittance rings, for example at MAX IV in Sweden. In this ring a design relying on a group of seven magnets, known as multi-bend achromats, will be employed to increase the intensity and brightness of the synchrotron X-ray light by focusing electron beams more tightly [5].

1.1.1 Bending Magnets

The first sources of synchrotron radiation were based on bending magnets installed in storage rings. This kind of magnets bend the electron trajectory in an uniform dipole magnetic field [2]. A schematic diagram of the radiation emitted by electrons in bending magnets is given in Figure 1.2.

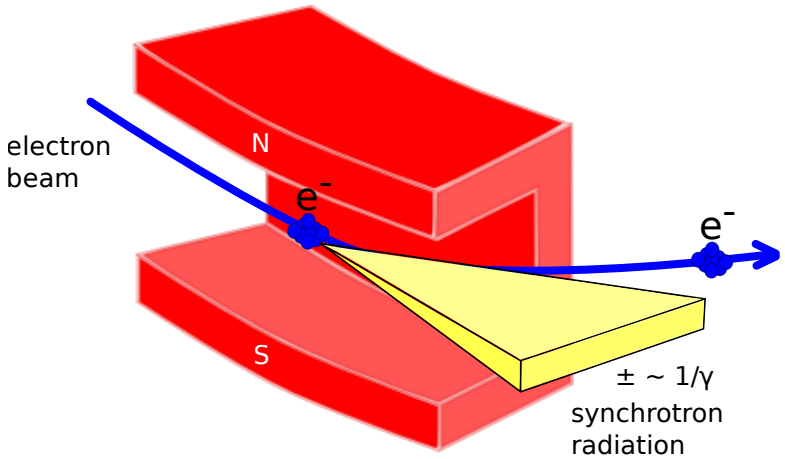

Figure 1.2: Schematic diagram of bending magnet radiation.

The radiation from these magnets is emitted tangentially from any point along the curved path. When the electron velocity approaches the velocity of light, the radiation generated along the electron trajectory inside of a bending magnet is emitted

into a cone of angle $\pm \sim 1/\gamma$, where γ is known as the relativistic Lorentz factor. This factor can be calculated as the ratio of the electron's energy to its rest mass energy ($\gamma = E/0.511\,\mathrm{MeV}$) [2].

1.1.2 Insertion Devices: Undulators and Wigglers

Special magnets were built and inserted into the straight sections of the third generation radiation sources. These Insertion Devices (IDs) produce high levels of flux in narrow angular cones and are light sources for the UV to X-Ray region [2]. IDs fall into two main categories, undulators and wigglers.

- The undulator is a device that consists of a periodic structure of dipole magnets that cause the electron beam to follow a sinusoidal trajectory about the axis of the undulator and this generates Coherent Synchrotron Radiation (CSR). The radiation wavefronts emitted overlap and interfere with each other. Due to this interference the undulator emits a line spectrum with significantly increased intensity at wavelengths with constructive interference. For these wavelengths at the same time the radiation cone is narrowed by a factor of $\sqrt{N}$ as compared to the bending magnets, where N is the number of periods of the undulator [2]. A schematic diagram of the radiation emitted by electrons in undulators is given in Figure 1.3.

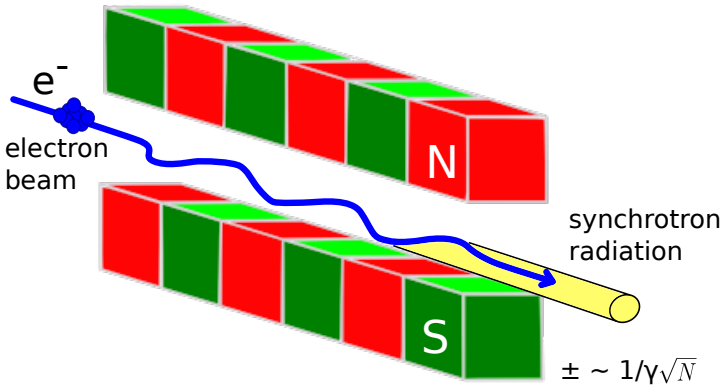

Figure 1.3: Schematic diagram of the undulator radiation.

- A wiggler has stronger magnetic field than an undulator. Thus the particles, which pass through it, move in the transverse position significantly more than for undulators and the electron beam trajectory cannot be approximated as moving along the axis. This prevents the wavefronts from overlapping, no interference effects are evident and this results in Incoherent Synchrotron Radiation. The advantage of this kind of ID over a bending magnet source is that each wiggle produces approximately the same number of photons as a bending magnet of the same field strength, with a opening angle for the emitted radiation of much greater than $1/\gamma$ [2]. A schematic diagram of the radiation emitted by electrons in wigglers is given in Figure 1.4.

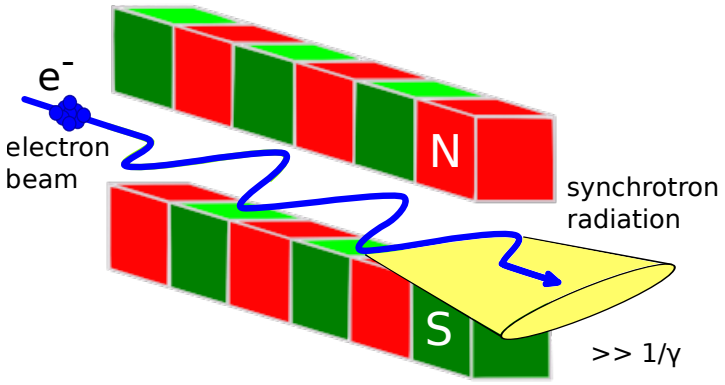

Figure 1.4: Schematic diagram of the wiggler radiation.

To distinguish between undulators and wigglers, the dimensionless undulator or deflection parameter K (1.1) is defined:

$$K = \frac{eB_0}{m_0 c}\frac{\lambda_u}{2\pi} = 93.36 B_0[\mathrm{T}]\lambda_u[\mathrm{m}]\,, \tag{1.1}$$

where e is the electron charge, B_0 is the magnetic field amplitude, λ_u is the period length of the device, m_0 is the rest mass of the electron and c is the speed of light [2]. If $K \lesssim 1$ the electron trajectory will overlap with the emitted radiation and interference effects can occur. This is the case of an undulator. On the other hand, if $K >> 1$ there will be little overlap and no interference. This is the case for a wiggler [2].

The wavelength of radiation from an undulator can be calculated from the undulator equation (1.2):

$$\lambda = \frac{\lambda_u}{2n\gamma^2}\left(1 + \frac{K^2}{2} + \Theta^2\gamma^2\right)\,, \tag{1.2}$$

where Θ is the observation angle and n is the harmonic number. The wavelength depends not only on the magnet period and the electron energy but also on the deflection parameter K, which is a function of the peak on-axis magnetic field and the undulator period again. So by changing the amplitude of the magnetic field the output wavelength of the undulator can be varied. For this reason undulators are almost always built with a smoothly adjustable magnetic field amplitude allowing the output wavelength to be varied continuously over the tuning range of the undulator [2].

The natural bandwidth $\Delta\lambda/\lambda$ at the n-th harmonic is set by the number of periods of the undulator N [2] and is defined by Equation (1.3):

$$\frac{\Delta\lambda}{\lambda} \approx \frac{1}{nN} \tag{1.3}$$

The general form of the radiation spectrum for bending magnets, wigglers and undulators is presented in Figure 1.5.

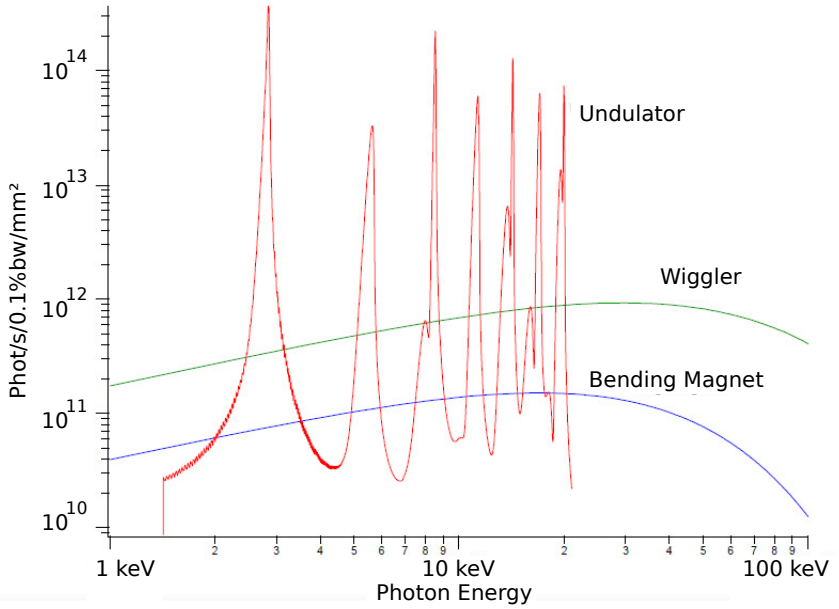

Figure 1.5: Comparison of the calculated radiation spectra emitted by a bending magnet, a 1.8 T wiggler and the SCU14 undulator from the European Synchrotron Radiation Facility (ESRF) [6].

1.2 Laser Wakefield Accelerators

The idea to accelerate particles in a plasma was proposed by Tajima and Dawson in 1979 [7]. They suggested that the longitudinal electric fields formed within laser-driven plasma waves could accelerate charged particles to relativistic high energies.

The plasma wave is excited by an intense femtosecond-laser pulse. This concept is known as the laser wakefield accelerator (LWFA). The acceleration gradients provided by this laser-driven plasma accelerators are three orders of magnitude greater than those generated by conventional accelerators [8]. Electron energies up to 1 GeV have been achieved in acceleration lengths in the order of a centimeter in laser-driven wakefield-accelerators [9].

Most experiments with LWFA are operated in the so-called self-injection regime, where the plasma wave amplitude strongly increases during the highly non-linear interaction until it breaks. During the breaking process, plasma background electrons are injected into the plasma wave following the exciting laser pulse [10]. A drawback of this acceleration process is a relatively large energy spread of the accelerated electron bunch in the order of $1 - 10\,\%$ as compared to conventional accelerators ($\sim 0.1\,\%$).

Undulator light sources driven by LWFA suffer from this energy spread since the monochromaticity and in turn the spectral intensity of the radiation drop rapidly with an increasing bandwidth of the electron energy. This is the case, if a conventional planar undulator with a transversely constant magnetic field is used.

In Figure 1.6 the simulated spectrum of a 100 periods planar undulator [11] is shown. The software WAVE [12] was used to calculated the flux density of the emitted radiation of a single electron with energies between 108 MeV and 132 MeV (20 % energy spread). The observation point is on axis and located at 100 m from

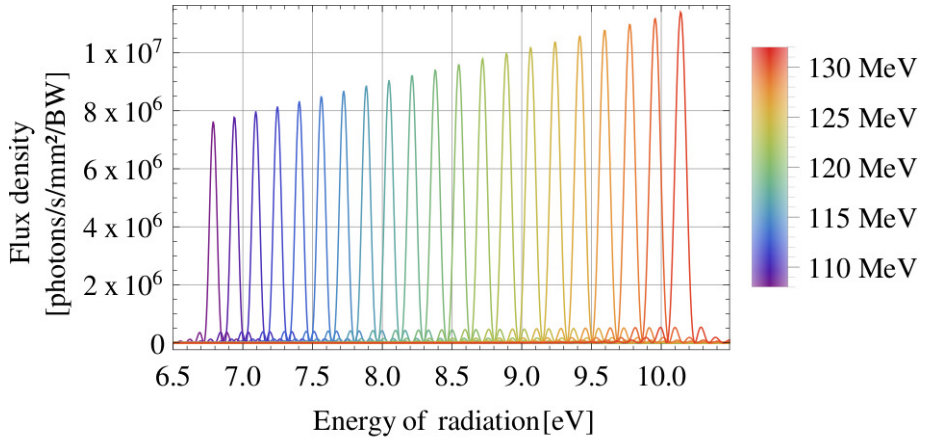

Figure 1.6: Simulated flux density of the emitted emission versus energy of radiation of a single electron with energies between 108 MeV and 132 MeV through a planar undulator [11].

the undulator. The calculated energy of radiation is shown on the x-axis and results a bandwidth of approximately 30 %. The spectrum generated exhibits an even larger energy bandwidth than the electron beam and the peak intensity drops.

Filtering the electron energies can restore the monochromaticity of the undulator radiation, but obviously only at the cost of vastly decreasing the number of particles and thereby again the radiation intensity. The basic feasibility of LWFA-driven light sources, but also their limitations, were experimentally shown in [13] and [14].

As an alternative approach, an experimental setup with a LWFA and a TGU will be realized at the Friedrich Schiller University in Jena (see schematic diagram Figure 1.7). A collaboration with the Laboratory for Applications of Synchrotron Radiation (LAS) at the Karlsruhe Institute of Technology (KIT) has been performed.

The motivation of the experiment in Jena is to develop a very compact high-brilliance X-ray radiation source by applying a compensation scheme for the relatively high energy spread according to the following idea: A magnetic chicane energetically disperses the electron beam in the x-z plane ($\gamma \rightarrow \gamma(x)$) and the electrons are sent through the TGU with a x-dependent flux density amplitude ($B \rightarrow B_y(x)$) off axis. The magnetic field, and therefore also the deflection parameter K, are

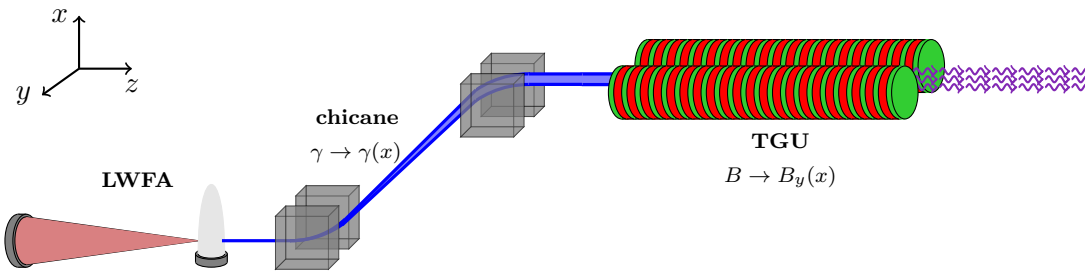

Figure 1.7: Experimental setup planned at the LWFA in Jena [15].

dependent on the transverse x-position and have to match the spatial energy distribution of the electrons after the chicane to get a constant wavelength [16].

The modified undulator equation (1.4) that defines the constant wavelength for this design is:

$$\lambda = \frac{\lambda_\mathrm{u}}{2\gamma(x)^2}\left(1 + \frac{K(x)^2}{2}\right) = \text{constant}, \tag{1.4}$$

where $\gamma(x) = E(x)/0.511\,\mathrm{MeV}$, $K(x) = 93.36 B_y(x)[\mathrm{T}]\lambda_\mathrm{u}[\mathrm{m}]$ and λ_u is the fixed undulator period length.

The optimization goal, for the TGU designed in this thesis, is to achieve a bandwidth of the undulator radiation in the order of the natural bandwidth. For $N = 100$ periods this results in the condition:

$$\frac{\Delta\lambda}{\lambda} \leq \frac{1}{N} \approx 1\,\%$$

1.3 Superconducting Undulators

Superconductivity was discovered in 1911 by Kamerlingh Onnes, when he investigated the conductivity of metals at low temperatures. He saw the sudden drop in resistance of mercury to an immeasurably low value at a temperature just below 4.15 K (the boiling temperature of liquid helium). The temperature at which the electrical resistivity of a metal drops to zero is called critical temperature T_c [17]. In Table 1.1 the critical temperatures of some superconducting materials are given.

Material	Type	Critical temperature $T_c[K]$	Critical magnetic field $B_c[T]$
Pb		7.19	0.08
Hg	1	4.15	0.04
Al		1.18	0.01
		$T_c[K]$	$B_{c2}[T]$
Nb		8.7	0.2
NbTi	2	9.2	14.5
Nb_3Sn		16	24

Table 1.1: Critical temperature and critical field of superconductors [18, 19].

In 1933, Meissner and Ochsenfeld discovered that superconductors expelled a weak magnetic field from its interior when cooled below T_c. This phenomenon was called Meissner effect. There are two types of superconductors classified according to their response to magnetic fields:

- Type I superconductors are pure metals such as lead (Pb), mercury (Hg) and aluminium (Al). They do not admit a magnetic field in the interior of the bulk material below their specified T_c. For this reason shielding currents flow in a very thin layer on the surface of the conductor. The London penetration depth parameter λ_L defines the thickness of this layer and is generally quite small, $20 - 50\,\mathrm{nm}$. When the strength of the applied magnetic field rises above a critical value B_c, the superconducting state breaks down (see Figure 1.8).

The typical values of B_c are usually less than 0.1 T as is shown in Table 1.1. This type of superconductors is not used for IDs because they are only superconducting at low fields [17].

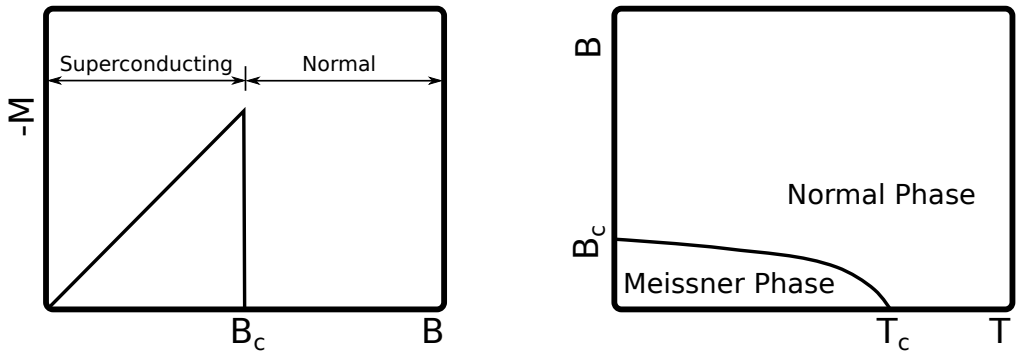

(a) (b)

Figure 1.8: Type I superconductors [18]: (a) Magnetization (magnetic moment per unit volume M) versus magnetic field. (b) Magnetic field versus temperature.

- Type II superconductors are alloys like niobium-titanium (NbTi) and niobium-tin (Nb_3Sn) and also the element Niobium (Nb). They are characterized by two critical fields, B_{c1} and B_{c2}. They exclude magnetic fields below B_{c1}, in the Meissner phase. In the range $B_{c1} < B < B_{c2}$ they are in a mixed-phase, where the magnetic field is not excluded completely, but is constrained in the form of flux tubes (see Figure 1.9). They are in the superconducting state up to much higher fields (10 T or more for the alloys) as is shown in Table 1.1 [17].

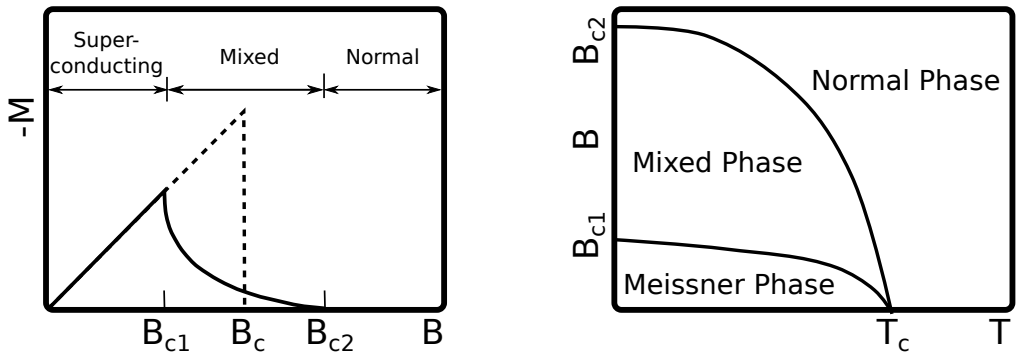

(a) (b)

Figure 1.9: Type II superconductors [18]: (a) Magnetization versus magnetic field. (b) Magnetic field versus temperature.

Type II superconductors are characterized by a critical surface (see Figure 1.10) in temperature (T), magnetic field (B) and current density (J) space. An increase in any of the properties produces a decrease in the other two. The critical surface indicates a first order phase transition between the superconducting (region below the surface) and the normal conducting state (above the surface) of the material. In practice, the usual operating temperature for superconducting magnets built with NbTi is 4.2 K [20].

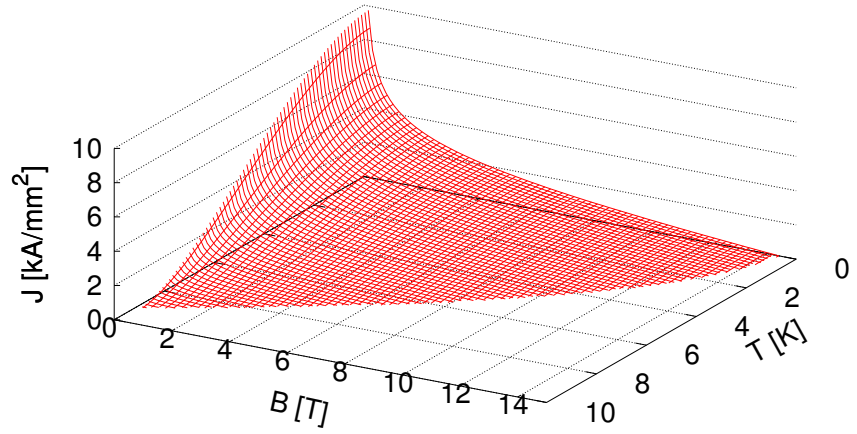

Figure 1.10: Critical surface for a NbTi cable. In the region below the red curve the material is in the superconducting state. Above the red curve the material is in its normal state.

At present the two materials most used for superconducting IDs are NbTi and Nb_3Sn [2]. In this thesis, only NbTi superconductors are considered. This superconductor is the preferred material to use because it is ductile and easy to form into coils. Superconducting wires of NbTi consist of many individual filaments (typically 20 μm diameter) held together in a copper matrix that provides mechanical stability, an electrical bypass when a filament goes normal conducting, and also a heat sink. A 1 mm diameter wire can contain hundreds or even thousands of filaments [2].

"Quench" is a term used to describe the process which occurs when any part of a magnet goes from the superconducting to the normal resistive state. The entire stored energy of the magnet will be dissipated as heat [20]. A reliable detection of quenches is important because a sudden increase in resistance in a coil that has very large current densities flowing within it, can easily damage or even destroy that coil. Protection systems must be included with the power supply so that in the event of a quench the current is rapidly (< 1 s) reduced to zero [2]. In most cases the dissipation of the stored energy in shunt resistors connected in parallel to the superconducting coils.

Interest in superconducting undulators (SCUs) is justified by the fact that they can reach, for the same gap and period length, higher field amplitudes than cryogenic permanent magnet undulators (CPMUs) [21]. There are a growing number of R&D projects worldwide where SCUs have recently been built or are in development, for example at: National Synchrotron Radiation Research Center (NSRRC) in Taiwan [22], Advanced Photon Source (APS) in USA [23], Diamond Light Source (DLS) in UK [24], Shangai Synchrotron Radiation Facility (SSRF) in China [25], European Synchrotron Radiation Facility (ESRF) in France [26] and Synchrotron Radiation Facility at KIT (ANKA) in Germany [27].

The idea of realizing extremely compact radiation sources and even table-top FELs by combining LWFAs with short-period undulators [28, 29, 30] begins with the advent of LWFAs in the 2000s [31, 32, 33]. Evidently SCUs are, next to CPMUs, promising candidates for this application. At a period length of $\lambda_u = 9$ mm, NbTi

SCUs can achieve a flux density on axis 25 % higher when compared with CPMUs (as discussed in [34]). The fixed-gap-tunability of electromagnets is an additional advantage.

1.4 Objectives of this thesis

In this thesis, the development of a novel transverse gradient undulator (TGU) is presented. This superconducting undulator is tailored to the electron beam properties of the LWFA at the University of Jena. The main targets of this thesis are summarized below:

- To select the TGU geometry through analytical and numerical methods.

  Developing an optimization for finding the optimal parameters of the undulator for the specific electron beam parameters given by the LWFA in Jena. The undulator magnetic field and the electron beam trajectories through the undulator will be simulated. The transversal drift of the trajectories will be analyzed and compensated through a correction field. The selection of a couple of correction coils inside the undulator will be introduced.

- To design the TGU tailored to the LWFA in Jena.

  The material for the construction of the undulator will be selected, after simulating several undulator models with different pole configurations to analyze the saturation of the magnetic parts. The geometrical parameters of the full-scale undulator and the correction coils will be specified, including the coil-pole structure and undulator support structure.

- To manufacture short models and the full model undulator.

  This will be included a first half period model and two periods models scaled to the full-scale TGU with 40 periods. The winding and the test of these short models will be employed to improve the coil support structure of the full model and to facilitate the winding of the superconducting coils. Quench tests and a first magnetic field of the short models will be performed to experimentally test the coils. The winding of the 40 periods TGU superconducting coils, including the correction coils, will be carried out at KIT-LAS.

- To characterize the 40 periods TGU.

  A first magnetic field measurement and quench tests of the full-scale TGU will be performed first at KIT, to test the technical concept and to characterize the undulator before the experiment in Jena. The correction coils will be also measured.

2. Superconducting Undulator Fundamentals

2.1 Working principle

Undulators are a periodic magnet structure composed of series of alternating magnet pairs, which cause the oscillation of the electron beam (see Figure 2.1). The magnetic fields in an undulator can be produced with either permanent magnets or electromagnets. In this thesis only superconducting electromagnets undulators are considered.

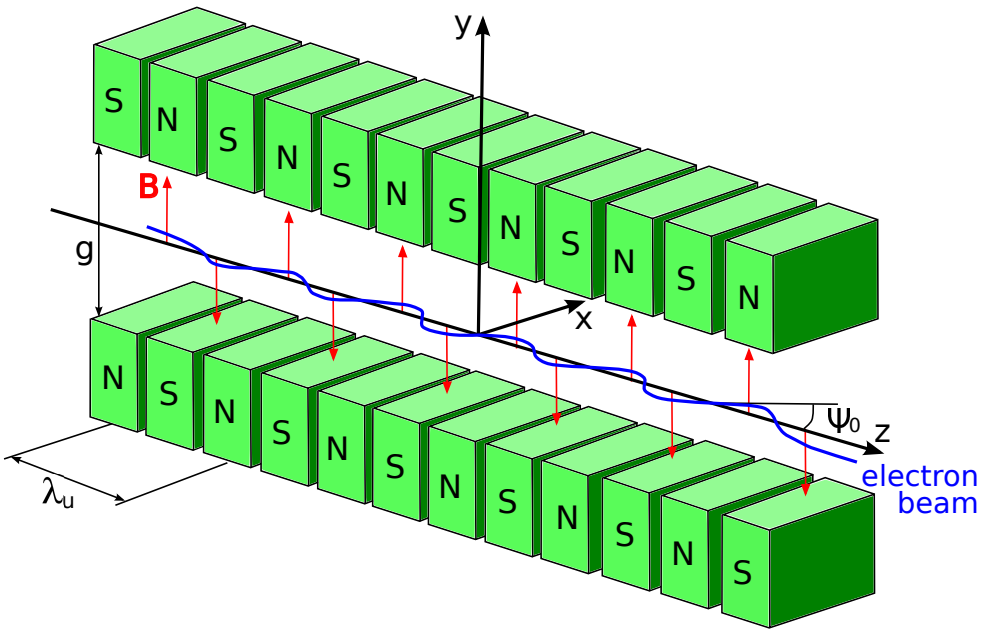

Figure 2.1: Principle layout of an planar undulator: the period length λ_u, the gap width g, the electron trajectory (in blue), the magnetic field (arrows in red) and the magnetic poles (blocks in green) [6].

A planar undulator with symmetry in the xz-plane produces a sinusoidal magnetic field, which is a periodic odd function and can be represented as a Fourier sine series [35]:

$$B_y(z) = -B_0 \sin\left(\frac{2\pi z}{\lambda_u}\right) = -B_0 \sin(k_u z) \tag{2.1}$$

$$B_y(z) = \sum_{i=1}^{\infty} (b_n \sin(n k_u z)) \tag{2.2}$$

where B_0 is the magnetic field amplitude, λ_u the undulator period length, $k_u = 2\pi/\lambda_u$ and b_n the Fourier coefficients.

Superconducting undulators produce the alternating magnetic field by superconducting coils powered with alternating polarity and wrapped into the grooves between the poles, as is shown in Figure 2.2.

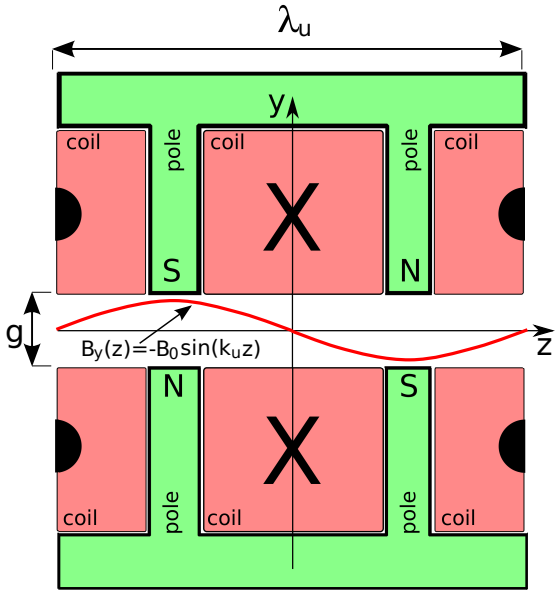

Figure 2.2: Longitudinal cut of one period of an electromagnetic undulator. Only the part of the undulator coil close to the beam axis is shown.

2.1.1 Electron trajectories

The magnetic field for a planar undulator on the beam plane ($y = 0$) is taken as:

$$\vec{B} = (0, B_0 \cos(k_u z), 0) \tag{2.3}$$

where B_0 is the magnetic field amplitude and $k_u = 2\pi/\lambda_u$. The absolute value of the electron velocity is constant: $v = c\beta$. It is assumed that the electrons traverses the origin $z = 0$ at time $t' = 0$. The chosen symmetry field condition results in the initial conditions [36, 6]:

$$z(0) = 0, \quad \dot{x}(0) = 0, \quad \dot{z}(0) = \beta c \tag{2.4}$$

with no transverse velocity at this moment. The Lorentz force on the electron in the magnetic undulator field,

$$\vec{F} = m_e \gamma \begin{pmatrix} \ddot{x} \\ \ddot{y} \\ \ddot{z} \end{pmatrix} = e(\vec{v} \times \vec{B}) = eB_0 \begin{pmatrix} -\cos(k_u z)\dot{z} \\ 0 \\ \cos(k_u z)\dot{x} \end{pmatrix} \tag{2.5}$$

leads to [36, 6]:

$$\ddot{x} = \frac{d^2x}{dt'^2} = -\frac{eB_0}{\gamma m_e}\cos(k_u z)\dot{z} \tag{2.6}$$

$$\ddot{z} = \frac{d^2z}{dt'^2} = \frac{eB_0}{\gamma m_e}\cos(k_u z)\dot{x} \tag{2.7}$$

where e is the elementary electric charge, γ the Lorentz Factor and m_e the rest mass of the electron.

The change in x-position along the z-axis corresponds to the integral of Equation (2.6):

$$\begin{aligned}\dot{x} = \frac{dx}{dz}(z) &= -\int \frac{eB_0}{\gamma m_e}\cos(k_u z)\,\mathrm{d}z \\ &= -\frac{eB_0}{\gamma m_e k_u}\sin(k_u z).\end{aligned} \tag{2.8}$$

The z-component of the velocity is obtained from the conservation of the energy [36, 6]:

$$\dot{x}^2 + \dot{z}^2 = \beta^2 c^2, \;\; \dot{z} = \beta c\sqrt{1 - \frac{\dot{x}^2}{\beta^2 c^2}} \tag{2.9}$$

As mentioned in Section 1.1.2 depending on the value of K there are two cases: wiggler if $K >> 1$ and undulator if $K \lesssim 1$. In the case of the undulator the radiation emitted by relativistic electrons is concentrated in a narrow cone around the forward direction (z-axis). Then the radiation receives contributions from various sections of the trajectory that overlap in space and interfere with each other [37].

The maximum deflection angle with respect to the z-axis is [2, 36]:

$$\psi_0 = \frac{K}{\gamma} \tag{2.10}$$

Depending on the magnitude of the deflection angle ψ_0 compared with the natural opening angle $1/\gamma$ of the emitted radiation, the undulators can be classified into [36, 6]:

- Weak-undulator: ψ_0 is smaller than $1/\gamma$ then $K < 1$. Undulator in the strict sense with quasi-monochromatic radiation.
- Strong-undulator: ψ_0 is larger than $1/\gamma$ then $K > 1$. Spectrum of undulator radiation with many harmonics.

In the case of a weak undulator the expression for the longitudinal velocity can be approximated to $\dot{z} \approx \beta c$. The derivative of x with respect to z is [36, 6]:

$$\begin{aligned}x'(z) = \frac{dx}{dz} = \frac{\dot{x}}{\dot{z}} &= -\frac{eB_0}{m_e k_u c\beta\gamma}\sin(k_u z) \\ &= -\frac{K}{\beta\gamma}\sin(k_u z)\end{aligned} \tag{2.11}$$

$$K = \beta\gamma\hat{x}' = \beta\gamma\psi_0 = \frac{eB_0}{m_e k_u c} \tag{2.12}$$

A good approximation of the electron trajectory on the xz-plane for the weak undulator is obtained with one more integration of Equation (2.11) [36]:

$$x(z) = \frac{K}{\beta\gamma k_u}\cos(k_u z) = a\cos(k_u z). \tag{2.13}$$

The trajectory as a function of the time t' written in Cartesian component is given by:

$$x(t') = \frac{K}{\beta\gamma k_u}\cos(\Omega_u t') \tag{2.14}$$

using the frequency of the periodic particle motion in the laboratory frame $\Omega_u = k_u\beta c$. The z-component, $z(t') = \beta c t'$, is obtained from the longitudinal motion $\dot{z} = \beta c$.

2.1.2 Interference

The constructive interference of wavefronts emitted by the same electron traveling through an undulator at different points in the magnet is shown in Figure 2.3 [36, 35].

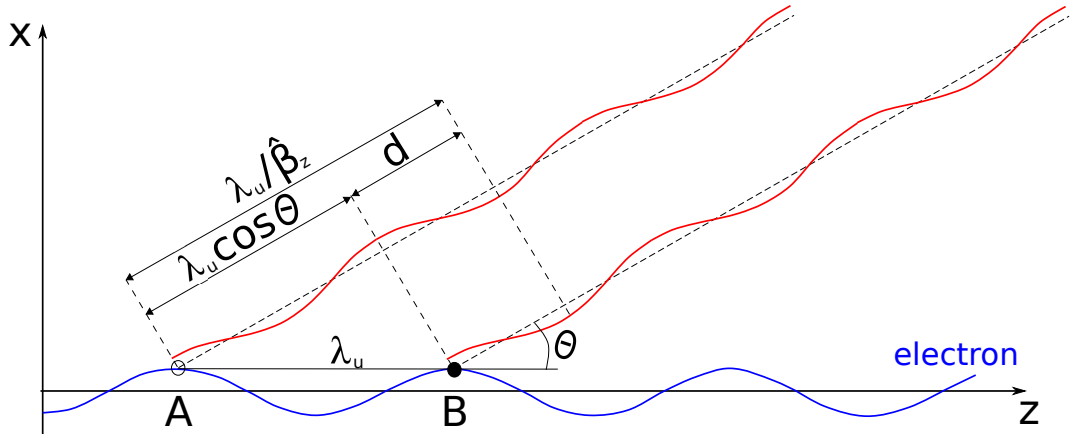

Figure 2.3: Constructive interference in an undulator.

If an electron is moving one period length λ_u between the point A and the point B, the time for this electron to travel one full period is $t_e = \lambda_u/c\hat{\beta}_z$ moving with the drift velocity $v_z = c\hat{\beta}_z$. The average relative velocity of the electron in the forward direction $\hat{\beta}_z$ is approximately [2]:

$$\begin{aligned}\hat{\beta}_z &\approx \beta - \frac{K^2}{4\beta\gamma^2} \\ &\approx 1 - \frac{1}{2\gamma^2} - \frac{K^2}{4\beta\gamma^2}\end{aligned} \tag{2.15}$$

The radiation wave emitted in the first period from A is propagating with velocity c at a time $t_\gamma = \lambda_u/c$. This first wave will have advanced a distance

$\lambda_u/\hat{\beta}_z$ when the electron has arrived to the point B. The radiation emitted in the second period from B is delayed with respect to the first wave by $\Delta t = t_e - t_\gamma$. The separation d between the two wavefronts is [2, 36]:

$$d = \frac{\lambda_u}{\hat{\beta}_z} - \lambda_u \cos(\Theta) \tag{2.16}$$

where Θ is the angle of emission with respect to the electron beam axis z, called too observation angle. For constructive interference to occur this separation must be a whole number of wavelength of radiation: $d = n\lambda$.

With the Taylor series expansion approximation $(1-x)^{-1} \approx (1+x)$ (valid for $|x| < 1$) and inserting the value of $\hat{\beta}_z$ from Equation (2.15), it results:

$$\begin{aligned} d = n\lambda &\approx \lambda_u \left(1 + \frac{1}{2\gamma^2} + \frac{K^2}{4\beta\gamma^2}\right) - \lambda_u \cos(\Theta) \\ &\approx \lambda_u \left(1 - \cos(\Theta)\right) + \frac{\lambda_u}{2\gamma^2} + \frac{\lambda_u K^2}{4\beta\gamma^2} \end{aligned} \tag{2.17}$$

It is necessary to employ the expression $1 - \cos(\Theta) = 2\sin^2(\Theta/2)$ and the approximation for small angles $\sin(\Theta) \approx \Theta$, which leads to the undulator equation to calculate the wavelength of radiation:

$$\lambda = \frac{\lambda_u}{2n\gamma^2}\left(1 + \frac{K^2}{2} + \Theta^2\gamma^2\right) \tag{2.18}$$

2.2 Magnetic field calculation

Analytical methods allow to calculate undulator magnetic fields and to optimize them with respect to various parameters faster than numerical methods. The analytical expressions used in this work were introduced in [38, 16] and they are valid for infinitely long undulators. For the simulation of the magnetic field in an undulator with finite number of periods N_u, Finite-Element Methods (FEMs) are employed, specially to simulate the magnetic field at the ends of the undulators. The employment of FEMs is also justified in the case of iron-pole undulators by the iron saturation. The field strength parameter $\tilde{B}$ required for the analytical calculation is found through the FEM. The results of analytical methods are compared with those obtained from the application of the FEM to validate them.

Analytical expressions for the calculation of the magnetic field of two transverse gradient undulators (TGUs) designs were employed. In this thesis only TGUs with tilted and cylindrical geometries, respectively, were considered (see Figure 2.4). In TGUs the magnetic field increases (or decreases) with the positive transverse x-axis, while this transverse gradient is zero in a conventional planar undulator.

2.2.1 Analytic expressions

The magnetic field in the gap of the undulator (where $\vec{J} = 0$) obeys the following time-independent Maxwell equations in vacuum [38, 39]:

$$\vec{\nabla} \cdot \vec{B} = 0 \tag{2.19}$$

$$\vec{\nabla} \times \vec{B} = 0 \tag{2.20}$$

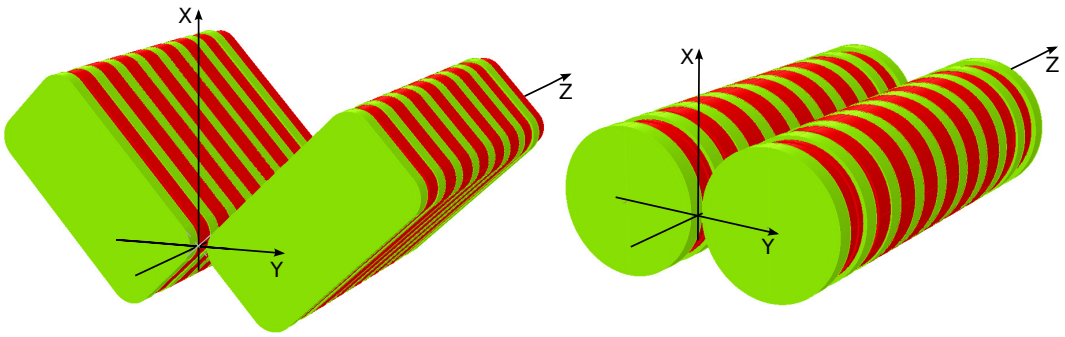

Figure 2.4: Transverse gradient undulator geometries considered in this thesis: tilted (left) and cylindrical (right).

For a vector field $\vec{V}$ with $\vec{\nabla} \times \vec{V} = 0$ exists a scalar potential ϕ with $\vec{V} := -\vec{\nabla}\phi$ and the following vector identity can be applied [38, 39]:

$$\vec{\nabla} \times (\vec{\nabla}\phi) = 0. \tag{2.21}$$

Then Equation (2.20) can be written as:

$$\vec{B} = -\vec{\nabla}\phi_{\text{magn.}}. \tag{2.22}$$

Thus, Equation (2.19) becomes Laplace's equation [40]:

$$\begin{aligned} \vec{\nabla} \cdot \vec{\nabla}\phi_{\text{magn.}} &= \vec{\nabla}^2\phi_{\text{magn.}} && (2.23) \\ &= \triangle\phi_{\text{magn.}} = 0. && (2.24) \end{aligned}$$

Laplace's equation is a linear and homogeneous partial differential equation, which is treated extensively in the literature. In an arbitrary orthogonal coordinate system (u_1, u_2, u_3), Laplace's equation reads [41]:

$$\begin{aligned} \triangle\phi(u_1, u_2, u_3) = \frac{1}{t_1 t_2 t_3} \Bigg[& \frac{\partial}{\partial u_1} \left(\frac{t_2 t_3}{t_1} \frac{\partial \phi}{\partial u_1} \right) \\ & + \frac{\partial}{\partial u_2} \left(\frac{t_1 t_3}{t_2} \frac{\partial \phi}{\partial u_2} \right) + \frac{\partial}{\partial u_3} \left(\frac{t_1 t_2}{t_3} \frac{\partial \phi}{\partial u_3} \right) \Bigg] \end{aligned} \tag{2.25}$$

where t_i are the metric coefficients defined as [41]:

$$t_i = \left| \frac{\partial \vec{r}(u_1, u_2, u_3)}{\partial u_i} \right| \tag{2.26}$$

with $\vec{r}$ is the position vector as a function of the coordinates u_i. Laplace's equation cannot be solved in arbitrary three-dimensional coordinate systems [36]. However, in separable coordinate systems a solution can be found. Separable means that if boundary conditions on a coordinate plane are given, then ϕ can be written as:

$$\phi(u_1, u_2, u_3) = \tilde{\Phi}_1(u_1)\tilde{\Phi}_2(u_2)\tilde{\Phi}_3(u_3). \tag{2.27}$$

Due to the periodic undulator field in the z-direction, the potential has to be periodic. In the following, u_3 is chosen as the beam direction z and a good approximation for the z-dependent factor of the potential is:

$$\tilde{\Phi}_3(u_3) = \tilde{\Phi}_z(z) = \sin(k_\text{u} z). \tag{2.28}$$

If a Fourier series expansion is applied, the simple sine function becomes:

$$\tilde{\Phi}_z(z) = \sum_{i=1}^{\infty} \left(b_\mathrm{n} \sin(n k_\mathrm{u} z)\right). \tag{2.29}$$

Thus, in a separable coordinate system Laplace's equation (2.25) becomes:

$$\begin{aligned}
\frac{\sin(k_\mathrm{u} z)}{t_1 t_2}\left[\tilde{\Phi}_2 \frac{\partial}{\partial u_1}\left(\frac{t_2}{t_1}\frac{\partial \tilde{\Phi}_1}{\partial u_1}\right) + \tilde{\Phi}_1 \frac{\partial}{\partial u_2}\left(\frac{t_1}{t_2}\frac{\partial \tilde{\Phi}_2}{\partial u_2}\right)\right] + \tilde{\Phi}_1\tilde{\Phi}_2 \frac{\partial^2}{\partial z^2}\sin(k_\mathrm{u} z) &= 0 \\
\frac{\sin(k_\mathrm{u} z)}{t_1 t_2}\left[\tilde{\Phi}_2 \frac{\partial}{\partial u_1}\left(\frac{t_2}{t_1}\frac{\partial \tilde{\Phi}_1}{\partial u_1}\right) + \tilde{\Phi}_1 \frac{\partial}{\partial u_2}\left(\frac{t_1}{t_2}\frac{\partial \tilde{\Phi}_2}{\partial u_2}\right)\right] - \tilde{\Phi}_1\tilde{\Phi}_2 k_\mathrm{u}^2 \sin(k_\mathrm{u} z) &= 0 \\
\frac{1}{t_1 t_2}\left[\tilde{\Phi}_2 \frac{\partial}{\partial u_1}\left(\frac{t_2}{t_1}\frac{\partial \tilde{\Phi}_1}{\partial u_1}\right) + \tilde{\Phi}_1 \frac{\partial}{\partial u_2}\left(\frac{t_1}{t_2}\frac{\partial \tilde{\Phi}_2}{\partial u_2}\right)\right] - \tilde{\Phi}_1\tilde{\Phi}_2 k_\mathrm{u}^2 &= 0
\end{aligned}$$

The sine term vanishes and the three-dimensional Laplace's equation thus reduces to the two-dimensional Helmholtz's equation [40]:

$$\frac{1}{t_1 t_2}\left[\tilde{\Phi}_2 \frac{\partial}{\partial u_1}\left(\frac{t_2}{t_1}\frac{\partial \tilde{\Phi}_1}{\partial u_1}\right) + \tilde{\Phi}_1 \frac{\partial}{\partial u_2}\left(\frac{t_1}{t_2}\frac{\partial \tilde{\Phi}_2}{\partial u_2}\right)\right] = \tilde{\Phi}_1\tilde{\Phi}_2 k_\mathrm{u}^2. \tag{2.30}$$

The magnetic field from Equation (2.22) can be obtained from the solutions of Equation (2.30).

2.2.1.1 Tilted Undulator

As a model for the tilted undulator are assumed two infinitely pole faces, which are tilted by the angle α' against each other and intersect at $x = 0$ and $y = 0$ [42]. The model and the coordinate system used are shown in Figure 2.5.

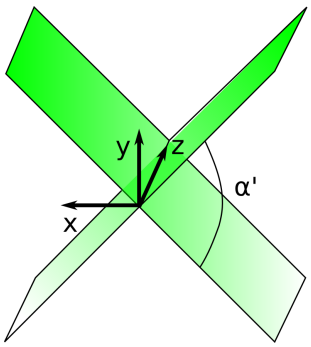

Figure 2.5: Model for the tilted undulator: two infinitely pole faces, which are tilted by an angle α' against each other and intersect at $x = 0$ and $y = 0$.

The magnetic induction of the tilted undulator was approximated by the sum of the fields of both undulator halves. In this case, after solving the Helmholtz's equation as detailed in [38], the induction field in an infinite tilted undulator is:

$$\vec{B} = \begin{pmatrix}
2\sin(\alpha)\tilde{B}(z) & [\cosh(k_\mathrm{u} x \sin(\alpha))\sinh(k_\mathrm{u} y \cos(\alpha)) - \\
& \sinh(k_\mathrm{u} x \sin(\alpha))\sinh(k_\mathrm{u} y \cos(\alpha))] \\
2\cos(\alpha)\tilde{B}(z) & [\sinh(k_\mathrm{u} x \sin(\alpha))\cosh(k_\mathrm{u} y \cos(\alpha)) - \\
& \cosh(k_\mathrm{u} x \sin(\alpha))\cosh(k_\mathrm{u} y \cos(\alpha))] \\
2\cos(k_\mathrm{u} z)\tilde{B}(z) & [\sinh(k_\mathrm{u} x \sin(\alpha))\sinh(k_\mathrm{u} y \cos(\alpha)) - \\
& \cosh(k_\mathrm{u} x \sin(\alpha))\sinh(k_\mathrm{u} y \cos(\alpha))]
\end{pmatrix}, \tag{2.31}$$

where $\alpha = \alpha'/2$ and the value of $\tilde{B}$ can be calculated as the field on the pole surface of the undulator through a simulation in 2D with a FEM-Software as is detailed in Section 3.2.3.

Because the ideal motion of the electrons is restricted to the xz-plane, $y = 0$ can be assumed and the y-component of the magnetic field from Equation (2.31) is:

$$B_y = 2\cos(\alpha)\tilde{B}\sin(k_\mathrm{u}z)\left[\sinh(k_\mathrm{u}x\sin(\alpha)) - \cosh(k_\mathrm{u}x\sin(\alpha))\right]$$

The hyperbolic functions can be defined in terms of exponentials as:

$$\sinh(x) = \frac{\mathrm{e}^{x} - \mathrm{e}^{-x}}{2}$$

$$\cosh(x) = \frac{\mathrm{e}^{x} + \mathrm{e}^{-x}}{2}$$

Thus, the magnetic field B_y can be written as:

$$B_y = 2\cos(\alpha)\tilde{B}\sin(k_\mathrm{u}z)\left[1/2\left(\mathrm{e}^{k_\mathrm{u}x\sin(\alpha)} - \mathrm{e}^{-k_\mathrm{u}x\sin(\alpha)}\right) - 1/2\left(\mathrm{e}^{k_\mathrm{u}x\sin(\alpha)} + \mathrm{e}^{-k_\mathrm{u}x\sin(\alpha)}\right)\right]$$

The analytical expression to calculate the magnetic field B_y in the infinite tilted undulator will be approximated by:

$$B_y = -2\cos(\alpha)\tilde{B}\sin(k_\mathrm{u}z)\mathrm{e}^{-k_\mathrm{u}x\sin(\alpha)} \tag{2.32}$$

2.2.1.2 Cylindrical Undulator

Two infinitely long cylinders are assumed as a model for the cylindrical undulator. These two cylinders have their axis in different coordinate systems, which are shifted by $\Delta y = g+2r$ against each other, where g is the gap width on symmetry axis and r the external pole radius of the cylindrical undulator. In the Cartesian undulator system the xz-plane is in the beam plane and the origins of the cylinders' local coordinate systems are lying at $r_{0,\mathrm{o}} = (0, (r + g/2), 0)$ and $r_{0,\mathrm{u}} = (0, -(r + g/2), 0)$ respectively. The model and the Cartesian coordinate system used are shown in Figure 2.6 (left).

Figure 2.6 (right) shows the upper and lower cylindrical coordinate system assumed for the cylindrical undulator. The radial coordinate $\rho_{\mathrm{o,u}}$ and the polar angle $\theta_{\mathrm{o,u}}$ of the upper and the lower cylindrical coordinate system, respectively, are added. z-coordinate has the same meaning as in Cartesian coordinates system. In this way, the magnetic field at point $P(x, y, z)$ can be calculated using the analytical expressions for the cylindrical undulator (see Equation (2.37)), which employs the upper and the lower cylindrical coordinates.

The Cartesian coordinates can be transformed to the radial coordinates of the upper and lower cylindrical coordinate system by making use of the transformation equations:

$$\rho_\mathrm{o} = \sqrt{x^2 + \left[y - (r + g/2)\right]^2} \tag{2.33}$$

$$\rho_\mathrm{u} = \sqrt{x^2 + \left[y + (r + g/2)\right]^2} \tag{2.34}$$

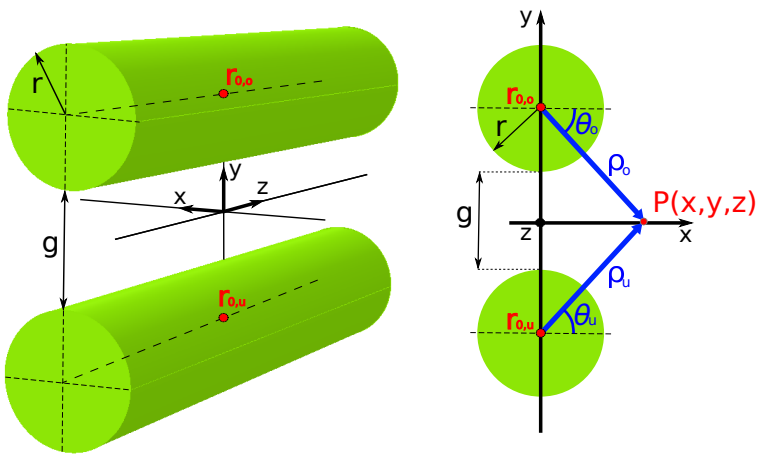

Figure 2.6: Model for the cylindrical undulator: two infinitely long cylinders with their axis shifted by $\Delta y = g + 2r$ against each other and the xz-plane in the beam plane. Left: Cartesian coordinate system. Right: upper and lower cylindrical coordinate system.

The polar angle of the upper and lower cylindrical coordinate system is given by:

$$\theta_\mathrm{o} = \tan^{-1}\left(\frac{y-(r+g/2)}{x}\right) \tag{2.35}$$

$$\theta_\mathrm{u} = \tan^{-1}\left(\frac{y+(r+g/2)}{x}\right) \tag{2.36}$$

The magnetic induction of the cylindrical undulator was approximated by the sum of the fields of both undulator halves. In this case, after solving the Helmholtz's equation as detailed in [38], the induction field in an infinite cylindrical undulator is:

$$\begin{aligned}\vec{B} \;=\; & \tilde{B}\left(\sin(k_\mathrm{u}z)\left[K_1\left(k_\mathrm{u}\rho_\mathrm{o}\right)\hat{e}_{\rho,\mathrm{o}} + K_1\left(k_\mathrm{u}\rho_\mathrm{u}\right)\hat{e}_{\rho,\mathrm{u}}\right]\right. \\ & \left. + \cos(k_\mathrm{u}z)\hat{e}_z\left[K_0\left(k_\mathrm{u}\rho_\mathrm{o}\right) + K_0\left(k_\mathrm{u}\rho_\mathrm{u}\right)\right]\right)\end{aligned} \tag{2.37}$$

where K_0 and K_1 are the modified Bessel functions and $\hat{e}_{\rho,o/u}$ the radial base vectors of the the upper and lower cylindrical coordinate systems.

Because the ideal motion of the electrons is restricted to the xz-plane, $y = 0$ can be assumed and the y-component of the magnetic field from Equation (2.37) is:

$$B_y = \tilde{B}\sin(k_\mathrm{u}z)\left[K_1\left(k_\mathrm{u}\rho_\mathrm{o}\right)\hat{e}_{\rho,\mathrm{o}} + K_1\left(k_\mathrm{u}\rho_\mathrm{u}\right)\hat{e}_{\rho,\mathrm{u}}\right]. \tag{2.38}$$

In Appendix C the magnetic flux density B_y is calculated in terms of a series Fourier expansion and results:

$$B_y = \sum_{n=0}^{\infty}\tilde{B}\sin(nk_\mathrm{u}z)\left[K_1\left(\mathrm{n}k_\mathrm{u}\rho_\mathrm{o}\right)\hat{e}_{\rho,\mathrm{o}} + K_1\left(\mathrm{n}k_\mathrm{u}\rho_\mathrm{u}\right)\hat{e}_{\rho,\mathrm{u}}\right] \tag{2.39}$$

where in this case $\tilde{B}$ is calculated using the Fourier components of the central period of the magnetic field $B_y(z)$ on the beam plane. These components are calculated through a simulation in 3D with a FEM-Software as is detailed in Section 3.2.4.

2.2.2 Numerical methods

In many different areas of engineering and physics the FEM has been widely employed, including magnetism, electrostatics, structural mechanics and so on [37]. Its application to electric and magnetic fields together with a comparison of the various techniques of field computation is given in [19, 43].

A large number of finite element codes are available to perform 2D and 3D field computations of magnetic fields [18, 37]. The commercially available packages such as ANSYS [44], ROXIE [45] and OPERA [46] provide more pre- and post-processing features and a more friendly user interface.

The use of a 3D finite element code is still not trivial and therefore analytical approaches are preferred whenever possible. FEMs are generally employed to obtain solutions to partial differential or integral equations that cannot be solved by analytic methods. Most finite element codes are organized around four main modules, which are usually run successively [37]. These modules are: pre-processor, mesh generator, solver and post-processor.

- The pre-processor is the first module to be executed. The magnetic properties and the geometry of each model component are defined: steel piece, coil, air, etc. Figure 2.7 shows the geometric model of the two full undulators, tilted and cylindrical, and the air is omitted.

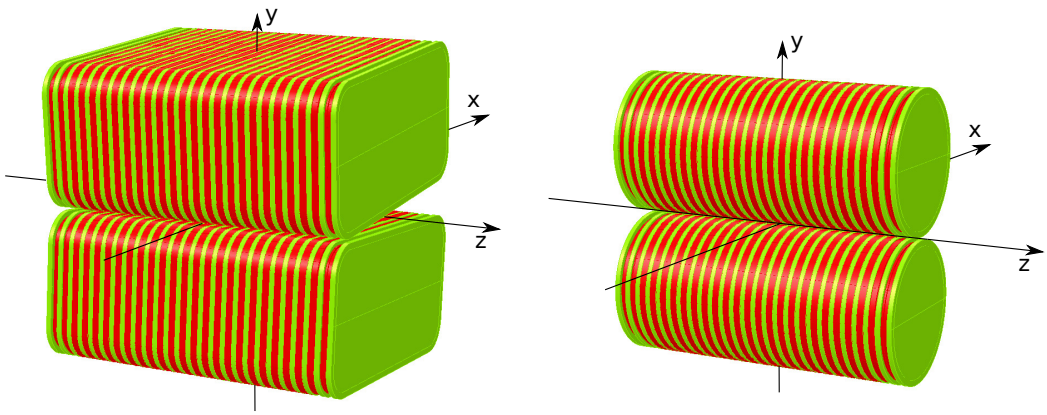

Figure 2.7: Geometric model of the tilted undulator (left) and the cylindrical undulator (right). Iron pieces are represented in green, coils in red and the air is omitted.

Making use of the periodicity and the symmetries, the volume of computation can be restricted. The smaller the volume the shorter the time for solving and the less memory is required. In the case of the tilted and cylindrical undulators is sufficient to analyze one period. This can be done by creating a background body, which encloses the central period. Employing symmetries, the cylindrical undulator background can be reduced to a quarter and the tilted undulator background to the half as is shown in Figure 2.8. The boundary conditions applied to the background faces are: normal magnetic in the xz-plane (B is perpendicular to this plane), tangential magnetic in the yz-plane (B is parallel to this plane) and periodicity in z-direction.

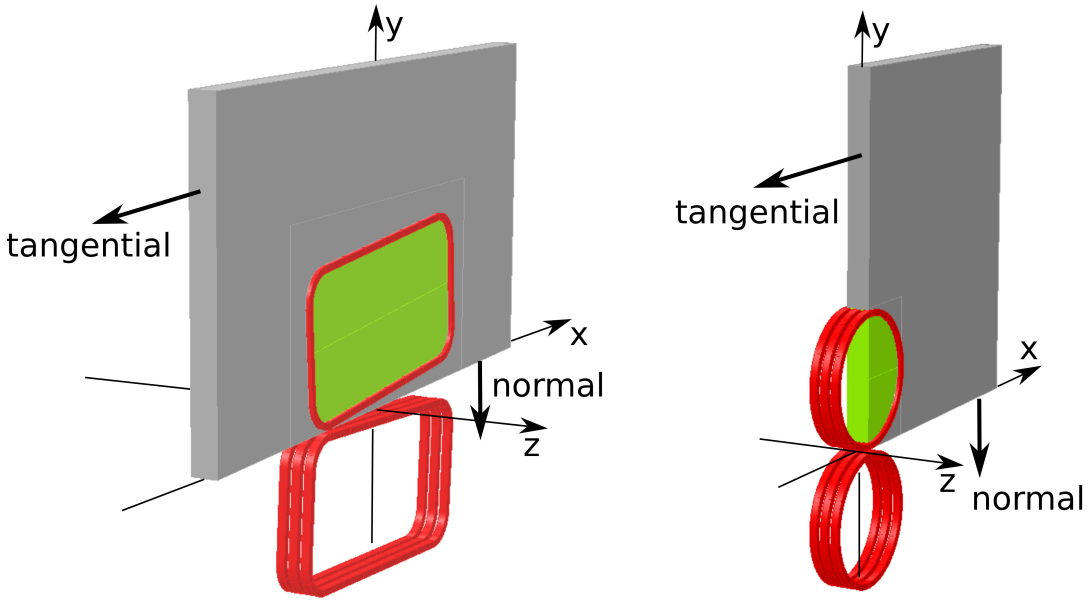

Figure 2.8: Background of both undulators: tilted (left) and cylindrical (right). Boundary conditions are applied to the background faces. Only the coils of the central period are displayed to see the background better.

- Mesh generator: In this module the volume of interest is divided into a number of smaller sub-volumes. The operation of partitioning is also called mesh generation. In the 3D Modeller the mesh generation is realized in two stages: the cells (surface of volumes) are first discretized into triangles or quadrangles. After this the volume mesh is done, starting from the surface mesh, each cell is subdivided into tetrahedra, hexahedra or prismatic elements. Figure 2.9 shows the model body with the mesh of both undulators:

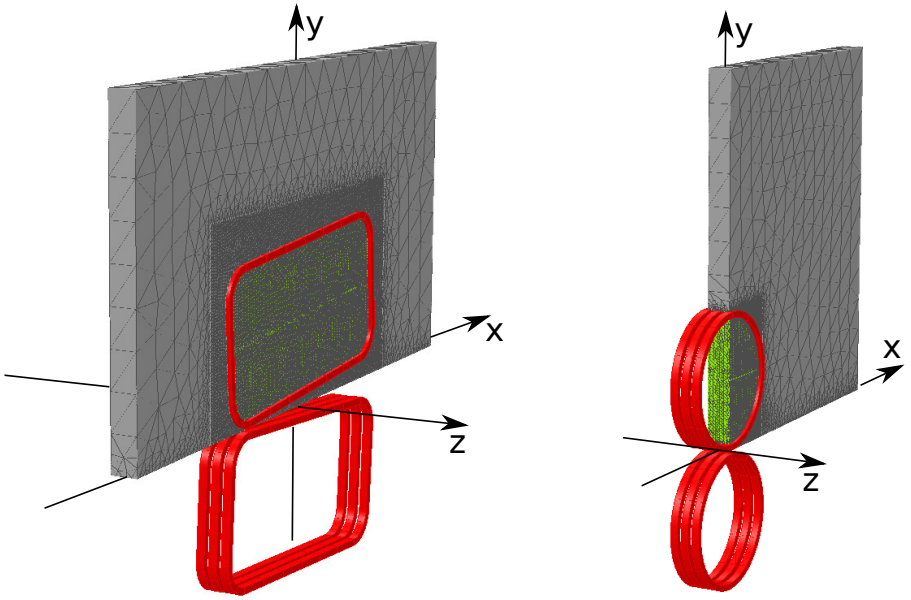

Figure 2.9: Model body with the mesh of both undulators: tilted (left) and cylindrical (right). Only the coils of the central period are displayed to see better the mesh.

The magnetic field is calculated later at each vertex point of each sub-volume. These vertex points are called nodes. It is necessary to adopt an optimal compromise between the precision and accuracy of the field computation on the one hand and the computing time on the other. Having to many elements results in an excessive time for solving. However, having too few elements gives poor precision [37].

A parametrization of both undulator models, tilted and cylindrical, was performed. This allows more rapidly to adjust the mesh element size in different parts of the model. It is common practice to vary the mesh size from one region to another and to use the smallest mesh size at places where a high precision in the field is required.

- Solver: This is a process, which may take from a few minutes to a few hours of CPU time depending on the number of nodes. In this thesis the software OPERA [46] was employed. The included package TOSCA-3D solves non-linear magnetostatic or electrostatic field and current flow models in three dimensions. TOSCA uses a formulation based on scalar potentials, solved using finite element discretization. Equations of Section 2.2.1 and the respective equations for material with finite, non-linear magnetic susceptibility are solved for each node. The solution for each node depends on the solutions for its neighbours, therefore the solution has to be iterated. When the output of two successive nonlinear solutions are similar (within a predefined tolerance), the nonlinear solution has converged. TOSCA solves numerically non-linear analysis using either Newton-Raphson which are fast or simple iterations which are very robust. When the solver terminates execution, the field is known at each node [46].

- Post-processor: It provides facilities to make linear plots, graphs, contour plots, etc. of the electromagnetic fields inside the computation volume. The field at any point is determined by a suitable interpolation of the potential computed at each node by the solver. Other important quantities can be computed by the post-processor such as the field integrals, magnetic forces or particle trajectories through the calculated fields.

All the model bodies included in this thesis are made at least ten full periods long in order to avoid field distortions due to finite length effects. In OPERA-3D the conductor fields are always calculated from all conductors even if they are not included in the model body [46].

2.2.2.1 BH curve

The TOSCA program uses material characteristics to relate flux density B and field intensity H of all materials (except air). The graph between B and H is known as the magnetization curve or BH curve of the material [47]. For soft magnetic materials the BH curve should be defined in the first quadrant, with the first values of B and H both zero. For magnetic materials, la relation between B and H is given by:

$$\frac{B}{H} = \mu = \mu_0 \mu_\mathrm{r} \tag{2.40}$$

where μ is the permeability of a specific material, $\mu_0 = 4\pi \times 10^{-7}\,\mathrm{Tm/A}$ is the vacuum permeability and μ_r is the relative permeability and is not constant but varies with H.

From the BH curve it can be seen that, as the flux density H is increased from zero, the flux B increases up to a certain maximum value of flux. The magnetic material is said to be saturated. Above saturation, B increases at a much smaller rate with respect to increasing H. This means that μ_r gets effectively smaller as B increases. In saturation, the slope dB/dH is approximately equal to μ_0.

OPERA has a library of materials containing BH curve data specific for use in a magnetic analysis. It is possible to create new BH curves saving in a datafile a table of pairs of values with at least five points that define the curve and the program extrapolates the data. The BH curve of OPERA called "tenten.bh", which is equivalent to low carbon steel AISI 1010, was used for the simulations of the iron models of both undulators. For this material, full saturation would be reached at $B_{min} = 2.13\,\mathrm{T}$, marked with a red point in Figure 2.10.

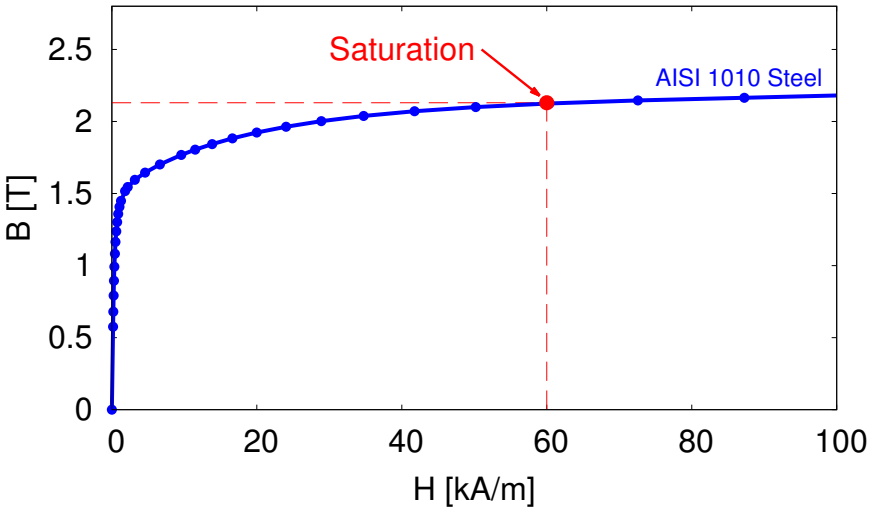

Figure 2.10: BH curve of the OPERA "tenten.bh" datafile equivalent to low carbon steel AISI 1010 [48].

2.2.2.2 Conductors

In TOSCA magnetostatic analysis conductors of different pre-defined shapes with a finite cross-section are used as the sources for the magnetic field. The current density J is uniform over the cross-section of the conductors. Used in this way, conductors are referred to as Biot-Savart conductors. Biot-Savart conductors are not part of the finite element mesh [48]. They are defined separately from the mesh and the magnetic fields created by a current circulating in a conductor can be computed using the Biot-Savart law:

$$\vec{B}\left(\vec{r'}\right) = \mu_0 \int\int\int J \frac{d\vec{l} \times \left(\vec{r} - \vec{r'}\right)}{\left|\vec{r} - \vec{r'}\right|^3} dS \tag{2.41}$$

where $\vec{r}$ is a point running along the conductor, $\int d\vec{l}$ is a longitudinal integration along the direction of the current and $\int\int dS$ is a 2D transverse integration made over the cross section of the conductor [37].

Equation (2.41) shows that for iron-free undulators the field on axis is proportional to the current density. If iron is involved, the field in undulators can not be calculated by using only the Biot-Savart law and the use of FEM is necessary [18]. In the case of iron-free undulator models, the magnetic fields can be evaluated by direct integration of the defined Biot-Savart conductors in the OPERA-3D post-processor. In this case any mesh is necessary, so the steps of building a Finite Element mesh and solving are omitted.

In this thesis only two pre-defined conductor geometries, solenoid and racetrack, are used. To enable conductors to be oriented in space correctly, local coordinate systems in OPERA-3D can be defined. The local coordinate system 1 ($LCS1$) is formed by displacing the origin with respect to the global origin to coordinates and rotating by Euler angles.

- Solenoid-coil: it shows rotational symmetry and can only be orientated with $LCS1$ without the Euler angles (see Figure 2.11). The quadrilateral cross section of the solenoids in the local xy-plane is defined by the coordinates of the 4 corners $(XP_1, YP_1, ..., XP_4, YP_4)$. Positive currents flow in the positive z-direction across the positive x-half of the xy-plane, assuming that the vertices of the cross section have been defined in a clock-wise sense, as shown in Figure 2.11; otherwise the direction of current flow is reversed.

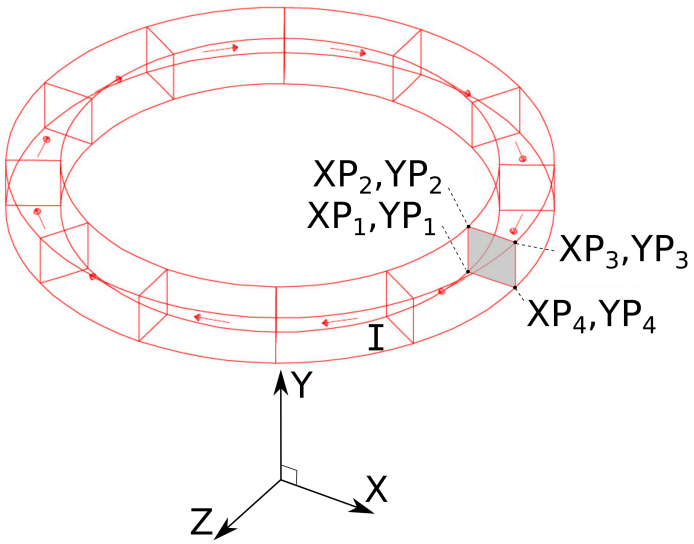

Figure 2.11: A solenoid in OPERA-3D [48].

- Racetrack-coil: it has a restricted set of symmetries can only be orientated with $LCS1$ without the Euler angles (see Figure 2.12). The racetrack is made up of four straight sections and four 90 degrees arcs. The cross section is rectangular, defined by its *width* in local x-direction and *thickness* in local y-direction. The coordinates of the bottom inside edge as it crosses the xy-plane are given by (XP_1, YP_1). The half-length of the z-directed straight is

H_1 and the inside radius of the corners is R_1, which must be greater than zero. Positive currents flow in the positive z-direction across the positive x-half of the xy-plane.

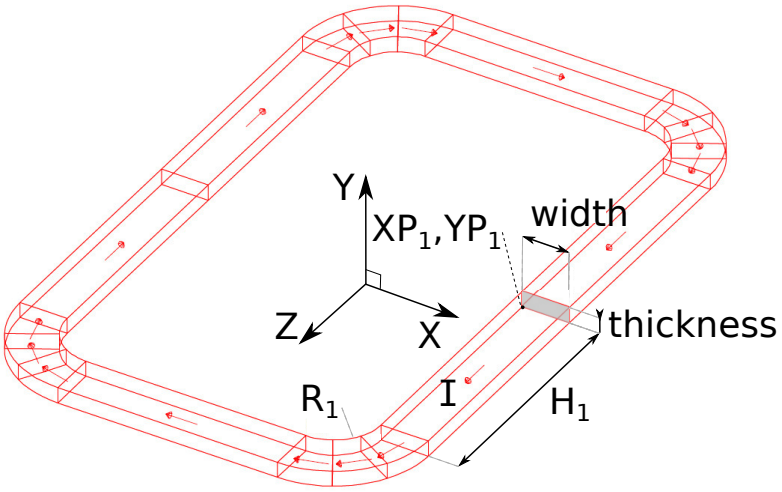

Figure 2.12: A racetrack in OPERA-3D [48].

3. TGU optimization

3.1 Magnetic chicane for beam dispersion

The idea to develop a very compact high-brilliance X-ray radiation source by applying a compensation scheme to the relatively high energy spread of the LWFA was introduced in Section 1.2. The parameters of the electron bunches generated by this laser vary with the operation parameters. For the design optimization of both TGU designs particularly for the LWFA at the University of Jena, a reference electron energy of $\mathrm{E}_0 = 120\,\mathrm{MeV}$ with an energy spread of $\Delta\mathrm{E}/\mathrm{E}_0 = \pm 10\,\%$ was assumed. The latter assumption is rather conservative taking into account not only the single bunch properties but also a reasonable range for shot-to-shot fluctuations.

The electron beam spatially dispersed ($\gamma \rightarrow \gamma(x)$) by a magnetic chicane is sent into the TGU with a x-dependent flux density amplitude ($B_0 \rightarrow B_y(x)$). The magnetic field $B_y(x)$ has to match the spatial energy distribution of the electrons after the chicane $\gamma(x)$ to get a constant wavelength [16]. The matching is achieved if the modified undulator equation (3.1)

$$\lambda = \frac{\lambda_\mathrm{u}}{2\gamma(x)^2}\left(1 + \frac{(93.36 B_y(x)[\mathrm{T}]\lambda_\mathrm{u}[\mathrm{m}])^2}{2}\right) = constant \tag{3.1}$$

is satisfied. The electron with different energies oscillate at the same amplitude and frequency. The optimization goal in this thesis is to match the TGU design and the electron beam dispersion such that the relative deviation of wavelengths emitted by the reference electrons of different energies is lower than the natural bandwidth:

$$\Delta\lambda/\lambda_0 = \left(\lambda_\mathrm{max} - \lambda_\mathrm{min}\right)/\lambda_0 \leq 1/\mathrm{N} \approx 1\,\% \tag{3.2}$$

with $\mathrm{N} = 100$ undulator periods.

In this thesis the dispersion of the electron beam $\gamma(x)$ is generated by a simplified model of a dogleg chicane consisting of two dipole magnets (see Figure 3.1). This assumption is sufficient as long as only the trajectories of the reference particles to different energies are considered. In contrast to that, the chicane that takes into

account the finite emittance of the electron beam is subject to a dedicated research project (which will not be covered by this thesis) [WAB+11, WAB+13b].

A particle with a momentum deviation $\delta = \triangle p/p_0 \approx \triangle E/E_0$ has a different bending angle in a dipole magnet [36]. The function D is called the dispersion function and $x_\delta = \delta D$ determines in linear approximation the offset of the ideal path from the reference trajectory for particles with a relative energy deviation δ from the ideal momentum cp_0 [51]. The beamlet has a finite transversal extension or width σ_x (see Figure 3.1).

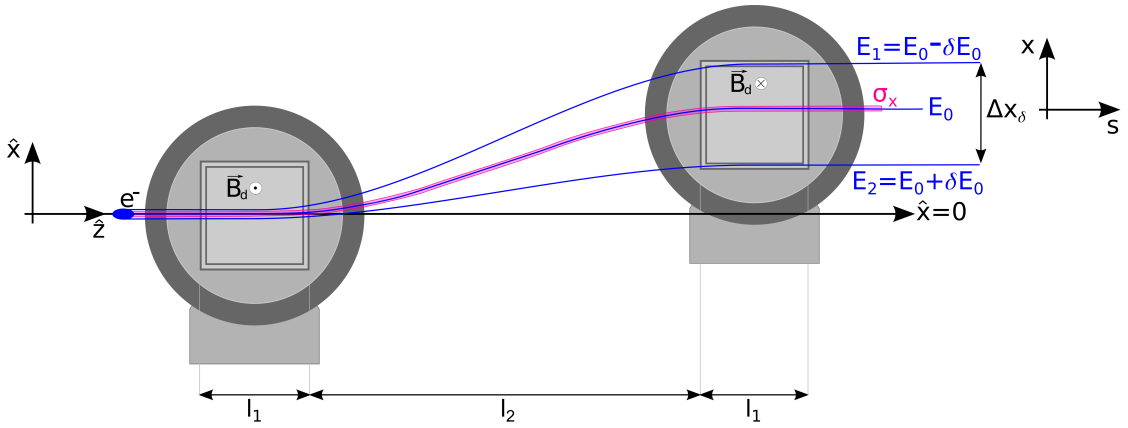

Figure 3.1: Schematic view of the simplified magnetic chicane consisting in two dipole magnets in gray. This setup separates the different electron energies, which are represented in blue and the beamlet width in pink.

The electrons describe a circular path with the Larmor radius for relativistic electrons (see Equation (3.3)) after traversing the first dipole magnet. Electrons with different energy show a different exit angle. The bending radius in the dipole is proportional to γ and is given by:

$$r_L(\gamma) = \frac{m_e c}{e B_d}\gamma \tag{3.3}$$

where all the terms are constant except γ. The constant terms are: m_e is the rest mass of the electron, c is the speed of light, e is the elementary electric charge and B_d is the homogeneous flux density in the dipoles.

After the second dipole magnet all electrons are brought again parallel to the z-axis, but beamlets with different energies are now separated. The two dipole magnets have the same field strength ($\vec{B_d}$), but reverse field direction. After the second dipole magnet ($z \geq 2l_1 + l_2$) the trajectories are displaced by:

$$\hat{x} = 2r_L(\gamma) - 2\sqrt{r_L^2(\gamma) - l_1^2} + \frac{l_1 l_2}{\sqrt{r_L^2(\gamma) - l_1^2}}, \tag{3.4}$$

where l_1 is the pole length and l_2 is the distance between the two dipoles. The dispersion is greater for the electron which has a lower energy. The total dispersive beam splitting is given by:

$$\Delta x_{\delta=\pm 10\,\%} = \hat{x}_{(E_0 - 10\,\% E_0)} - \hat{x}_{(E_0 + 10\,\% E_0)} \approx D\delta_1 - D\delta_2 \tag{3.5}$$

in the fixed reference system $(\hat{x}, \hat{z})$ and in the moving reference system (x, s) respectively. It should not exceed the value of $\Delta x_{\delta=\pm 10\,\%} \approx \pm 2\,\mathrm{mm}$ at the entrance of the undulator by the beam optics.

Figure 3.2 shows the calculation of the maximum value of Δx_δ through the extreme energies (E_1 and E_2), which produce undulator radiation at different locations (x_{E1} and x_{E2}). The radiation cone of these extreme energies should overlap at a fixed observation point. The half-angle of the "central radiation cone" is given by [52]:

$$\Theta_0 \approx \frac{1}{\gamma\sqrt{\mathrm{N}}}. \tag{3.6}$$

The radiation cone of each electron energy produces at the observation point a radiation spot with a width:

$$\Delta x_\mathrm{E} = \mathrm{d}\tan\left(\Theta_0\right) = \mathrm{d}\tan\left(\frac{1}{\gamma\sqrt{\mathrm{N}}}\right), \tag{3.7}$$

where d is the distance to the observation point.

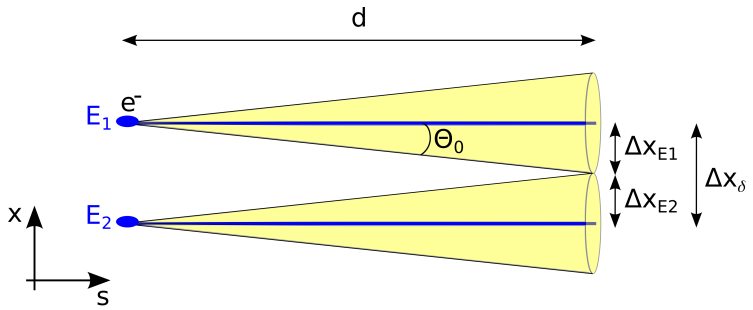

Figure 3.2: Maximum value of the total dispersive beam splitting Δx_δ for the energies between E_1 and E_2, which is calculated through the overlap of the radiation cones at a distance d to the observation point.

Therefore the maximum value of the total dispersive beam splitting for the energies between E_1 and E_2 should not exceed $\Delta x_\delta = \Delta x_{\mathrm{E1}} + \Delta x_{\mathrm{E2}}$, since then the radiation cones of both energies just have an overlap. It applies:

$$\Delta x_\delta = \mathrm{d}\left[\tan\left(\frac{1}{\gamma_{\mathrm{E1}}\sqrt{\mathrm{N}}}\right) + \tan\left(\frac{1}{\gamma_{\mathrm{E2}}\sqrt{\mathrm{N}}}\right)\right]. \tag{3.8}$$

The goal is the development of a very compact radiation source. For this reason a distance to the observation point of $\mathrm{d} = 5\,\mathrm{m}$ is selected. For a 100 periods undulator and extreme energies of $\mathrm{E}_1 = 108\,\mathrm{MeV}$ and $\mathrm{E}_2 = 132\,\mathrm{MeV}$, the maximum value of the total dispersive beam splitting is $\Delta x_\delta = 4.3\,\mathrm{mm}$.

The dipole parameters used in the calculations above are taken from the real dipole parameters magnets (see Figure 3.3) foreseen to be used in the experiment in Jena. The complete characterization of these dipole magnets can be seen in [53]. The fixed dipole parameters used in the analytical calculation of this thesis were the width of the pole l_1 and the homogeneous flux density B_d. Table 3.1 shows the values of these parameters.

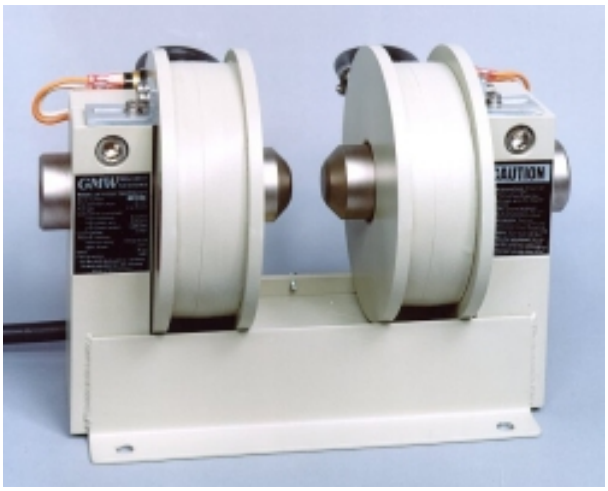

Figure 3.3: GMW Electromagnetic Dipole used in the chicane.

Description	**Parameter**	**Value**
Pole width	l_1	50 mm
Extra square poles	-	50×50 mm
Pole gap	-	20 mm
Max. continuous power (water)	-	5 A, 44 V, 0.22 kW
Homogeneous flux density	B_d	0.46 T

Table 3.1: Dipole parameters.

Using Equation (3.4) the displacement of the trajectories $\hat{x}$ for the energies between E = 120 MeV ± 10 % is calculated and it is shown in Figure 3.4. In these calculations the chicane parameters are kept constant except the distance between the two dipoles l_2, which can vary between 0 and 1.2 m (maximum space assumed for the chicane in the laboratory). In the experiment with the real chicane, there is only limited space to vary l_2 because of additional magnets placed in between the dipoles. Therefore one would rather vary B_d.

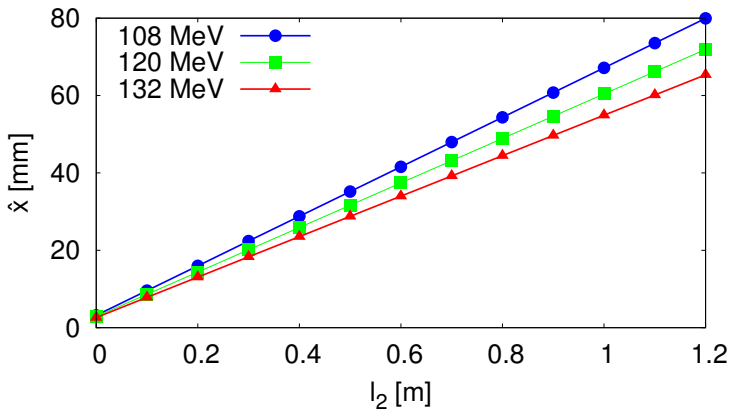

Figure 3.4: Displacement of the electron trajectories after the second dipole ($\hat{x}$) for the energies 108 MeV, 120 MeV and 132 MeV versus the distance between the two dipoles (l_2).

The total dispersive beam splitting $\Delta x_{\delta=\pm 10\,\%}$ is calculated using Equation (3.5), which result is shown in Figure 3.5. By the optimization of l_2 the total dispersive beam splitting and thereby the position of each electron energy x_{E} at the entrance of the undulator are optimized.

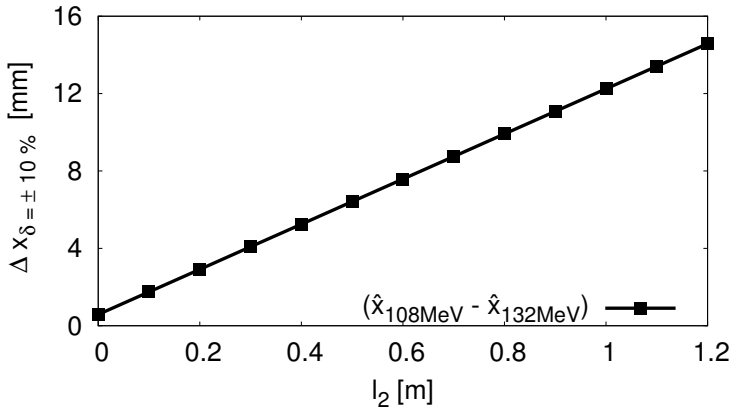

Figure 3.5: Total dispersive beam splitting ($\Delta x_{\delta=\pm 10\,\%}$) versus the distance between the two dipoles (l_2).

3.2 Downhill simplex optimization method

In this thesis the downhill simplex algorithm was employed to optimize the geometry of the TGU. The description of this algorithm and the source code in C++ from [54] employed in this thesis is shown in Appendix A.1.

3.2.1 Selection of the parameters to optimize

Figure 3.6 shows a schematic view of the tilted undulator and its main parameters. The alternating magnetic field with a period length λ_{u} is produced by superconducting coils powered with alternate polarity. The coils are wound into grooves between the steel poles. In this kind of undulator the two coils are tilted against each other about the z-axis by the angle $\alpha' = 2\alpha$.

As discussed in Section 3.1, the parameter l_2 (distance between the two dipoles in the chicane) is optimized and with it the total dispersive beam splitting $\Delta x_{\delta=\pm 10\,\%}$ and the transverse electron position $x(E)$.

From Equation (2.32) it can be seen that the transverse field gradient of the tilted undulator depends on the parameter α and $\tilde{B}$ for a fixed period length λ_{u}. $\tilde{B}$ is calculated with a FEM-Software and it depends on λ_{u}, the operating current density and the material of the undulator. Hence the second parameter to be optimized in the case of the tilted parameter is the angle α.

The transverse position of the beam center x_{E_0} depends on the gap width $\mathrm{g}_{\mathrm{E}_0}$ and the value of α. It is calculated through the expression

$$x_{\mathrm{E}_0} = \frac{g_{\mathrm{E}_0}/2}{\tan(\alpha)}. \tag{3.9}$$

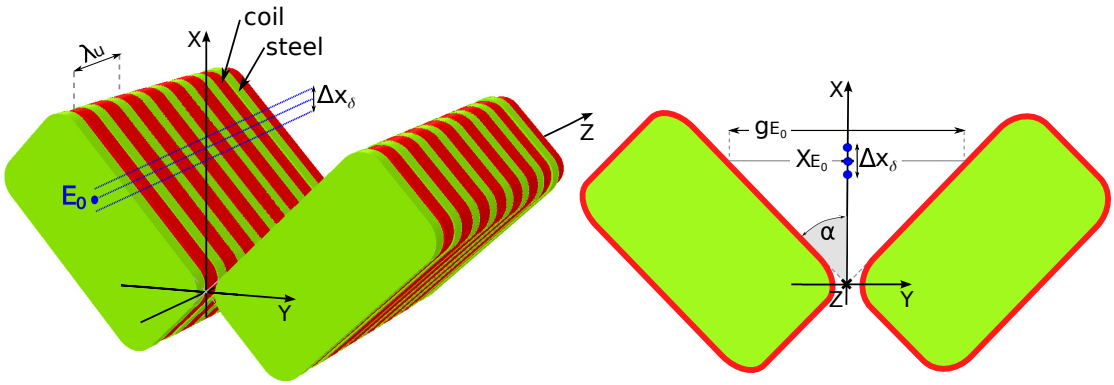

Figure 3.6: Schematic view of the tilted undulator and its parameters.

The desirable minimum gap width is $g_{E_0} = 2\,\text{mm}$. It is recommended that the transverse position of the beam center $x_{E_0} >> g_{E_0}$, to avoid undesired magnetic fields produced at the edges of the tilted undulator (in $x = 0$) [38]. Therefore the minimum $x_{E_0} = 20\,\text{mm}$ is selected. For the minimum g_{E_0} and minimum x_{E_0}, the value of the angle is $\alpha = 2.86\,\text{degrees}$.

The value of α is obtained by the optimization of the tilted undulator. If this value is $\alpha < 2.86\,\text{degrees}$, then $g_{E_0} = 2\,\text{mm}$ is taken to calculate the value of x_{E_0}, which results $> 20\,\text{mm}$. Else for values of $\alpha \geq 2.86\,\text{degrees}$, the value of x_{E_0} is fixed to the minimum 20 mm and the value of g_{E_0} is $> 2\,\text{mm}$.

The schematic view of the cylindrical undulator is shown in Figure 3.7. The geometric parameters of this kind of undulators with a fixed period length λ_u are: the external pole radius (r) and the gap on symmetry axis (g).

Like in the case of the tilted undulator, the parameter l_2 (distance between the two dipoles in the chicane) is optimized and with it the total dispersive beam splitting $\Delta x_{\delta=\pm 10\,\%}$ and the transverse electron position $x(E)$.

From Equation (2.38) it can be seen that the transverse field gradient of the cylindrical undulator depends on the parameters g, r and $\tilde{B}$ for a fixed period length λ_u. The maximal flux density in the beam plane $B_0 = B_y^{\max} = B_y(x = 0, y = 0, z = \lambda_u/4)$ modifies the field gradient of the cylindrical undulator and its value depends on the values of g, r and $\tilde{B}$. For this reason $B_y^{\max}$ is selected as the second parameter to be optimized.

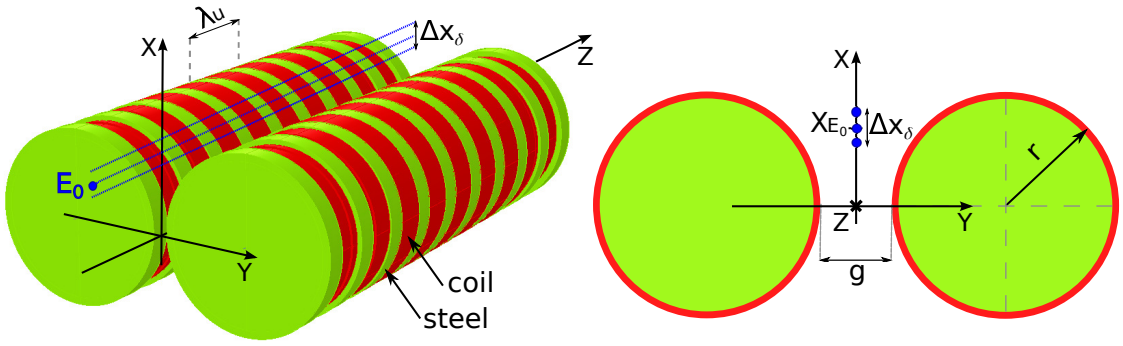

Figure 3.7: Schematic view of the cylindrical undulator and its parameters.

In summary, the two parameters selected to optimize the tilted undulator are l_2 and α and in the case of the cylindrical undulator l_2 and $B_y^{\max}$.

3.2.2 Function to minimize

As introduced in Section 3.1, the optimization goal is to get a constant wavelength of the undulator radiation despite the $\pm 10\,\%$ energy spread. The magnetic field $B_y(x)$ has to match the spatial energy distribution of the electrons after the chicane $\gamma(x)$ to get a constant wavelength equal to the wavelength emitted for the central energy λ_0. The objective function selected to be minimized is:

$$f(x) = \frac{\Delta\lambda}{\lambda_0} = \frac{(\lambda_{\max} - \lambda_{\min})}{\lambda_0}, \tag{3.10}$$

where the wavelength for each beamlet is calculated using directly the undulator equation.

3.2.3 Field on the pole surface of the tilted undulator

It is necessary to know the value of the magnetic field $\tilde{B}$, before performing the optimization of the tilted undulator. $\tilde{B}$ is the field on the pole surface of the undulator, which is required to calculate B_y by using Equation (2.32). The value of $\tilde{B}$ is calculated using the FEM-software OPERA-2D. Figure 3.8 (left) shows the tilted undulator and a plane perpendicular to its surface. The cut produced by this perpendicular plane in one central period of the undulator is the view represented in OPERA-2D (see Figure 3.8 (right)). It is necessary to assume a large gap to simulate only one half of the undulator.

The value of $\tilde{B}$ depends on the undulator design parameters. Table 3.2 summarizes the main parameters assumed to calculate $\tilde{B}$ in three tilted undulator models with different period lengths and pole widths. After solving the model in OPERA-2D, the $\tilde{B}$ is obtained in the post-processor by calculating the field on a point at the center of the surface of one pole.

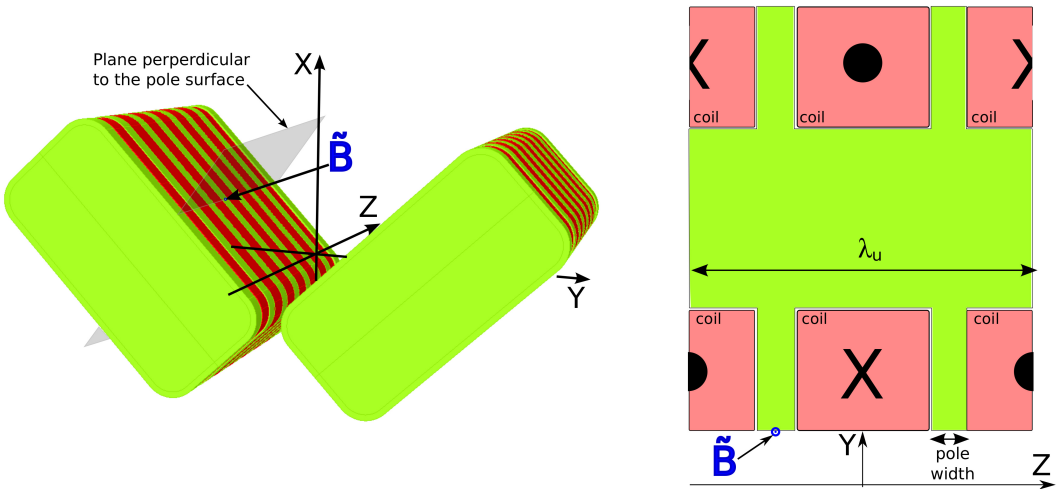

Figure 3.8: Left: plane perpendicular to the surface of the tilted undulator pole. Right: longitudinal view of half tilted undulator. It is shown only the central period of the undulator to calculate $\tilde{B}$ in OPERA-2D.

Common design parameters:		
Gap (perpendicular surface): $g_\perp = 20\,\text{mm}$		
Current density: $J = 1000\,\text{A/mm}^2$		
Wire cross-section (insulated): $0.77\,\text{mm} \times 0.51\,\text{mm}$		
Coil winding package: $5\,\text{layers} \times 4\,\text{turns}$		
Material: steel AISI 1010		
λ_u [mm]	pole width [mm]	$\tilde{B}$ [T]
8	0.92	1.768
10	1.92	1.689
15	4.42	1.231

Table 3.2: Calculation of $\tilde{B}$ with OPERA-2D for different tilted undulator models.

3.2.4 Fourier expansion of the cylindrical undulator field

Before starting the optimization process of a cylindrical undulator, it is necessary to calculate the value of $\tilde{B}$, which is employed to calculate analytically the magnetic field through Equation (2.38). In the case of the cylindrical undulator, $\tilde{B}$ is calculated through the maximal field on axis $B_y^{\max}$, which depends on the undulator design parameters. Table 3.3 summarizes the main parameters assumed to simulate an example of a cylindrical undulator model. After solving this model in OPERA-3D, $B_y^{\max}$ is obtained in the post-processor by calculating the magnetic field on a point at $(x, y, z) = (0, 0, \lambda_u/4)$.

Design parameters:
Period length: $\lambda_u = 10\,\text{mm}$
Gap width on axis: $g = 1.5\,\text{mm}$
Pole radius: $r = 30\,\text{mm}$
Current density: $J = 1200\,\text{A/mm}^2$
Wire cross-section (insulated): $1.0\,\text{mm} \times 0.6\,\text{mm}$
Coil winding package: $6\,\text{layers} \times 4\,\text{turns}$
Material: steel AISI 1010
$B_y^{\max} = 2.438\,\text{T}$

Table 3.3: Calculation of $B_y^{\max}$ with OPERA-3D for a cylindrical undulator model.

The value of $\tilde{B}$ is cleared from Equation (2.38) and results:

$$\tilde{B}(0, 0, \lambda_u/4) = \frac{B_y^{\max}}{\sin(k_u z)\left[K_1\left(k_u \rho_o\right)\hat{e}_{\rho,o} + K_1\left(k_u \rho_u\right)\hat{e}_{\rho,u}\right]}.$$

Figure 3.9 shows the difference between the transverse field gradient $B_y(x)$ calculated analytically with Equation (2.38) and the field exported directly from the FEM-software OPERA-3D.

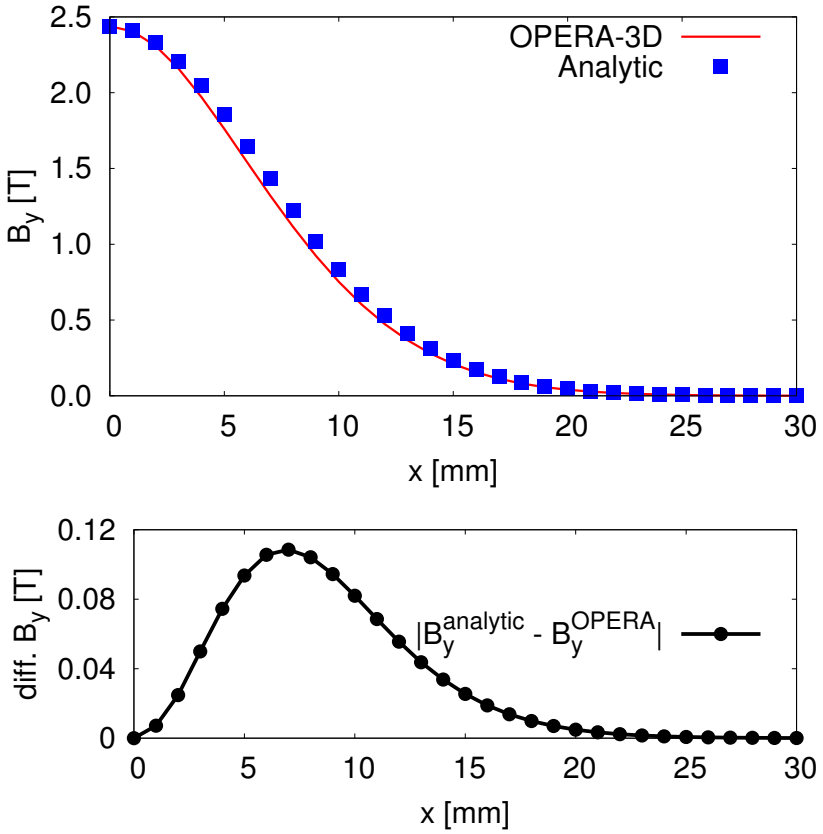

Figure 3.9: Top: B_y as function of x-position as calculated by OPERA-3D (red line) and by Equation (2.38) (blue points). Bottom: absolute difference between both magnetic fields (black line-points).

The reason of this difference is that the z-dependence of the field is not purely sinusoidal as assumed in the analytical model but exhibits higher harmonics. Therefore a Fourier series expansion (see Appendix C) has to be applied in the separation ansatz for the Laplace Equation (2.29) instead of the simple sine function (Equation (2.28)). This results in a series expansion also for the magnetic flux density calculated by Equation (2.39). To correct this difference, a modification of the analytical Equation (2.38) is done to add the Fourier coefficients of the magnetic field.

The field $B_y(z)$ (see Figure 3.10) on a line at $x = 0$ $y = 0$ and z-values between $-\lambda_u/2$ and $+\lambda_u/2$ is calculated in OPERA-3D for the same cylindrical undulator model. Then the Fourier coefficients b_n of $B_y(z)$ are exported and employed in the analytical calculations of the magnetic field through Equation (2.39).

Figure 3.11 compares the transverse field gradient $B_y(x)$ calculated with the analytical expressions with Fourier coefficients and the field exported directly from the FEM-software OPERA-3D. The difference is reduced 10 times compared to the first analytical approach that takes into account only the $B_y^{\max}$. For this reason Equation (2.39) considering the Fourier coefficients of $B_y(z)$ is selected as a better approximation for the analytical calculation of the magnetic field of the cylindrical undulator.

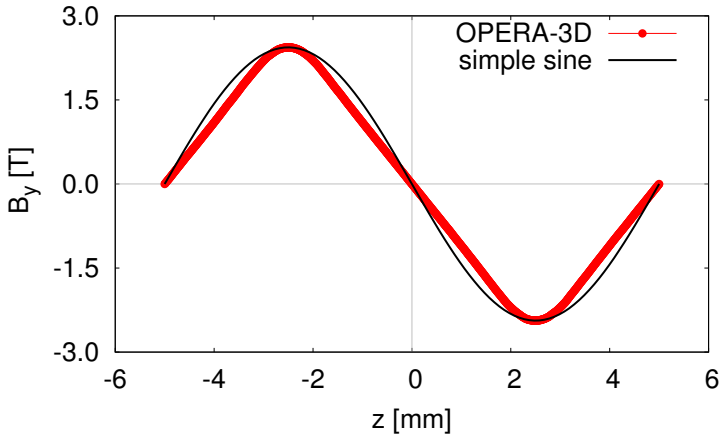

Figure 3.10: B_y as function of z-position, which is calculated in OPERA-3D (red line-points) for the central period of a cylindrical undulator model (design parameters are in Table 3.3). The dashed line (black line) represents the simple sine function: $-B_y^{\max} \sin(\mathrm{k_u} z)$.

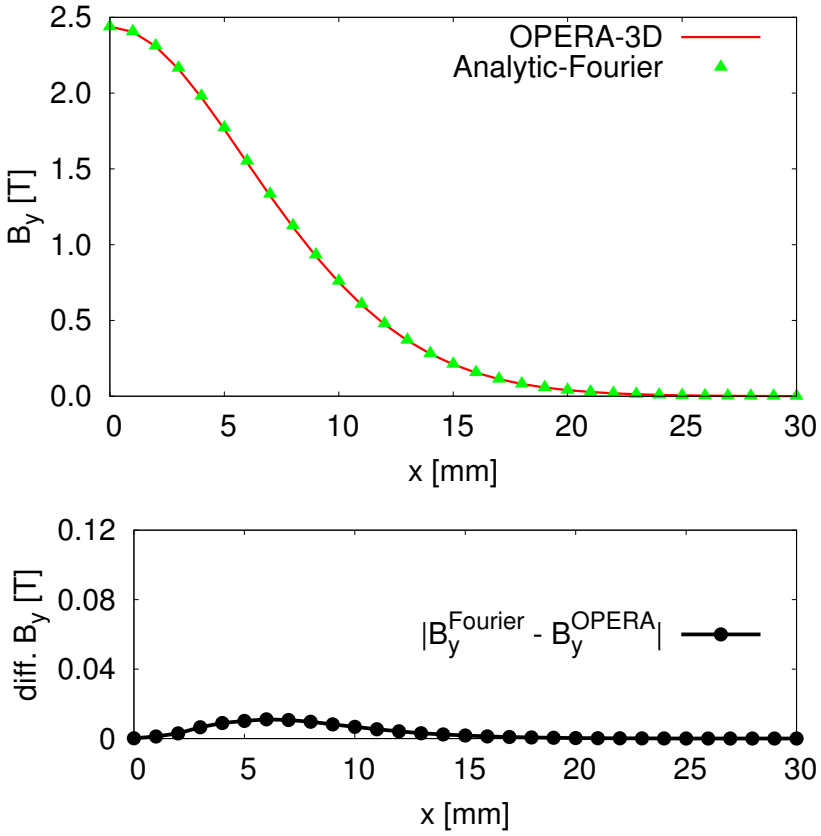

Figure 3.11: Top: B_y as function of x-position as calculated by OPERA-3D (red line) and by Equation (2.39) with Fourier coefficients (green points). Bottom: absolute difference between both magnetic fields (black line-points).

3.3 TGU geometry selection

3.3.1 Undulator optimization for several electron energies

The optimization of several tilted and cylindrical undulator models was performed for different central electron energies E_0: 100 MeV, 120 MeV, 200 MeV and 500 MeV. In all the cases the energy spread employed was $\delta = \pm 10\,\%$ and models with period lengths of 10 mm and 15 mm were simulated. Table 3.2 (in Section 3.2.3) and Table 3.4 show the main parameters of the tilted and cylindrical undulator models respectively.

Design parameters:
Gap width on axis: g = 2.5 mm
Pole radius: r = 30 mm
Current density: J = 1000 A/mm^2
Wire cross-section (insulated): 0.77 mm × 0.51 mm
Coil winding package: 5 layers × 4 turns
Material: steel AISI 1010

Table 3.4: Main parameters of the simulated cylindrical undulator models, which were employed in the optimization for different values of E_0.

The simplex with a size of [2×3] includes three initial iterations of the parameters to optimize. l_2 and α have to be optimized for the tilted undulators and l_2 and $B_y^{\max}$ for the cylindrical undulators. The three vertices of the triangle are formed with these values, as explained in Appendix A.1. Table 3.5 and Table 3.6 summarize the optimization results for the tilted and cylindrical undulator models respectively.

Table 3.5 shows that the relative deviation of wavelengths $\Delta\lambda/\lambda_0$ emitted for the tilted undulator models after their optimization is lower than 1 %. The value of $\Delta\lambda/\lambda_0$ for the models with 15 mm period length is about ten times lower than

E_0[MeV]	λ_u[mm]	Simplex l_2[m]	Simplex α[degrees]	Iter.	$f(x)$ $\Delta\lambda/\lambda_0$[%]	optimal l_2[mm]	optimal α[degrees]
100	10	[1.20, 0.80, 0.40]	[3.5, 1.0, 5.0]	147	0.457	741	2.86
	15	[1.25, 0.75, 0.35]	[3.5, 1.2, 5.0]	124	0.050	756	3.63
120	10	[0.50, 0.80, 1.50]	[2.3, 5.0, 4.0]	111	0.460	902	2.86
	15	[1.35, 0.50, 0.80]	[5.5, 2.0, 3.0]	94	0.050	922	3.65
200	10	[1.00, 2.00, 0.70]	[3.8, 5.0, 2.0]	140	0.467	1541	2.86
	15	[1.25, 2.00, 0.65]	[4.2, 6.5, 5.5]	120	0.050	1581	3.63
500	10	[2.30, 1.20, 1.75]	[5.0, 3.5, 2.5]	93	0.470	3933	2.86
	15	[0.30, 1.50, 2.70]	[1.5, 5.0, 2.1]	116	0.050	4041	3.62

Table 3.5: Optimization results of tilted undulator models with 10 mm and 15 mm period lengths. The tilted undulator parameter α and the chicane parameter l_2 are optimized to get the minimum $\Delta\lambda/\lambda_0$. Several central electron energies are taken in consideration.

E_0[MeV]	λ_u[mm]	Simplex l_2[m]	Simplex B_y^{max}[T]	Iter.	$f(x)$ $\Delta\lambda/\lambda_0$[%]	optimal l_2[mm]	optimal B_y^{max}[T]
100	10	[0.4, 1.0, 1.6]	[1.5, 1.7, 2.2]	103	0.482	242	1.830
	15	[0.4, 0.3, 0.1]	[1.9, 2.1, 1.3]	118	0.473	298	1.251
120	10	[0.4, 0.3, 0.1]	[1.9, 2.1, 1.3]	87	0.481	300	1.831
	15	[0.4, 1.2, 0.7]	[1.5, 1.7, 2.0]	98	0.472	368	1.252
200	10	[0.3, 0.5, 1.0]	[1.4, 1.7, 2.0]	91	0.480	535	1.833
	15	[2.6, 1.5, 0.2]	[1.0, 2.2, 0.8]	114	0.470	648	1.253
500	10	[0.7, 0.2, 0.5]	[1.5, 2.1, 1.8]	102	0.479	1413	1.834
	15	[2.6, 1.5, 0.2]	[1.0, 2.2, 0.8]	101	0.469	1696	1.254

Table 3.6: Optimization results of cylindrical undulator models with 10 mm and 15 mm period lengths. The maximal field on axis B_y^{max} and the chicane parameter l_2 are optimized to get the minimum $\Delta\lambda/\lambda_0$. Several central electron energies are taken in consideration.

the models with 10 mm period length, independent of E_0. The optimal values of l_2 are lower than 1.2 m for $E_0 \leq 120$ MeV. The optimal value of the half inclination angle α is independent of E_0 and is slightly higher for the models with 15 mm period length.

In the case of the optimized cylindrical models the value $\Delta\lambda/\lambda_0 < 1\,\%$ is also achieved independent of E_0, as shown in Table 3.6. For the models with 15 mm period length $\Delta\lambda/\lambda_0$ is slightly lower than with 10 mm period length. Only in the case of $E_0 = 500$ MeV the optimal value of l_2 is greater than 1.2 m. The optimal value of B_y^{max} is independent of the central energy value and its value is 1.83 T for the 10 mm period length and 1.25 T for the 15 mm period length.

3.3.2 Total dispersive beam splitting and beamlet width

Once the optimization of the parameters was realized, the calculation of the total dispersive beam splitting Δx_δ and the minimum beamlet width σ_x for each case was performed. The value of σ_x indicates the limit value of the beamlet width in x-direction, where $\Delta\lambda/\lambda_0 = 1\,\%$ is achieved. This means, that if the electron is drifted from its trajectory more than this value, then $\Delta\lambda/\lambda_0 > 1\,\%$. Table 3.7 and Table 3.8 summarizes the results for the tilted and cylindrical undulator models respectively. The x-position and the emitted wavelength λ_0 by the central electron energy are included. The C++ code used to perform these calculations is shown in Appendix A.2.

The total dispersive beam splitting for tilted undulator models (see Table 3.7) is always $\Delta x_\delta > 11$ mm. This value is independent of the value of E_0 and should not exceed ± 2 mm. For cylindrical models (see Table 3.8) however, the values of Δx_δ are always lower than 5 mm. The value of the beamlet width (σ_x) is larger than 0.2 mm for the tilted models and around 0.1 mm for the cylindrical models.

Figure 3.12 and Figure 3.13 compare the results of $\lambda(x)$ for both the tilted and the cylindrical undulator models. In all the graphs the results are calculated for

E_0[MeV]	λ_u[mm]	opt. l_2[mm]	opt. α[degrees]	x_0[mm]	λ_0[nm]	$\Delta\lambda/\lambda_0$[%]	Δx_δ[mm]	Min. σ_x[mm]
100	10	741	2.86	20.02	315	0.465	11.10	0.240
	15	756	3.63	20.00	593	0.050	11.31	0.256
120	10	902	2.86	20.02	219	0.469	11.10	0.240
	15	922	3.65	20.00	413	0.050	11.34	0.256
200	10	1541	2.86	20.02	79	0.469	11.10	0.240
	15	1581	3.63	20.00	149	0.050	11.38	0.258
500	10	3933	2.86	20.02	13	0.478	11.10	0.240
	15	4041	3.62	20.00	24	0.050	11.40	0.258

Table 3.7: Calculations of the relative deviation of wavelengths emitted ($\Delta\lambda/\lambda_0$), the total dispersive beam splitting (Δx_δ) and the beamlet width (σ_x) for the optimized tilted undulator at different central energies.

E_0[MeV]	λ_u[mm]	opt. l_2[mm]	opt. B_y^{max}[T]	x_0[mm]	λ_0[nm]	$\Delta\lambda/\lambda_0$[%]	Δx_δ[mm]	Min. σ_x[mm]
100	10	242	1.830	6.56	204	0.482	4.10	0.096
	15	298	1.251	8.50	307	0.473	4.88	0.114
120	10	300	1.831	6.56	142	0.481	4.09	0.096
	15	368	1.252	8.50	214	0.472	4.88	0.114
200	10	535	1.833	6.56	51	0.480	4.08	0.096
	15	648	1.253	8.50	77	0.470	4.87	0.114
500	10	1413	1.835	6.56	8	0.479	4.08	0.096
	15	1696	1.254	8.50	12	0.470	4.87	0.114

Table 3.8: Calculation of the relative deviation of wavelengths emitted $\Delta\lambda/\lambda_0$, total dispersive beam splitting Δx_δ and beamlet width σ_x of the optimized cylindrical undulator for different central energies.

different E_0 values. The results of the models with a period length of 10 mm are shown in the graphs on the left and with a period length of 15 mm on the right. For the same period lengths and central energies the wavelengths emitted for the tilted models are much larger than for the cylindrical models.

3.3.3 Final selection of the undulator geometry

The central energy of 120 MeV was finally assumed. The period length of 10 mm was selected, because of resulting the lowest emitted wavelength values. Table 3.9 summarizes the results of the total dispersive beam splitting for several tilted undulator models with different α values. Cylindrical undulator models with different g values (gap width on axis) were simulated, which results are summarized in Table 3.10.

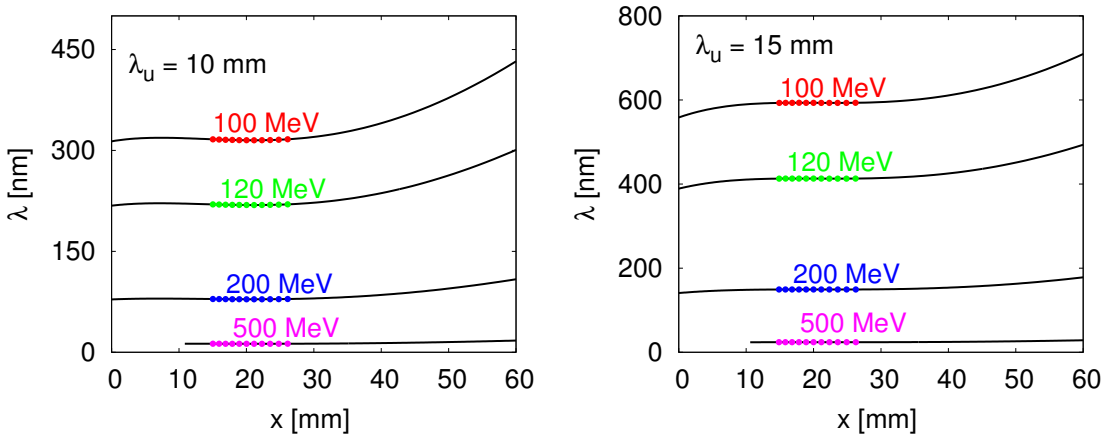

Figure 3.12: Simulated resulting wavelength of the radiation emitted as a function of x-position (black lines). The wavelengths are optimized for different central energies (in color points), for the tilted undulator models with period lengths of 10 mm (left) and 15 mm (right).

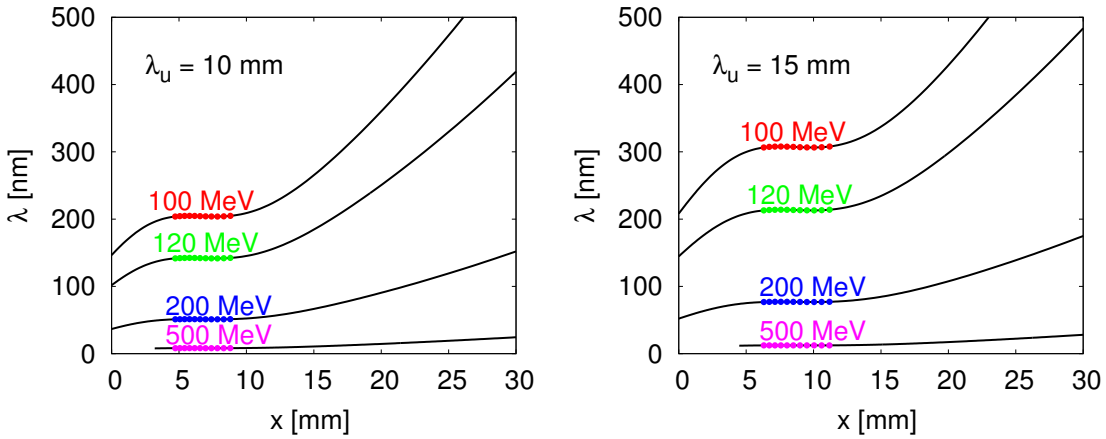

Figure 3.13: Simulated resulting wavelength of the radiation emitted as a function of x-position (black lines). The wavelengths are optimized for different central energies (in color points), for the cylindrical undulator models with period lengths of 10 mm (left) and 15 mm (right).

Table 3.9 shows that for tilted undulator models with angles $\alpha \leq 2.5$ degrees the optimized parameter $l_2 > 1.2$ m. However, for $\alpha \leq 3.5$ degrees the value of $\Delta\lambda/\lambda_0$ remains lower than 1 %. Δx_δ and σ_x values increase with decreasing α. With $\alpha = 2.86$ degrees, the minimum value of $\Delta\lambda/\lambda_0$ as well as the lowest value of Δx_δ are obtained. Figure 3.14 shows the results of the magnetic field and emitted wavelength for all the simulated tilted undulator models with different tilted angles.

Table 3.10 shows that the variation of the g values (gap width on axis) in the cylindrical undulator models does not affect the values obtained of $\Delta\lambda/\lambda_0$, Δx_δ and σ_x. For this reason the simulated magnetic field $B_y(x)$ and the emitted wavelength of only the cylindrical undulator model with g = 1.5 mm is shown in Figure 3.15.

Figure 3.16 shows the variation of $\Delta\lambda/\lambda_0$ and Δx_δ for different tilted angles α between 0.5 degrees and 4 degrees with a step size of 0.01 degrees. The Δx_δ values are always larger than 10 mm. The x_{E_0} is limited to a minimum value of 20 mm, as

α[degrees]	opt. l_2[mm]	x_0[mm]	λ_0[nm]	$\Delta\lambda/\lambda_0$[%]	Δx_δ[mm]	Min. σ_x[mm]
1.50	1764	38.19	219	0.461	21.16	0.460
2.00	1311	28.64	219	0.462	15.87	0.344
2.50	1039	22.90	219	0.462	12.70	0.276
2.86	902	20.02	219	0.463	11.10	0.240
3.50	836	20.00	188	0.937	10.33	0.214
4.00	820	20.00	168	1.412	10.15	-

Table 3.9: Calculation of the relative deviation of wavelengths emitted ($\Delta\lambda/\lambda_0$), the total dispersive beam splitting (Δx_δ) and the beamlet width (σ_x) for tilted undulator models with 10 mm period length and different tilted angles α. The central energy is 120 MeV.

g[mm]	opt. l_2[mm]	opt. $B_y^{\max}$[T]	x_0[mm]	λ_0[nm]	$\Delta\lambda/\lambda_0$[%]	Δx_δ[mm]	Min. σ_x[mm]
0.9	294	1.803	6.258	142	0.511	4.01	0.094
1.1	295	1.808	6.306	142	0.504	4.02	0.094
1.3	297	1.810	6.338	142	0.499	4.04	0.094
1.5	298	1.813	6.374	142	0.495	4.06	0.094
1.7	298	1.817	6.421	142	0.492	4.06	0.094
2.5	300	1.831	6.559	142	0.481	4.09	0.096

Table 3.10: Calculation of the relative deviation of wavelengths emitted ($\Delta\lambda/\lambda_0$), the total dispersive beam splitting (Δx_δ) and the beamlet width (σ_x) for several cylindrical undulator models with pole radius r = 30 mm and with different gap widths. The central energy is 120 MeV.

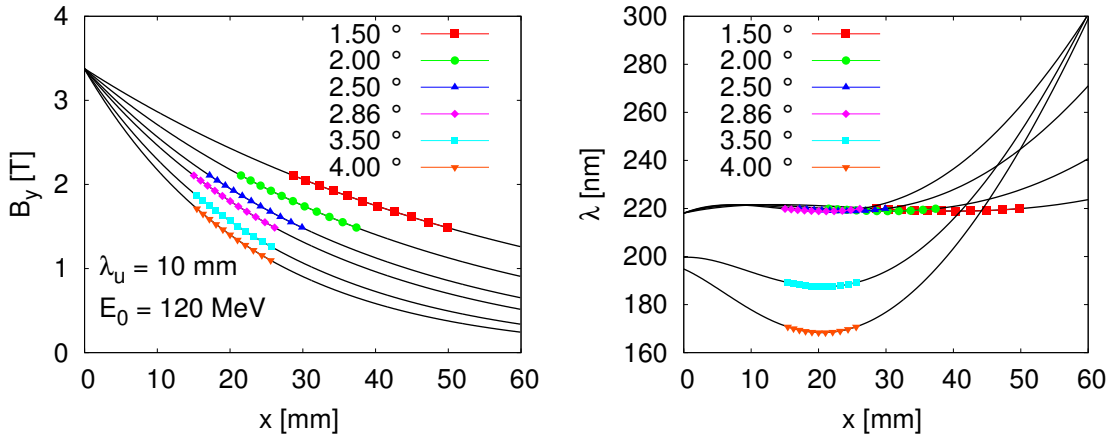

Figure 3.14: Tilted undulator models simulations with 10 mm period length and with different tilted angles α (in color points). Left: calculated magnetic field $B_y(x)$ (black lines). Right: resulting emitted wavelength $\lambda(x)$ (black lines).

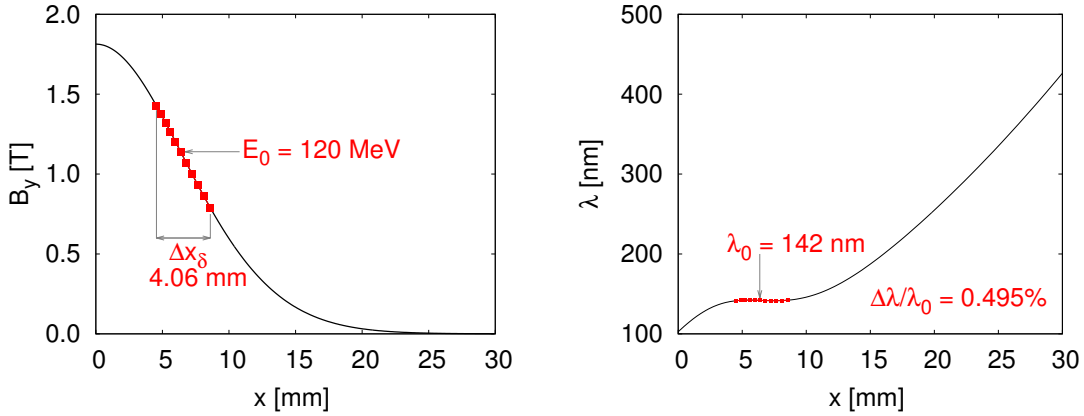

Figure 3.15: Simulation for a cylindrical undulator model with 10 mm period length and 1.5 mm gap width on axis (red points). Left: calculated magnetic field $B_y(x)$ (black lines). Right: resulting emitted wavelength $\lambda(x)$ (black lines).

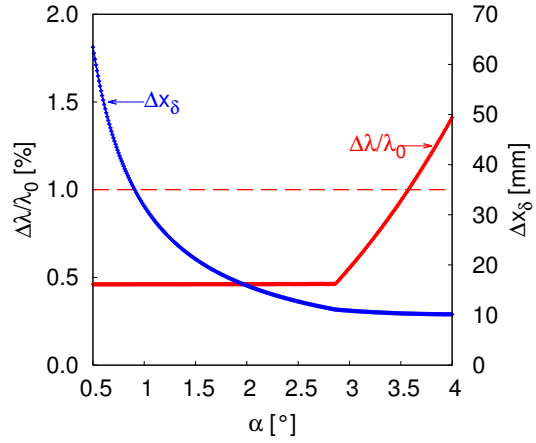

Figure 3.16: Calculation of $\Delta\lambda/\lambda_0$ (left axis, red line-points) and Δx_δ (right axis, blue line-points) for tilted undulator models with 10 mm period length and the tilted angle α between 0.5 degrees and 4 degrees. The red dashed line limits the maximum desired $\Delta\lambda/\lambda_0$ value to 1 %. The central energy is 120 MeV.

explained in Section 3.2.1. Therefore the lowest $\Delta\lambda/\lambda_0$ with a value almost constant of 0.462 % occurs from $\alpha = 0.5$ degrees to $\alpha = 2.86$ degrees. The minimum value of $\Delta\lambda/\lambda_0$ as well as the lowest Δx_δ are obtained for $\alpha = 2.86$ degrees.

Although with the tilted undulator geometry and technically realistic parameters it is possible to decrease the effect of the energy spread on the relative deviation of wavelengths emitted $\Delta\lambda/\lambda_0$, the required total dispersive beam splitting Δx_δ became too large (> 10 mm), as shown in Figure 3.16. The tilted model should not be completely ruled in other electron beam condition, that means with a lower energy spread. In this thesis, however, the energy spread remains $\delta = \pm 10$ % and the tilted geometry was discarded. From the results obtained there are several undulator cylindrical models, which met all design criteria: the relative deviation of wavelengths emitted by the reference electrons of different energies is required to be lower than the natural bandwidth $\Delta\lambda/\lambda_0 < 1$ % and the total dispersive beam splitting value around $\Delta x_\delta = \pm 2$ mm. For these reasons, the cylindrical geometry was selected.

3.4 Iron cylindrical undulator

3.4.1 Coil winding package configuration

Several cylindrical undulator models with different period lengths and coil winding package configurations were taken into consideration. Figure 3.17 shows the coil winding package configurations used for the cylindrical undulator models with period lengths of 5 mm, 7 mm and 10 mm.

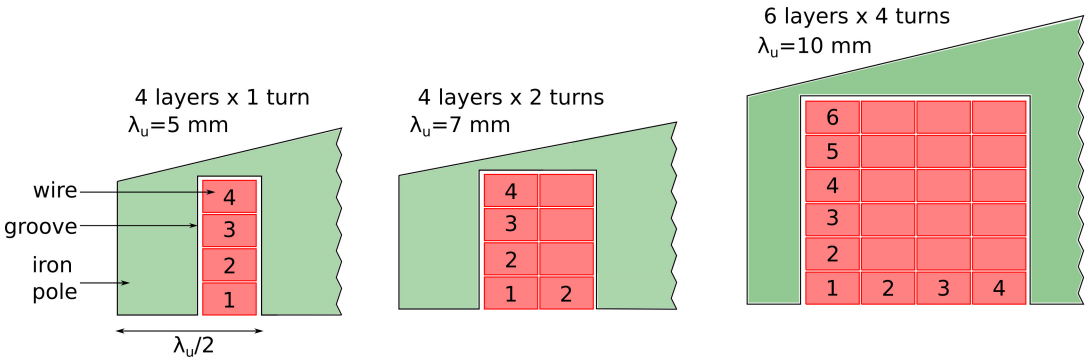

Figure 3.17: Different coil winding package configurations employed for the cylindrical undulator models with several period lengths (λ_u).

For each period length, two different models with gap width on axis (0.1 mm and 1.5 mm) were simulated to obtain the range of achievable B_y^{max} for each model. Table 3.11 shows the common parameters of all these models.

Design parameters:
Pole radius: r = 30 mm
Current density: J = 1200 A/mm^2
Wire cross-section (insulated): 1.08 mm × 0.68 mm
Material: steel AISI 1010

Table 3.11: Common design parameters for the simulated cylindrical undulator models with different coil winding package configurations.

The central energy of $E_0 = 120$ MeV and an energy spread of $\delta = \pm 10\,\%$ are assumed in all these calculations. Table 3.12 summarizes the optimization results of all these cylindrical models. These results show that the optimal magnetic field B_y^{max} can be only reached by the undulator models with $\lambda_u = 10$ mm. In these models with the gap widths on axis between 0.1 mm and 1.5 mm, the magnetic fields B_y^{max} simulated in OPERA are greater than the optimal values.

Table 3.13 shows the calculation of $\Delta\lambda/\lambda_0$, Δx_δ and σ_x for all the cylindrical models. The best results were obtained with the 10 mm period length undulator and the coil winding package configuration of 6 layers×4 turns. The values of $\Delta\lambda/\lambda_0$, Δx_δ and σ_x also depend on the geometrical undulator parameters, the current density and the wire parameters. Therefore a database to select the optimal cylindrical model was generated (see next Section 3.4.2).

Gap width on axis: g = 0.1 mm							
λ_u[mm]	OPERA B_y^{max}[T]	Simplex l_2[m]	Simplex B_y^{max}[T]	Iter.	$f(x)$ $\Delta\lambda/\lambda_0$[%]	optimal l_2[mm]	optimal B_y^{max}[T]
5	2.658	[0.8, 1.0, 0.6]	[2.0, 1.5, 1.7]	113	0.468	179	3.849
7	3.350	[0.7, 1.1, 0.4]	[2.1, 1.4, 1.7]	102	0.504	224	2.681
10	4.699	[0.7, 1.9, 1.3]	[1.1, 1.8, 2.4]	99	0.443	258	2.169

Gap width on axis: g = 1.5 mm							
λ_u[mm]	OPERA B_y^{max}[T]	Simplex l_2[m]	Simplex B_y^{max}[T]	Iter.	$f(x)$ $\Delta\lambda/\lambda_0$[%]	optimal l_2[mm]	optimal B_y^{max}[T]
5	0.943	[1.2, 0.4, 0.8]	[2.3, 1.7, 3.0]	97	0.454	190	3.811
7	1.588	[1.7, 0.5, 1.2]	[1.1, 0.4, 0.7]	120	0.475	240	2.637
10	2.439	[0.4, 1.6, 1.0]	[0.9, 1.6, 2.2]	120	0.518	310	1.748

Table 3.12: Optimization results of the simulated cylindrical undulator models with different gap widths on axis and period lengths.

Gap width on axis: g = 0.1 mm							
λ_u[mm]	opt. l_2[mm]	opt. B_y^{max}[T]	x_0[mm]	λ_0[nm]	$\Delta\lambda/\lambda_0$[%]	Δx_δ[mm]	Min. σ_x[mm]
5	179	3.849	5.20	071	0.468	2.67	0.062
7	224	2.682	5.41	100	0.504	3.19	0.074
10	258	2.169	8.62	143	0.443	3.59	0.084

Gap width on axis: g = 1.5 mm							
λ_u[mm]	opt. l_2[mm]	opt. B_y^{max}[T]	x_0[mm]	λ_0[nm]	$\Delta\lambda/\lambda_0$[%]	Δx_δ[mm]	Min. σ_x[mm]
5	190	3.811	5.05	071	0.454	2.80	0.066
7	240	2.637	5.58	099	0.475	3.38	0.078
10	310	1.748	5.88	141	0.518	4.19	0.098

Table 3.13: Calculation of $\Delta\lambda/\lambda_0$, Δx_δ and σ_x for the simulated cylindrical undulator models with different gap widths on axis and period lengths.

3.4.2 Iron cylindrical undulator database information.

A database with the optimized results for 81 iron cylindrical undulator models was made. The number of models came from a combination of the following parameters:

- Pole radius (r), ranging from 25 mm to 35 mm in steps of 5 mm.
- Gap width on axis (g), ranging from 1.1 mm to 1.5 mm in steps of 0.2 mm.

- Period length (λ_u), ranging from 8 mm to 12 mm in steps of 2 mm.
- Current density (J), ranging from 800 A/mm^2 and 1200 A/mm^2 in steps of 200 A/mm^2.

Table 3.14 shows the common parameters of all these models. Again, the central energy of $E_0 = 120$ MeV and an energy spread of $\delta = \pm 10\,\%$ are assumed in all these calculations. The magnetic field $B_y(z)$ and the Fourier components b_n were calculated with the software OPERA-3D. The mesh size of the undulator models was selected as small as affordable without increasing the calculation time per model above two hours. After that, the parameter l_2 (distance between the two dipoles) was optimized to obtain the minimum $\Delta\lambda/\lambda_0$ for each model. The total dispersive beam splitting Δx_δ for each undulator model was also calculated. In Appendix B the results of each model are summarized.

Design parameters:
Wire cross-section (insulated): 1.08 mm × 0.68 mm
Coil winding package:
8 layers × 3 turns with $\lambda_u = 8$ mm
6 layers × 4 turns with $\lambda_u = 10$ mm
8 layers × 5 turns with $\lambda_u = 12$ mm
Material: steel AISI 1010

Table 3.14: Common design parameters for the cylindrical undulators simulated for the database.

The lowest $\Delta\lambda/\lambda_0$ values and therefore the best results among all the simulated cylindrical undulator models, were obtained with r = 30 mm (see Figure 3.18).

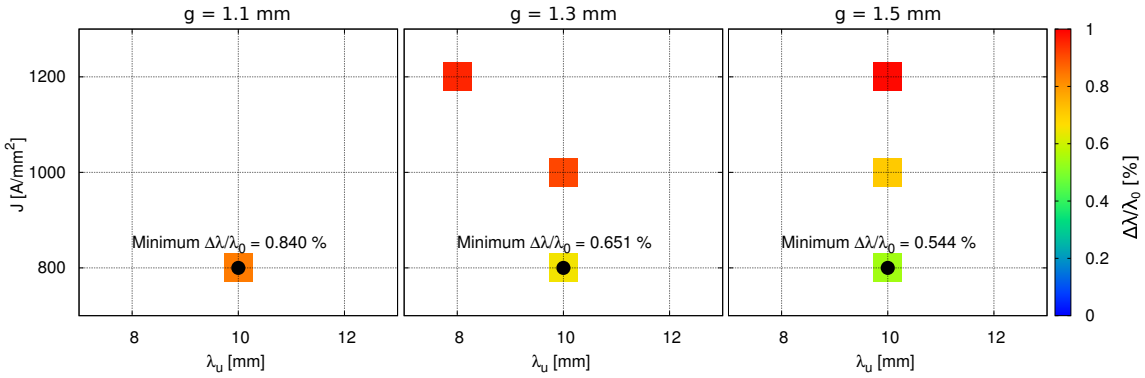

Figure 3.18: Calculation of $\Delta\lambda/\lambda_0$ for several cylindrical undulator models with external pole radius r = 30 mm. On the x-axis is λ_u and on the y-axis is J. The values of $\Delta\lambda/\lambda_0$ are displayed with a color scale between 0 and 1 % and each colored square represents the result of an undulator model. Left: models with g = 1.1 mm. Center: models with g = 1.3 mm. Right: models with g = 1.5 mm. The best results (with minimum $\Delta\lambda/\lambda_0$) are marked with a black dot.

The minimum $\Delta\lambda/\lambda_0 = 0.544\,\%$ was found for the model with r = 30 mm, g = 1.5 mm, λ_u = 10 mm and J = 800 A/mm^2. The results of the models with λ_u = 12 mm were not shown because only values of $\Delta\lambda/\lambda_0 > 1\,\%$ were obtained. The results for the other external radius values are quite similar, as can be seen in Appendix B.

3.4.3 Selection of the optimal model

Table 3.15 summarizes the parameters of the selected iron cylindrical undulator and Table 3.16 collects in more detail all the calculated values.

Design parameters:
Period length: $\lambda_u = 10$ mm
Pole radius: r = 30 mm
Gap width on axis: g = 1.5 mm
Current density: J = 800 A/mm^2
Wire cross-section (insulated): 1.08 mm × 0.68 mm
Coil winding package: 6 layers × 4 turns
Material: steel AISI 1010

Table 3.15: Design parameters for the selected iron cylindrical undulator.

E[MeV]	$\gamma(x)$	$x(E)$[mm]	$B_y(x)$[T]	$K(x)$	$\lambda(x)$[nm]	σ_x[mm]
132.0	258.32	3.779	1.43	1.34	141.82	0.106
129.6	253.62	4.127	1.38	1.29	142.30	0.102
127.2	248.92	4.489	1.33	1.24	142.54	0.100
124.8	244.23	4.864	1.27	1.18	142.59	0.098
122.4	239.53	5.255	1.21	1.13	142.49	0.098
120.0	234.83	5.661	1.14	1.07	142.29	0.098
117.6	230.14	6.084	1.08	1.00	142.06	0.100
115.2	225.44	6.524	1.01	0.94	141.87	0.104
112.8	220.74	6.984	0.94	0.87	141.82	0.110
110.4	216.05	7.463	0.86	0.81	142.00	0.118
108.0	211.35	7.964	0.79	0.74	142.50	0.128

Table 3.16: Summary of results for the optimized iron cylindrical TGU.

The magnetic field $B_y(x)$ produced for the optimized iron cylindrical TGU was calculated by Equation (2.39). The x-dependent undulator parameter was determined by $K(x) = 93.36 B_y(x)[\mathrm{T}]\lambda_u[\mathrm{m}]$. Using the modified undulator Equation (3.1) the wavelength of the emitted undulator radiation $\lambda(x)$ for each energy $E(x)$ was calculated. The maximum beamlet width σ_x for each energy was also determined and is shown in the last column of this table.

Table 3.17 summarizes the results, including the x-position and the emitted wavelength by the central energy, the total dispersive beam splitting Δx_δ and the minimum beamlet width σ_x. The goal was to obtain an optimized bandwidth of the undulator radiation smaller than 1 %. The bandwidth for the optimized iron cylindrical undulator resulted in $\Delta\lambda/\lambda_0 = (\lambda_{\max} - \lambda_{\min})/\lambda_0 = 0.54\,\%$. The total dispersive beam splitting $\Delta x_\delta \approx 4\,\text{mm}$ is necessary.

opt. $B_y^{\max}$[T]	opt. l_2[mm]	x_0[mm]	λ_0[nm]	$\Delta\lambda/\lambda_0$[%]	Δx_δ[mm]	Min. σ_x[mm]
1.741	309	5.661	142	0.540	4.185	0.098

Table 3.17: Calculation of the relative deviation of wavelengths emitted ($\Delta\lambda/\lambda_0$), the total dispersive beam splitting (Δx_δ) and the beamlet width (σ_x) of the selected iron cylindrical undulator model.

The values of $\gamma(x)$ required from the chicane after the optimization for the energies values 120 MeV ± 10 % is shown in Figure 3.19-left. In Figure 3.19-right the calculated $B_y(x)$ for the selected iron cylindrical model is shown and the required x-position of the electron beam $x(E)$ given from the chicane.

Figure 3.20-left shows the $\lambda(x)$ values and the almost constant emitted wavelength for the electron energy interval of interest. Figure 3.20-right is a zoom of the emitted wavelength $\lambda(x)$ for the energy values 120 MeV ± 10 %.

3.4.4 Electron trajectories, drift and its correction

For analyzing the motion of a single electron through the cylindrical undulator, equations in [55] were used. The program written in [38] with some minor modifications was employed and the C++ source code is shown in Appendix A.3.

The transverse gradient of the magnetic flux density causes a ponderomotive drift of the electron trajectories in the x-direction. The reason can be seen in Figure 3.21. The electron moves in the xz-plane. When the electron moves towards

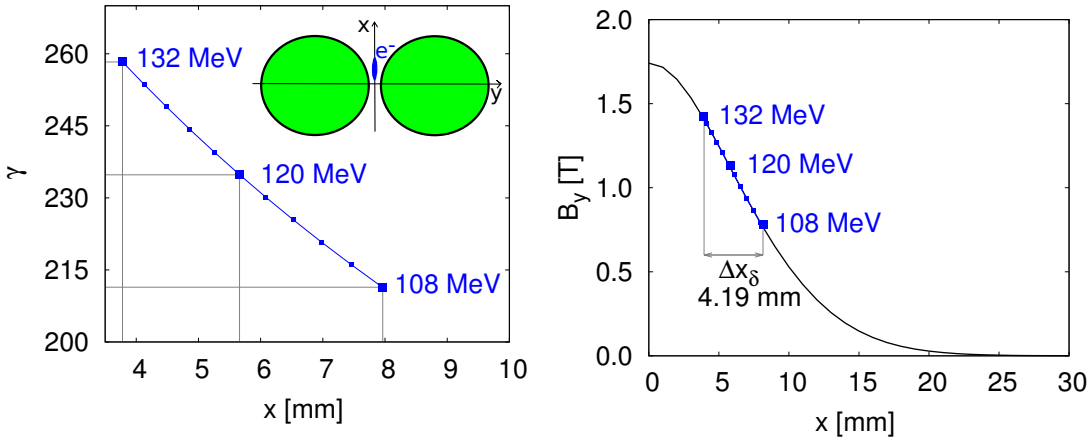

Figure 3.19: Calculation of the magnetic flux density produced for the selected iron cylindrical TGU. Left: required $\gamma(x)$ from chicane after the optimization. Right: calculated $B_y(x)$ for this undulator model (black line) and field required from chicane (blue points).

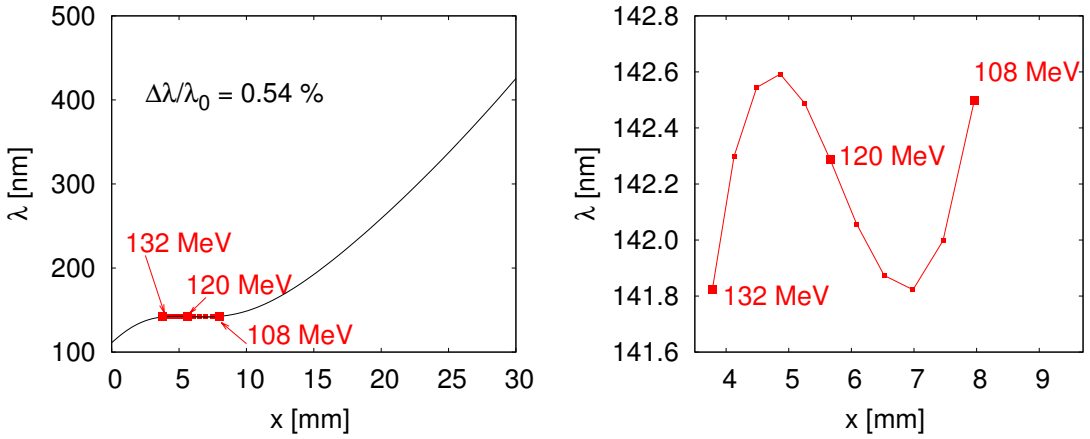

Figure 3.20: Resulting emitted wavelength for the selected iron cylindrical TGU. Left: total $\lambda(x)$ (black line) and emitted for the electron beam (red points). Right: zoom of $\lambda(x)$ for the energy values 120 MeV $\pm$ 10 % (red points).

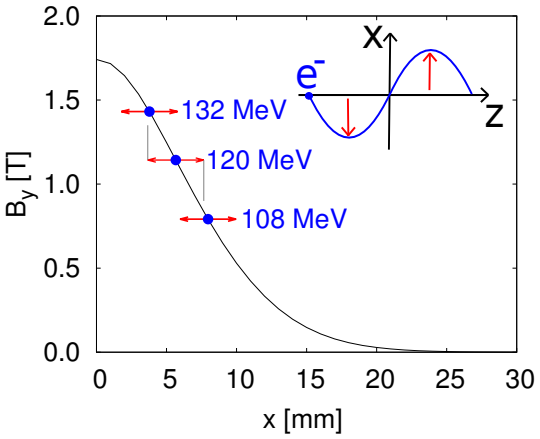

Figure 3.21: Reason of the ponderomotive drift in x-direction of the electron trajectories.

x-values smaller than the central x-value, the electron sees more flux density than when the electron moves in the other direction with x-values larger than the central x-value. The x-values after one period $x(z_i + \lambda_u)$ are larger as the initial x-value $x(z_i)$ produces a positive drift.

The relative electron trajectories in the xz-plane with the starting points of the trajectories shifted at $x = 0$ were calculated. These relative trajectories for the electron energies 108 MeV, 120 MeV and 132 MeV are shown in Figure 3.22. The trajectories amplitudes and the drifts were smaller than 10 μm. After ten periods, the value of the drifts was as large as the amplitude of the trajectories and therefore these drifts have to be corrected as will be explained below.

Additionally, the drift after one period has a different value for each energy due to the field gradient, as can be seen in Figure 3.23-left. These values increase 100 times after ten periods as shown in Figure 3.23-right. Such a drift could be problematic for some reasons [38]:

- The wavelength of the emitted radiation changes when the x-position of the electrons vary.

- If there are trajectory drifts, the trajectory angles are different from zero. These trajectory angles also modify the period length projected to the mean trajectory and therefore the emitted wavelengths.
- If the drift is too large, the radiation wavefronts emitted will not overlap with each other and the desired interference effects will not take place.

The trajectory drifts can be corrected adding a correction field to the undulator field, to compensate the undulator field gradient. It is necessary to correct the electron drift after the first period to cancel the total drift through the undulator. The drift for a single electron energy can be corrected by a dipole field. Therefore a correction field for different electron energies, which represents a "local dipole field", can be used. Because the electron are moving through the undulator in xz-plane at different x-positions, the correction field has to vary also in the x-direction but can be constant in the z-direction. The correction field $B_y^{\mathrm{corr}}(x)$ for each energy is given by Equation (3.11):

$$B_y^{\mathrm{corr}}(x) = \frac{\mathrm{m_e c}}{e} \frac{\gamma(x)}{r_L(x)} \tag{3.11}$$

where $r_L(x)$ is the bending radius, which varies in x-direction.

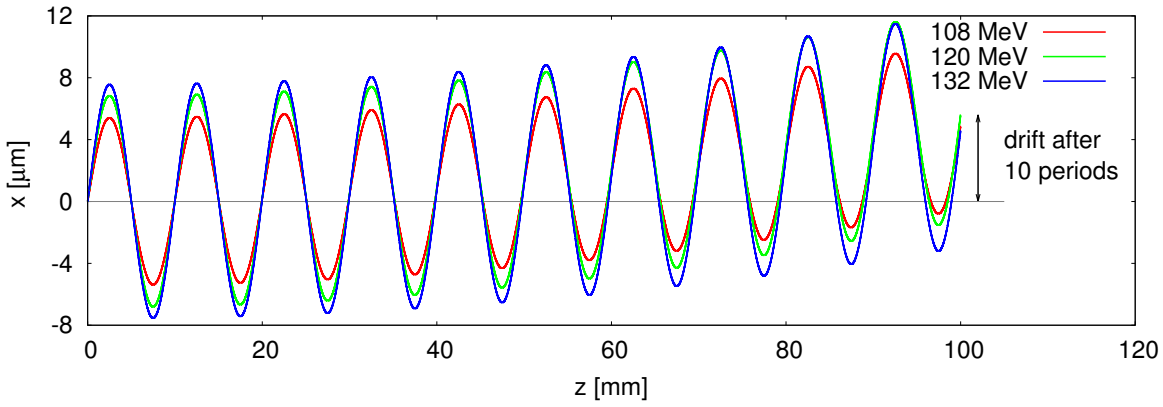

Figure 3.22: Relative electron trajectories after ten periods with energies 108 MeV, 120 MeV and 132 MeV for the optimized iron cylindrical TGU.

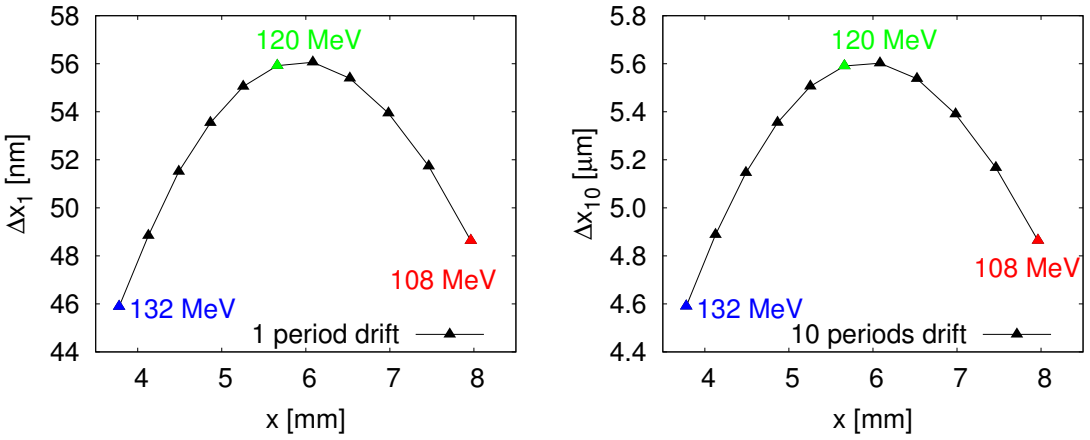

Figure 3.23: Drift of the trajectories for different energy values. Left: after one period. Right: after ten periods.

The required bending radius can be determined by Equation (3.12):

$$r_L(x) = \frac{\lambda_u^2 + (\Delta x_1(x))^2}{2\Delta x_1(x)} \tag{3.12}$$

All values used to calculate the correction field $B_y^{\text{corr}}(x)$ are collected in Table 3.18, including the bending radius and the drift values after one period, for the optimized iron cylindrical TGU. The correction field is a weak field, compared with the undulator field.

E[MeV]	$x(E)$[mm]	Δx_1[nm]	$r_L(x)[m]$	$B_y^{\text{corr}}(x)[mT]$
132.0	3.779	45.89	1090	-0.404
129.6	4.127	48.84	1024	-0.422
127.2	4.489	51.51	971	-0.437
124.8	4.864	53.54	934	-0.446
122.4	5.255	55.05	908	-0.450
120.0	5.661	55.92	894	-0.448
117.6	6.084	56.06	892	-0.440
115.2	6.524	55.39	903	-0.426
112.8	6.984	53.94	927	-0.406
110.4	7.463	51.73	967	-0.381
108.0	7.964	48.63	1028	-0.350

Table 3.18: Summary of values used to calculate the correction field $B_y^{\text{corr}}(x)$ for the optimized iron cylindrical TGU.

Figure 3.24 shows the calculated correction field $B_y^{\text{corr}}(x)$, which fits very well to a quadratic function or parabola $f1(x)$ [38]. The quadratic function can be rewritten as:

$$\begin{aligned} B_y^{\text{corr}}(x) = f1(x) &= ax^2 + bx + c \\ &= gx^2 + (2eg)x + (e^2 + d) \\ &= g(x+e)^2 + d \\ &= B_y^{\text{sextupole}} + B_y^{\text{dipole}} \end{aligned} \tag{3.13}$$

However the required correction field in this thesis is calculated using the fit to a cubic function $f2(x) = kx^3 + mx^2 + nx + o$ with the data $B_y^{\text{corr}}(x)$ of Table 3.18. The coefficients values are given by:

$$\begin{aligned} k &= -\,1339.94 \pm 62.97\,\text{T/m}^3 \\ m &= +\,38.94 \pm 1.11\,\text{T/m}^2 \\ n &= -\,0.300 \pm 0.006\,\text{T/m} \\ o &= +\,0.246 \pm 0.012\,\text{mT} \end{aligned}$$

and in Figure 3.24 can be seen that the cubic function $f2(x)$ is the best fit through the required set of correction field points.

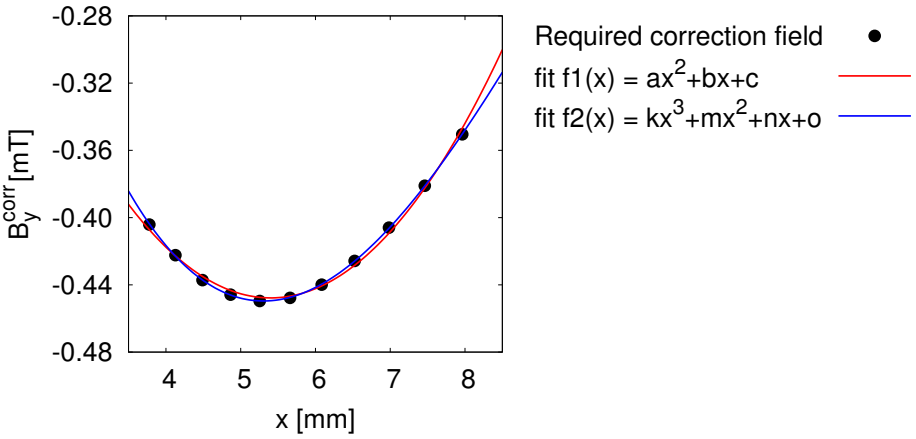

Figure 3.24: Required correction field $B_y^{\text{corr}}(x)$ (black points) and the fit of the data to a quadratic function $f1(x)$ (red line) and a cubic function $f2(x)$ (blue line).

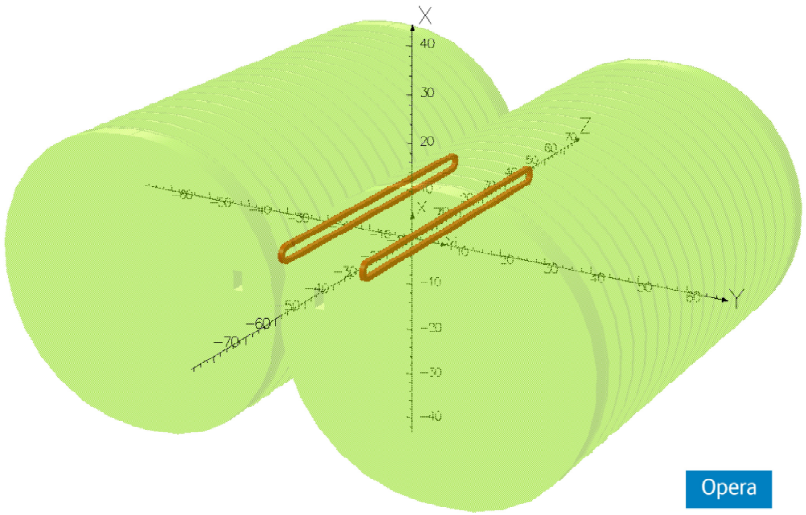

Figure 3.25: Correction coils placed inside the undulator coil former to produce the correction coil.

This correction field can be generated by coils placed inside the undulator coil former as shown in Figure 3.25 (for more details, see Section 4.2.2).

In order to verify the efficiency of the correction field previously calculated, the electron trajectories were again simulated but this time adding the correction field to the field produced by the undulator. The relative trajectories for the electron energies 108 MeV, 120 MeV and 132 MeV after adding the correction field are shown in Figure 3.26.

After the correction field was added, the resulting drift after ten periods is lower than $\pm$ 7 nm for all the energy values between 120 MeV $\pm$ 10 %. The drift after 100 periods for the electron energies 108 MeV, 120 MeV and 132 MeV are shown in Table 3.19. To achieve the optimization goal $\Delta\lambda/\lambda_0 \leq 1\,\%$, these drifts have to be smaller than the beamlet width σ_x of each energy.

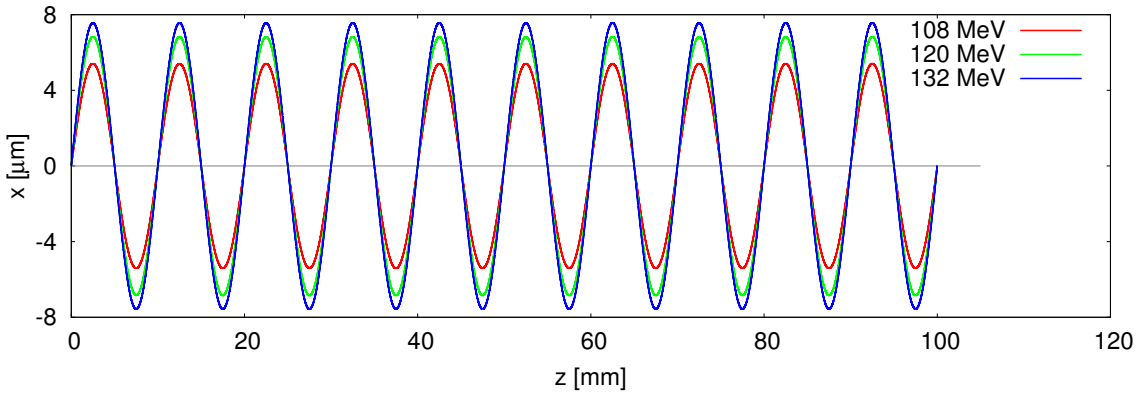

Figure 3.26: Corrected relative electron trajectories after ten periods with energies 108 MeV, 120 MeV and 132 MeV for the optimized iron cylindrical TGU.

E[MeV]	$\Delta x_{100}[\mu m]$	σ_x[mm]
132	0.3890	0.106
120	0.2943	0.098
108	0.5431	0.128

Table 3.19: Summary of values used to calculate the correction field $B_y^{\text{corr}}(x)$ for the optimized iron cylindrical TGU.

3.4.5 Iron saturation

As mentioned in Section 3.4.4, a weak correction field has to be superimposed to the undulator field in order to correct the electron trajectories inside the undulator. Therefore it has to be ensured that the correction field source is not screened by unsaturated soft magnetic material, which is usually employed in superconducting undulators in order to increase the flux density. Thus, all soft magnetic parts of the undulator are required to be completely saturated or, as an alternative, the undulator has to be iron-free. The material employed in the cylindrical undulator, low carbon steel AISI 1010, reaches the full saturation at $B_{\text{min}} = 2.13\,\text{T}$ (see Section 2.2.2.1).

Several undulator models with different pole configurations were simulated. The modulus of the magnetic field was calculated by the software OPERA-3D [48]. The models are presented in the sequence of increasing difficulty of technical realization:

- The undulator model showed in Figure 3.27 (a) has the coil former completely manufactured of magnetic material. This model shows large, completely unmagnetized regions. The minimum flux density inside the magnetic material is $B_{\text{min}} = 0\,\text{T}$.
- Figure 3.27 (b) shows a coil former with a central cylindrical hole of non magnetic material, and around a tube with poles of magnetic material. In this case the $B_{\text{min}} = 1.39\,\text{T}$ and therefore the saturation was not achieved.
- A last model, where only the pole insets were made of magnetic material, is shown in Figure 3.27 (c). The $B_{\text{min}} = 2.11\,\text{T}$ calculated for this model is close to the saturation point $B_{\text{min}} = 2.13\,\text{T}$.

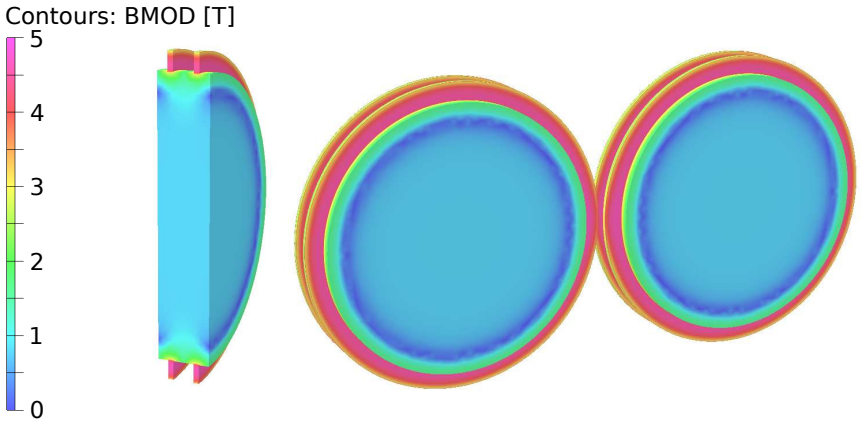

(a) Model with coil former completely of magnetic material.

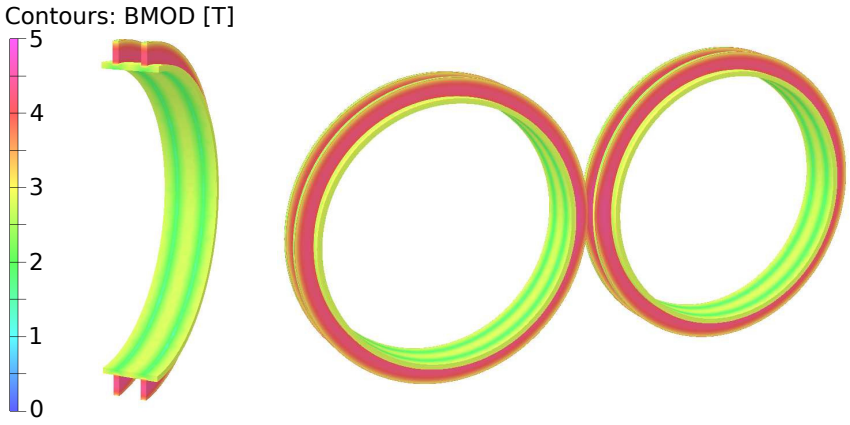

(b) Model with part of coil former and poles of magnetic material.

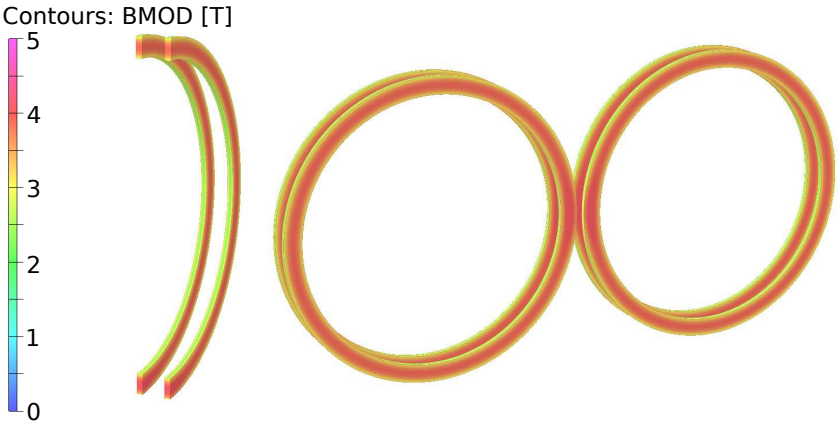

(c) Model with only pole insets of magnetic material.

Figure 3.27: Modulus of the magnetic field for three cylindrical undulator models.

Only with the last undulator model (Figure 3.27 (c)) the full saturation appears achievable, because B_{min} is near to the saturation point. Such an arrangement is technically very challenging in terms of thermally induced stress and mechanical accuracy particularly at the poles, which strongly influence the field quality. Therefore an iron-free design was finally chosen for the implementation of the cylindrical undulator. The material selected to manufacture the coil former and the support was copper. The optimized copper cylindrical TGU will be presented in Section 3.5.

3.5 Copper cylindrical undulator

Figure 3.28 compares two cylindrical undulator models simulated in OPERA-3D: left shows the iron model (the magnetic parts of iron, cores and poles, are represented in green) and right shows the model of copper, where it is only necessary simulate the coils (in red). The time required to perform the copper model simulations is greatly reduced by the fact that it is not necessary to solve the meshed models, like in the case of the iron undulators. The magnetic field produced by the coils is directly calculated in the post-processor, which saves the step of creating the database and the magnetostatic solver. Then the Fourier coefficients of the magnetic field produced by each undulator model are exported from OPERA and used in the optimization and analytical calculations. Both cylindrical undulator models were simulated using the same design parameters, which are summarized in Table 3.20.

The geometrical parameters (λ_u, r and g) are the same parameters as the selected for the iron model, which were selected in Section 3.4.3. The critical current density

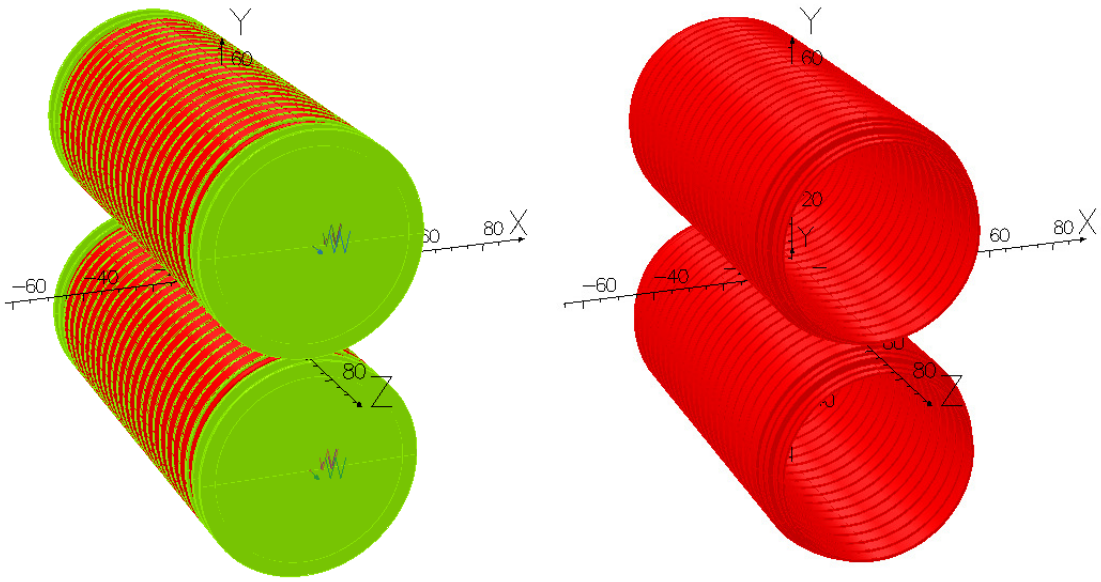

Figure 3.28: Comparison both cylindrical undulator models simulated in OPERA-3D. Left: iron model, with cores and poles in green. Right: copper model, only coils in red.

Design parameters:
Period length: $\lambda_u = 10\,\text{mm}$
Pole radius: $r = 30\,\text{mm}$
Gap width on axis: $g = 1.5\,\text{mm}$
Current density: $J = 1020\,\text{A/mm}^2$
Wire cross-section (insulated): $1.08\,\text{mm} \times 0.68\,\text{mm}$
Coil winding package: 6 layers × 4 turns

Table 3.20: Cylindrical undulator parameters for both iron and copper undulator models.

of the NbTi superconductor wire with a cross section (insulated) of 1.08 mm × 0.68 mm used for the construction of the undulator coils was assumed to be around $J_c = 1200\,\mathrm{A/mm^2}$. The current density used in the simulations of both models was limited to be 85% of the critical current to avoid undulator quenching in normal operations.

The magnetic field produced for an iron-core undulator is much stronger than the strength of the field produced for the coils alone or copper-core undulator. The iron core increases the magnetic field due to the high magnetic permeability μ of the material. The simulation in OPERA shows that the maximal field on axis produced for the iron model is around 2 T, whereas the copper model produces a smaller magnetic field of about 1.5 T. Table 3.21 shows the optimization results of both models using a reference electron energy of $\mathrm{E_0} = 120\,\mathrm{MeV}$ with an energy spread of $\delta = \pm 10\,\%$.

Material	OPERA $B_y^{\max}$[T]	opt. $B_y^{\max}$[T]	opt. l_2[mm]	x_0[mm]	λ_0[nm]	$\Delta\lambda/\lambda_0$[%]	Δx_δ[mm]	Min. σ_x[mm]
iron	2.075	1.735	313	5.77	141.22	0.521	4.23	0.098
copper	1.470	1.812	301	6.36	141.92	0.486	4.10	0.096

Table 3.21: Optimization and calculation of $\Delta\lambda/\lambda_0$, Δx_δ and σ_x for both iron and copper cylindrical undulator models.

The optimal $B_y^{\max}$ obtained for the iron model is lower than the $B_y^{\max} \approx 2\,\mathrm{T}$ produced for the simulated undulator in OPERA. That means, that with a lower current density (around $800\,\mathrm{A/mm^2}$) the iron model can achieve the optimal $B_y^{\max} = 1.735\,\mathrm{T}$. This was already shown in Section 3.4.3, where the optimized iron cylindrical undulator was selected.

In the case of the copper model, the optimal $B_y^{\max}$ obtained is greater than the $B_y^{\max} \approx 1.5\,\mathrm{T}$ produced for the simulated undulator in OPERA. To achieve the optimal $B_y^{\max}$ value, the current density of the simulated undulator should be increased and greater than 85% of the critical current, which is not desired. Other option is to search other undulator model, changing slightly the geometric parameter values of the copper model until that the optimal $B_y^{\max}$ achieves the $B_y^{\max}$ simulated, as is shown in Section 3.5.1.

3.5.1 Selection of the optimal model

(a) In this case, models with different external pole radius r are simulated and their optimization is performed. The period length value is kept at $\lambda_\mathrm{u} = 10\,\mathrm{mm}$ and the gap width on axis, $\mathrm{g} = 1.3\,\mathrm{mm}$, is slightly lower to increase the produced $B_y^{\max}$. The optimal $B_y^{\max}$ and the $B_y^{\max}$ produced for all these models are compared in Figure 3.29 (a). Any of these models produce $B_y^{\max}$ lower than the optimal. Results are summarized in Table 3.22.

(b) The next models are simulated for different g (gap-width on axis) values, fixed $\mathrm{r} = 30\,\mathrm{mm}$ and $\lambda_\mathrm{u} = 10\,\mathrm{mm}$. The optimal $B_y^{\max}$ and the $B_y^{\max}$ produced for all these models are compared in Figure 3.29 (b). Only the model with $\mathrm{g} = 0.9\,\mathrm{mm}$ can produce $B_y^{\max}$ slightly greater than the optimal $B_y^{\max}$. Their optimized results are summarized in Table 3.23.

(c) Next models with different period lengths, λ_u, fixed r = 30 mm and g = 1.3 mm are simulated. The optimal B_y^{max} and the B_y^{max} produced for all these models are compared in Figure 3.29 (c). It can be clearly seen that the produced B_y^{max} increases with increasing the period length. In contrast the optimal B_y^{max} decreases. The models with $\lambda_u \geq 11$ mm produce a B_y^{max} greater than the optimal B_y^{max}. The optimized results are summarized in Table 3.24.

(d) To finish, several models with different gap width on axis and with fixed λ_u = 10.5 mm and r = 30 mm are simulated. Their optimization is performed and the results are summarized in Table 3.25. The optimal B_y^{max} and the B_y^{max} produced for all these models are compared in Figure 3.29 (d). The final selected copper model with g = 1.1 mm is shaded in gray in Table 3.25. This cylindrical model satisfies the desired condition that B_y^{max} produced is slightly higher than the optimal B_y^{max}.

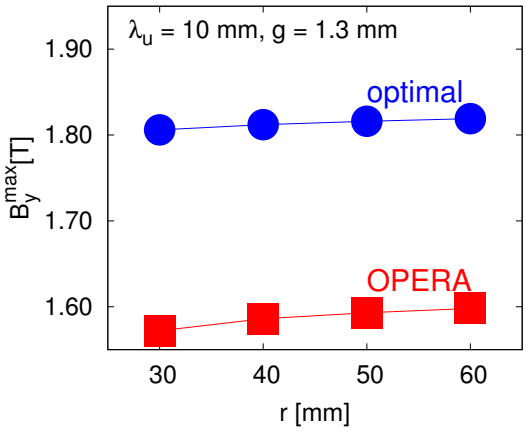

(a) With different external pole radius.

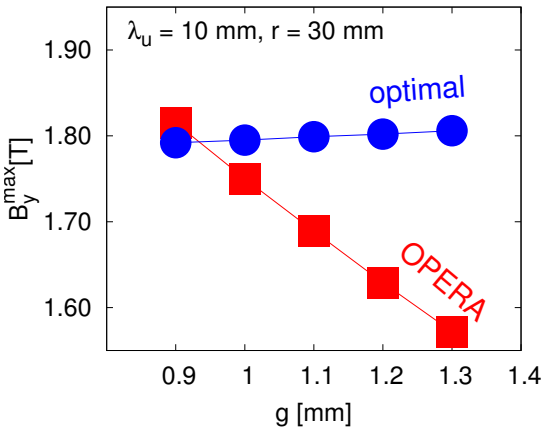

(b) With different gap widths on axis.

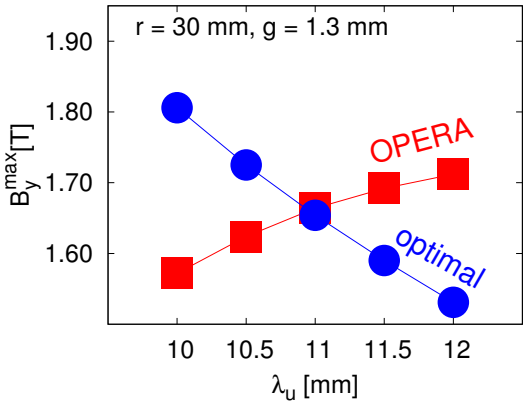

(c) With different period lengths.

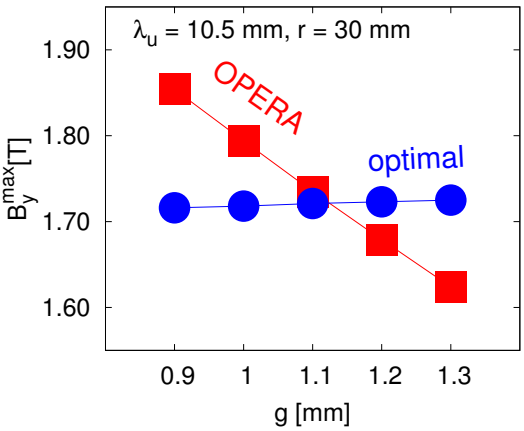

(d) With different gap widths on axis.

Figure 3.29: B_y^{max} produced for several cylindrical undulator models simulated in OPERA (in red) and optimal values (in blue).

r[mm]	OPERA $B_y^{\max}$[T]	opt. $B_y^{\max}$[T]	opt. l_2[mm]	x_0[mm]	λ_0[nm]	$\Delta\lambda/\lambda_0$[%]	Δx_δ[mm]	Min. σ_x[mm]
30	1.572	1.806	301	6.30	141.87	0.489	4.10	0.096
40	1.586	1.812	355	7.34	141.87	0.484	4.72	0.110
50	1.593	1.816	402	8.25	141.88	0.481	5.28	0.124
60	1.598	1.819	445	9.07	141.88	0.479	5.78	0.136

Table 3.22: Optimization results for several cylindrical undulator models with different external pole radius and with fixed g = 1.3 mm and λ_u = 10 mm.

g[mm]	OPERA $B_y^{\max}$[T]	opt. $B_y^{\max}$[T]	opt. l_2[mm]	x_0[mm]	λ_0[nm]	$\Delta\lambda/\lambda_0$[%]	Δx_δ[mm]	Min. σ_x[mm]
0.9	1.815	1.792	301.78	6.18	141.75	0.496	4.10	0.096
1.0	1.750	1.795	301.65	6.21	141.78	0.494	4.10	0.096
1.1	1.689	1.799	301.45	6.24	141.82	0.492	4.10	0.096
1.2	1.629	1.802	301.35	6.27	141.84	0.490	4.10	0.096
1.3	1.572	1.806	301.19	6.30	141.87	0.489	4.10	0.096

Table 3.23: Optimization results for several cylindrical undulator models with different gap widths on axis and fixed r = 30 mm and λ_u = 10 mm.

λ_u[mm]	OPERA $B_y^{\max}$[T]	opt. $B_y^{\max}$[T]	opt. l_2[mm]	x_0[mm]	λ_0[nm]	$\Delta\lambda/\lambda_0$[%]	Δx_δ[mm]	Min. σ_x[mm]
10.0	1.572	1.806	301	6.30	141.87	0.489	4.10	0.096
10.5	1.624	1.725	308	6.51	149.01	0.488	4.18	0.098
11.0	1.664	1.654	315	6.73	156.16	0.487	4.26	0.100
11.5	1.692	1.590	321	6.96	163.34	0.486	4.33	0.102
12.0	1.712	1.531	327	7.19	170.51	0.484	4.40	0.104

Table 3.24: Optimization results for several cylindrical undulator models with different period lengths and fixed r = 30 mm and g = 1.3 mm.

g[mm]	OPERA $B_y^{\max}$[T]	opt. $B_y^{\max}$[T]	opt. l_2[mm]	x_0[mm]	λ_0[nm]	$\Delta\lambda/\lambda_0$[%]	Δx_δ[mm]	Min. σ_x[mm]
0.9	1.854	1.716	307.89	6.42	148.92	0.495	4.17	0.098
1.0	1.794	1.718	308.09	6.45	148.93	0.493	4.18	0.098
1.1	1.735	1.721	308.11	6.47	148.97	0.491	4.18	0.098
1.2	1.679	1.723	308.25	6.49	148.99	0.490	4.18	0.098
1.3	1.624	1.725	308.32	6.51	149.01	0.488	4.18	0.098

Table 3.25: Optimization results for several cylindrical undulator models with different gap widths on axis and with fixed r = 30 mm and λ_u = 10.5 mm. Best result: copper model with g = 1.1 mm (shaded in gray).

Table 3.26 shows in detail the results obtained for all the energy values after optimizing the selected copper model with g = 1.1 mm, r = 30 mm and λ_u = 10.5 mm. In this case the optimal values of the optimized parameters are: B_y^{max} = 1.721 T and l_2 = 308.11 mm.

Figure 3.30-left shows the calculated $B_y(x)$ for the selected copper cylindrical model. The required x-position of the electron beam $x(E)$ is given from the chicane. The reference electron energy is E_0 = 120 MeV with an energy spread of $\Delta E/E_0 = \pm 10\,\%$. Figure 3.30-right shows the total $\lambda(x)$ values and the almost constant emitted wavelength for the selected copper cylindrical undulator. The total dispersive beam splitting Δx_δ and the relative deviation of wavelengths emitted by the reference electrons of the different energies $\Delta\lambda/\lambda_0$ is slightly lower than with the iron model.

E[MeV]	$\gamma(x)$	$x(E)$[mm]	$B_y(x)$[T]	$K(x)$	$\lambda(x)$[nm]	σ_x[mm]
132.0	258.32	4.589	1.36	1.33	148.53	0.104
129.6	253.62	4.937	1.31	1.28	148.98	0.100
127.2	248.92	5.297	1.26	1.23	149.22	0.098
124.8	244.23	5.672	1.20	1.18	149.27	0.098
122.4	239.53	6.062	1.15	1.12	149.16	0.098
120.0	234.83	6.467	1.08	1.06	148.97	0.098
117.6	230.14	6.889	1.02	1.00	148.75	0.100
115.2	225.44	7.328	0.96	0.94	148.57	0.104
112.8	220.74	7.787	0.89	0.87	148.53	0.110
110.4	216.05	8.265	0.82	0.80	148.73	0.118
108.0	211.35	8.765	0.75	0.73	149.27	0.128

Table 3.26: Summary of results for the optimized copper cylindrical TGU.

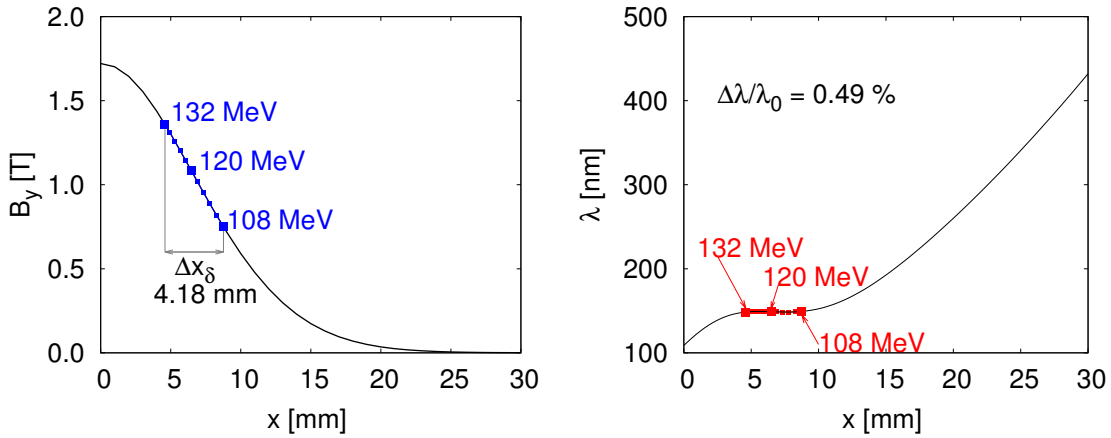

Figure 3.30: Selected copper cylindrical TGU. Left: calculated $B_y(x)$ for this undulator model (black line) and field required from chicane (blue points). Right: resulting total wavelength $\lambda(x)$ (black line) and emitted for the electron beam (red points).

3.5.2 Electron trajectories, drift and correction

The relatives trajectories for the electron energies 108 MeV, 120 MeV and 132 MeV are shown in Figure 3.31. After ten periods, the value of the drifts are almost as large as the amplitude of the trajectories, therefore these drifts have to be corrected as will be explained below. Additionally the drift has different values for each energy after one period due to the field gradient, as shown in Figure 3.32-left. Figure 3.32-right shows how the drift values increase by 100 times after ten periods.

All values used to calculate the correction field $B_y^{\text{corr}}(x)$ are collected in Table 3.27, including the bending radius and the drift values, for the optimized copper cylindrical TGU after one period. Figure 3.33 shows the calculated correction field $B_y^{\text{corr}}(x)$, which fits were performed with a quadratic function or parabola and with a cubic function. The coefficients of the quadratic function $f1(x) = ax^2 + bx + c$, which fit the data of Table 3.27, are given by:

$$\begin{aligned} a &= +\,14.62 \pm 0.76\,\mathrm{T/m^2} \\ b &= -\,0.16 \pm 0.01\,\mathrm{T/m} \\ c &= -\,0.116 \pm 0.033\,\mu\mathrm{T} \end{aligned}$$

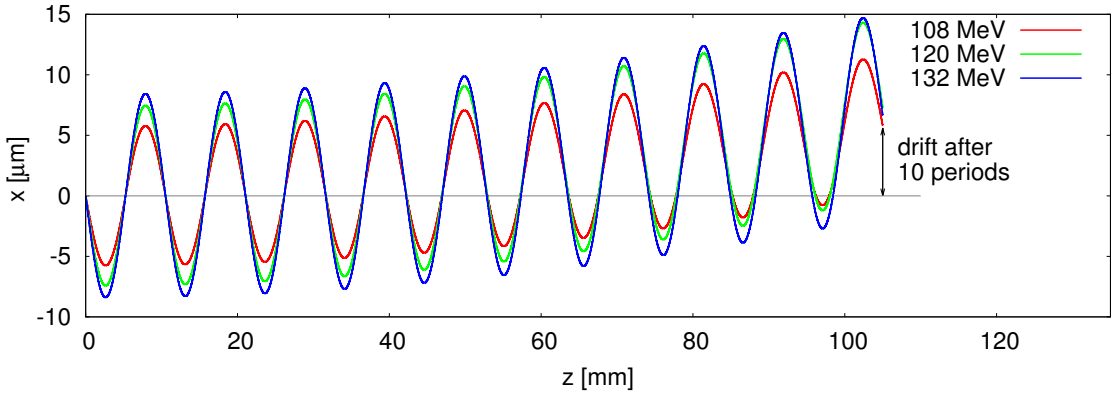

Figure 3.31: Electron trajectories after ten periods with energies between 120 MeV ± 10 % for the optimized copper cylindrical TGU.

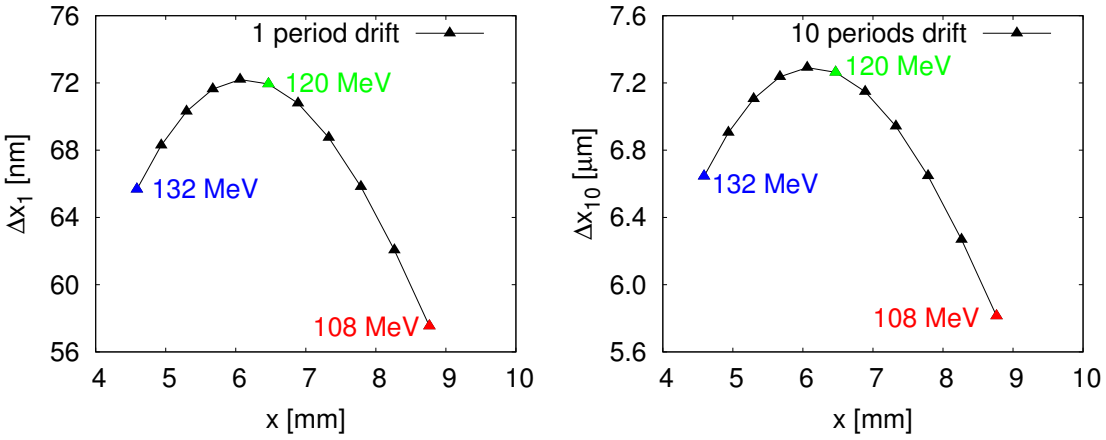

Figure 3.32: Drift of the trajectories for different energy values. Left: after one period. Right: after ten periods.

As for the case of the iron undulator, the correction field in this thesis is calculated using the fit to a cubic function $f2(x) = kx^3 + mx^2 + nx + o$. For the copper undulator the function fits with the data $B_y^{\text{corr}}(x)$ of Table 3.27. The coefficients values are given by:

$$\begin{aligned} k &= -\,1928.23 \pm 41.34\,\text{T/m}^3 \\ m &= +\,53.19 \pm 0.83\,\text{T/m}^2 \\ n &= -\,0.408 \pm 0.005\,\text{T/m} \\ o &= +\,0.416 \pm 0.012\,\text{mT} \end{aligned}$$

Figure 3.33 demonstrates that the cubic function $f2(x)$ is the best fit through the required set of correction field points.

E[MeV]	$x(E)$[mm]	Δx_1[nm]	$r_L(x)[m]$	$B_y^{\text{corr}}(x)[mT]$
132.0	4.589	65.67	839	-0.525
129.6	4.937	68.29	807	-0.536
127.2	5.297	70.31	784	-0.541
124.8	5.672	71.64	770	-0.541
122.4	6.062	72.20	763	-0.534
120.0	6.467	71.94	766	-0.522
117.6	6.889	70.79	779	-0.504
115.2	7.328	68.75	802	-0.479
112.8	7.787	65.82	837	-0.449
110.4	8.265	62.05	888	-0.414
108.0	8.765	57.53	958	-0.376

Table 3.27: Summary of values used to calculate the correction field $B_y^{\text{corr}}(x)$ for the optimized copper cylindrical TGU.

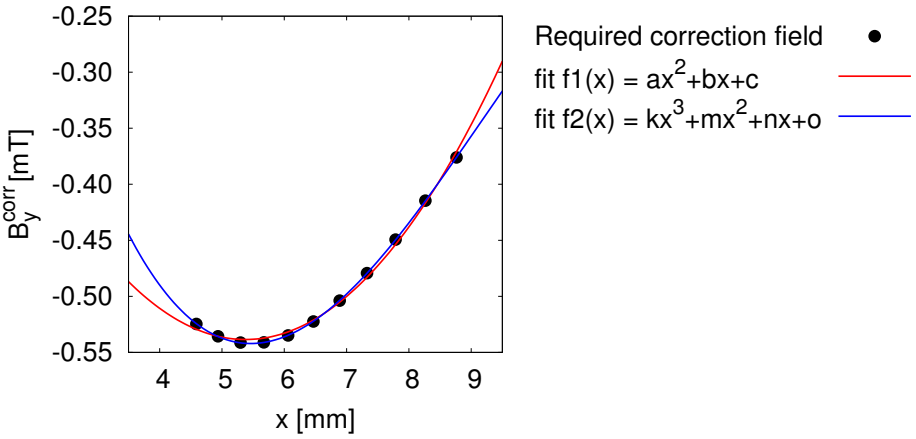

Figure 3.33: Required correction field $B_y^{\text{corr}}(x)$ (black points). The red line shows the fit of the data using a quadratic function $f1(x)$, while the blue line shows the fit using a cubic function $f2(x)$.

In order to verify the efficiency of the correction field, the electron trajectories were again simulated by adding the correction field to the field produced by the undulator. The relative trajectories for the electron energies 108 MeV, 120 MeV and 132 MeV after adding the correction field are shown in Figure 3.34.

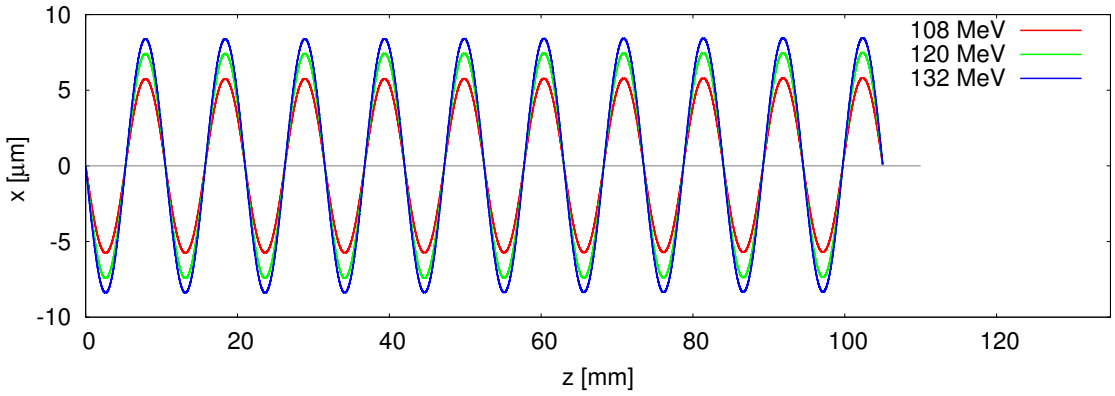

Figure 3.34: Corrected relative electron trajectories after ten periods with energies 108 MeV, 120 MeV and 132 MeV for the optimized copper cylindrical TGU.

After the correction field was added, the drift value after ten periods is found to be between 60 nm and 80 nm for all the energy values between 120 MeV ± 10 %. The drift after 100 periods for the electron energies 108 MeV, 120 MeV and 132 MeV are shown in Table 3.28. To achieve the optimization goal $\Delta\lambda/\lambda_0 \leq 1\,\%$, these drifts have to be smaller than the beamlet width σ_x of each energy.

E[MeV]	$\Delta x_{100}[\mu\text{m}]$	σ_x[mm]
132	8.0041	0.104
120	7.3708	0.098
108	6.3489	0.128

Table 3.28: Summary of values used to calculate the correction field $B_y^{\text{corr}}(x)$ for the optimized copper cylindrical TGU.

4. TGU technical design considerations

In this chapter, the technical design for the transversal gradient undulator and the correction coils are discussed. Furthermore, mechanical tolerances are simulated and the TGU coil formers, the support structure and the cryostat are presented.

4.1 Superconducting undulator coils

4.1.1 Superconducting wire specifications

A commercially available NbTi superconducting (sc) wire has been chosen for the fabrication of the copper undulator with $\lambda_u = 10.5\,\text{mm}$, $r = 30\,\text{mm}$, $g = 1.1\,\text{mm}$ and the selected coil winding package of 6 layers $\times$ 4 turns (see Section 3.4.1). The main parameters of the commercial sc wire are listed in Table 4.1.

Supplier:	OST
Composition:	NbTi/Cu
Cu/SC ratio:	1.3:1
Shape:	rectangular
Insulated cross-section:	$1.08\,\text{mm} \times 0.68\,\text{mm}$
Number of filaments:	54
Critical current @ 4.2 K and 6 T:	443 A

Table 4.1: Specification of the NbTi sc wire employed for the undulator coils.

This sc wire has a rectangular shape with bare dimension of $1.00\,\text{mm} \times 0.60\,\text{mm}$. By choosing a rectangular wire instead of a round wire, a higher packing factor can be achieved and better control of the wire positioning in the grooves is possible. The necessary average current density in the coil is around $1\,\text{kA/mm}^2$ to achieve the optimal magnetic field on axis of about 1.7 T. A pole width of approximately 1 mm is required.

4.1.2 Fit function for the critical current density

As discussed in Section 1.3, the critical surface of NbTi alloy material is defined by the critical temperature T_c, the upper critical magnetic field B_{c2} and the critical current density J_c. The critical field dependence on temperature and the critical temperature dependence on field is obtained from Lubell's equations [56]:

$$\mathrm{B_{c2}(T)} = \mathrm{B_{c20}}\left[1 - \left(\frac{\mathrm{T}}{\mathrm{T_{c0}}}\right)^{1.7}\right] \tag{4.1}$$

$$\mathrm{T_c(B)} = \mathrm{T_{c0}}\left[1 - \left(\frac{\mathrm{B}}{\mathrm{B_{c20}}}\right)^{1/1.7}\right] \tag{4.2}$$

where:
$\mathrm{B_{c0}} = 14.4\,\mathrm{T}$ is the maximum upper critical field at $\mathrm{T} = 0$,
$\mathrm{T_{c0}} = 9.2\,\mathrm{K}$ is the maximum critical temperature at $\mathrm{B} = 0$,
$\mathrm{T} = 4.2\,\mathrm{K}$ is the operating temperature.

A fit function, which gives the critical surface for NbTi superconductors as function of applied magnetic flux density and temperature, was published in [57] by L. Bottura and is given by:

$$\mathrm{J_c(B,T)} = \mathrm{J_{c,ref}}\frac{\mathrm{C_0}}{\mathrm{B}}\left[\frac{\mathrm{B}}{\mathrm{B_{c2}(T)}}\right]^{\alpha}\left[1 - \frac{\mathrm{B}}{\mathrm{B_{c2}(T)}}\right]^{\beta}\left[1 - \left(\frac{\mathrm{T}}{\mathrm{T_{c0}}}\right)^{1.7}\right]^{\gamma} \tag{4.3}$$

where $\mathrm{J_{c,ref}} = \mathrm{J_c}(5\,\mathrm{T}, 4.2\,\mathrm{K})$ and $\mathrm{C_0}$, α, β and γ are free fit parameters. $\mathrm{C_0}$ is a normalization constant, the two parameters α and β describe the dependence on the reduced field and γ is a parameter which describes the dependence on the reduced temperature. The range of variation of the fit parameters α, β and γ is restricted and given by Bottura as: α is of the order of 0.5 to 0.8, β close to 1 and γ in the range of 2.

The critical current density versus magnetic field curve $\mathrm{J_c(B)}$ at the operating temperature 4.2 K for the undulator NbTi wire is given in Figure 4.1. A total of seven data points have been fitted with Equation (4.3), where the data at high field in the range 6 T to 9 T are given by the wire manufacturer and the data at low field have been measured by [58]. The values for the fit parameters are shown in Table 4.2.

$\mathrm{J_{c,ref}[A/mm^2]}$	$\mathrm{C_0}$	α	β	γ
800	32.9	0.88	1.13	1.7

Table 4.2: Parameters of the Bottura's fit function for the undulator sc wire.

The straight line, usually known as the load line (see Figure 4.1), represents the peak field experienced by the undulator winding as a function of the current flowing in it. The predicted load line of the undulator was calculated using OPERA-3D. The simulations show a peak field at the conductor of 1.18 T with a current density of $500\,\mathrm{A/mm^2}$ and 2.37 T with $1000\,\mathrm{A/mm^2}$. The undulator will go resistive or "quench" when the load line crosses the fitted curve at $\mathrm{J_c} = 1214\,\mathrm{A/mm^2}$.

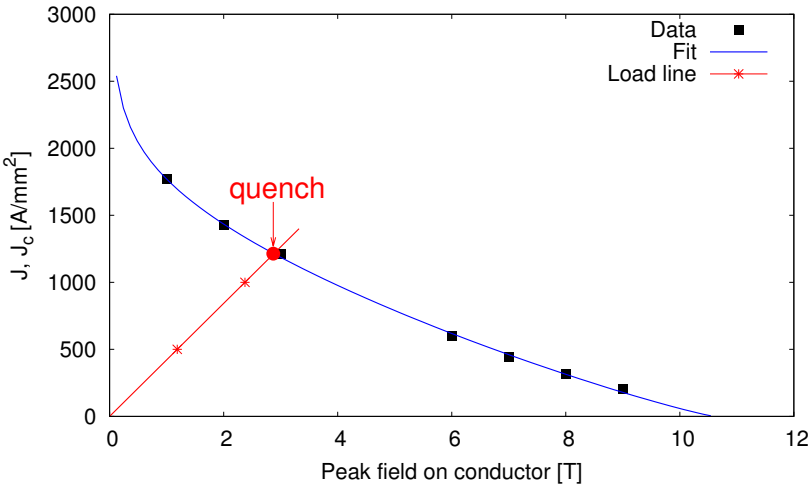

Figure 4.1: Critical current density versus magnetic field curve at 4.2 K. Data wire fitted with a curve (in blue) using Bottura's Equation. The predicted load line (in red) of the copper undulator and expected quench.

4.1.3 Matching coils

The undulator should have the least possible net effect on the electron beam. It is critical that the electron trajectories through the undulator are straight: the angle under which the beam enters the undulator, the exit angle and the exit x-position should ideally equal zero [2]. The design of the field terminations for the undulator at the entrance and exit of the device has to be adapted to keep the trajectories straight. That can be done modifying the winding packages of the first and second end coils, which are named matching coils. Several combinations of winding packages were tested. In this thesis only two of these combinations are shown because the best results were obtained with them (see Figure 4.2). They are called in the following MC8&16 and MC6&18. These matching coils have in common that the sum of turns of the first and second coil is 24 turns. That is the total of the selected undulator coils turns (4 single turns × 6 layers).

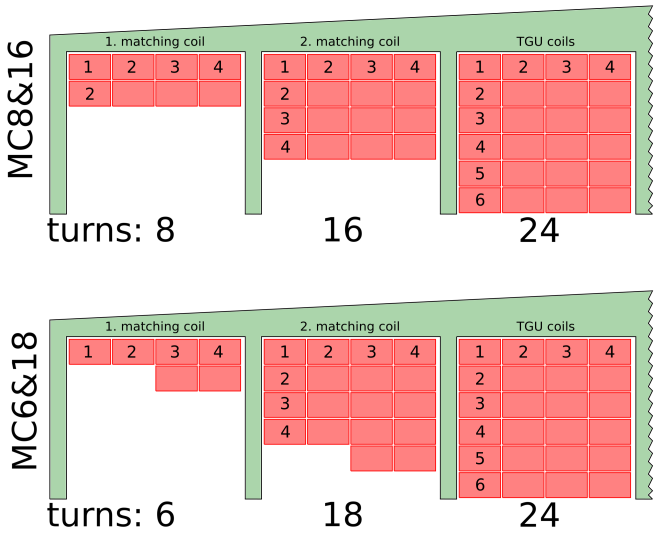

Figure 4.2: Matching coils with two different combinations of winding packages.

Undulator models with these two different matching coils were modeled in OPERA-3D and the trajectories for the central energy $E_0 = 120\,\mathrm{MeV}$ were simulated. Figure 4.3 shows the results and compares them with the trajectory without matching coils. The best trajectories are achieved with the first and second matching coils with 6 and 18 turns respectively. This combination of winding packages produces a sinusoidal magnetic function $B_y(z)$ with the peak amplitudes of $-1/4$, $3/4$, -1, 1, ... as shown in Figure 4.4.

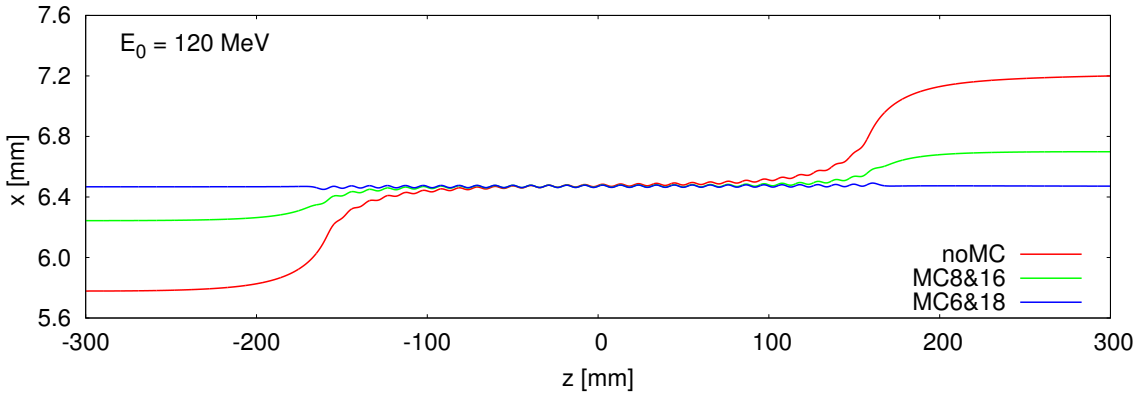

Figure 4.3: Comparison of the trajectories for $E_0 = 120\,\mathrm{MeV}$ through two undulators with different matching coils (MC8&16 and MC6&18) and an undulator without them (noMC).

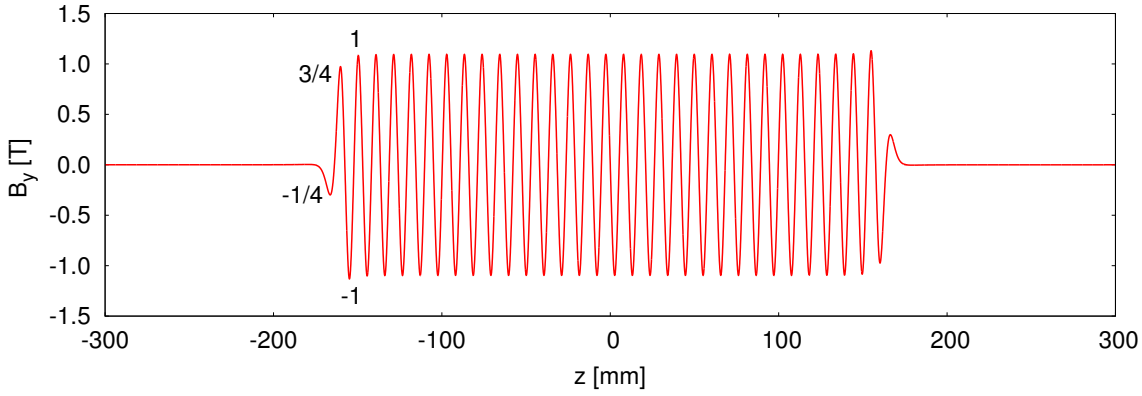

Figure 4.4: Magnetic field $B_y(z)$ for a 30 period undulator with the matching coils MC6&18 illustrated in Figure 4.2.

4.1.4 Undulator coil geometry selection

The ideal cylindrical undulator consists only of solenoid coils. For the selected superconducting wire ($1.08\,\mathrm{mm} \times 0.68\,\mathrm{mm}$) and the winding package with 4 turns $\times$ 6 layers, the space between two adjacent packages is lower than 1 mm for a 10.5 mm period length undulator. This space is smaller than the dimension of the superconducting wire. Therefore it is required to lay out every second winding package as an upright racetrack coil. Two possible coil geometries result of this solution:

a) Symmetrical form: a mirror symmetrical coil geometry with respect to the undulator center (xz-plane). The same type of coil, solenoid or racetrack, is

located on both sides of the undulator. All winding packages with a current flow in one direction have a different shape than those with a current flow in the other direction.

b) Antisymmetrical form: an antisymmetrical coil geometry with respect to the undulator center. A solenoid winding package in the top coils is facing a racetrack winding package in the bottom coils and vice versa.

Figure 4.5 shows the cross-section of two central periods of both undulator coils for the ideal cylindrical, symmetrical and antisymmetrical coil forms. Solenoid coils are marked with the letter S and racetracks with R, followed by the number of the coils.

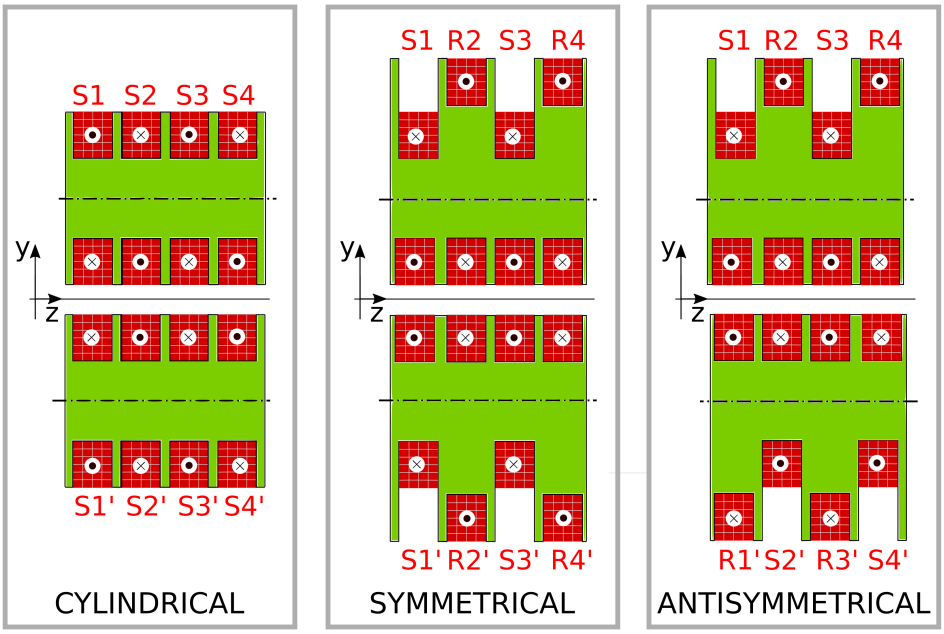

Figure 4.5: Coil geometry forms: cylindrical (only solenoid coils), symmetrical (same type of coil in both sides) and antisymmetrical (solenoids in front of racetracks and vice versa).

The absolute value of the y-component of the magnetic flux density $|B_y|$ produced by the cylindrical and antisymetrical undulator is exactly the same, as is shown in Figure 4.6. In contrast, it can be also observed in this figure that the symmetrical undulator produces a net field $|B_y|$ superimposed to the ideal cylindrical undulator magnetic field. With the antisymmetrical configuration the unwanted net fields of top and bottom coil cancel each other out.

The simulated electron trajectories in the xz-plane through the antisymmetrical and cylindrical undulator coincide and show an insignificant deviation from the ideal straight path after the first undulator periods. However, the net field superimposed to the ideal field in the symmetrical undulator significantly deflects the electron trajectories from the ideal straight path, as it is shown in Figure 4.7.

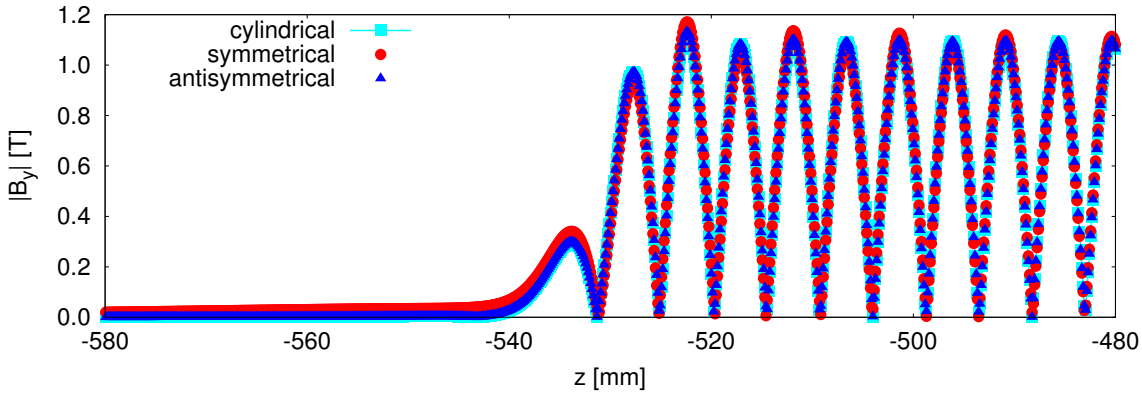

Figure 4.6: Comparison of the absolute magnetic field $|B_y|$ produced at the beginning of the undulators with cylindrical (cyan line-points), symmetrical (red points) and antisymmetrical (blue points) forms.

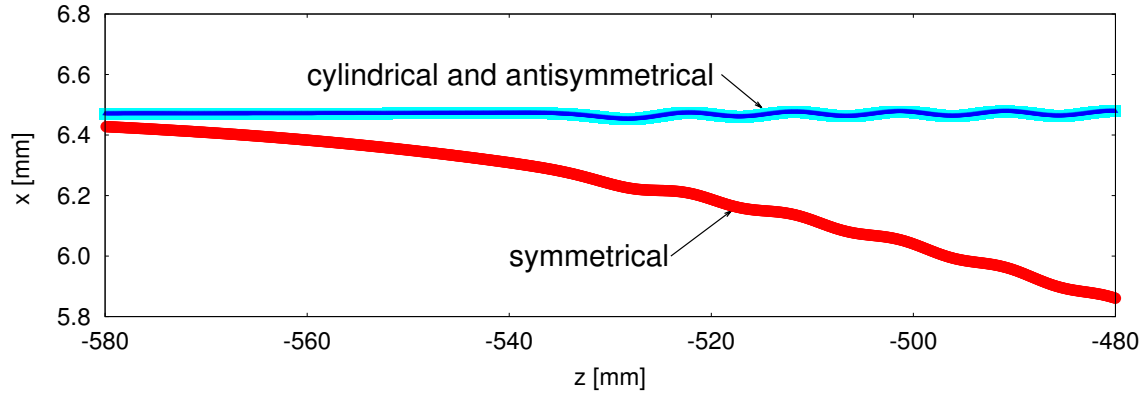

Figure 4.7: Comparison of the electron trajectories in the xz-plane after the first five undulator periods with $E_0 = 120\,\mathrm{MeV}$ through undulators with cylindrical (cyan points), symmetrical (red points) and antisymmetrical (blue points) forms. The high drift produced after the first periods with the symmetrical undulator is shown.

Figure 4.8 shows the comparison of the simulated magnetic flux density component B_x through a patch in xy-plane placed just before entering the different undulator models. In the case of the cylindrical and symmetrical undulators, B_x is compensated and vanishes on the x-axis, where the electrons travel through the undulator in the xz-plane. In contrast, B_x is not compensated in case of the antisymmetrical undulator (see Figure 4.9).

The B_x peak value varies also with the x-position as is shown in Figure 4.9. Taking into account the spectral dispersion of the electrons, $x(\mathrm{E})$, it turns out that the low energy electrons (108 MeV) experience a larger vertically deflecting field B_x than the high energy electrons (see Figure 4.9). Figure 4.10 shows the resulting drift of the electron trajectories in the yz-plane appearing in the antisymmetrical undulator model.

The drift of the electron trajectories in both xz- and yz-planes has to be corrected. It is easier compensate B_x than B_y and minimize the drift through the antisymmetrical undulator, as it is shown in Section 4.4.2. This is achieved

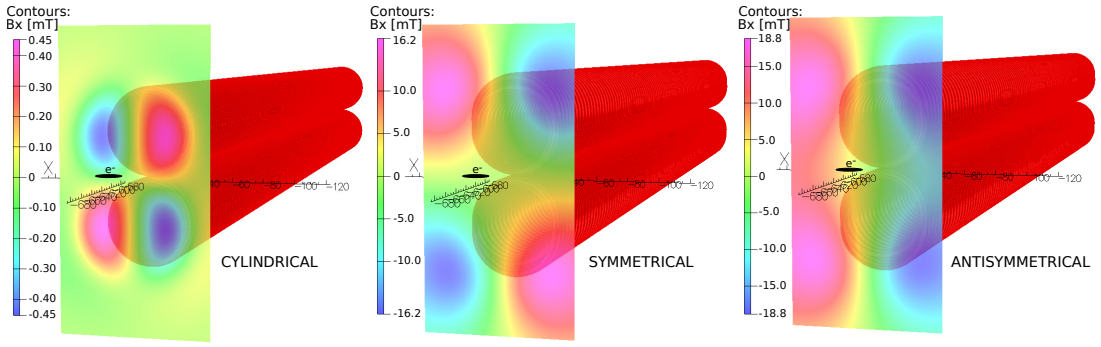

Figure 4.8: Comparison of the simulated magnetic field B_x through a patch in xy-plane placed just before entering the different undulator models.

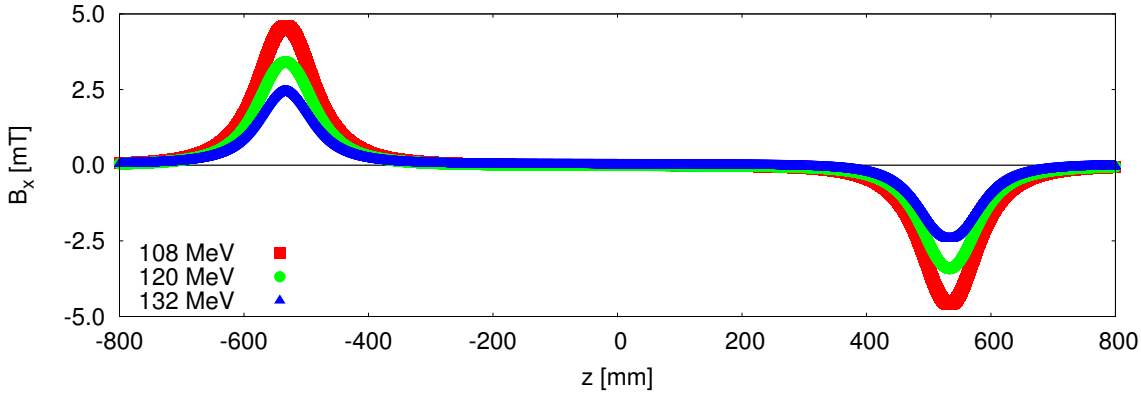

Figure 4.9: Magnetic field $B_x(z)$ produced for the antisymmetrical undulator.

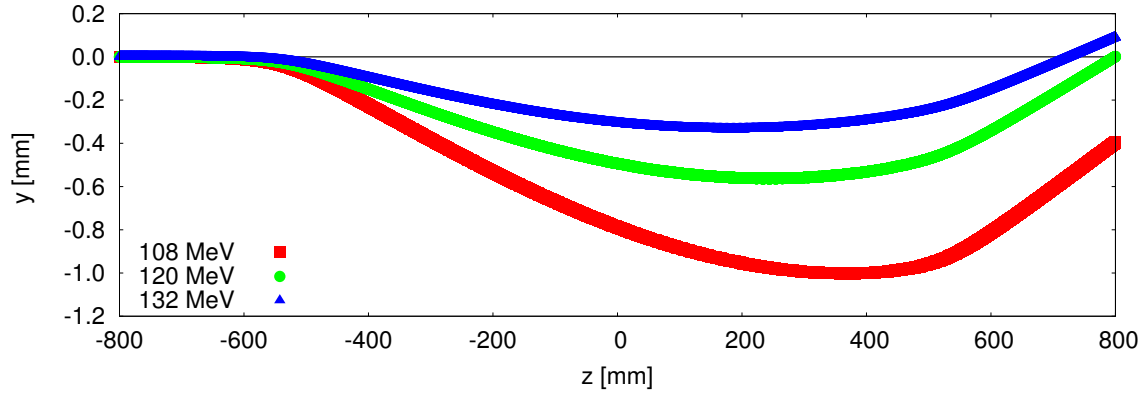

Figure 4.10: Electron trajectories in the yz-plane through undulators with antisymmetrical form.

optimizing an offset in the start y-position and the start angle Θ_{yz} of the electron trajectories together with the current density of the correction coils.

The antisymmetrical model was finally chosen for the construction of the undulator coil formers. Figure 4.11 shows schematically the cross-section of the matching period and two periods of both undulator coils and indicates the winding scheme for the antisymmetrical undulator. The undulator coils are junction free and wound with a single wire. The winding packages consist of 4 turns $\times$ 6 layers and are wound in the order 1...n. The wire is fed through to the next winding package above or

below the neighboring groove (red line connecting the coil packs in Figure 4.11). Since the number of layers is even, the winding has to start at the back side of the winding package.

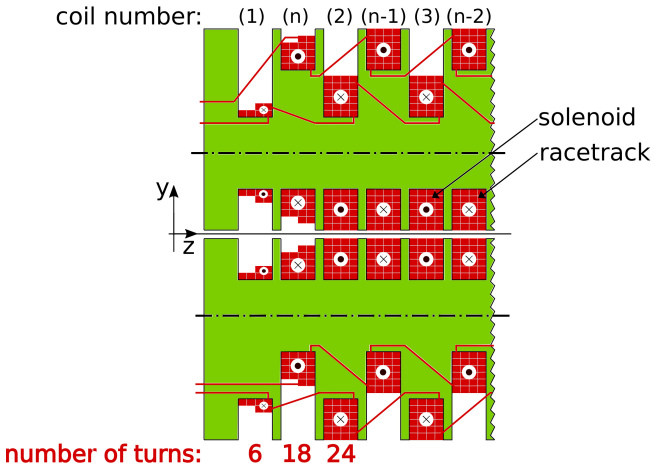

Figure 4.11: Winding scheme of the selected antisymmetrical undulator, cross-section of the 1/4 and 3/4 matching coils at the undulator entrance and two full periods.

4.2 Superconducting correction coils

4.2.1 Superconducting wire specification

As mentioned in Section 3.4.4, a weak field of about −50 mT has to be superimposed to the undulator field in order to correct the electron trajectories inside the undulator. This correction field is generated by correction coils and the main parameters of the commercial superconducting wire used in their construction are given in Table 4.3.

Supplier:	EAS
Composition:	NbTi/Cu
Cu/SC ratio:	1.5:1
Shape:	round
Insulated cross-section:	⌀ 0.232 mm
Number of filaments:	1
Critical current @ 4.2 K and 5 T:	26 A

Table 4.3: Specification of the NbTi wire employed for the correction coils.

This superconducting wire consists of one NbTi filament in a Cu matrix with a copper-to-superconductor area ratio of 1.5. The wire has a circular cross section with a diameter of 0.2 mm (bare). In the following a winding cross section of the correction coils of $1 \times 1\,\mathrm{mm}^2$ is assumed, which corresponds to 14 turns of the wire employed.

4.2.2 Correction coil geometry selection

The required correction field $B_y^{\text{corr}}(x)$ for the cylindrical copper undulator was calculated in Section 3.5.2. This correction field can be produced by a group of coils around and/or inside the undulator. Several correction coil models with different geometries were simulated [59] and the correction field produced for them was calculated by the software OPERA-3D. The boundary conditions taken into account in the design of the correction coils are:

- The correction field $B_y^{\text{corr}}(x)$ has to be close to the ideal curve of the required correction field.
- The correction field $B_x^{\text{corr}}(x, y) << B_y^{\text{corr}}(x)$ in the area of the beam to avoid perturbations in the electron trajectories.
- The correction magnet must not overlap with the electron beam ($x = 4.5\,\text{mm}$ to $9.5\,\text{mm}$ and $y = \pm\ 0.55\,\text{mm}$).
- The current of the correction coils should not be too high to avoid thermal load.

During the design of the correction coils four cases have been studied:

a) Two symmetrical dipole-bedstead coils placed around the undulator coil formers (see Figure 4.12 (a)). Using this type of coils has the advantage that the area where the electron beam passes remains completely free. With an average current density of about $32\,\text{A/mm}^2$ the correction field produced by these coils in comparison with the ideal correction field is shown in Figure 4.13.

b) Two racetrack coils simulated by four long straight wires on the undulator surface. The position of both coils is not parallel but inclined to the xz-plane, as shown in Figure 4.12 (b). The correction field produced by this kind of coils was very similar to the bedsteads coils (see Figure 4.13), but with a higher current density of about $40\,\text{A/mm}^2$.

c) Three racetrack coils simulated by six long straight wires are shown in Figure 4.12 (c). It is the same configuration as case (b) built with an additional coil between the undulator coil formers (on the xz-plane). In this case an additional power supply is necessary. The current density is about $64\,\text{A/mm}^2$ for the coils on the undulator surface and about $4.5\,\text{A/mm}^2$ for the central coil. The correction field produced by these three coils is very close to the ideal correction field as shown in Figure 4.13. The disadvantage is that the electron beam must travel between the straight parts of the central coil and therefore this configuration is very difficult to realize.

d) Two racetracks coils simulated by four long straight wires inside the coil formers (see Figure 4.12 (d)). These coils are parallel to the xz-plane. The correction field produced by these coils with a current density of about $38\,\text{A/mm}^2$ matches very well with the ideal curve (see Figure 4.13). This correction coil configuration was selected because the best results were obtained with it and it meets all the boundary conditions.

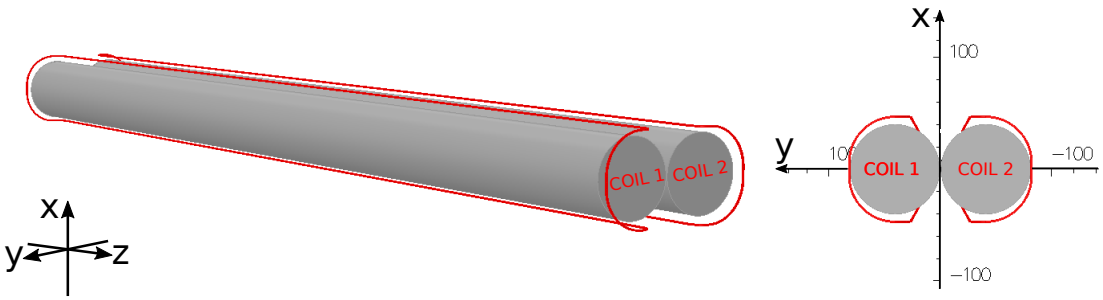

(a) Two dipole-bedstead coils around the undulator.

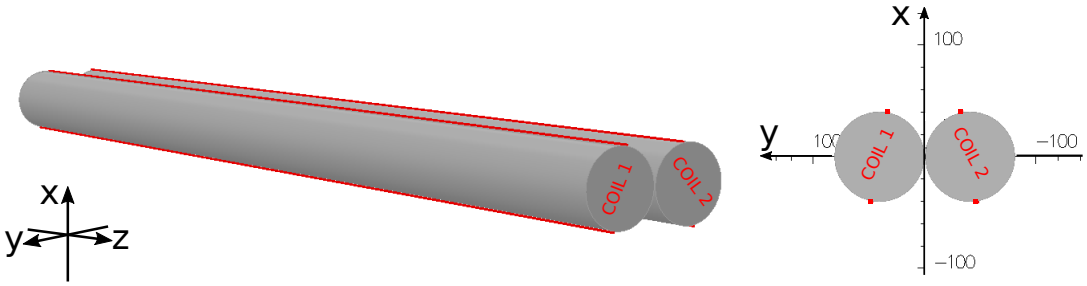

(b) Two racetrack coils (four long straight wires) on the undulator surface.

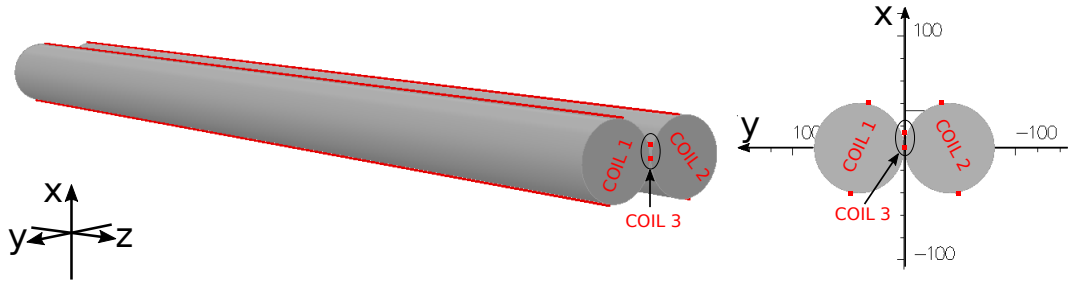

(c) Three racetrack coils (six long straight wires): one coil between the undulator and the other two coils on the undulator surface.

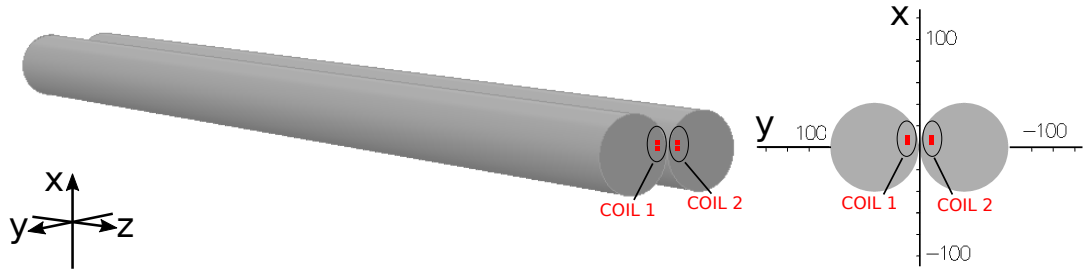

(d) Two racetrack coils (four long straight wires) inside the undulator coil formers.

Figure 4.12: Several correction coil geometries (red lines) for the cylindrical copper undulator (in grey).

Figure 4.13 compares the required correction field B_y as function of the transverse position x with the correction field produced for the four simulated correction coil geometries. The best results were obtained with the two racetracks-coils inside the undulator coil formers, where the correction field matches with the ideal curve. This correction coil configuration was selected for the construction inside the undulator.

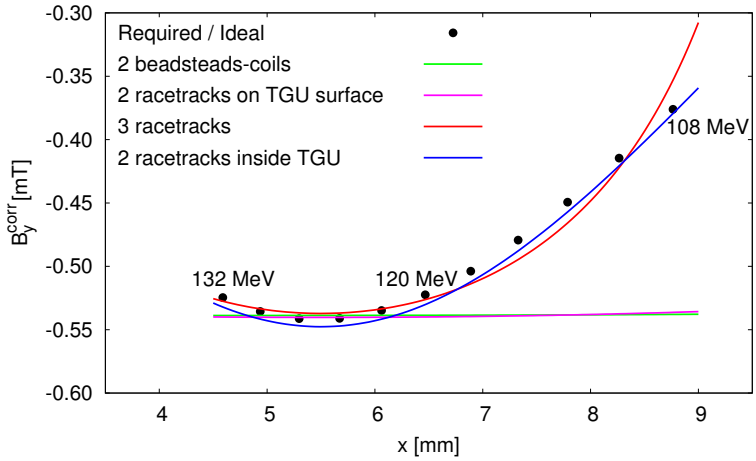

Figure 4.13: Comparison of $B_y^{\mathrm{corr}}(x)$: required or ideal (black points) and produced with different correction coil geometries: two beadsteads-coils (green line), two racetracks on TGU surface (pink line), three racetracks (red line) and two racetracks inside TGU (blue line).

4.2.3 Optimization of the correction coil parameters

Figure 4.14 shows the correction coils inside the undulator. The correction coil winding package width and thickness are assumed to be 1 mm × 1 mm. Both racetracks-coils are parallel to the xz-plane and the distance to this plane is fixed and equal to $y_{\mathrm{p1}} = 8.5\,\mathrm{mm}$. Their position inside the undulator coil formers is also restricted by the undulator coil position, which is defined for their external and internal pole radius. The internal pole radius $\mathrm{r_i} = 25.92\,\mathrm{mm}$ can be calculated through the undulator wire specifications (see Section 4.1.1) and the coil winding package of 6 layers × 4 turns.

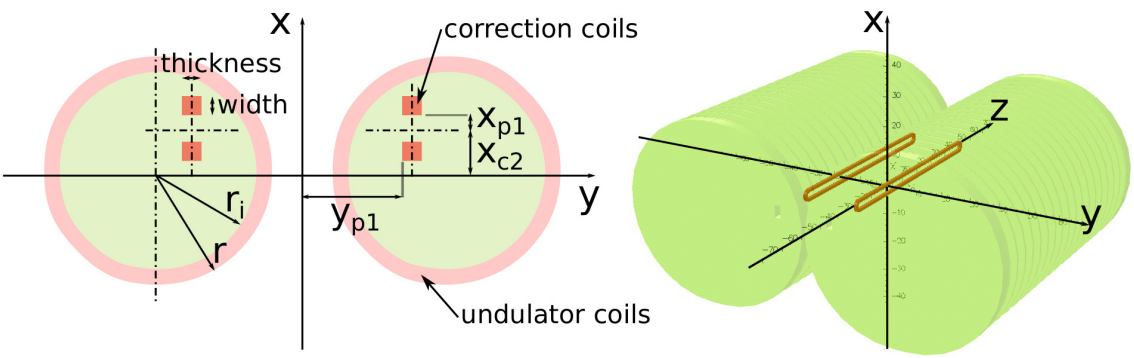

Figure 4.14: Correction coil design parameters.

Some parameters of the correction coil can be optimized to correct the exit angle of the trajectories. The parameters to optimize are: the distance x_{c2} from the center of the racetrack-coil to the yz-plane, the half-internal width of the racetrack coil x_{p1}, the current density of the correction coils and an offset in the start x-position of the electron trajectories. This offset affects by equal to all the electron energies and it is achieved with a vertical displacement of the TGU.

The maximal values of x for each undulator period (x_{N}^{max}) are calculated and compared with the ideal maximal values of x for the straight trajectories (x_{ideal}^{max}) for each energy. The goal of this optimization using the simplex method is to minimize the electron trajectories drift in the xz-plane.

The design and optimized parameters employed to perform the correction coil optimization are summarized in Table 4.4. Figure 4.15 shows the relative trajectories before and after the optimization with the electron energies of 108 MeV, 120 MeV and 132 MeV.

Design parameters:		
Winding package width:	width	1 mm
Winding package thickness:	thickness	1 mm
Distance to xz-plane:	y_{p1}	8.5 mm
TGU external pole radius:	r	30 mm
TGU internal pole radius:	$\mathrm{r_i}$	25.92 mm
Optimized parameters:		
Correction current density:	$\mathrm{J_{corr}}$	32.69 A/mm^2
Half-internal width:	x_{p1}	1.455 mm
Distance to yz-plane:	x_{c2}	5.719 mm
Trajectories offset:	x^{offset}	0.727 μm

Table 4.4: Design and optimized correction coils parameters.

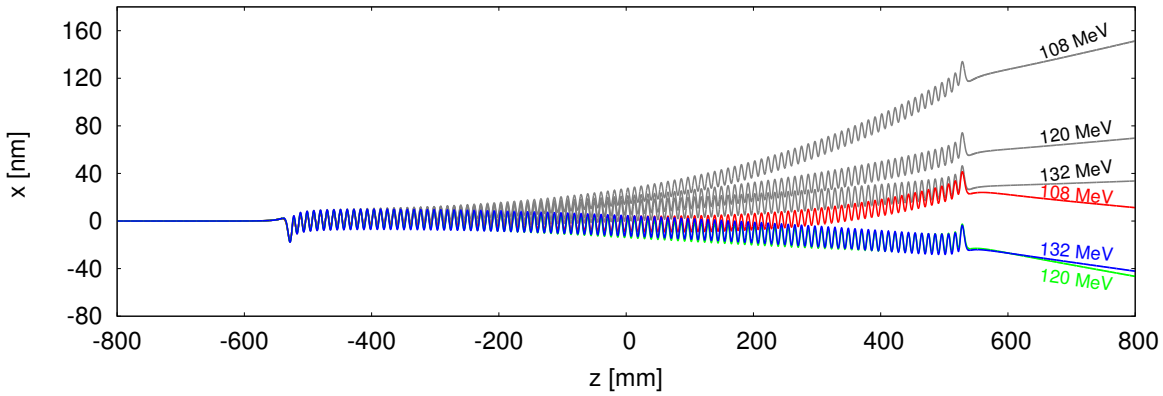

Figure 4.15: Simulation of the relative electron trajectories: before the optimization (grey lines) and after the optimization of the correction coil parameters (red/blue/-green lines).

The parameters of the correction coil before the optimization are: $J_{corr} = 38\,A/mm^2$, $x_{p1} = 1.5\,mm$, $x_{c2} = 5.5\,mm$ and $x^{offset} = 0$. The magnetic field produced with this parameters fits with the ideal correction field shows in Figure 4.13. The highest drift after 100 undulator periods was obtained with an electron energy of 108 MeV. After the optimization this drift was reduced around four times. With 120 MeV the drift was reduced by around half from its original value.

The optimization depends on the number of undulator periods. A final optimization of the real model TGU is shown in Section 4.4.2 to correct the trajectories also in the yz-plane. Therefore two new parameters are optimized: y^{offset} and Θ_{yz}.

4.3 Mechanical tolerances

4.3.1 Types of mechanical deviations

The finite tolerances in the construction of the coil formers lead to field errors, which produce changes and unexpected drifts in the electron trajectories. Figure 4.16 shows a longitudinal cut of an electromagnetic copper undulator and the two mechanical deviations considered in this thesis. Both deviations are deliberately shown in an exaggerated way to illustrate the idea. A more detailed analysis can be found in [Kar13].

The first deviation shown is the deviation of half period length ($\lambda_u/2 \pm$ tolerance), measured from the axes of two adjacent superconducting coils. This deviation varies the width of the poles along the undulator and with it the position of the coil in z direction. The second deviation is the variation of the internal pole radius ($r_i \pm$ tolerance), which varies the position of the superconducting coils in y-direction.

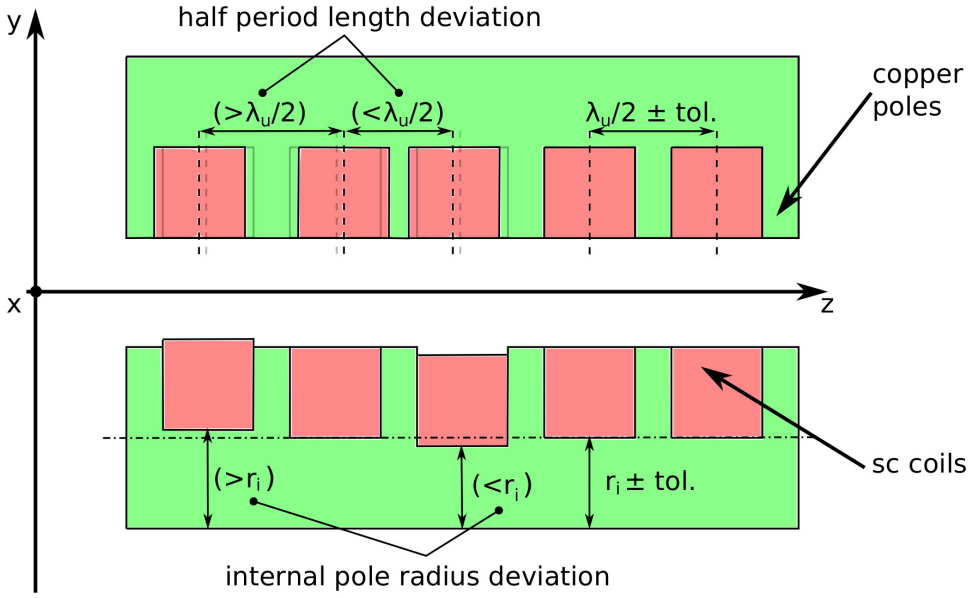

Figure 4.16: Longitudinal cut of an electromagnetic undulator to show the mechanical deviation of the half period length and the deviation of the internal pole radius. Only the part of the undulator coil close to the beam axis is shown.

The influences of these two different mechanical deviations on the electron trajectories along a 100 period antisymmetrical undulator were simulated with OPERA-3D. This undulator has a period length $\lambda_u = 10.5\,mm$, an external pole radius $r = 30\,mm$, a gap on axis $g = 1.1\,mm$ and a current density $J = 1020\,A/mm^2$. The correction coil employed in the simulations are optimized in Section 4.2.3 with a correction current density of $J_{corr} = 32.69\,A/mm^2$ and the optimal offset in the x-position $x^{offset} = 0.727\,\mu m$. Table 4.5 summarizes the x start position and the peak amplitudes of the energies used to perform the simulations. The peak amplitudes are calculated analytically for ideal trajectories excluding the effect produced by the matching coil.

E [MeV]	x_E [mm]	Peak-amplitude [μm]
108	8.738	5.85
120	6.471	7.51
132	4.618	8.47

Table 4.5: Parameters for the simulation of the electron trajectories through 100 periods asymmetrical undulator with mechanical deviations.

4.3.2 Statistically distributed deviations

Simulations with statistically distributed mechanical errors have been performed to quantify the effects on the electron trajectories. Both mechanical deviations are considered separately. Each simulation consists of one undulator without deviation and ten undulators with deviations to compare the results between them and calculate the standard deviation produced for each energy and the total deviation.

Figure 4.17(a) shows a general example to explain how the standard deviation is calculated. The electron trajectories for one energy are shown: in red without a mechanical deviation and in blue with it. The maximal values of x for each undulator period (x_N^{max}) are calculated for both cases separately. The ideal maximal values of x for the straight trajectories (x_{ideal}^{max}) can be calculated adding x_{start} to the peak-amplitude. These both values depends on the electron energy (see Table 4.5). The absolute difference of the x values ($|\Delta_x|$) for the both trajectories of this example is shown in green in Figure 4.17(b).

The standard deviation of the electron trajectories for each energy ($\sigma_{\hat{x}}(E)$) is given by Equation 4.4.

$$\sigma_{\hat{x}}(E) = \sqrt{\frac{\sum_{i=0}^{N}(x_{ideal}^{max} - x_N^{max})^2}{N}} \tag{4.4}$$

where N is the number of undulator periods.

4.3.3 Deviation results

The selection criteria of the tolerance for the two mechanical deviations considered in this thesis is that the deviations are smaller than the beamlet width (see Table 3.26). Therefore is ensured that $\Delta\lambda/\lambda_0 \leq 1\,\%$ for a 100 periods undulator.

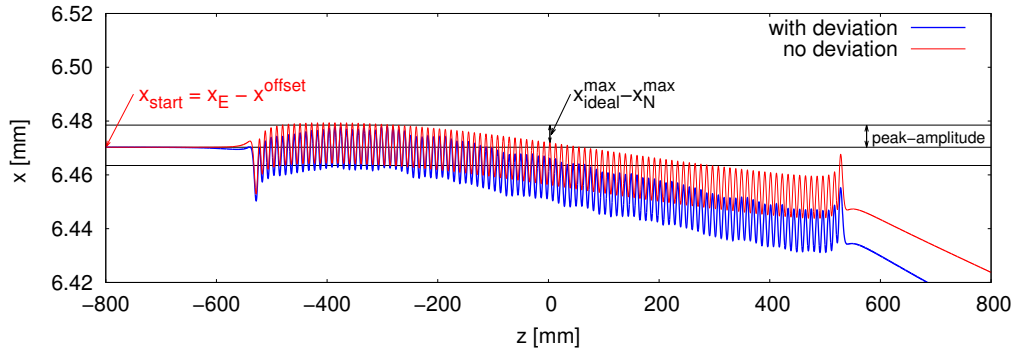

(a) Simulated electron trajectories on the xz-plane with a mechanical deviation (blue) and without deviation (red).

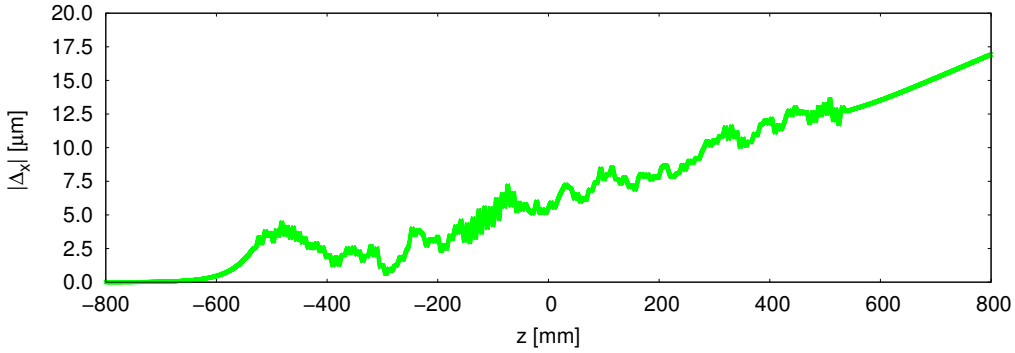

(b) Absolute difference of the x values between the trajectories through an undulator with a mechanical deviation and without deviation.

Figure 4.17: Example of the variation of the electron trajectories produced for a mechanical deviation.

a) For the construction of the undulator coil formers, two different tolerances of the internal pole radius were considered: ±0.008 mm and ± 0.01 mm. Deviation number 0 represents the values of the undulator without mechanical deviation. The deviation numbers between 1 and 10 shows the results for the ten undulators simulated with a statistically distributed error in the internal pole radius. Each superconducting coil has a different error limited for the tolerance values. Figure 4.18 (a) shows the deviation results with a tolerance of ± 0.008 mm. For the ten cases considered the values of the total deviation remains below 14 μm. In the case with a tolerance of ± 0.01 mm, the total deviation remains below 18 μm, as shown in Figure 4.18 (b). If the tolerance of ± 0.008 mm is selected, the undulator price is considerably more expensive than with a higher tolerance. For this reason, the tolerance of ± 0.01 mm is selected for the internal pole radius.

b) In the case of the mechanical deviation on the half period length, two different tolerance values ± 0.01 mm and ± 0.05 mm were considered. Figure 4.19 (a) shows the deviations with tolerances of ± 0.01 mm. They are practically constant and the value of the total deviation remains below 10 μm, as the value of the deviation number 0 without mechanical deviation. However with a tolerance of ± 0.05 mm the total deviation reaches 20 μm (see Figure 4.19 (b)). The tolerance of ± 0.01 mm is selected for the half pole length deviation.

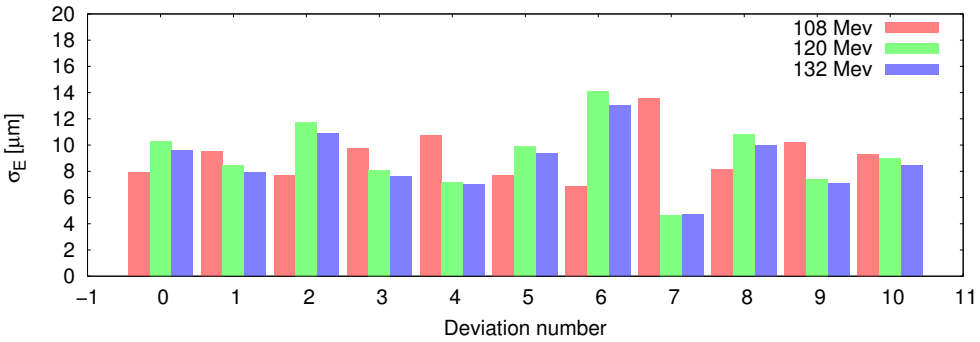

(a) With ± 0.008 mm tolerance

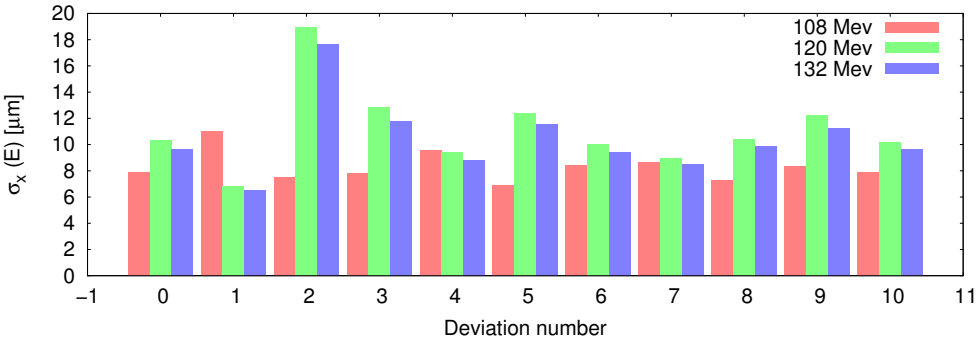

(b) With ± 0.01 mm tolerance.

Figure 4.18: Standard deviations of simulated undulators with internal pole radius mechanical errors.

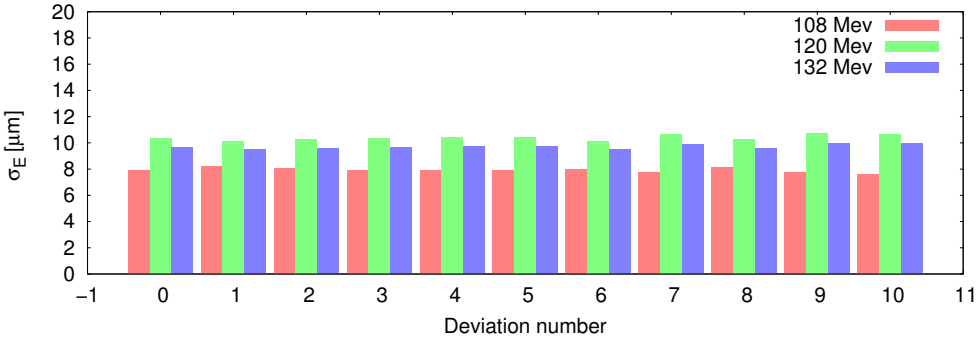

(a) With ± 0.01 mm tolerance

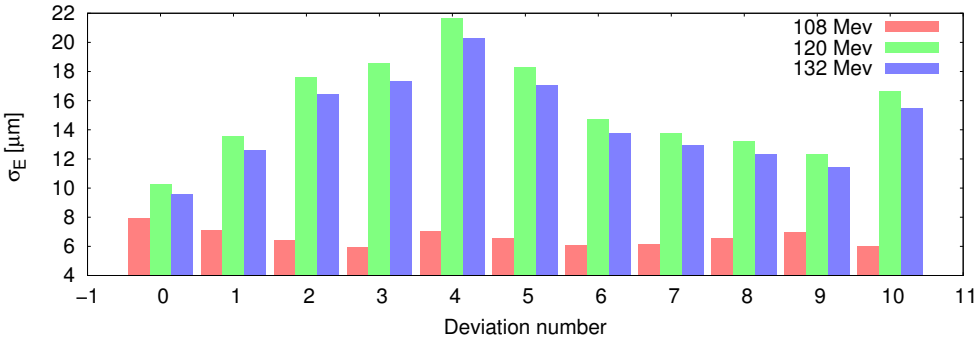

(b) With ± 0.05 mm tolerance.

Figure 4.19: Standard deviations of simulated undulators with half period length mechanical errors.

4.4 TGU coil formers and support structure

4.4.1 Mechanical layout

Although the design optimization described in this thesis was performed for a 100 periods undulator, the full-scale prototype built at KIT for the proof-of-principle experiment has 40 periods (called TGU40). Each coil former is composed of three modules (see Figure 4.20 (left)), which are assembled before winding the superconducting coils. This assembly is in principle extendable to 100 periods by four times repeating the inner coil modules. The superconducting coils are wound on a copper former in order to ensure good heat conduction and to minimize thermally induced mechanical stress. The coil assembly is supported by a bolted clamping structure, which is made of copper for the same reasons (see Figure 4.20 (right)).

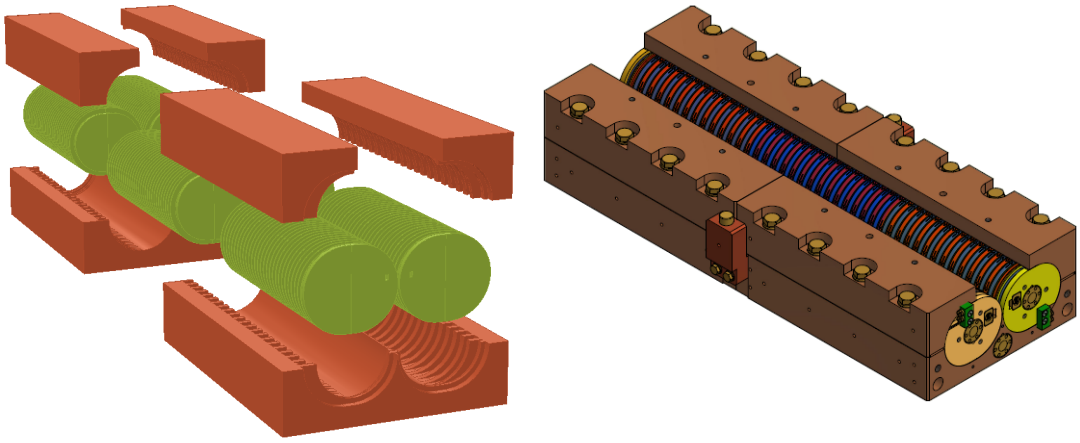

Figure 4.20: Schematic mechanical layout of the TGU. Exploded View (left): coil former (green) and coil support structure (brown). Undulator coil assembly supported by a bolted clamping structure (right) [61].

The support structure defines the magnetic gap of the undulator, applies compressive prestress to the outer parts of the racetrack winding packages (see Figure 4.21) and takes up the magnetic forces acting on the undulator coils as a whole. Since the electron beam travels about 6.5 mm off axis through the undulator, it is possible to fill one half of the gap with the spacer precisely defining the position of the coils with respect to each other. Furthermore in this configuration no net torque due to magnetic forces acts on the coils. The forces on the coils with a maximal current density of 1348 A/mm^2 were calculated with OPERA-3D [46] and applied in the mechanical analysis.

Simulations of the structural mechanics of a ten periods antisymetrical undulator (with matching coils) were calculated [62]. The analysis was performed with Autodesk Inventor Stress Analysis [63], which is based on the FEM (finite element method) and on the von Mises failure theory. The static analysis determines the stress in materials and structures subjected to static or dynamic forces or loads. The aim of this analysis is to determine whether the element or structure can safely withstand the specified forces and loads. This is achieved when the determined stress from the applied force(s) is less than the yield strength of the material.

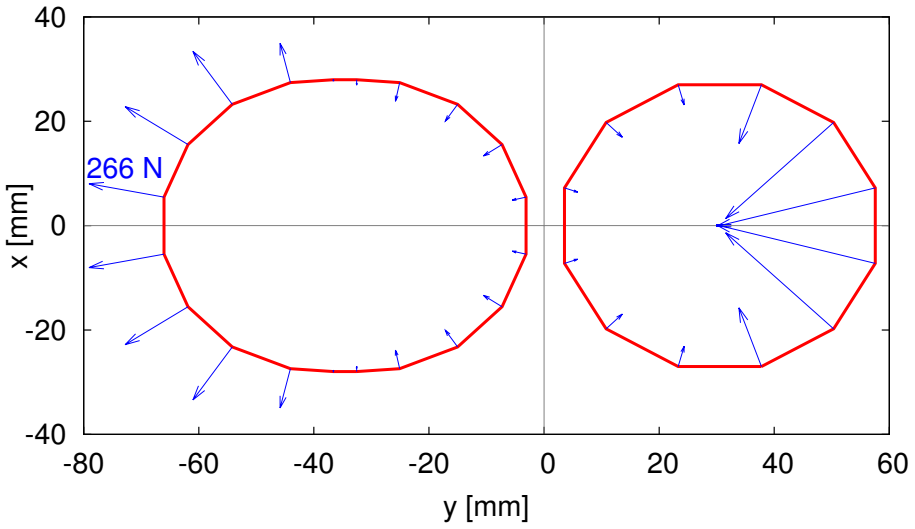

Figure 4.21: Force distribution in the central racetrack and solenoid TGU-coils.

This stress relationship is referred to as factor of safety (FOS) and is used as an indicator of success or failure in analysis of the mechanical structure [64]:

$$\text{FOS} = \frac{\text{Yield strength}}{\text{Calculated stress}} = \frac{\text{Ultimate strength}}{\text{Calculated stress}} \tag{4.5}$$

where the yield strength S_y is defined as the stress at which a material begins to deform plastically. The FOS can be also based on the ultimate tensile strength of the material, which is defined as the maximum stress that the material can withstand while being stretched or pulled before failing or breaking. If the minimum value of the calculated FOS is larger than 1.0 indicates that the material is safe. If not, the material has failed.

It is a requirement that the elastic deformations remain within the allowable mechanical tolerances. The displacement of the coil former affects directly the quality of the magnetic field. Therefore it has to stay within the mechanical tolerance of $\pm$ 0.01 mm, which was selected in Section 4.3. Undulator quenches caused by the forces acting on the superconducting wire were experimentally determined.

Table 4.6 summarizes the properties of the material used in the design of the undulator coil formers. The material chosen for the production was finally Cu-ETP, which is cheaper than Cu-OF. The material characteristic values "Yield Strength" and "Ultimate tensile strength" of Cu-OF were adopted very conservative, this affects the factor of safety FOS negatively. The elastic deformation of Cu-ETP will be smaller and the safety factor of this material will be greater.

Young's modulus E describes the stiffness of the material (where a higher value produce a stronger material (e.g. copper or titanium) and a lower value a weaker material (e.g. glass)). It can be calculated by:

$$\text{E} = \frac{\sigma}{\epsilon} \tag{4.6}$$

where σ is the tensile stress and ϵ is the extensional strain in the elastic (initial, linear) portion of the strain curve. Strain is a normalized measure of deformation

Name	**Copper (2.0040 - Cu-OF)**	
General	Mass Density	8.94 g/cm^3
	Yield strength	70 MPa
	Ultimate tensile strength	230 MPa
Stress	Young's Modulus	127 GPa
	Poisson's Ratio	0.345

Table 4.6: Properties of the material used for the FEM stress analysis of the TGU coil formers.

and is defined as the ratio of elongation with respect to the original length. When a material is compressed in one direction, it usually tends to expand in the other two directions perpendicular to the direction of compression. This effect is defined by Poisson's Ratio ν.

The different stresses are classified into two groups for the analysis: normal stresses and shear stresses. The normal stress is perpendicular to the area under consideration, while the shear stress acts parallel to the area. The normal stresses are represented by σ_x, σ_y and σ_z in the x, y and z directions. Tensile stresses are considered to be positive, while compressive stresses are negative. The shear stresses are denoted by τ with two subscripts. The first subscript denotes the normal to the plane on which the force acts, and the second subscript identifies the direction of the force [64]. The principal normal stresses are:

$$\sigma_1 = \frac{\sigma_x + \sigma_y}{2} + \sqrt{\left(\frac{\sigma_x - \sigma_y}{2}\right)^2 + \tau_{xy}^2} \tag{4.7}$$

$$\sigma_2 = \frac{\sigma_x + \sigma_y}{2} - \sqrt{\left(\frac{\sigma_x - \sigma_y}{2}\right)^2 + \tau_{xy}^2} \tag{4.8}$$

and the principal shear stress is:

$$\tau_{max} = \pm\sqrt{\left(\frac{\sigma_x - \sigma_y}{2}\right)^2 + \tau_{xy}^2} \tag{4.9}$$

The von Mises criterion postulates that failure is caused by the elastic energy associated with shear deformation. This theory is valid for ductile materials and predicts yielding under combined loading with greater accuracy than any other recognized theory [65]. The von Mises stress σ_e for a triaxial stress state is calculated by:

$$\sigma_e = \sqrt{\left(\frac{(\sigma_1 - \sigma_2)^2 + (\sigma_2 - \sigma_3)^2 + (\sigma_1 - \sigma_3)^2}{2}\right)} \tag{4.10}$$

If the nomenclature $\sigma_1 \geq \sigma_2 \geq \sigma_3$ is used for the principal stresses, the shear stress says that yielding will occur when:

$$\sigma_1 - \sigma_3 = \frac{\mathrm{S}_y}{\mathrm{FOS}} \tag{4.11}$$

For a biaxial stress state, assuming $\sigma_3 = 0$,

$$\sigma_e = \sqrt{\sigma_1^2 + \sigma_2^2 - \sigma_1\sigma_2} \tag{4.12}$$

Thus, the von Mises criterion predicts failure if:

$$\sigma_e \geq \frac{\mathrm{S}_y}{\mathrm{FOS}} \tag{4.13}$$

For the stress analysis in Autodesk Inventor, a part of the undulator was simulated. The antisymetrical undulator model has two different coil formers. Both can be distinguished by the shape of the central groove, which is designed for winding either a solenoid or a racetrack coil. The coil former with a central groove for the solenoid coil was selected for the stress analysis.

Some boundary conditions were applied. A contact force is created by the screw rod and nuts, which compress the coil modules. A value of 5 kN was assumed for this force. Other boundary condition are the total external magnetic forces. These forces are part of the forces on the adjacent coil modules, which do not go directly into the coil formers and where a magnitude of 312.5 N was estimated. The sum of the forces on the coils was calculated in OPERA-3D and it was $\mathrm{F}_z = +26.25$ kN on the solenoids and $\mathrm{F}_z = -24.75$ kN on the racetracks.

These forces will cause a maximum displacement of the coil former shown in Figure 4.22 (a) with 3 μm maximum. This value is acceptable because it is less than the mechanical tolerance of $\pm$ 10 μm. The safety factor (FOS) obtained is shown in Figure 4.22 (b) with a minimum value of 1.61. Because the minimum FOS is greater than 1.0, it indicates that the material is safe.

Table 4.7 summarizes the results obtained for the stress analysis of the undulator coil former:

Name	Minimum	Maximum
Von Mises stress	0.01 MPa	43.61 MPa
1st principal stress	−28.74 MPa	49.46 MPa
3rd principal stress	−56.17 MPa	22.12 MPa
Displacement	0 mm	3.02 μm
Factor of safety (FOS)	1.61	15
Volume	358893 mm^3	
Mass	3.21 kg	

Table 4.7: Summary of the stress analysis results.

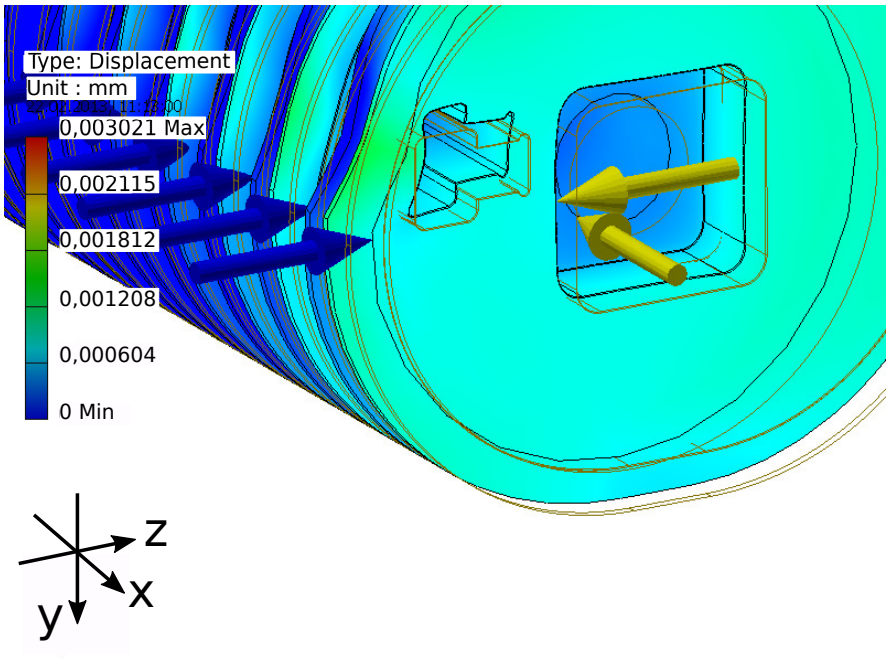

(a) Displacement of the coil former. Maximum displacement $\sim 3\,\mu$m.

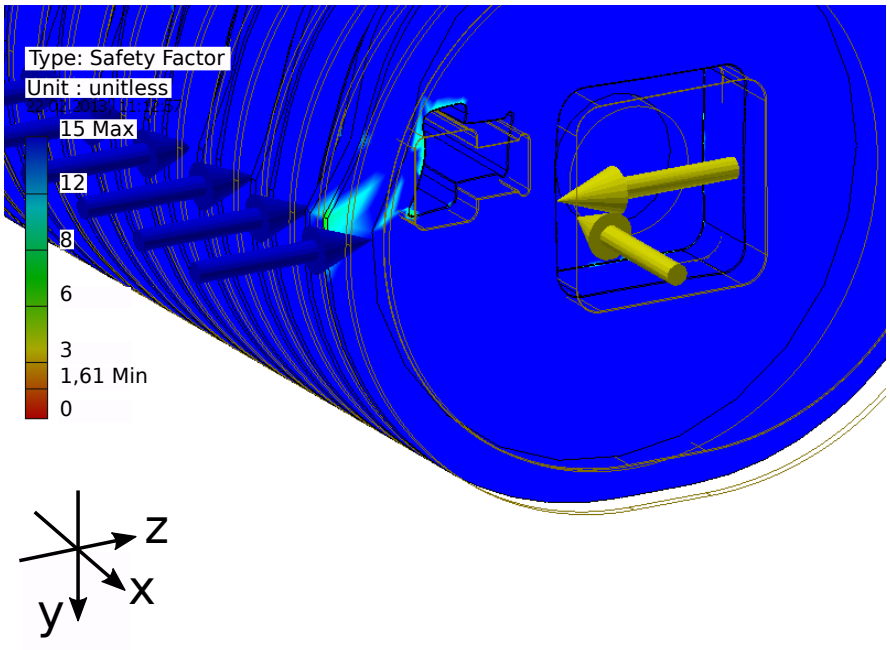

(b) Distribution of factor of safety (FOS) on the coil former. Minimum FOS 1.61.

Figure 4.22: Stress analysis result of the coil former with central groove for the solenoid-coil. Boundary conditions on the coil former: a contact force (arrow in yellow), which compress the coils modules in x direction. Total external magnetic forces (arrow in yellow), part of the forces on the adjacent coil modules in z direction. Sum of the forces on the solenoid coils in z direction (arrows in blue).

4.4.2 Optimization of the simulated electron trajectories through the TGU40

All optimizations performed in the previous sections were performed for a 100 periods undulator. Because the magnetic field components are not the same in the real 40 periods undulator, the optimization must be recalculated.

Table 4.8 collects in detail all the values calculated analytically for the TGU40, including the start x-position ($x(E)$[mm]) and the maximum beamlet width (σ_x[mm]) for each energy.

Table 4.9 summarizes the results, including the x-position and the emitted wavelength by the central energy, the total dispersive beam splitting Δx_δ and the minimum beamlet width σ_x.

By optimizing the current in the correction coils, an offset in the start y-position and an angle Θ_{yz} of the reference trajectories, it is possible to keep the overall drift within a tolerable range. For achieving the targeted radiation bandwidth in the order of the natural bandwidth ($\Delta\lambda/\lambda_0 \leq 1/40 = 2.5\,\%$), the trajectory drifts have to be smaller than the minimum beamlet width. The results of the optimization using the simplex method are summarized in Table 4.10. Figure 4.23 shows the relative trajectories on the xz-plane after the optimization and with the electron energies of 108 MeV, 120 MeV and 132 MeV. The optimization corrected the drift of the trajectories but not the angle at the undulator end, which should be zero.

E[MeV]	$\gamma(x)$	$x(E)$[mm]	$B_y(x)$[T]	$K(x)$	$\lambda(x)$[nm]	σ_x[mm]
132.0	258.32	4.618	1.37	1.34	149.63	0.258
129.6	253.62	4.961	1.32	1.30	150.09	0.250
127.2	248.92	5.317	1.27	1.24	150.33	0.246
124.8	244.23	5.687	1.21	1.19	150.38	0.242
122.4	239.53	6.071	1.16	1.13	150.29	0.242
120.0	234.83	6.471	1.10	1.07	150.10	0.244
117.6	230.14	6.887	1.03	1.01	149.87	0.250
115.2	225.44	7.321	0.97	0.95	149.69	0.258
112.8	220.74	7.773	0.90	0.88	149.63	0.272
110.4	216.05	8.245	0.83	0.81	149.80	0.290
108.0	211.35	8.738	0.76	0.75	150.30	0.316

Table 4.8: Summary of results for the TGU40.

opt. $B_y^{\max}$[T]	opt. l_2[mm]	x_0[mm]	λ_0[nm]	$\Delta\lambda/\lambda_0$[%]	Δx_δ[mm]	Min. σ_x[mm]
1.740	303	6.471	150	0.501	4.120	0.242

Table 4.9: Calculation of the relative deviation of wavelengths emitted ($\Delta\lambda/\lambda_0$), the total dispersive beam splitting (Δx_δ) and the beamlet width (σ_x) of the TGU40.

J_{corr} :	$32.084\,A/mm^2$
Θ_{yz}:	$0.0579°$
y^{offset}:	$-0.109\,mm$

Table 4.10: Optimized parameters employed to perform the optimization of the electron trajectories through the TGU40.

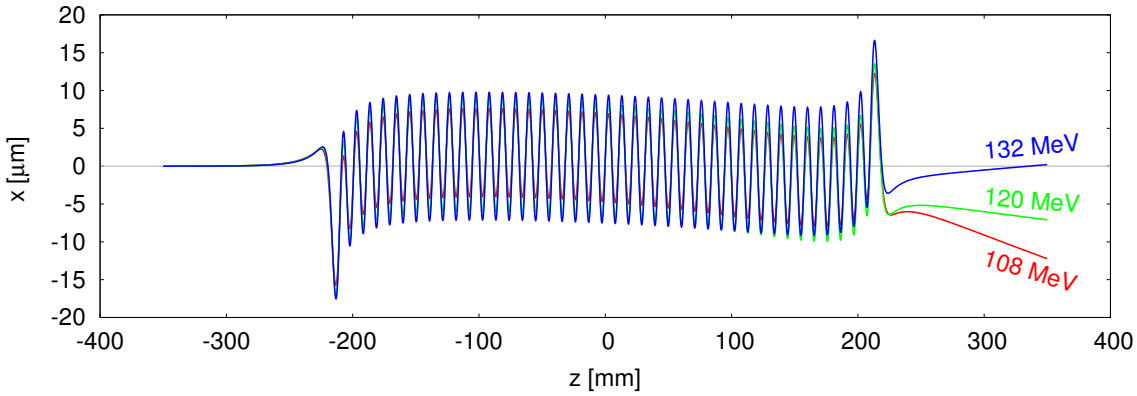

Figure 4.23: Simulated relative electron trajectories on the xz-plane through the TGU40 after optimization of the start parameters.

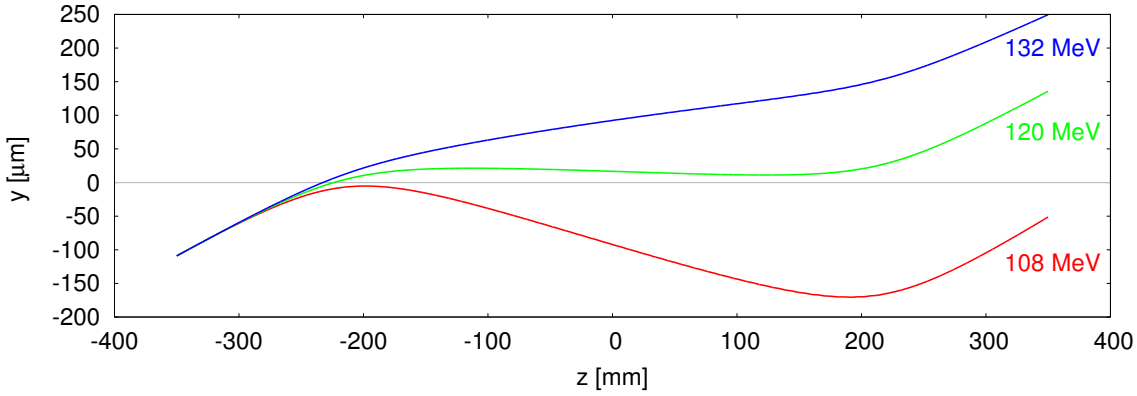

Figure 4.24: Simulated electron trajectories on the yz-plane through the TGU40 after optimization of the start parameters.

The trajectories on the yz-plane are shown in Figure 4.24. With the optimized current density in the correction coils and the optimized start parameters of the trajectories ($y^{offset} \approx -110\,\mu m$ and $\Theta_{yz} \approx 1\,mrad$), it is possible to keep the drift within $\pm\ 250\,\mu m$.

Figure 4.25 shows $B_y(y)$ at $z = 200\,mm$, where the maximum drift of the trajectories on the yz-plane through the TGU40 occurs (see Figure 4.24). It is observed that the field amplitude B_y is practically constant over the y-range between $y = -200\,\mu m$ and $y = 250\,\mu m$.

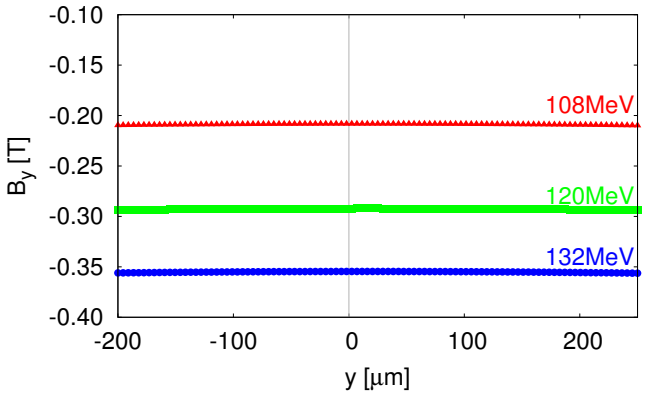

Figure 4.25: Flux density component B_y as function of y-position calculated at $z = 200\,\text{mm}$ produced for the TGU40.

4.5 The TGU40 cryostat

A cryostat capable of accommodating a (full-length) TGU of 100 periods was designed and built by the company CryoVac (Troisdorf, Germany). Inside the cryostat the undulator is placed in vacuum and conduction-cooled. Figure 4.26 shows a front view of the horizontal cryostat assembly. A plate heat exchanger will be bolted to the bottom of the support structure. The cryostat has a shell-like structure, to facilitate the installation of the undulator inside the cryostat.

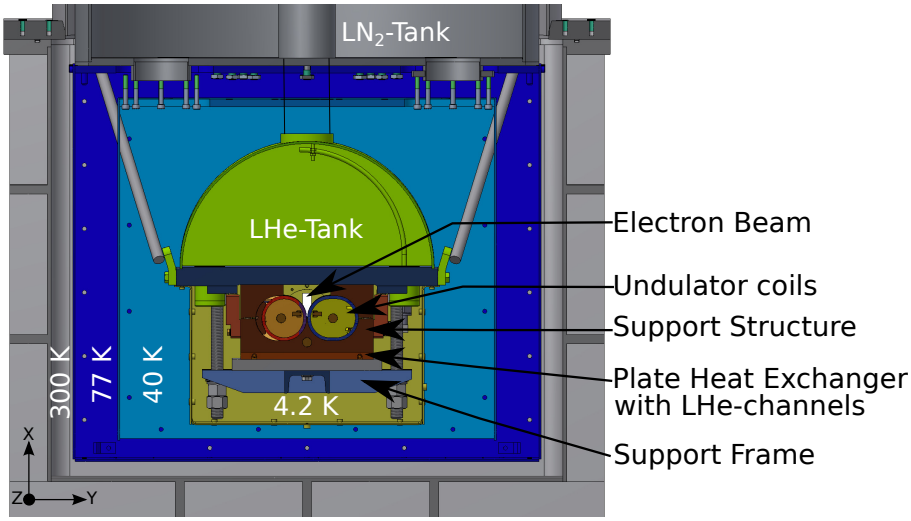

Figure 4.26: Front view of the horizontal cryostat assembly with the TGU installed on the support frame [61]. Different temperature regions are marked.

The structure consists of an external recipient at 300 K and three plates at 77 K, 40 K and 4.2 K with respective shields. Cooling to 77 K is done with liquid nitrogen reservoir place on the second plate. The 40 K plate is cooled with the He gas from the LHe reservoir. The cooling channels of the heat exchanger are connected to a 50 liter liquid helium reservoir placed above the coils, constituting a thermosiphon cooling scheme. The bottom of this reservoir is the 4.2 K plate and is cooled directly with liquid helium. Figure 4.27 shows a 3D-view of the cryostat.

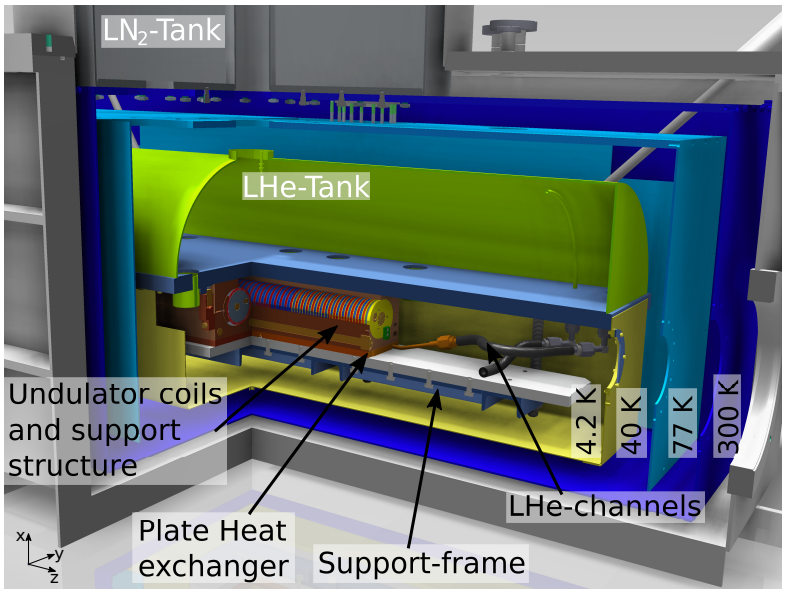

Figure 4.27: 3D-view of the horizontal cryostat assembly with a 1/4 cut off for visibility [61].

DT-670 silicon diodes temperature sensors are mounted at several positions on the undulator in the 4.2 K shield to measure at the low temperature more precisely than the PT100 temperature sensors, which are placed in the external shields. The operation temperature of the undulator in this cryostat is expected not to exceed 5 K.

5. TGU construction and winding

In the following, the construction of several short models and the full-scale TGU are described. The winding of the superconducting undulator and correction coils are discussed in detail. Moreover, the support structure of the undulator coils and the support assembly to mount the TGU inside the own horizontal cryostat are presented.

5.1 Short Prototypes

5.1.1 Half period TGU

A first short prototype with a single groove was built (see Figure 5.1). The purpose of this half period TGU was to verify the groove dimensions and the winding process with the superconducting (sc) wire described in Section 4.1.1. This first model has a cylindrical form with an external pole radius of 30 mm and the material selected for the coil former is copper.

The height and width of the single groove are given by the dimensions of a winding package of 6 layers $\times$ 4 turns. In the geometry of a single groove, it is important for the bending of the superconducting wire after each turn to begin the next turn in the correct position next to the preceding turn. The wire properties showed that once the wire is bent, it is difficult to recover its original shape and its insulation can be damaged. If the coil is wound correctly, the last layer is flush with the winding area of the coil former.

The test proved the feasibility of the winding geometry and allowed some improvements in the design of the following prototype, which were:

- The modification of the superconducting wire clamp was made. In this first prototype, the end of the superconducting wire was soldered to the side of the coil former (see Figure 5.1 (a)). An improvement was designed increasing the width of the end of the coil former to install an insulated plate and a pair of small screws and washers (of non-magnetic material). This enables both terminals of the coil end to be clamped together.

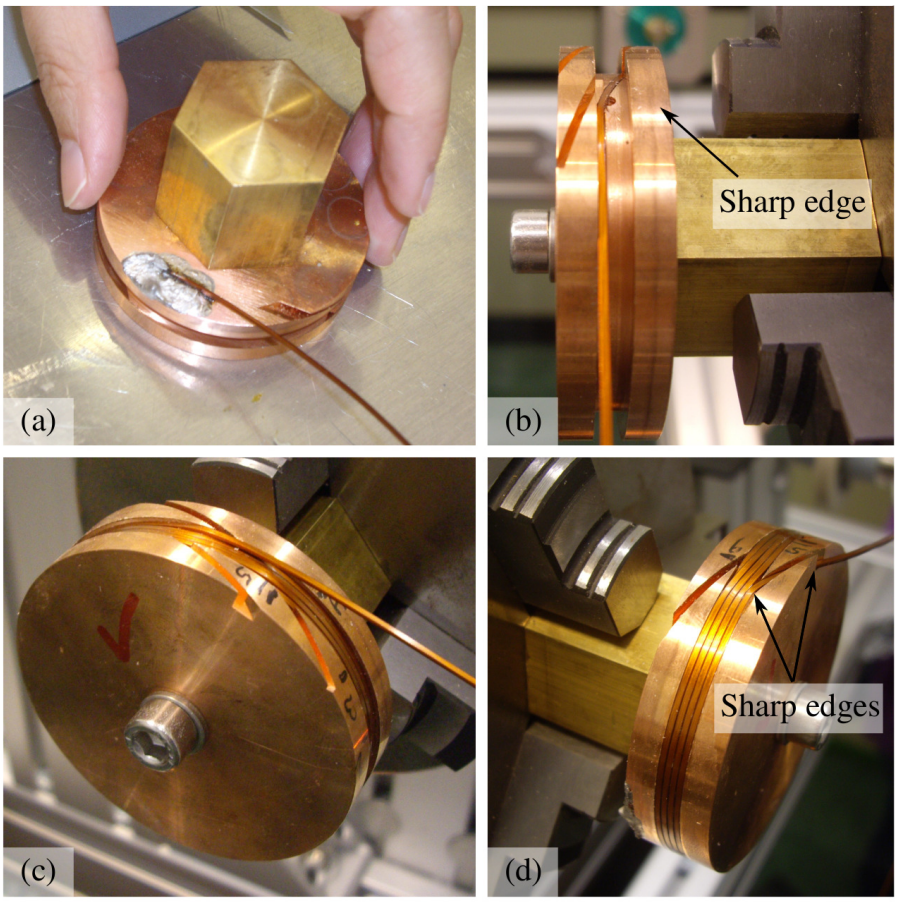

Figure 5.1: Coil winding of the first short prototype: (a) solder sc wire, (b) start of the winding, (c) end of the fifth layer and (d) sharp edges at the winding end.

- All sharp edges, where the superconducting wire passed through, were rounded (see Figure 5.1 (b) and (d)). This prevents damaging the insulation of the wire, which will cause short-circuit or quenches.
- The width of the groove was enlarged taking into account the tolerance of the superconducting cable of 6 μm. In this prototype the help of a hammer was necessary to align the four turns of wire into the groove. This can cause damage to the superconducting wire and should be avoided. If the turns are not aligned, a vertical displacement of the layers occurs and thereby the center-of-mass position of the coil moves relative to the center of the groove.

For the next prototypes with more than one groove, a couple of extra tools were designed to change the direction of the wire. A minimum internal bending radius of the superconducting wire of ≈ 7 mm was obeyed, which is approximately ten times the wire width.

5.1.2 Two periods TGU

A second prototype with four grooves was designed and built (see Figure 5.2). This prototype is not only an ideal cylindrical undulator coil former with grooves for solenoid coil packages. In addition every second groove has a groove for containing a racetrack coil package (see Figure 5.2 (a)). All the coils are aligned on one side of

the coil former. This prototype with two undulator periods is called TGU2. Before starting the winding of the solenoid coil on the first groove, the superconducting wire is fixed between the insulate plate and the screws (see Figure 5.2 (a)).

Two aluminum rings, which fill the grooves of the racetrack coils, are used to maintain the shape of the empty grooves (see Figure 5.2 (b)). After the second solenoid coil is wound on the third groove, the superconducting wire is turned by means of two small pieces mounted on the side of the coil former (see Figure 5.2 (c)). Thus, the racetrack coils are wound in the other direction as shown in Figure 5.2 (d). Once the last racetrack coil is wound, the two ends of the coil have to be fixed to maintain its tension before cutting the superconducting wire (see Figure 5.2 (e)). In Figure 5.2 (e) is shown that the superconducting wire is not mechanically supported at the wire-jumps over the solenoid coils. Special half-bridge pieces were built to hold the superconducting wires in these positions and avoid their movement, which can cause quenchs during the operation of the undulator.

A second coil was wound, but this time the installation of the half-bridges as shown in Figure 5.3 was included. The half-bridges feature a narrow groove where the superconducting wire passes from one racetrack coil to the next one. The half-bridges are made of copper and as many of them as solenoid coils are employed. Their width must be slightly smaller than the groove width.

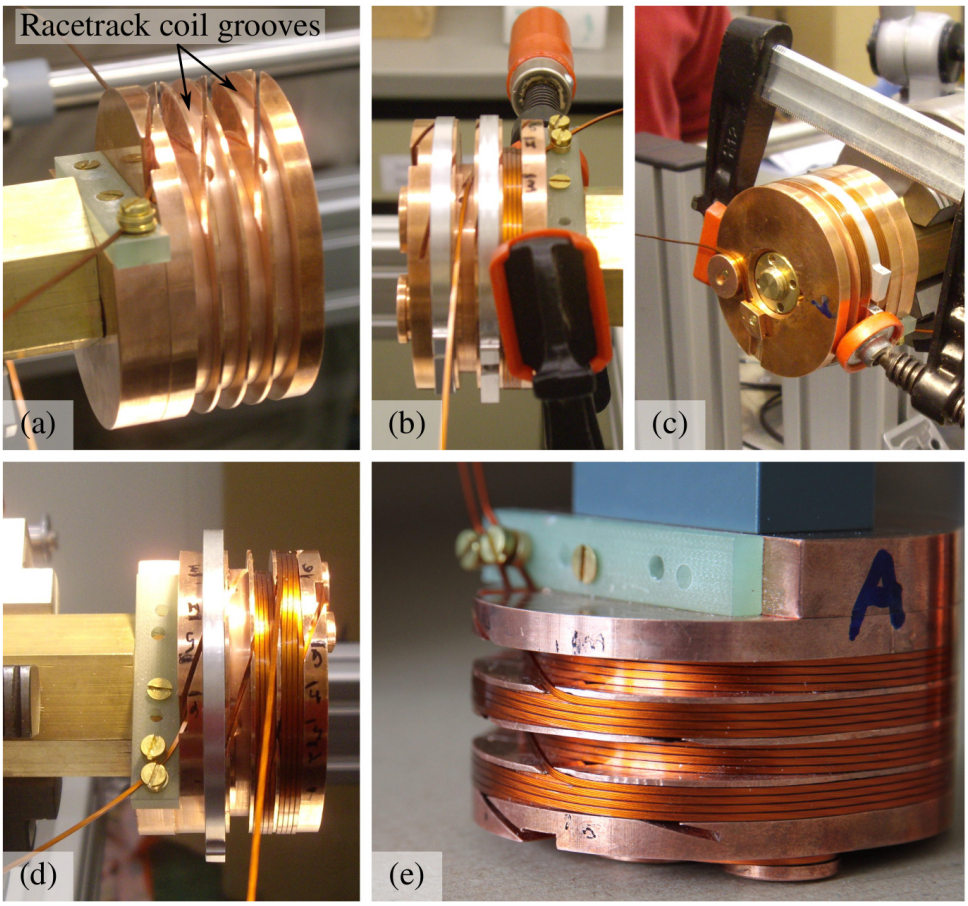

Figure 5.2: Short prototype coil former with two undulator periods: (a) clamping sc wire, (b) aluminium rings, (c) turn of the sc wire, (d) racetrack coil winding and (e) TGU2 without half-bridges.

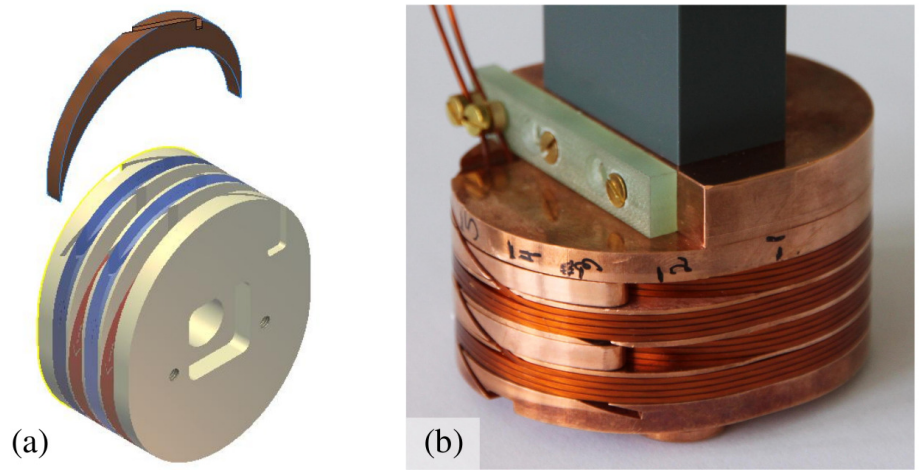

Figure 5.3: Modification of the short prototype coil former adding half-bridges on the solenoid coils: (a) 3D-view of the half-bridge and (b) TGU2 with half-bridges.

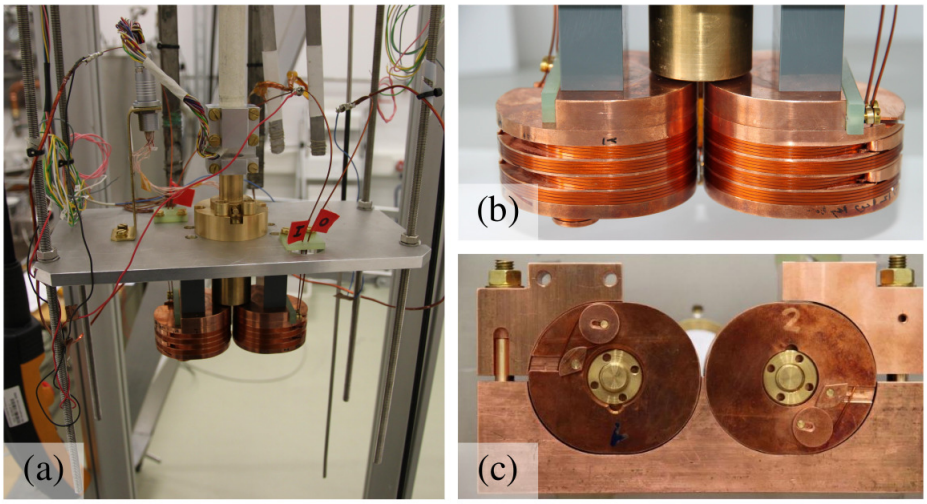

Figure 5.4: TGU2 setup assembly to perform the magnetic measurements inside the cryostat: (a) structure to hold the TGU2, (b) TGU2 coils and (c) coil support structure.

Both prototypes, without and with half-bridges, were employed to perform magnetic measurements (see Section 6.2.1). Also quench test were performed and as expected the best results were obtained with the second prototype, the undulator coil with half-bridges.

Figure 5.4 (a) shows the structure designed to hold both coils together during the measurements inside a cryostat at 4.2 K. Also a coil support structure was designed and tested (see Figure 5.4 (c)). This coil support is the same as for the full-scale TGU but scaled down to the two periods. More details about the final structure and the measurements of the TGU2 are found in [66].

5.2 Full scale TGU40

5.2.1 Coil former modules

The full-scale 40 periods undulator is called TGU40. Each coil former is composed of three modules (see Figure 5.5), which are assembled before winding the superconducting coils. The total number of grooves of each coil former for the TGU40 is 85. The central modules have 30 grooves each, equivalent to 15 undulator periods. Both lateral modules of each coil former have a total of 55 grooves. This assembly is in principle extendable to 100 periods by four times repeating the inner coils modules.

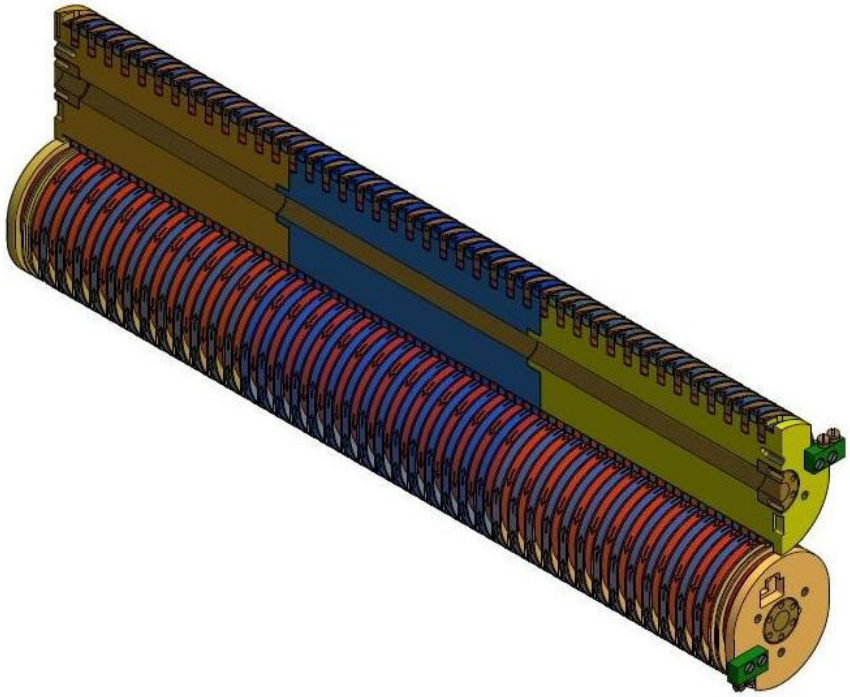

Figure 5.5: 3D-view of the TGU40 coil formers composed for three modules each. The coil on the top with 1/2 is cut off for better visibility [61].

The six coil former modules and a total of 210 half-bridges were manufactured by KIT-TEC (Technik-Haus). Improvements over the model TGU2 were taken into account in the manufacture of the model TGU40. Figure 5.6 shows photographs taking during the production of the coil formers. The material selected is CU-OF. The weight of each coil former after the assembly of the three modules and before winding is about 10 kg. The manufacturing drawings of each coil former module and the whole TGU40 assembly are presented in Appendix D [61].

The modules that compose each coil former must be precisely aligned. Measurements of the relative deviation of the height of each groove base were made at KIT [67]. The deviations were smaller than 25 μm over the length of the two coil formers. The zero point was determined for each coil former separately. Figure 5.7 shows a photograph during the measurement performed with a digital 3D-Sensor. The results measured in the center of each coil former module are summarized in Appendix D.

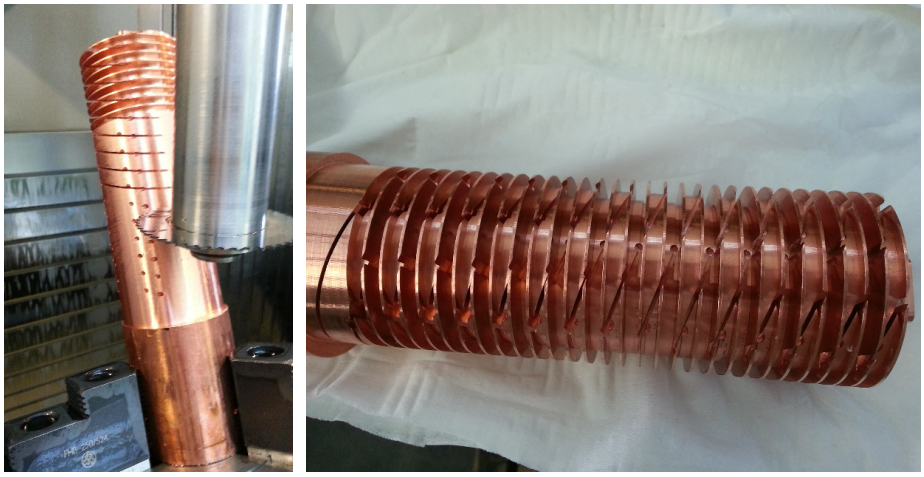

Figure 5.6: Production steps of the coil former modules for the TGU40 by KIT-TEC.

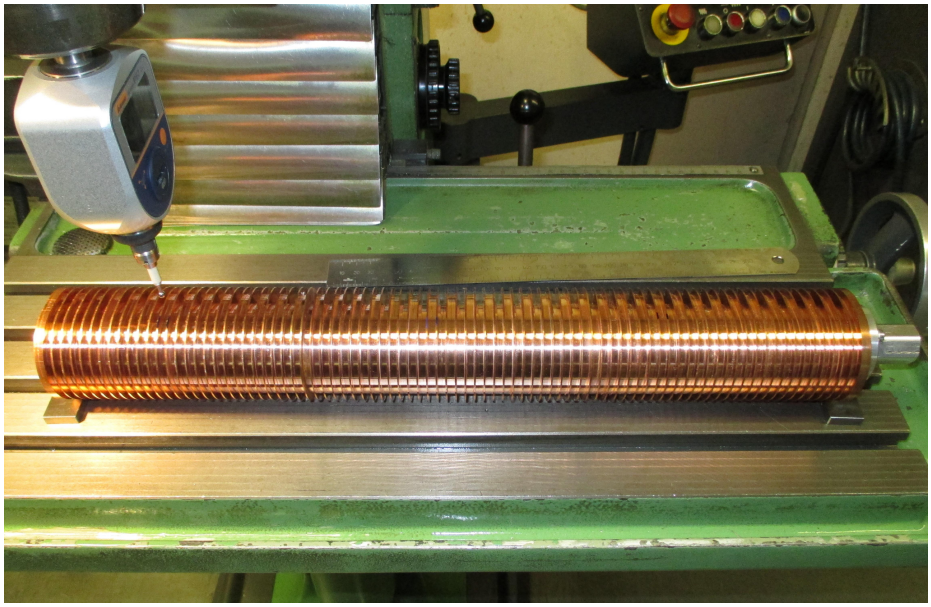

Figure 5.7: Measurement of the relative deviation of the height of each groove base to determine the total deviation of the coil former modules.

The tension on the superconducting wire must be controlled during the winding process. The maximum recommended tensile stress that the superconducting wire can stand before breaking is $100\,\mathrm{N/mm^2}$. The superconducting wire selected for the winding of the TGU40 has a bare surface of $0.6\,\mathrm{mm^2}$ (see Section 4.1.1). Therefore the maximal tension on the wire must not exceed 60 N, which is equivalent to $\approx 6\,\mathrm{kg}$. If higher tension levels are employed during the winding process, there is a potential to induce mechanical defects in the superconducting wire, which will results in a degraded critical current density J_c.

A simulation of the tension on the wire on the center of the coil former was performed [62] using Autodesk Inventor [63]. The result shows that the main body is elastically deformed by $\approx 0.0013\,\mathrm{mm}$ for a tension on the wire of 60 N. The tension on the superconducting wire was measured with an analog balance before starting the winding process and its value was $3.4\,\mathrm{kg}$.

5.2.2 Winding of the undulator coils

The TGU coils were wound on a semi-automatic winding machine in the Laboratory for Applications of Synchrotron Radiation (LAS) at KIT. Before starting the winding of the undulator coils, both coil formers were cleaned thoroughly and manually with isopropanol (see Figure 5.8 (a)). Four small brass tools were designed to guide the superconducting wire into the groove and to align the single turns one next to the other, as shown in Figure 5.8 (b). A winding package consists in 24 turns (4 single turns × 6 layers).

Figure 5.8 (c) shows an aluminium support to hold the long coil former. This piece can be moved horizontally and is composed of a ring surrounding the coil former, a profile and four rolling bearings. The two aluminum rings employed in the TGU2 winding are also shown in Figure 5.8 (c). They are placed beside the groove where a solenoid coil is being wound. These rings are used to maintain the shape of the empty grooves, which are later filled with racetrack coils. A miniature vice was employed in order to bend the superconducting wire at the end of each turn with the same bending radius, as shown in Figure 5.8 (d). The position of each layer jump was marked on the surface of the coil former.

Both undulator coil formers can be distinguished by the shape of the central groove, which is designed for winding either a solenoid or a racetrack coil package. Figure 5.9 shows photographs of the first undulator coil wound, which central groove was for a solenoid coil.

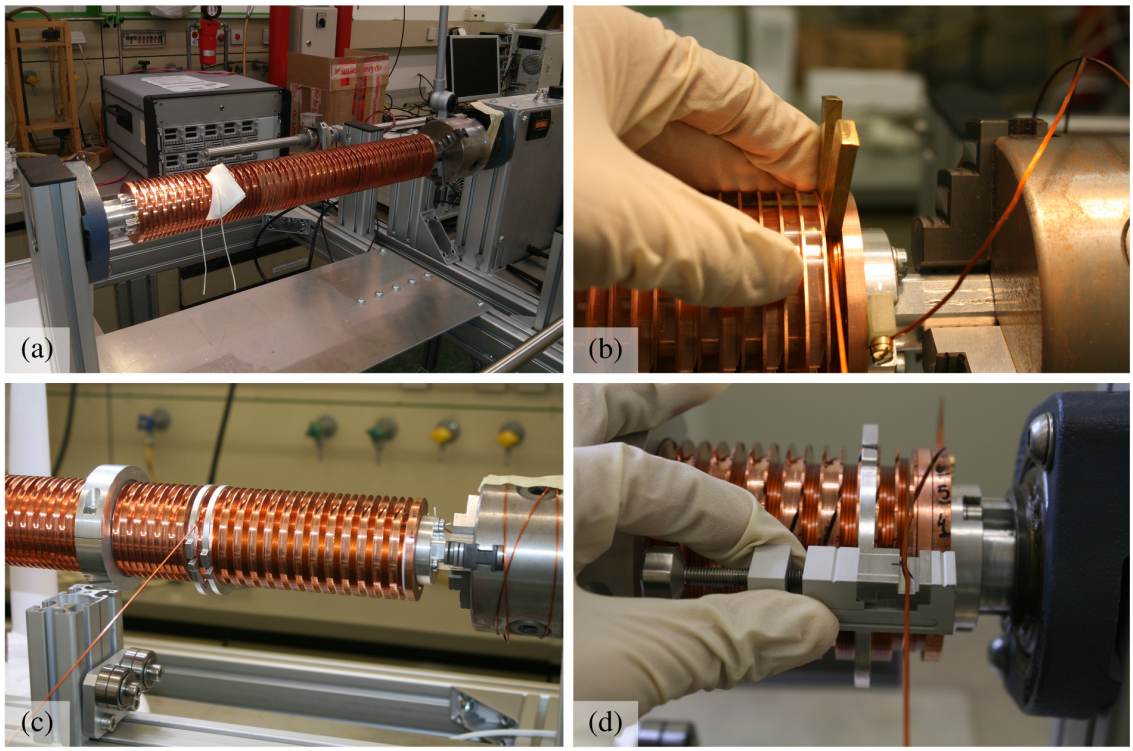

Figure 5.8: Accessories to facilitate the winding process of the undulator coils: (a) cleaning of the coil former, (b) brass tools, (c) aluminium support and rings and (d) miniature vice.

The winding in this coil former was started with the matching coil 1/4 in the first groove. The next solenoid coils were wound in the same direction (see Figure 5.9 (a)), leaving free the grooves for the racetrack coils to wind the wire in the other direction. After winding all the solenoid coils, a loop of superconducting wire with a length of 185 mm was left over and clamped by two small brass screws on the surface of the coil former, as shown in Figure 5.9 (b). This loop of wire enables the rotation of the wire once the two coils are mounted on the support structure (see Section 5.2.4).

The winding process was continued with the racetrack coils in the opposite direction. The first coil wound on this side was the matching coil 3/4. Before winding each racetrack coil package, a half-bridge piece was placed over each previous solenoid coil, to hold the superconducting wire (see Figure 5.9 (c)). Figure 5.9 (c) shows also how the superconducting wire was clamped with a vice between two pieces of red plastic at the end of the work day. This prevents the loss of the tension on the wire, if the winding machine is accidentally turned off.

It took about one hour per groove to wind each winding package with 24 turns and about four weeks to complete the first undulator coil. This time winding is acceptable based on experience in the LAS at KIT. Figure 5.9 (d) shows the first undulator coil at the end of the winding process, when the last racetrack coils were being wound. One meter of superconducting wire was left in each undulator coil terminal.

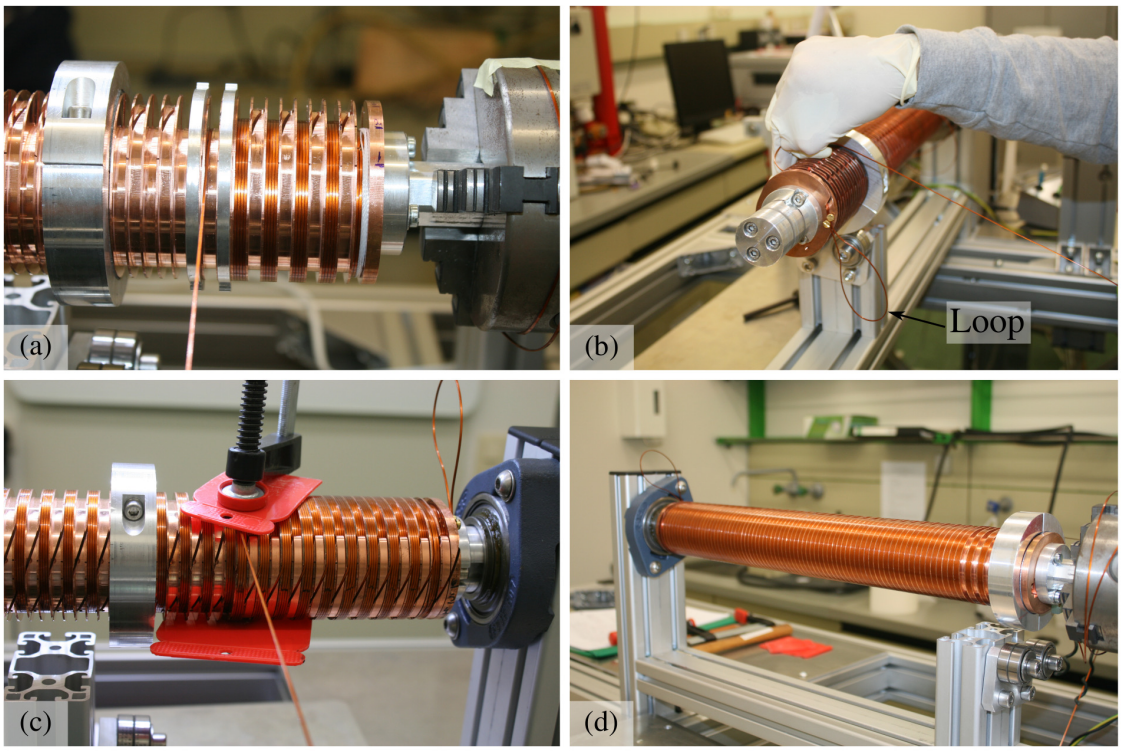

Figure 5.9: Winding of the first undulator coil with the central groove designed for winding a solenoid coil package: (a) start of the winding in the first groove, (b) loop of the sc wire, (c) half-bridges and racetrack coils and (d) end of the first undulator coil.

Photographs of the second undulator coil, which central groove was a racetrack coil package, are shown in Figure 5.10. The winding in this coil former was started with the matching coil 3/4 in the second groove (see Figure 5.10 (a)). After that, the other solenoid coils were wound in same direction, like with the first undulator coil. In this case, a loop of superconducting wire of 340 mm was left over and clamped on the surface at the end of the coil former (see Figure 5.10 (b)).

As with the first undulator coil, the winding process was continued with the racetrack coils on the other side. The superconducting wire of the last two turns in the matching coil 1/4 moved out (see Figure 5.10 (c)). For fixing its position, a ring tailored for each matching coil 1/4 was designed for filling the groove and preventing the movement of the superconducting wire. Figure 5.10 (d) shows the ring that holds the superconducting wire at the end of the winding. These rings were installed before cutting the superconducting wire. In addition the bottom of each matching coil 3/4 was filled using a half ring with a width of two times the width of the superconducting cable. The top of these matching coils was already covered with half-bridges. For the first undulator coil, only the half rings over the bottom of the matching coils were employed.

Although the sharp edges of the coil former were filed off, the insulation of the superconducting wire was slightly damaged and produced short circuits to ground and between turns of the coils. The first short circuits to ground were detected when the solenoid coil number 21 of the first undulator coil and the solenoid coil number 10

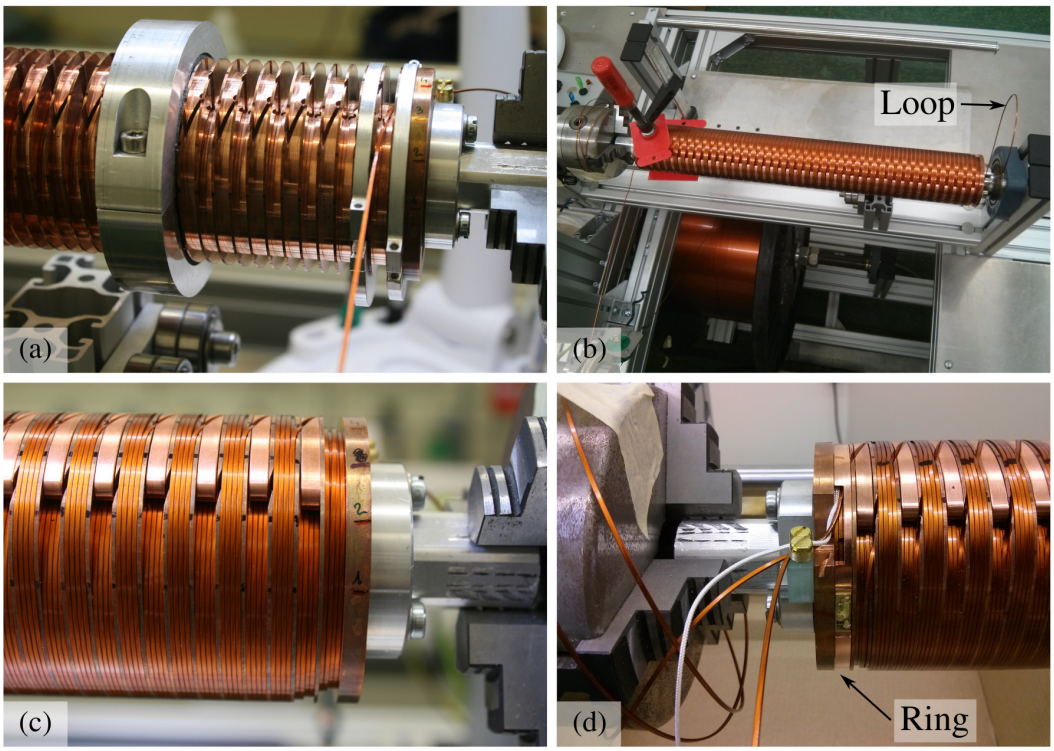

Figure 5.10: Winding of the second undulator coil with the central groove designed for winding a racetrack coil package: (a) start of the winding in the second groove, (b) loop of the sc wire, (c) matching coil detail and (d) end of the second undulator coil.

of the second undulator coil were being wound. The short circuits produce transient effects on the Hall voltages (see Section 6.2.4).

Electromagnetic forces try to force the superconducting wires within the undulator to move. This movement must be completely restrained because even the smallest wire movement will generate heat due to friction and can quench the undulator. Most superconducting magnets are potted using epoxy, ceramic, or some other material to restrain wire movements. The potting method is tedious and expensive and for this reason, the superconducting coils of the TGU40 described in this thesis were not potted. The superconducting wire movements were completely restrained with the coil winding configuration detailed in this Section and with the installation of pieces as the half-bridges over the solenoids coils and the rings on the matching coils.

5.2.3 Winding of the correction coils

Figure 5.11 shows the beginning steps of the correction coil winding. One screw is employed to guide the superconducting wire together with a small screw clamp to hold the wire during the winding. The lateral edge of the coil former structure is manually rounded and covered with Kapton adhesive tape to prevent damaging the superconducting wire.

The superconducting wire selected for the winding of the correction coils has a bare diameter of 0.2 mm (see Section 4.2.1). For a surface 0.0314 mm^2, the maximal tension on the wire must not be exceed 3.14 N, which is equivalent to $\approx$ 0.314 kg. Before starting the winding process of the correction coils, the tension on the wire was measured and its value was 0.2 kg.

Figure 5.12 left shows a circular support of aluminium with three screws, which is designed to hold the center of the correction coil former to the winding machine. The coil former of the correction coils is about 44 cm long. In Appendix D is given the manufacturing drawing of the correction coil former. Figure 5.12 right shows a picture made during the winding of the first correction coil, where the winding package is composed of a total of 14 turns over 4 layers.

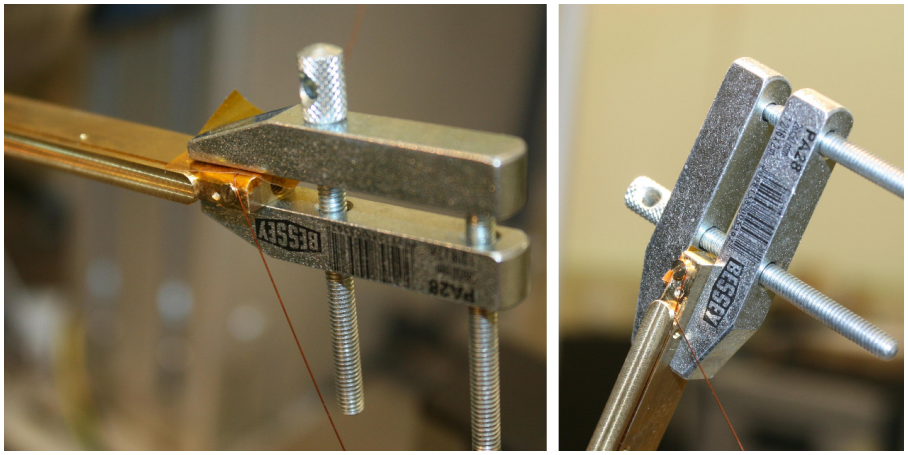

Figure 5.11: Clamping of the superconducting cable through a small screw clamp, before starting the winding process of the correction coil.

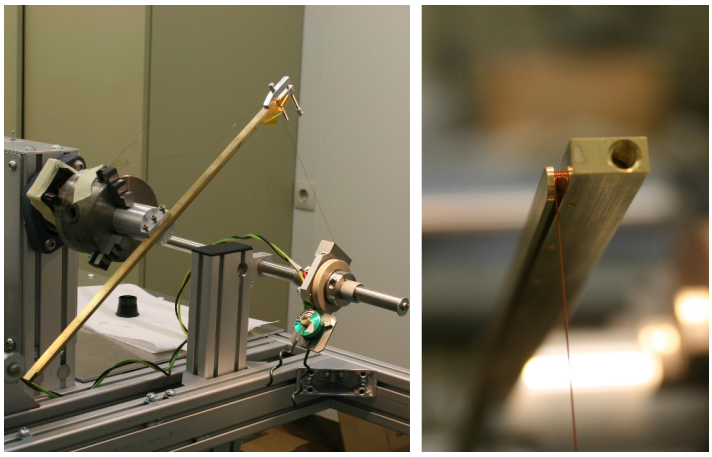

Figure 5.12: Winding of one correction coil: circular support holds the center of the correction coil former to the winding machine (left) and detail of the winding (right).

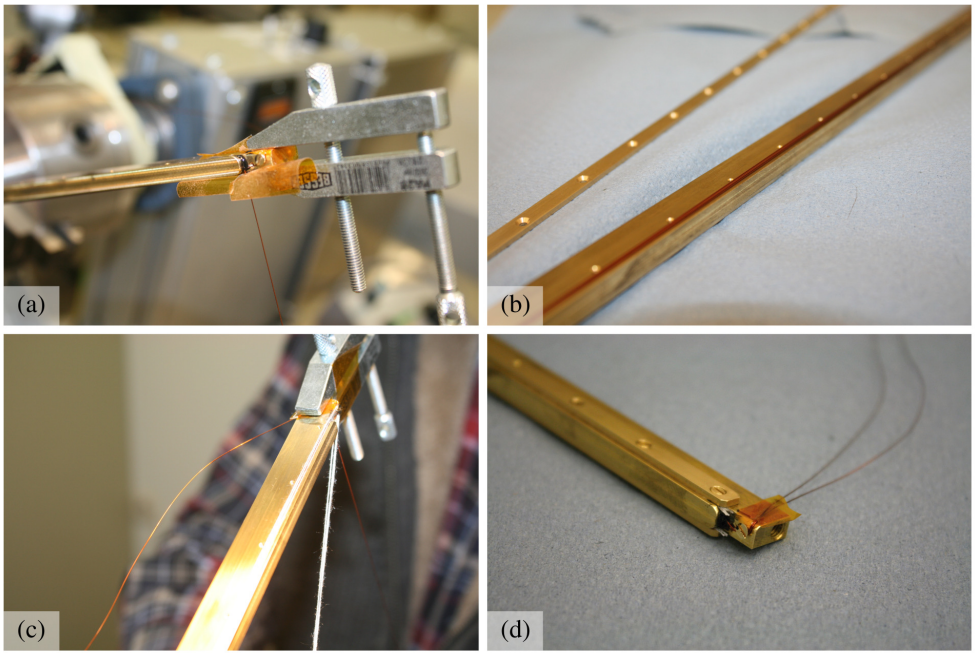

Figure 5.13: Detail of the end of the superconducting correction coil winding: (a) dab of glue to fix the sc wire, (b) sc wire outside of the coil former, (c) braided fiberglass sleeve and (d) correction coil finished.

Figure 5.13 (a) shows how the winding was fixed. A dab of a thermal conducting glue on the end of the winding was employed: Stycast 2850FT epoxy with hardener 24LV [68], whose color is black. After three days the glue had completely dried and then the superconducting wire was cut, leaving one meter wire in each correction coil terminal. In Figure 5.13 (b) can be observed how the superconducting wire comes outside of the coil former in the center of the correction coil. This problem was solved by filling the gap between the superconducting wires and the covers with a braided fiberglass sleeve (see Figure 5.13 (c)). A cover plate on each side of the coil former was screwed to restrain the wire movements (see Figure 5.13 (d)). The correction coils were also not potted.

5.2.4 Support structure

Figure 5.14 (left) shows the bolted clamping structure, which supports the coil assembly. The support structure not only defines the magnetic gap of the undulator of 1.1 mm, but also applies compressive prestressing to the outer parts of the racetrack coils and takes up the magnetic forces acting on the undulator coils as a whole (see more details in Section 4.3.1).

The support structure is made of copper as the coil formers in order to ensure good heat conduction and to minimize thermally induced mechanical stress. The support structure is cooled to 4.2 K inside the cryostat (see Section 4.5). To achieve this temperature in the superconducting undulator coils, the gaps between the support structure and the coils are filled with 50 μm thick indium foils. This material is a good interface and is used to reduce thermal contact resistance. The manufacturing drawings of the support structure are shown in Appendix D [61].

Each correction coil was inserted in an undulator coil as shown in Figure 5.14 (right), once the respective undulator coil was wound. The position in its interior is fixed by two screws at the end of the coil former.

As explained in Section 5.2.2, during the winding of the undulator coils a loop of superconducting wire was left over after winding all the solenoid coils in one direction and preliminary fixed to the side of its coil former. Then the alternate racetrack coils were wound in the opposite direction. Once both coils are wound, the loops are fixed to the support structure. These loops were used to reverse the winding direction between the winding packages. The magnetic flux produced by these loops is compensated by attaching both loops to the support structure as shown in Figure 5.15.

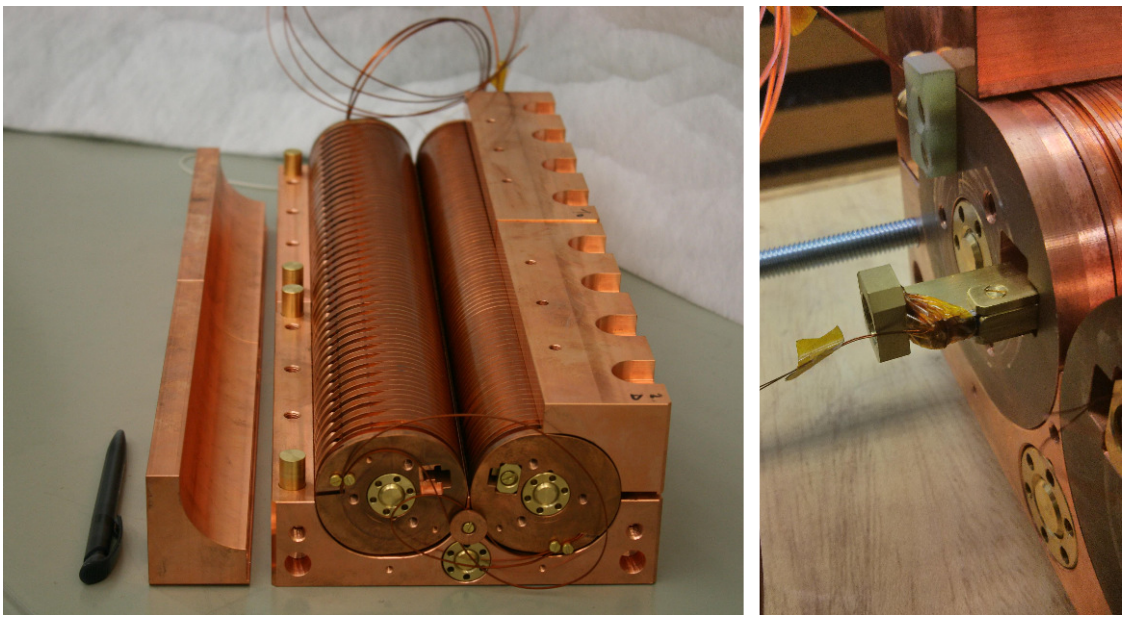

Figure 5.14: Support structure to hold the undulator coils (left) and insertion of the correction coil inside the undulator coil (right).

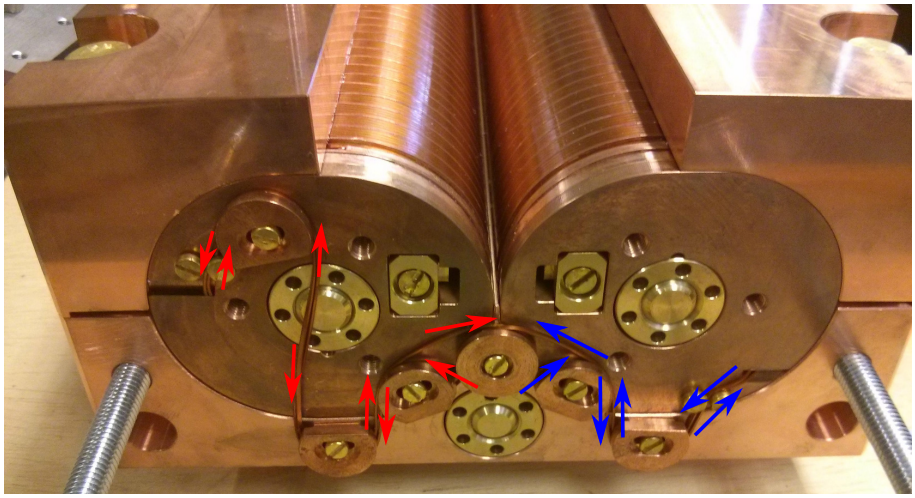

Figure 5.15: Superconducting wire loops of each undulator coil attached to the support structure. The arrows indicate the direction of the current flow in each coil.

5.3 Cryostat support assembly

The superconducting undulator coils will be conduction-cooled in its custom horizontal TGU cryostat in future measurements, as introduced in Section 4.5. Figure 5.16 (a) shows a 3D-view of the two plate heat exchangers bolted to the bottom of the TGU40 support structure. The cooling channels of both heat exchanger plates are connected through flexible stainless steel bellow hoses to the liquid helium reservoir. Furthermore the LHe-reservoir bottom is in direct contact with the top of the TGU40 support structure.

Figure 5.16 (b) shows the support frame, which was designed to mount the undulator assembly inside the 4.2 K shield. This support frame is clamped to the bottom of the LHe-reservoir through eigth threaded shafts and double nuts (see Figure 5.16 (c)). Both the support frame and the plate heat exchangers may be reused in the future with the 100 periods undulator.

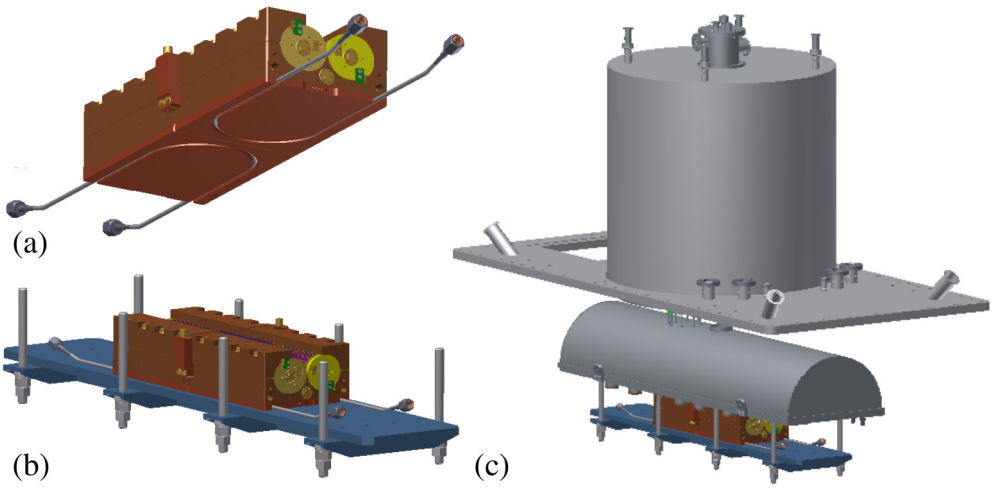

Figure 5.16: 3D-view of the cryostat support assembly for the TGU40 [61]: (a) plate heat exchangers, (b) TGU40 support structure and (c) support structure inside the cryostat.

6. Undulator measurements

An experiment has been performed at KIT to measure for the first time the transverse field gradient of the full-scale TGU. In the following the experimental setup is described and the measurement results are presented and discussed.

6.1 Hall probe

Hall probes are magnetic field sensors based on the Hall effect: when a current is run through a conductor in a magnetic field, a voltage is induced perpendicular to the current direction. This voltage is proportional to the applied field, so Hall probes are very easy to use as direct and quantitative magnetic field sensors with high precision.

6.1.1 The Hall effect

Figure 6.1 describes the Hall effect. The control current I flows through the plate in the y direction while the sense contact, S1 and S2, are used for the measurement of the Hall voltage V_{H}. The magnetic field $\vec{\mathrm{B}}$ is perpendicular to the plate [69].

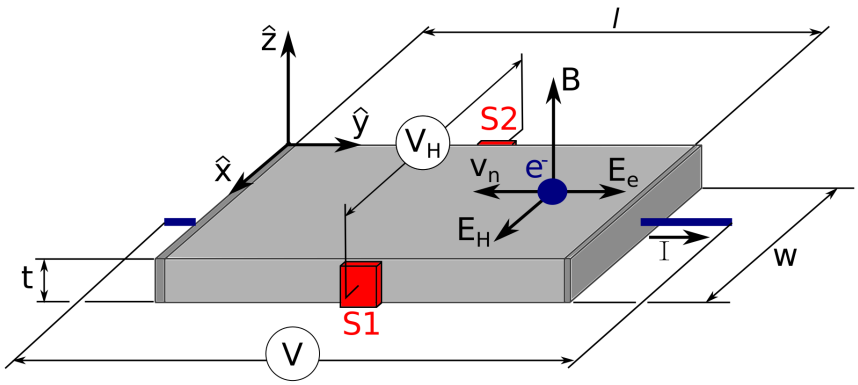

Figure 6.1: Sketch of a Hall generator, which consists of a thin semiconductor plate of length l, width w and thickness t.

The electrons with a velocity $\vec{v}_n$ move under the action of the Lorentz force $\vec{F}_L$ in response to the magnetic field $\vec{B}$ and the external electric field $\vec{E}_e$. The Lorentz force is given by:

$$\vec{F}_L = q\left(\vec{E}_e + \vec{v}_n \times \vec{B}\right) \tag{6.1}$$

where $q = -e$ for electrons.

The electrons are moving by the magnetic force towards one edge of the plate. Consequently, the concentration of the electrons at the other edge is decreasing. An electric field $\vec{E}_H$ called Hall field is created between the two edges and is given by:

$$\vec{E}_H = -\left(\vec{v}_n \times \vec{B}\right) \tag{6.2}$$

The Hall voltage V_H is a measurable transverse voltage, which appears across the two sense electrodes (S1 and S2) and is calculated along the width of the plate by:

$$V_H = \int_{S1}^{S2} \vec{E}_H d\vec{w} = -\frac{J}{ne} Bw \tag{6.3}$$

where n is the density of electrons and the current density is $J = I/wt$. The Hall voltage is expressed as a function of the current and the magnetic field by:

$$V_H = \frac{R_H}{t} IB \tag{6.4}$$

where $R_H = -1/ne$ is called the Hall coefficient [70].

6.1.2 Hall probe array

For the magnetic field measurements of the undulator, a Hall probe array of the manufacturer Arepoc was employed [71]. The array consists of seven independent Hall probes, which lie in a single line of 0.85 mm length equidistantly spaced, as shown in Figure 6.2.

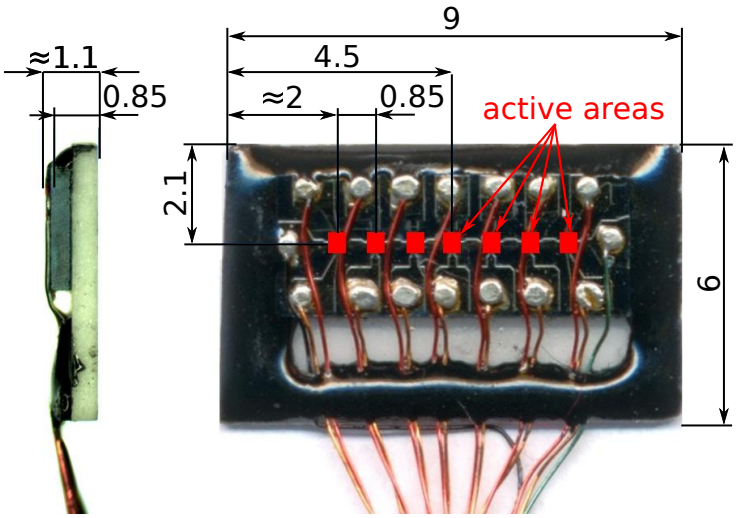

Figure 6.2: Dimensions of the Hall probe array (M7-TH5) with seven Hall probes (all units mm).

The probes are connected in series to a common supply current circuit with a control current of 10 mA. The Hall voltage of each individual probe is picked up by a twisted wire pair. The abbreviation used in this thesis for Hall probe is "HP" followed for the number of the probe from 1 to 7.

One advantage of this array design is that seven measurements at different locations can be done simultaneously for each magnetic field measurement. Another advantage is the small size of the entire Hall probe array of $9 \times 6 \times 1.1$ mm (height, width, thickness). The active area dimension is $100 \times 100\,\mu$m.

As shown in Figure 6.3, the Hall probe array was glued on a MACOR piece (white machinable glass ceramic [72]), which allows to reuse it easily in different magnetic measurement setups. The thermal expansion of MACOR matches that of the Hall probe array aluminium oxide substrate so that no thermally induced stress occurs [71]. In addition, MACOR is non-conducting, i.e. no eddy currents are induced when the array is moved in an alternating field. A good thermal conducting glue, Stycast 2850FT epoxy with hardener 24LV [68], was used to join the Hall probe array to the MACOR ceramic piece. Stycast 2850FT can be used in low temperature applications and has a low thermal expansion close to that of MACOR. Thermal stresses are caused by the mismatch of coefficients of thermal expansion between materials when cooling down, which can produce irreversible damage to the Hall probe array [66].

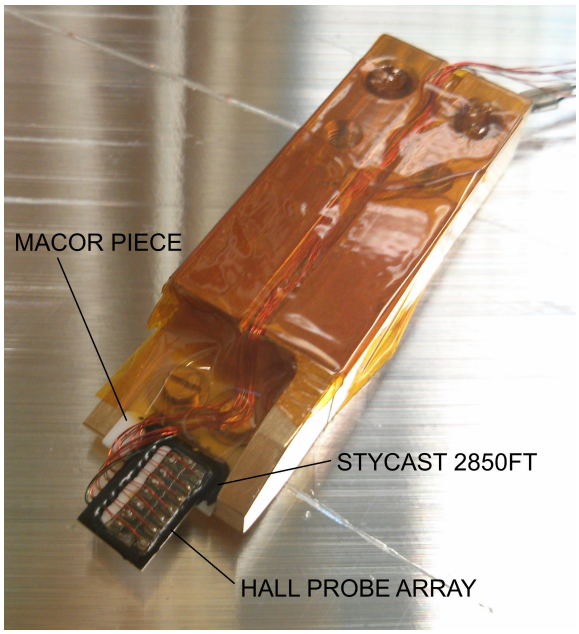

Figure 6.3: The Hall probe array glued to the MACOR ceramic piece and installed on a support. The wires are attached to the support with Kapton tape.

The sensitivity of the Hall probes depends on many factors such as the material of the sensor, sensor dimensions but also on sensor technology. The absolute sensitivity $S = V_{\mathrm{H}}/\mathrm{B}$ is determined for the nominal control current. The sensitivity data at 77 K of each Hall probe are shown in Table 6.1. The sensitivity data, the mean linearity error $< 0.5\,\%$ and the mean sensitivity error $< 0.5\,\%$ are provided by the manufacturer.

HP Number	1	2	3	4	5	6	7
S_{77K} [mV/T]	53.6	54.4	56.7	55.5	58.3	57.2	58.1
$S_{4.2K}$ [mV/T]	51.6	52.3	54.5	53.4	56.1	55.0	55.9

Table 6.1: Sensitivity at $I_n = 10\,mA$ of the Hall probe array (M7-TH5).

The calibration data of six single Hall probes at 4.2 K provided by the manufacturer Arepoc were employed to calculate a calibration factor between the sensitivity at 4.2 K and 77 K for the Hall probe array (M7-HP5). The calculated calibration factor is 0.9618 ± 0.0016. The calibration error is added to the sensitivity and linearity errors to calculate the total systematic error (see Section 6.2.2).

6.1.3 Experimental setup

The test of the TGU40 was performed in a bath cryostat of KIT called CASPER (Characterization Setup for Field Error Reduction) [73] in liquid Helium at 4.2 K. Figure 6.4 shows a cut of the inside of this cryostat, where the TGU40 is installed. Its dimensions are: external diameter of 550 mm, height of 1825 mm and inner diameter of 370 mm. Two pairs of vapor-cooled current leads for maximum 1500 A and 500 A provide the most efficient way to transfer current from 300 K to 4.2 K. The current leads consist of copper rods in the room temperature section and high temperature superconductors in between 60 K and the 4.2 K section.

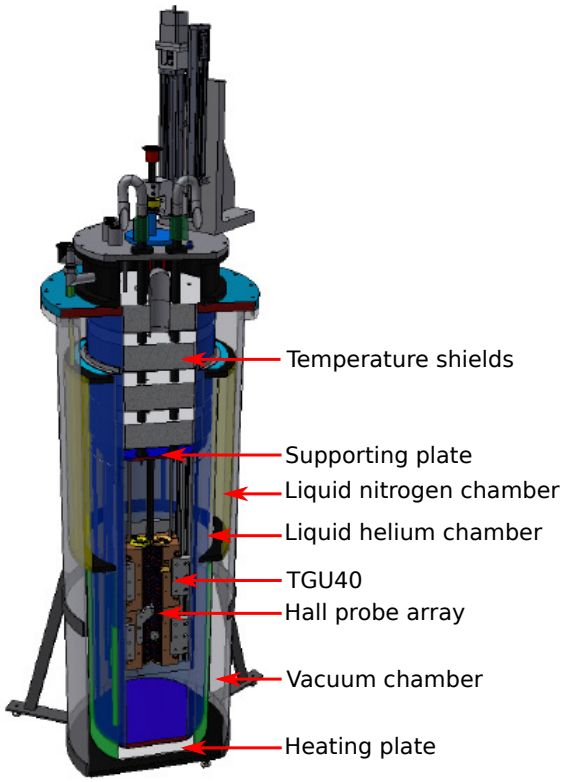

Figure 6.4: Cut through the CASPER-cryostat assembly together with the TGU40 and the Hall probe array [61].

Figure 6.5 (left) shows the entire setup to install the TGU40 within CASPER. A plate on the back and another on the bottom together with four profiles and four small plates are used for attaching the coil support to the supporting plate in the cryostat. All these pieces are made of aluminium because this material is non-magnetic, low cost and easy to machine. Figure 6.5 (right) shows a zoom to see better the Hall probe array support. This is is located between the undulator coils in the center of the TGU40 and made of brass because this material is also non-magnetic and has similar thermal properties to copper at low temperatures. The top of the CASPER-cryostat with the TGU40 is introduced into the cryostat (see Figure 6.6).

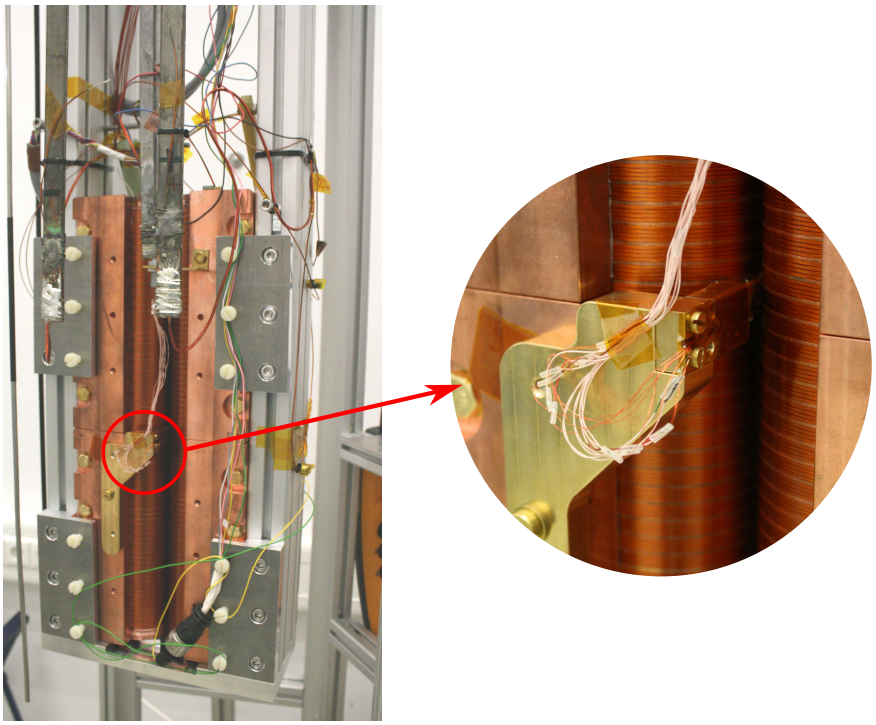

Figure 6.5: Setup to install the TGU40 inside CASPER-cryostat (left) and a zoom of the Hall probe array brass support (right).

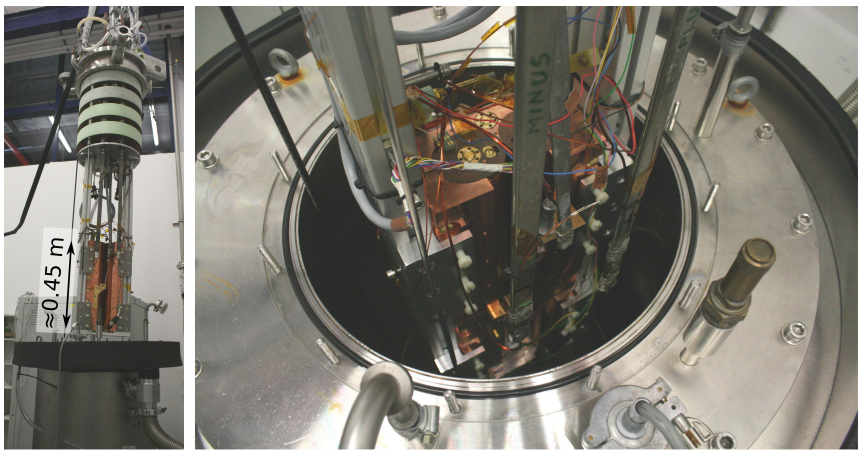

Figure 6.6: Top of the cryostat with the TGU40 is moved by a crane (left). View of the TGU40 when is introduced in the CASPER-cryostat (right).

With this setup it was possible to measure the vertical component of the magnetic flux density as a function of transverse position $B_y(x_i)$ with $(i = 1, ..., 7)$ at one fixed longitudinal position z. For the measurement $z = -2.625\,\text{mm}$ (position of the pole neighbouring the central coil) and x_i in the range between 4 mm and 10 mm were chosen. Figure 6.7 shows the position of the Hall probe array and of each Hall probe with respect to the center of undulator.

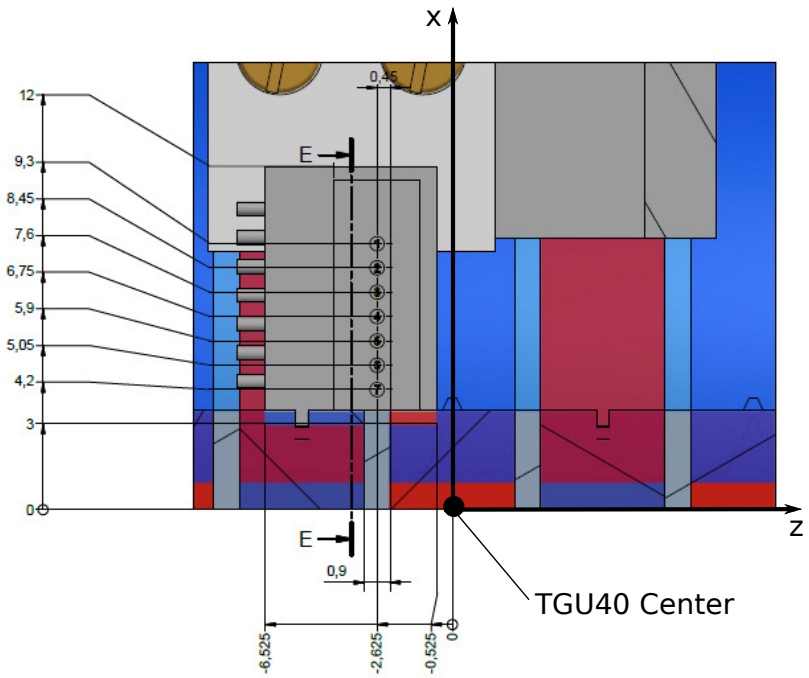

(a) 2D-view on the x-z plane

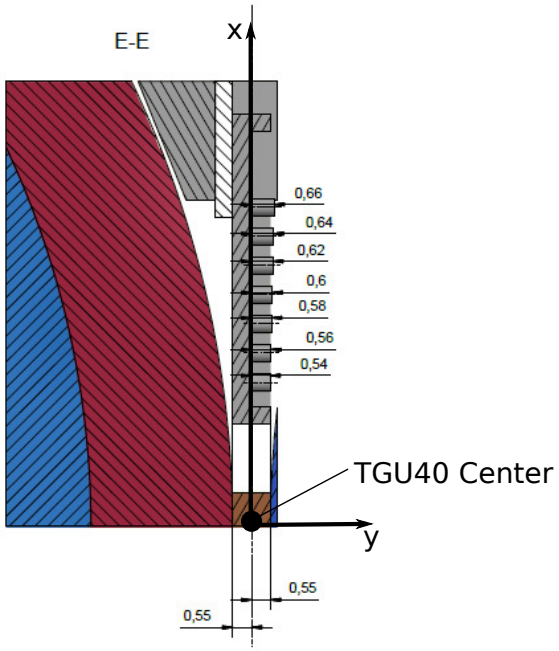

(b) 2D-view on the x-y plane

Figure 6.7: Position of the Hall probe array and each Hall probe with respect to the center of the undulator (all units mm) [61].

6.2 TGU40 coils characterization

6.2.1 Introduction to the magnetic field measurement

Before manufacturing the coils of the full-scale undulator TGU40, a magnetic field measurement of the two periods short model TGU2 was performed at KIT in the cryostat CASPER (see details in [66]). Figure 6.8 shows the measurement system designed for this purpose. The Hall probe array was installed between the two coils and allowed a longitudinal magnetic measurement and also a rotation about the z-axis. A coil support structure, which is the same as for the full-scale TGU but scaled down to the two periods, was also tested.

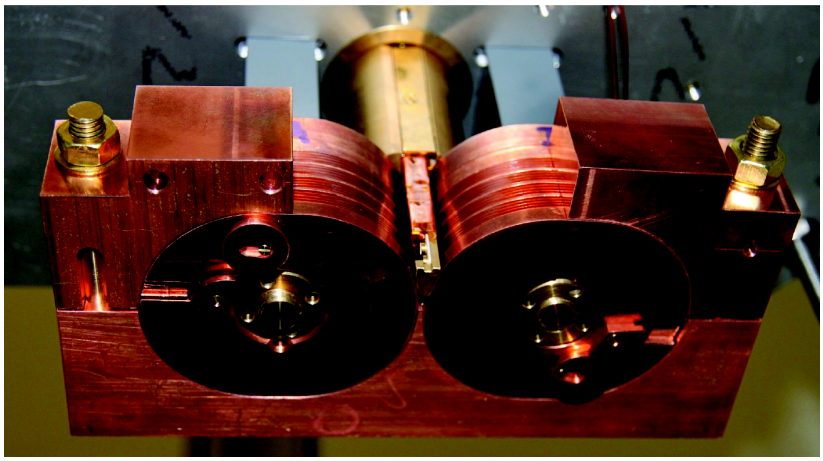

Figure 6.8: Field measurement system for the two periods short undulator model TGU2. The Hall probe array support is installed between the two coils.

This design allowed to measure the magnetic flux densities B_y along the longitudinal position z and provides a range of measurement of $\Delta z = 50\,\text{mm}$ from $z = -10\,\text{mm}$ up to $z = 40\,\text{mm}$. The magnetic field was measured with an array of 7 Hall probes (see Section 6.1.2) arranged along the x-axis between $x = 4\,\text{mm}$ and $x = 10\,\text{mm}$. Figure 6.9 shows a side view of the Hall probe array support with one of the coils behind.

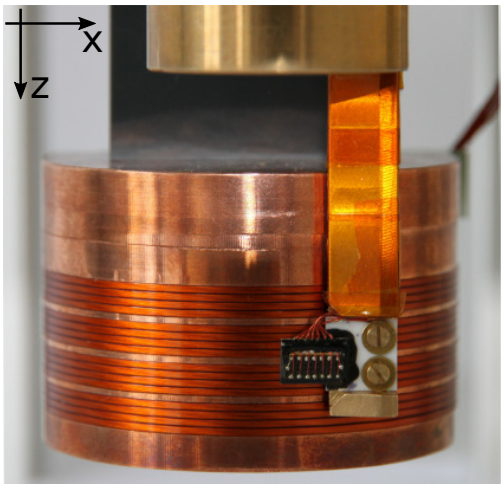

Figure 6.9: Detail side view of the Hall probe array support.

Figure 6.10 shows measured data of the magnetic field B_y with the the Hall probe (HP) 1, 4 and 7 along the longitudinal position z compared with the simulated field for $I = 750\,\mathrm{A}$ [66]. The measurement shows an excellent agreement with the theoretical expectations.

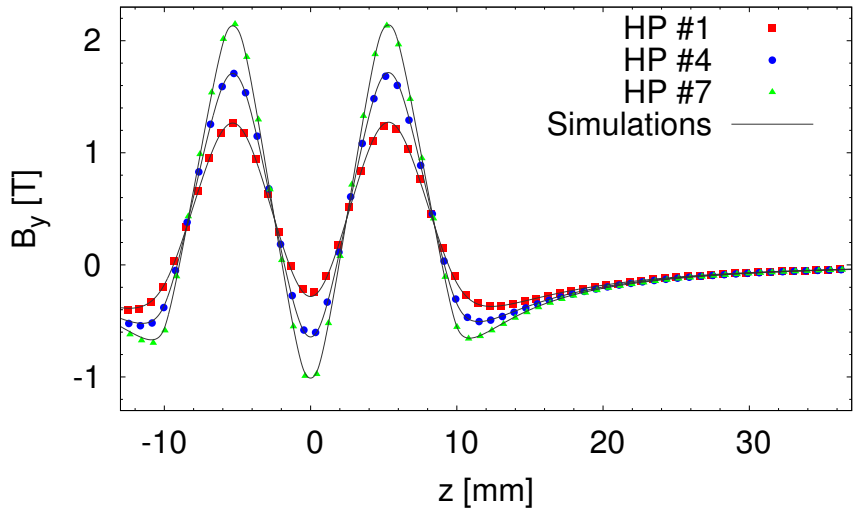

Figure 6.10: Magnetic field B_y measured along the longitudinal position z (points in colors) for $I = 750\,\mathrm{A}$ in comparison with the simulated values (black lines), for the short model TGU2. Only the values obtained with the Hall probes 1, 4 and 7 are shown for better visibility.

As already mentioned above for this thesis a similar measurement for the TGU40 was performed for one fixed z-position (see Section 6.2.4). In a future experiment the magnetic field along the longitudinal position z will be measured within its custom cryostat designed for the full-scale TGU (see Section 6.4).

6.2.2 Error analysis for the magnetic field measurement

It is assumed that a set of data obtained by repeated analysis in the same sample under the same conditions has a normal or Gaussian distribution. The perpendicular field measured with each Hall probe is given by:

$$\bar{B}_\perp[\mathrm{T}] = \frac{\bar{V}_\mathrm{H}[\mathrm{mV}] - \bar{V}_\mathrm{off}[\mathrm{mV}]}{\mathrm{S}_{4.2\mathrm{K}}[\mathrm{mV/T}]} \tag{6.5}$$

where $\bar{V}_\mathrm{H}$ is the measured Hall voltage mean, $\bar{V}_\mathrm{off}$ is the offset voltage mean and $\mathrm{S}_{4.2\mathrm{K}}$ is the sensitivity of the Hall probe at 4.2 K (see Table 6.1). The offset voltage is the Hall voltage that is measured before each field measurement at zero current (see Section 6.2.3).

The propagation of error of an experimental measurement is the combination of different statistical errors due to measurement limitations. The standard devia-

tion of the perpendicular magnetic field $\sigma_{\bar{B}_\perp}$ measured with the Hall probe array is calculated as:

$$\begin{aligned}\sigma_{\bar{B}_\perp} &= \sqrt{\left(\frac{\partial B_\perp}{\partial V_\mathrm{H}}\right)^2 \left(\sigma_{\bar{V}_\mathrm{H}}\right)^2 + \left(\frac{\partial B_\perp}{\partial V_\mathrm{off}}\right)^2 \left(\sigma_{\bar{V}_\mathrm{off}}\right)^2} \\ &= \frac{1}{\mathrm{S}_{4.2\mathrm{K}}}\sqrt{\left(\sigma_{\bar{V}_\mathrm{H}}\right)^2 + \left(\sigma_{\bar{V}_\mathrm{off}}\right)^2}\end{aligned} \tag{6.6}$$

where:

- $\sigma_{\bar{V}_\mathrm{H}}$ is the standard deviation of the Hall voltage measurements.
- $\sigma_{\bar{V}_\mathrm{off}}$ is the standard deviation of the offset voltage measurements.
- $\partial B_\perp/\partial V_\mathrm{H}$ and $\partial B_\perp/\partial V_\mathrm{off}$ are the partial derivative of the function $B_\perp$ with respect to V_H and with respect to V_off respectively and are given by:

$$\frac{\partial B_\perp}{\partial V_\mathrm{H}} = \frac{\partial}{\partial V_\mathrm{H}}\left(\frac{\bar{V}_\mathrm{H}}{\mathrm{S}_{4.2\mathrm{K}}} - \frac{\bar{V}_\mathrm{off}}{\mathrm{S}_{4.2\mathrm{K}}}\right) = \frac{1}{\mathrm{S}_{4.2\mathrm{K}}}$$

$$\frac{\partial B_\perp}{\partial V_\mathrm{off}} = \frac{\partial}{\partial V_\mathrm{off}}\left(\frac{\bar{V}_\mathrm{H}}{\mathrm{S}_{4.2\mathrm{K}}} - \frac{\bar{V}_\mathrm{off}}{\mathrm{S}_{4.2\mathrm{K}}}\right) = \frac{-1}{\mathrm{S}_{4.2\mathrm{K}}}$$

The total systematic error in the magnetic measurement $\Delta_{B_\perp}$ performed with the Hall probe array is given by:

$$\Delta_{B_\perp} = \frac{\partial B_\perp}{\partial S}(\Delta_S + \Delta_L + \Delta_T) = \left(\frac{\bar{V}_\mathrm{off} - \bar{V}_\mathrm{H}}{{\mathrm{S}_{4.2\mathrm{K}}}^2}\right)(0.0116\ \mathrm{S}_{4.2\mathrm{K}}) \tag{6.7}$$

where:

- Δ_S is the systematic sensitivity error, $\Delta_S = 0.005\ \mathrm{S}_{4.2\mathrm{K}}$.
- Δ_L is the systematic linearity error, $\Delta_L = 0.005\ \mathrm{S}_{4.2\mathrm{K}}$.
- Δ_T is the systematic calibration temperature error between the sensitivity data at 4.2 K and 77 K, $\Delta_T = 0.0016\ \mathrm{S}_{4.2\mathrm{K}}$ (see Section 6.1.2).
- $\partial B_\perp/\partial S$ is the partial derivative of the function $B_\perp$ with respect to S and is given by:

$$\frac{\partial B_\perp}{\partial S} = \frac{\partial}{\partial S}\left(\frac{\bar{V}_\mathrm{H}}{\mathrm{S}_{4.2\mathrm{K}}} - \frac{\bar{V}_\mathrm{off}}{\mathrm{S}_{4.2\mathrm{K}}}\right) = \frac{\bar{V}_\mathrm{off} - \bar{V}_\mathrm{H}}{{\mathrm{S}_{4.2\mathrm{K}}}^2}$$

The systematic error Δ_T can be compensate in future measurements with the calibration field of the Hall probe array at 4.2 K using an electromagnetic dipole and reading the field with a nuclear magnetic resonance (NMR) probe.

The measured Hall voltage $\bar{V}_\mathrm{H} \pm \sigma_{\bar{V}_\mathrm{H}}$, the calculated perpendicular field $\bar{B}_\perp \pm \sigma_{\bar{B}_\perp}$ and $\Delta_{B_\perp}$ are shown in Section 6.2.4 for the undulator coils and in Section 6.2.5 for the correction coils respectively.

6.2.3 Calibration of the Hall probe

Before starting a new measurement at 4.2 K, a number of samples were taken to determine the offset voltage V_{off} of each Hall probe at zero current in the undulator and correction coils. The offset voltage is generally due to imperfections of the manufacturing process, inhomogeneity of materials, misalignment and asymmetry of the Hall probe contacts [71]. This explains that the offset voltages of the seven probes are different.

Figure 6.11 shows the $(V_{\text{off}} - \bar{V}_{\text{off}})$ of each Hall probe with an offset voltage error $\sigma_{\bar{V}_{\text{off}}} < \pm 0.22\,\mu\text{V}$ for all the probes. The magnetic measurements were performed over three consecutive days. The correction coils were measured the first day and the undulator coils the second and third day.

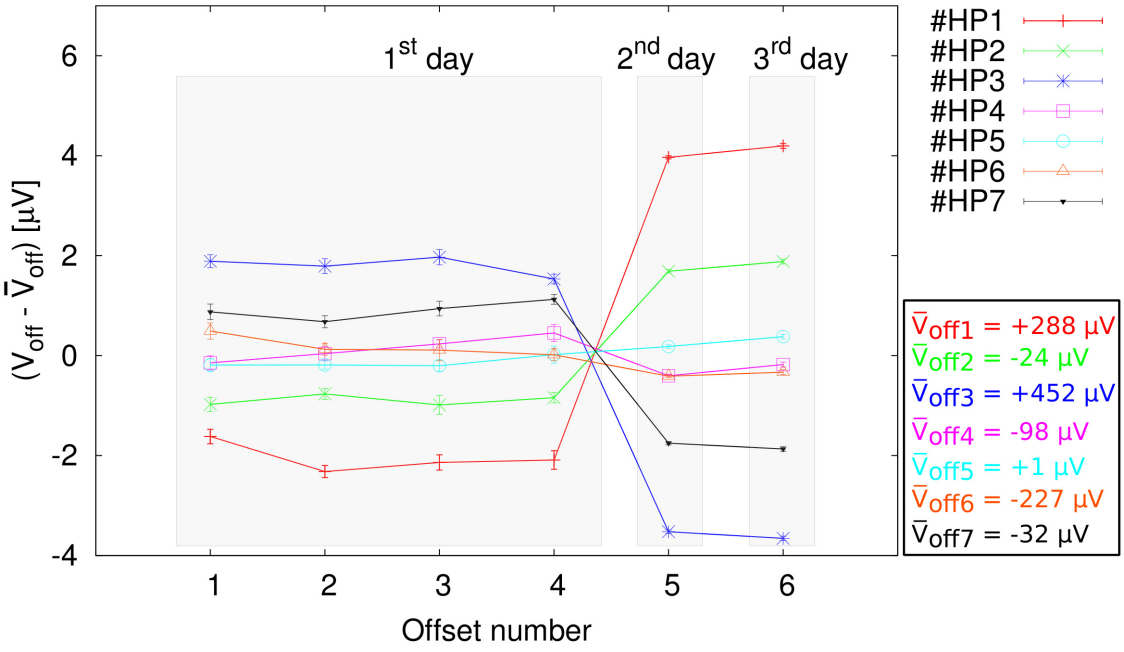

Figure 6.11: Experimentally measured offset voltage minus the mean offset voltage $(V_{\text{off}} - \bar{V}_{\text{off}})$ of each Hall probe over three consecutive days at 4.2 K.

6.2.4 Magnetic measurement of the undulator coils

To perform the magnetic measurement, the two superconducting undulator coils were connected in series as shown in Figure 6.12. Both coils can be distinguished by the shape of the central groove, which is designed for winding either a solenoid or a racetrack coil. The coil former with a central groove for the solenoid coil is called in this thesis U_{SZ} and for the racetrack coil U_{RZ}.

A regulated current supply that provides currents up to 1000 A is connected to the coils in series. In addition two current lead connections supporting 500 A are connected to the center tap between the coils. Therefore, the undulator coils could be tested each one separately as single coils and finally in series.

Figure 6.13 shows the Hall voltages V_{H}, which were measured with the Hall probe array, for the single coils and the coils in series. The current is linearly ramped from

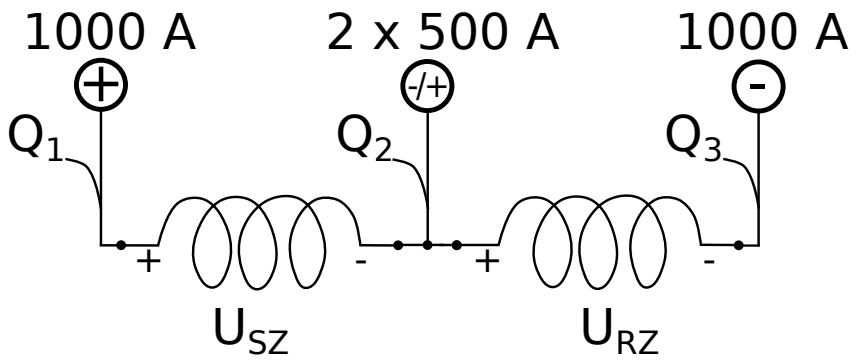

Figure 6.12: Schematic of current lead connections and quench detectors Q1-Q3 of the undulator coils inside the cryostat CASPER stand.

zero to the operating current of 750 A with a current ramp of 50 A/min. Once the operating current is reached, the measurement continues over a long period of time of around one hour. Within one hour after ramping, the Hall voltage showed a transient behavior similar to that observed in [74] and [75] with relatively long time constants. The transients are due to short-circuits to ground and between turns of the superconducting undulator coils (see Section 5.2.2).

The V_{H} values for each Hall probe after the operating current of 750 A has been reached are shown in Figure 6.14. To calculate the perpendicular magnetic field measured for each Hall probe using Equation 6.6, it is first necessary to know through a fit function the V_{H} values of each Hall probe at infinite times. The Hall probe array measures the transverse field gradient $B_y(x)$ at one fixed longitudinal position z and at the x-range between 4 mm and 10 mm. Therefore the V_{H} values are so different for each Hall probe. The Hall probe array is not completely centered at $y = 0$ between the undulator coils, but closer to the undulator coil $\mathrm{U_{SZ}}$. This explains that the V_{H} values measured with the undulator coil $\mathrm{U_{SZ}}$ (see Figure 6.14 (a)) are larger than with the undulator coil $\mathrm{U_{RZ}}$ (see Figure 6.14 (b)).

The V_{H} values were fitted using a best fit double exponential (see Equation 6.8). The data set of Hall voltage at 750 A shown in Figure 6.14 are used to calculate the best fit of each measurement. The curve rises rapidly for a short period of time and then flattens out to a limiting final value. A two-phase model is used when the measured outcome is the result of the sum of a fast and slow exponential decay. This is also called a double exponential decay.

$$V_{\mathrm{H}}(\mathrm{t}) = \mathrm{K}_0 + \mathrm{K}_1 e^{-\mathrm{t}/\tau_1} + \mathrm{K}_2 e^{-\mathrm{t}/\tau_2} \tag{6.8}$$

where: K_0 is the V_{H} value at infinite times, τ_1 and τ_2 are the decay time constants and K_1 and K_2 are their respective amplitudes. Table 6.2 compiles the fitted parameters and standard deviations obtained using Equation 6.8 and the data of the measurements shown in Figure 6.14.

The parameters were fit using gnuplot [76], which contains an implementation of the nonlinear least-squares (NLLS) Marquardt-Levenberg algorithm and calculates the standard deviations of each parameter. The perpendicular field measured with each Hall probe is calculated with the values $\bar{V}_{\mathrm{H}} \approx \mathrm{K}_0$ and $\sigma_{\bar{V}_{\mathrm{H}}} = \pm\sigma_{\mathrm{K}_0}$ from Table 6.2.

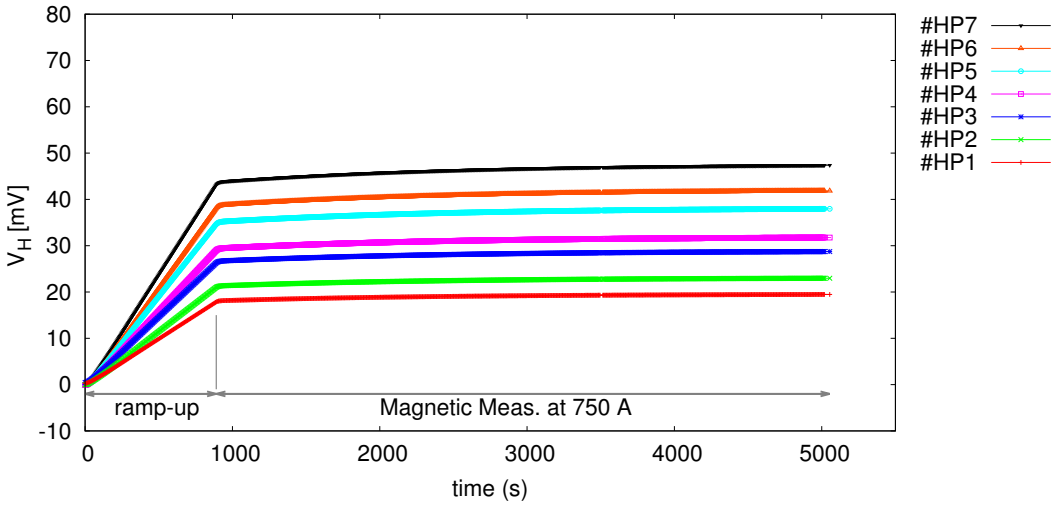

(a) Undulator coil U_{SZ}.

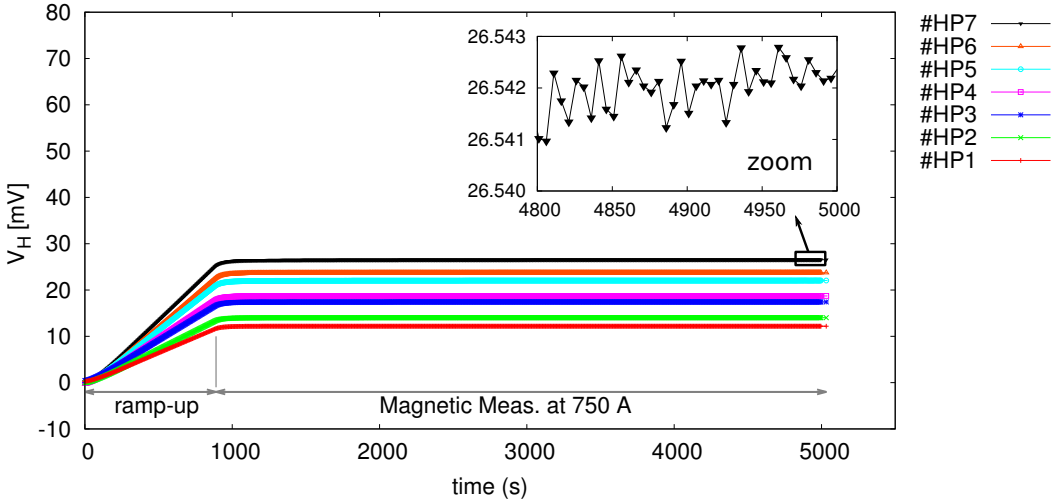

(b) Undulator coil U_{RZ}.

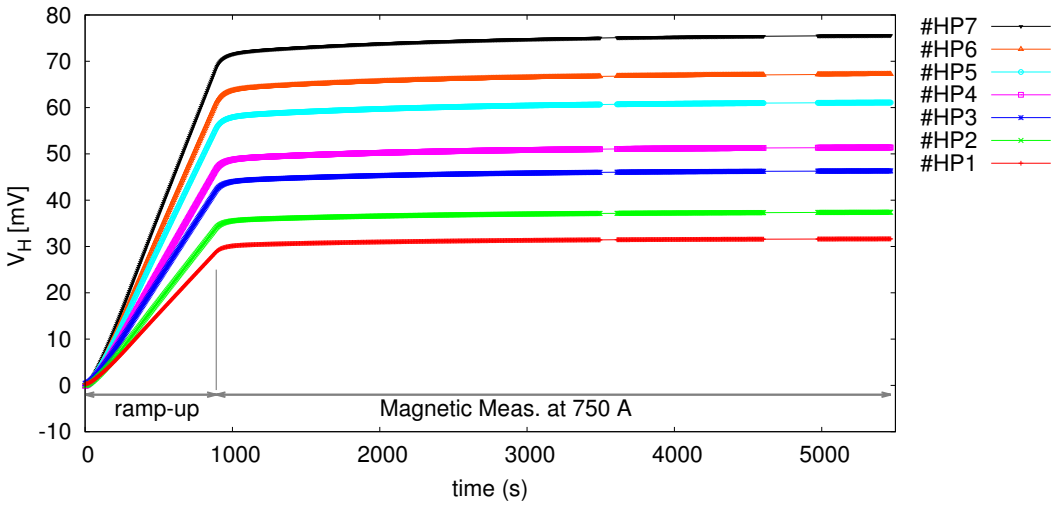

(c) Undulator coils U_{SZ} and U_{RZ} in series.

Figure 6.13: Hall voltage V_H measured over long periods of time including the current ramp from zero to the operating current of 750 A. A measurement is taken every 5 seconds. The error bars are smaller than the data point size.

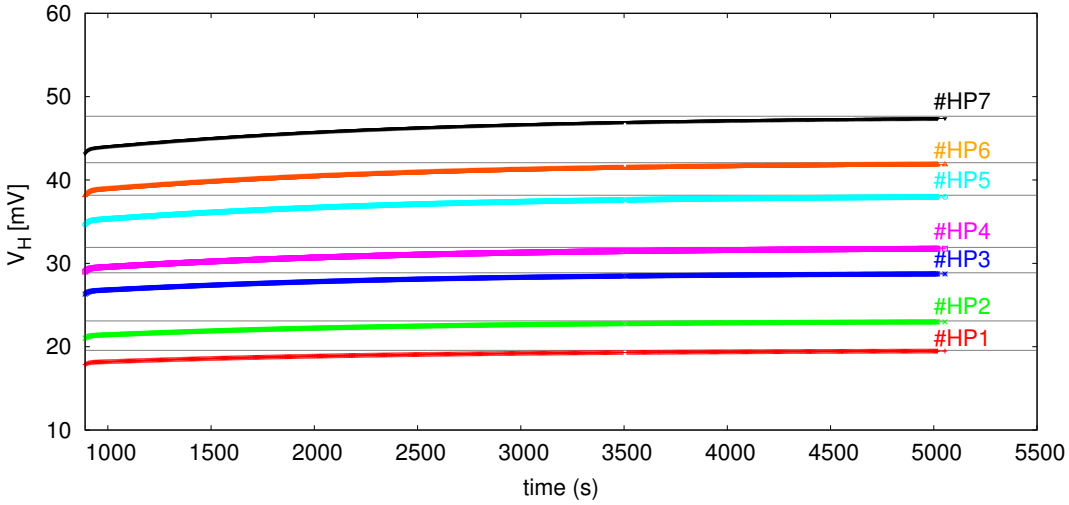

(a) Undulator coil U_{SZ}.

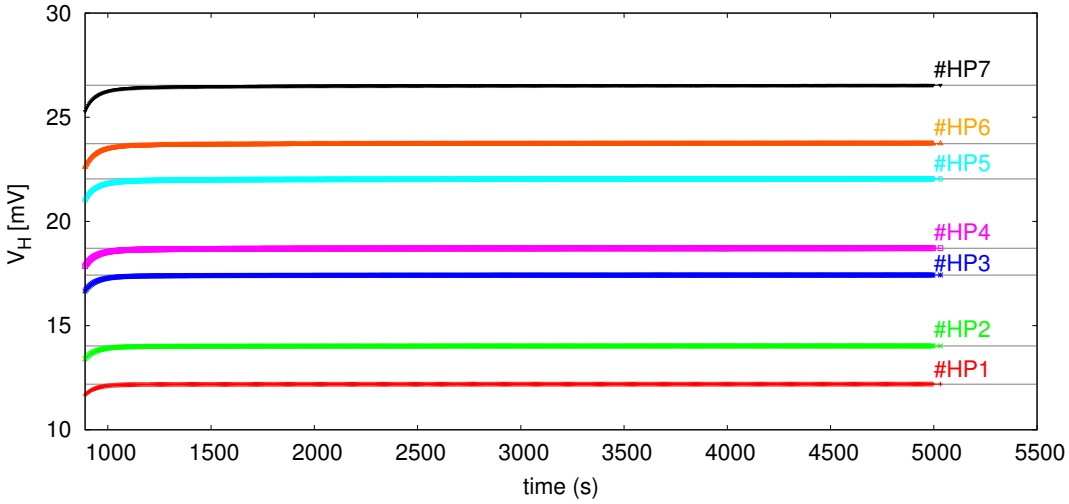

(b) Undulator coil U_{RZ}.

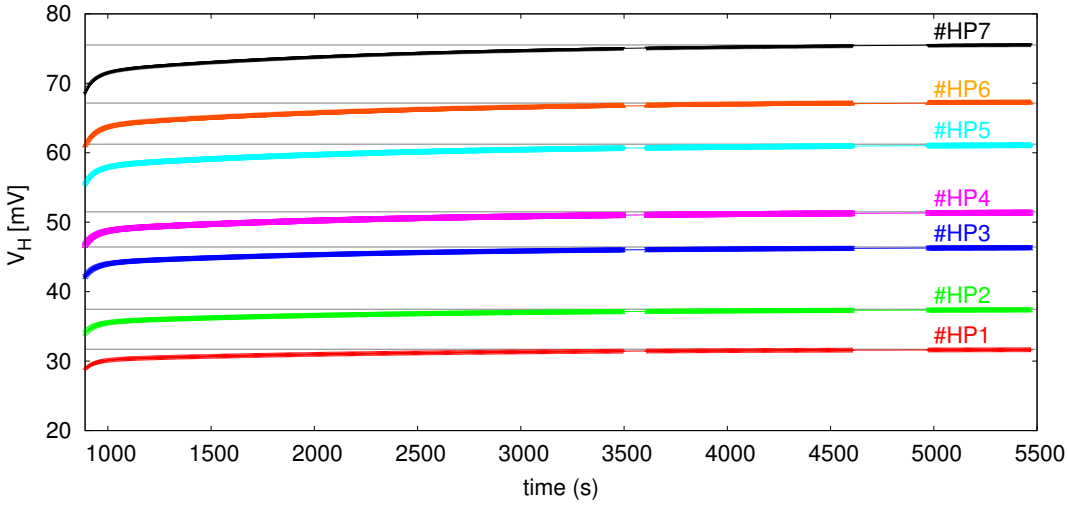

(c) Undulator coils in series.

Figure 6.14: Hall voltages V_H measured with the Hall probe array at the operating current of 750 A (color points-lines). The V_H values at infinite times (K_0 values in Table 6.2) are superimposed in each graph (gray lines).

Undulator coil U_{SZ}					
#HP	K_0[mV]	K_1[mV]	$\tau_1[s^{-1}]$	K_2[mV]	$\tau_2[s^{-1}]$
1	19.5672 ± 0.0002	-1.4737 ± 0.0002	1509.8 ± 0.7	-0.246 ± 0.001	12.7 ± 0.1
2	23.0887 ± 0.0003	-1.7897 ± 0.0002	1519.8 ± 0.7	-0.292 ± 0.001	13.0 ± 0.1
3	28.8783 ± 0.0003	-2.2308 ± 0.0003	1526.9 ± 0.7	-0.357 ± 0.002	13.2 ± 0.1
4	31.9278 ± 0.0004	-2.5376 ± 0.0004	1532.7 ± 0.7	-0.399 ± 0.002	13.3 ± 0.1
5	38.1719 ± 0.0005	-3.0560 ± 0.0004	1538.5 ± 0.7	-0.472 ± 0.003	13.3 ± 0.1
6	42.0771 ± 0.0006	-3.4307 ± 0.0005	1543.2 ± 0.8	-0.518 ± 0.003	13.4 ± 0.1
7	47.6516 ± 0.0007	-3.9117 ± 0.0006	1548.2 ± 0.8	-0.581 ± 0.004	13.2 ± 0.1
Undulator coil U_{RZ}					
#HP	K_0[mV]	K_1[mV]	$\tau_1[s^{-1}]$	K_2[mV]	$\tau_2[s^{-1}]$
1	12.1904 ± 0.0001	-0.0188 ± 0.0003	849.6 ± 23.3	-0.4884 ± 0.0006	52.9 ± 0.1
2	14.0241 ± 0.0001	-0.0374 ± 0.0005	722.4 ± 13.4	-0.5685 ± 0.0009	53.5 ± 0.2
3	17.4257 ± 0.0001	-0.0611 ± 0.0006	708.3 ± 10.6	-0.6827 ± 0.0012	54.1 ± 0.2
4	18.7134 ± 0.0002	-0.0817 ± 0.0008	719.7 ± 10.3	-0.7532 ± 0.0015	54.8 ± 0.2
5	22.0404 ± 0.0002	-0.1103 ± 0.0010	709.4 ± 9.3	-0.8794 ± 0.0018	55.3 ± 0.2
6	23.7315 ± 0.0002	-0.1302 ± 0.0011	710.2 ± 9.1	-0.9582 ± 0.0021	55.5 ± 0.2
7	26.5373 ± 0.0002	-0.1519 ± 0.0013	684.6 ± 8.2	-1.0613 ± 0.0023	55.5 ± 0.2
Undulator coils in series					
#HP	K_0[mV]	K_1[mV]	$\tau_1[s^{-1}]$	K_2[mV]	$\tau_2[s^{-1}]$
1	31.7098 ± 0.0006	-1.5359 ± 0.0006	1509.5 ± 1.9	-1.280 ± 0.002	52.8 ± 0.2
2	37.4714 ± 0.0007	-1.8710 ± 0.0008	1506.0 ± 2.0	-1.512 ± 0.003	53.5 ± 0.2
3	46.4324 ± 0.0009	-2.3414 ± 0.0010	1504.1 ± 2.0	-1.512 ± 0.003	54.1 ± 0.2
4	51.4996 ± 0.0010	-2.6671 ± 0.0011	1503.9 ± 2.0	-2.054 ± 0.004	54.5 ± 0.2
5	61.2349 ± 0.0012	-2.6671 ± 0.0011	1502.0 ± 2.0	-2.418 ± 0.004	54.7 ± 0.2
6	67.161 ± 0.017	-3.960 ± 0.025	1121.6 ± 18.7	-	-
7	75.521 ± 0.019	-4.488 ± 0.028	1127.7 ± 18.5	-	-

Table 6.2: Compilation of the fitted parameters using Equation 6.8. Double-exponential fit of the V_H values obtained from the undulator coil measurements at 750 A (data are shown in Figure 6.14).

The time constants for the undulator coil U_{SZ} and U_{RZ} are quite different. Therefore, the undulator coil in series represents a more complex behavior over the time than the undulator single coils. The calculated values for K_0 (V_H value at infinite times) employed to calculate the measured $B_\perp$ are eventually subject to systematic errors. To investigate this, it should be considered in future to perform the magnetic measurements over a longer period of time.

Table 6.3 shows a summary of the resulting perpendicular magnetic field measurements and the simulated values. The magnetic field values are calculated using Equation 6.5. The position of the Hall probe array employed to simulate the magnetic field produced for the undulator coils is not the ideal position shown in

Figure 6.7, but the reconstructed position calculated in Section 6.2.6. The transversal perpendicular field $B_\perp$ measured for the Hall probe array is shown in Figure 6.15 and compared with the simulated values obtained in OPERA-3D.

Table 6.4 summarizes the systematic errors in the magnetic measurements of the undulator coils using Equation 6.7. The systematic errors can be compensated in future magnetic measurements with the calibration of the Hall probe array at 4.2 K. The single coil measurements show an excellent agreement of the measured vs. the simulated perpendicular fields. However a small deviation is observed in the measurement of the undulator coils in series, which can be produced for the calculated K_0 values.

The targeted radiation bandwidth produced for the TGU40 has to be in the order of the natural bandwidth: $\Delta\lambda/\lambda_0 < 2.5\,\%$. It is possible to compare the errors produced for the measured magnetic field of the undulator coils in series with

	Measurement			Simulation		
	U_{SZ}	U_{RZ}	In series	U_{SZ}	U_{RZ}	In series
#HP	$B_\perp$[mT]	$B_\perp$[mT]	$B_\perp$[mT]	$B_\perp$[mT]	$B_\perp$[mT]	$B_\perp$[mT]
1	373.895 ± 0.004	230.797 ± 0.002	609.433 ± 0.012	372.181	229.965	602.146
2	441.715 ± 0.006	268.465 ± 0.002	716.604 ± 0.013	441.715	268.465	710.180
3	521.325 ± 0.006	311.319 ± 0.002	843.217 ± 0.017	517.667	309.290	826.957
4	599.962 ± 0.008	352.404 ± 0.004	966.613 ± 0.019	598.837	351.524	950.361
5	680.739 ± 0.009	393.047 ± 0.004	1092.042 ± 0.021	683.434	394.040	1077.474
6	768.956 ± 0.011	435.489 ± 0.004	1224.903 ± 0.309	768.956	435.489	1204.445
7	853.340 ± 0.013	475.496 ± 0.004	1352.072 ± 0.340	852.175	474.381	1326.556

Table 6.3: Summary of the resulting perpendicular magnetic field measurements vs simulations at 750 A for the undulator single coils and coils in series.

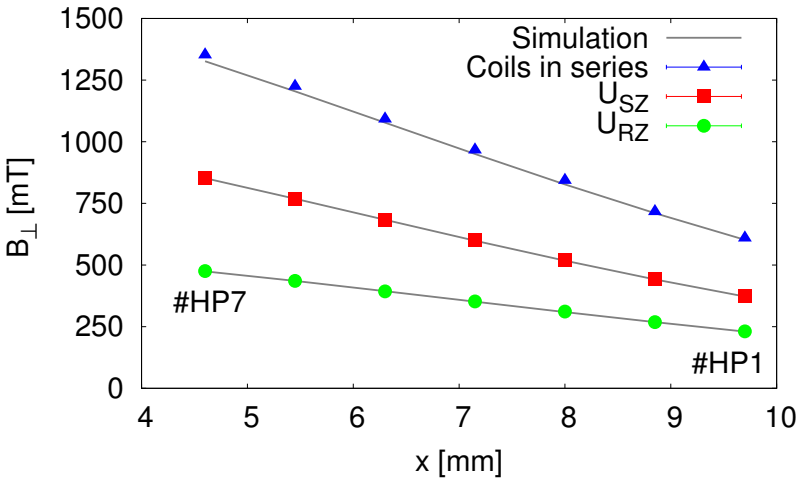

Figure 6.15: Results of the transversal perpendicular field $B_\perp$ at at 750 A measured using the Hall probe array and compared with the simulated values. The error is estimated to be less than ± 0.3 mT. The error bars are smaller than the data point size.

#HP	U_{SZ} $\Delta_{B_\perp}$[mT]	U_{RZ} $\Delta_{B_\perp}$[mT]	In series $\Delta_{B_\perp}$[mT]
1	± 4.337	± 2.677	± 7.069
2	± 5.124	± 3.114	± 8.313
3	± 6.047	± 3.611	± 9.781
4	± 6.960	± 4.088	± 11.213
5	± 7.897	± 4.559	± 12.668
6	± 8.920	± 5.052	± 14.209
7	± 9.899	± 5.516	± 15.684

Table 6.4: Systematic errors in the magnetic measurements of the undulator coils performed with the Hall probe array.

the desired maximum relative deviation of wavelengths ($\Delta\lambda/\lambda_0$). Therefore the statistical and systematic errors of the wavelength are calculated using the measured magnetic fields and the undulator equation as following:

$$\begin{aligned}\lambda &= \frac{\lambda_u}{2\gamma^2}(1+\frac{K^2}{2}) \\ &= \frac{\lambda_u}{2\gamma^2} + \frac{\lambda_u}{4\gamma^2}(93.36\ B_y[\mathrm{T}]\ \lambda_u[\mathrm{m}])^2 \\ &= \frac{\lambda_u}{2\gamma^2} + a\ B_\perp^2 \\ &= \frac{\lambda_u}{2\gamma^2} + \frac{a}{S^2}(\bar{V}_\mathrm{H}^2 - 2\ \bar{V}_\mathrm{H}\bar{V}_\mathrm{off} + \bar{V}_\mathrm{off}^2)\end{aligned} \tag{6.9}$$

where $B_y \approx B_\perp$ and the parameter a is given by:

$$a = \frac{93.36^2\ \lambda_u^3}{4\gamma^2} \tag{6.10}$$

The statistical and systematic errors of the wavelength are calculated as:

$$\sigma_{\lambda_{stat}} = \sqrt{\left(\frac{\partial\lambda}{\partial V_\mathrm{H}}\right)^2 \left(\sigma_{\bar{V}_\mathrm{H}}\right)^2 + \left(\frac{\partial\lambda}{\partial V_\mathrm{off}}\right)^2 \left(\sigma_{\bar{V}_\mathrm{off}}\right)^2} \tag{6.11}$$

$$\Delta_{\lambda_{syst}} = \frac{\partial\lambda}{\partial S}\sigma_{\bar{S}} \tag{6.12}$$

where $\partial\lambda/\partial V_\mathrm{H}$, $\partial\lambda/\partial V_\mathrm{off}$ and $\partial\lambda/\partial V_\mathrm{S}$ are the partial derivative of the wavelength λ with respect to V_H, V_off and S respectively and are given by:

$$\frac{\partial\lambda}{\partial V_\mathrm{H}} = \frac{2a}{S^2}\left(\bar{V}_\mathrm{H} - \bar{V}_\mathrm{off}\right)$$

$$\frac{\partial\lambda}{\partial V_\mathrm{off}} = \frac{2a}{S^2}\left(\bar{V}_\mathrm{off} - \bar{V}_\mathrm{H}\right)$$

$$\frac{\partial\lambda}{\partial S} = \frac{-2a}{S^3}\left(\bar{V}_{\text{off}} - \bar{V}_{\text{H}}\right)^2$$

Table 6.5 summarizes the results of wavelengths and errors calculated with the data of the measured magnetic fields produced for the undulator coils in series at 750 A (see Table 6.3). The values of the x position and gamma are approximate.

The maximum systematic error of the wavelength obtained is about 1.6 nm. In Section 4.4.2 the optimal wavelength by the central energy $\lambda_0 = 150\,\text{nm}$ and the relative deviation of wavelengths emitted $\Delta\lambda/\lambda_0 = 0.5\,\%$ were calculated. Due to the small deviations in the magnetic measurement of the undulator coils in series the accuracy of the measurement is $\approx 1.1\,\% = 100 * 1.6\,\text{nm}/150\,\text{nm}$. That is efficient to show that the relative deviation of wavelengths is lower than 2.5 %. In order to proof the design value of $\Delta\lambda/\lambda_0 = 0.5\,\%$ in future measurements, it is necessary to calibrate the Hall probe array at 4.2 K.

With the first magnetic measurement of the undulator coils, a lists of statistical and systematic errors are identified. The results show that the position of the Hall probe has to be reconstructed for matching the results with the Hall probe array data. The TGU40 magnetic measurements shows excellent agreement with the simulation results obtained with OPERA-3D. The small deviations observed could be attributed to the systematic errors, which should be compensate in future measurements. This includes the calibration of the Hall probe array at 4.2 K and measurements over a longer period of time to find the K_0 parameter (V_{H} value at infinite times) with a lower uncertainty.

#HP	$\approx x$[mm]	$\approx \gamma$	$B_\perp$[T]	λ[nm]	$\sigma_{\lambda_{stat}}$[nm]	$\Delta_{\lambda_{syst}}$[nm]
1	9.70	200	0.61	154	0.0009	0.5413
2	8.85	210	0.72	148	0.0011	0.6810
3	8.00	220	0.84	146	0.0015	0.8616
4	7.15	229	0.97	144	0.0017	1.0386
5	6.30	239	1.09	144	0.0021	1.2203
6	5.45	249	1.22	146	0.0308	1.4181
7	4.60	259	1.35	148	0.0347	1.6007

Table 6.5: Summary of the results of the wavelengths and errors calculated with the measured magnetic fields.

6.2.5 Magnetic measurement of the correction coils

The electric circuits to perform the magnetic measurements of the two superconducting correction coils is shown in Figure 6.16. In this case, the correction coil K_{SZ} is located inside the undulator coil former with the central groove for the solenoid coil, and the correction coil K_{RZ} is inside the undulator coil former with the central groove for the racetrack coil. The correction coils can be tested as single coils and in series.

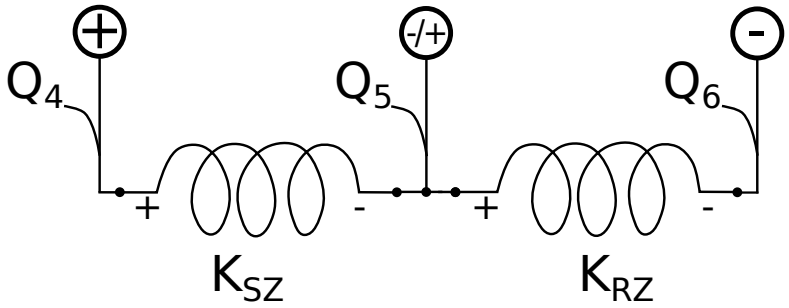

Figure 6.16: Schematic of current lead connections and quench detectors Q4-Q6 of the correction coils inside the cryostat CASPER stand.

Figure 6.17 shows the relative Hall voltages produced by the correction coils. It was measured every 0.2 A during current ramp-up, from 0 to 2.8 A. After waiting a few seconds it was measured also every 0.2 A during current ramp-down, from 2.8 A to 0. The measurements show a difference between the V_H values at each current during current ramp-up and ramp-down especially with the correction coils in series. These differences can be due to a transient behavior, which was not taken into account during measurement. Table 6.6 summarizes the values of the Hall voltages measured at 2.8 A calculated as the average of the 20 samples.

A summary of the resulting correction field measurements and the simulated values is shown in Table 6.7. The magnetic field values are calculated using Equation 6.5 where the V_H values are shown in Table 6.6. The position of the Hall probe array employed to simulate the magnetic field produced for the correction coils is not the ideal position shown in Figure 6.7, but the reconstructed position calculated in Section 6.2.6.

The correction field $B_\perp$ measured for the Hall probe array is shown in Figure 6.19 and compared with the simulated values obtained in OPERA-3D. Table 6.8 summarizes the systematic errors in the magnetic measurements of the correction coils using Equation 6.7.

#HP	K_{SZ} $V_H[\mu V]$	K_{RZ} $V_H[\mu V]$	In series $V_H[\mu V]$
1	277.179 ± 0.116	278.217 ± 0.119	269.675 ± 0.103
2	-36.154 ± 0.084	-34.726 ± 0.106	-45.258 ± 0.079
3	439.470 ± 0.086	442.127 ± 0.101	427.913 ± 0.118
4	-113.472 ± 0.106	-110.426 ± 0.073	-126.399 ± 0.090
5	-18.073 ± 0.097	-14.510 ± 0.111	-33.028 ± 0.108
6	-245.886 ± 0.118	-242.043 ± 0.100	-261.535 ± 0.105
7	-51.556 ± 0.113	-47.116 ± 0.086	-67.723 ± 0.084

Table 6.6: Compilation of the Hall voltages V_H measured at 2.8 A.

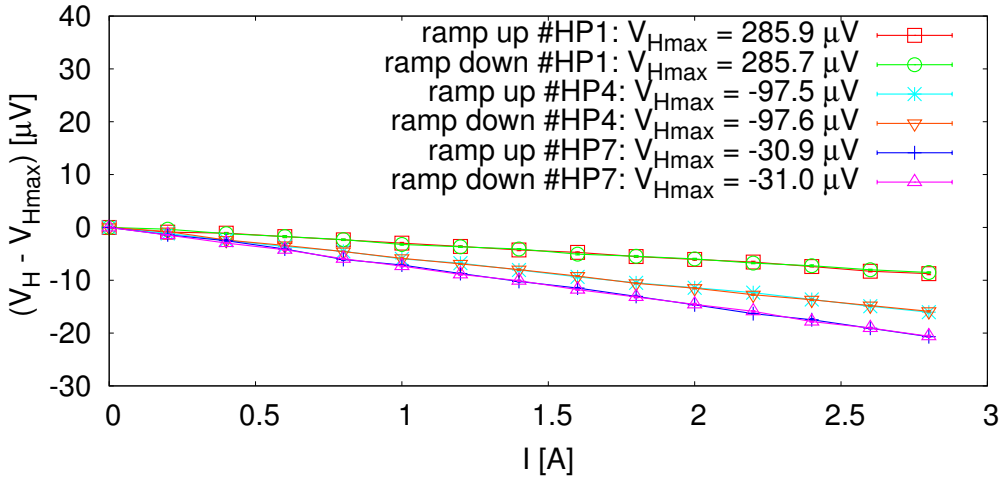

(a) Correction coil K_{SZ}.

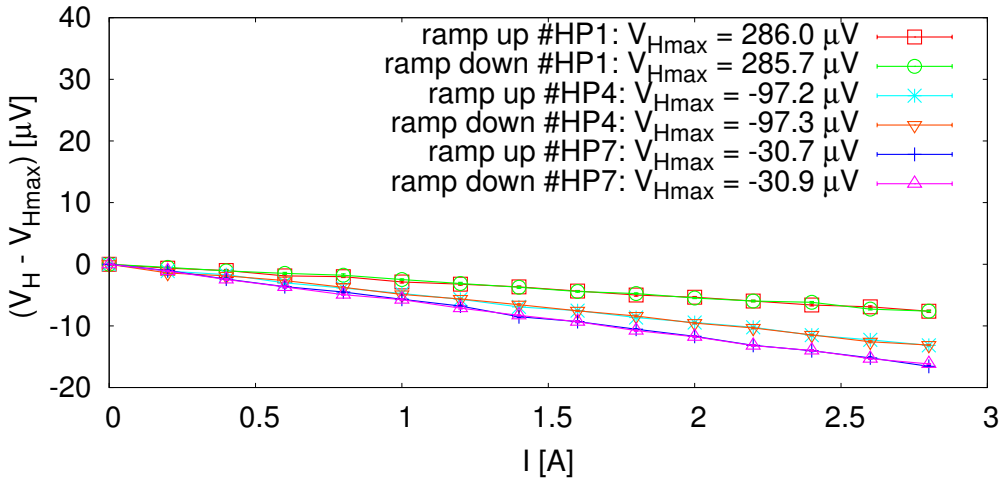

(b) Correction coil K_{RZ}.

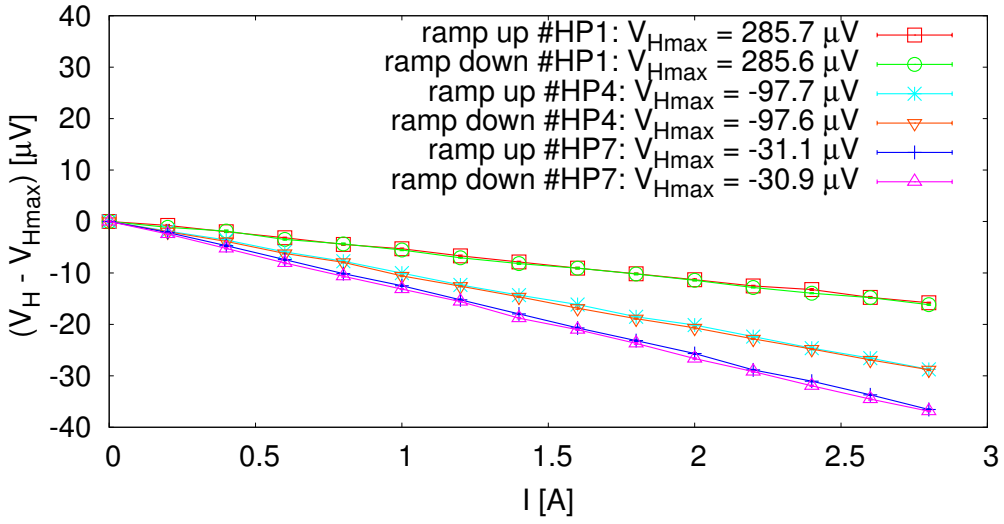

(c) Correction coils in series.

Figure 6.17: Relative Hall voltages V_H measured with the Hall probe array during current ramp-up and ramp-down from zero to 2.8 A and vice versa. The current ramp was 5 A/min and at each current were measured ten samples. The error bars are smaller than the data point size. Only the values obtained with the Hall probes 1, 4 and 7 are shown for better visibility.

	Measurement			Simulation		
	K_{SZ}	K_{RZ}	In series	K_{SZ}	K_{RZ}	In series
#HP	$B_\perp$[mT]	$B_\perp$[mT]	$B_\perp$[mT]	$B_\perp$[mT]	$B_\perp$[mT]	$B_\perp$[mT]
1	-0.169 ± 0.004	-0.150 ± 0.004	-0.311 ± 0.003	-0.202	-0.190	-0.392
2	-0.206 ± 0.004	-0.182 ± 0.003	-0.384 ± 0.003	-0.252	-0.227	-0.480
3	-0.263 ± 0.003	-0.206 ± 0.003	-0.472 ± 0.003	-0.299	-0.260	-0.560
4	-0.300 ± 0.002	-0.247 ± 0.003	-0.538 ± 0.003	-0.337	-0.286	-0.622
5	-0.331 ± 0.003	-0.272 ± 0.004	-0.598 ± 0.002	-0.360	-0.300	-0.660
6	-0.353 ± 0.004	-0.282 ± 0.003	-0.638 ± 0.003	-0.365	-0.301	-0.666
7	-0.370 ± 0.003	-0.294 ± 0.002	-0.655 ± 0.003	-0.352	-0.289	-0.640

Table 6.7: Summary of the resulting perpendicular magnetic field measurements vs simulations at 2.8 A for the correction single coils and coils in series.

	K_{SZ}	K_{RZ}	In series
#HP	$\Delta_{B_\perp}$[mT]	$\Delta_{B_\perp}$[mT]	$\Delta_{B_\perp}$[mT]
1	± 0.002	± 0.002	± 0.004
2	± 0.002	± 0.002	± 0.004
3	± 0.003	± 0.002	± 0.005
4	± 0.003	± 0.003	± 0.006
5	± 0.004	± 0.003	± 0.007
6	± 0.004	± 0.003	± 0.007
7	± 0.004	± 0.003	± 0.008

Table 6.8: Systematic errors in the magnetic measurements of the correction coils performed with the Hall probe array.

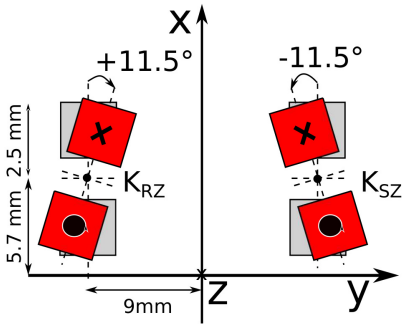

Figure 6.18: Comparison of the ideal (in gray) and rotated (in red) correction coils. The drawing is not drawn to scale.

The differences between the magnetic field measured and simulated showed in Figure 6.19 can be due to a mechanical deviation, an error in the position of the correction coils. These long racetrack coils must be placed inside the undulator coils parallel to the xz-plane (see Figure 4.14). Such a small displacement is imperceptible to the naked eye, but can be detected with the magnetic measurements.

The two correction coils are tilted against each other about the z-axis by an angle of ≈ 11.5 degrees. Figure 6.18 shows the ideal position and the approximated position of the correction coils, which is found through simulations in OPERA-3D. Figure 6.20 compares the magnetic measurements with the simulations where the correction coils are tilted by an angle. This mechanical deviations produces an error in the correction field and therefore an undesirable drift of the electron trajectories, which were optimized in Section 4.2.3. For achieving the targeted radiation bandwidth in the order of the natural bandwidth ($\Delta\lambda/\lambda_0 < 2.5\,\%$), the trajectory drifts have to be smaller than the minimum beamlet width (242 μm). It is necessary to correct their alignment before performing the next magnetic measurements.

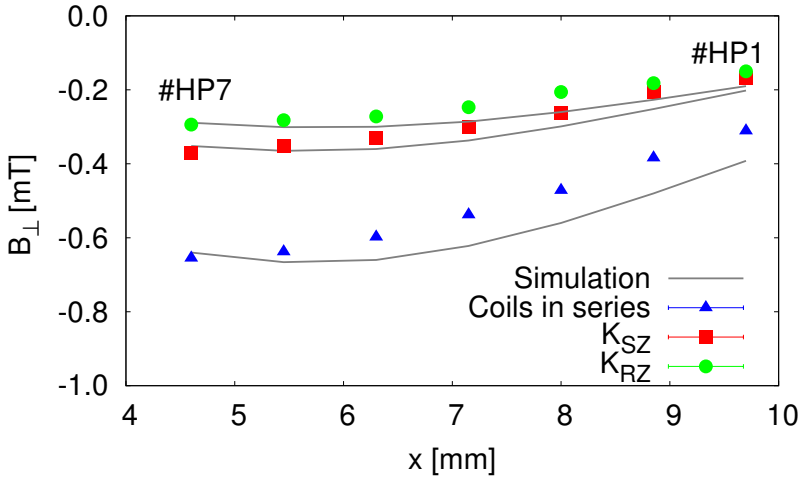

Figure 6.19: Results of the perpendicular field $B_\perp$ at at 2.8 A measured using the Hall probe array and compared with the simulated values. The error is estimated to be less than $\pm 4\,\mu$T. The error bars are smaller than the data point size.

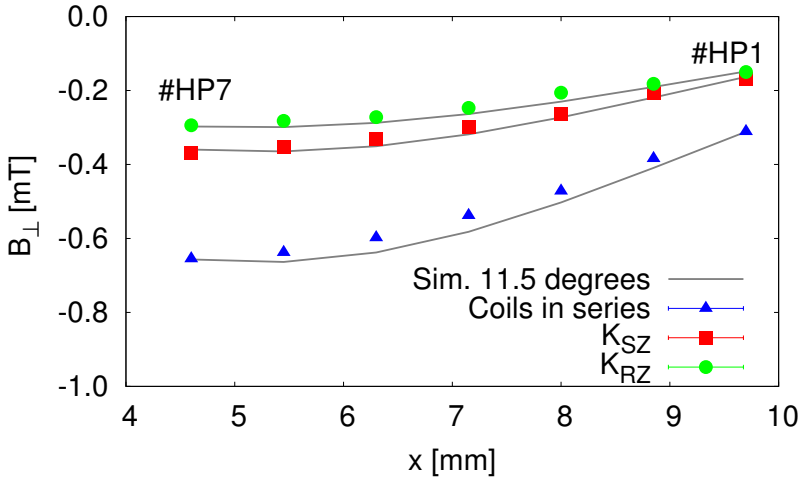

Figure 6.20: Perpendicular magnetic field 2.8 A measured and compared with the simulated values with the corrections coils rotated ≈ 11.5 degrees about the z-axis.

6.2.6 Self-consistent reconstruction of the Hall probe array position

The Hall probe array position with respect to the TGU40 center was measured before introducing the undulator in the cryostat and before starting the magnetic measurement. A displacement of the Hall probe array of approximately +0.5 mm in x direction relative to the ideal positions was measured. The ideal positions of each Hall probe are shown in Figure 6.7.

Figure 6.21 compares the measured perpendicular magnetic field of the undulator coils (a) and correction coils (b) with the simulations calculated with the ideal position of the Hall probe array. Only the measurement of the single undulator coil U_{RZ} shows a good agreement with the simulation data. This is due to the displacement of the Hall probe array. Before comparing measurements with simulation results, it is necessary look for the reconstructed position.

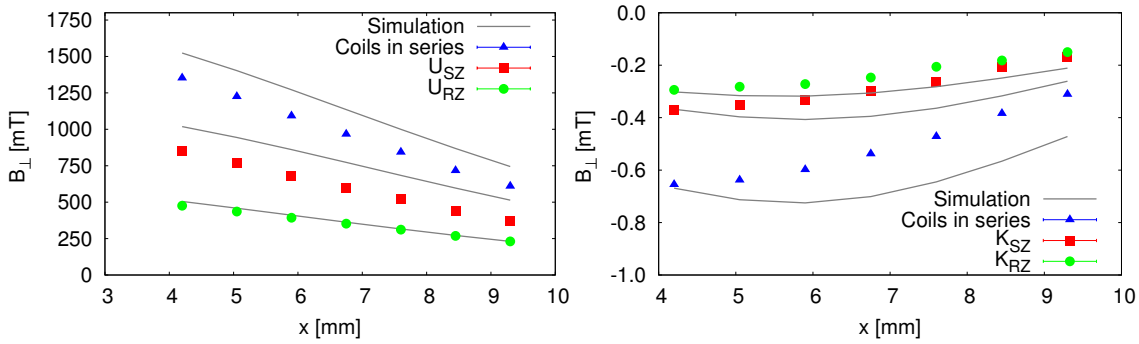

(a) Undulator coils (b) Correction coils

Figure 6.21: Comparison of the transversal perpendicular field $B_\perp$ measured with the simulated values, which are calculated using the ideal position of the Hall probe array (see Figure 6.7).

The Hall probe array position is searched through the Simplex method [77], which requires a function evaluation to find a minimum (at least a local minimum). The function compares the measurements of the perpendicular magnetic field with the simulated data of the single undulator coils at 750 A (see Table 6.3) and of the single correction coils at 2.8 A (see Table 6.7). In each iteration the values of the optimized parameters are slightly varied and the function is evaluated to find the minimum. The optimization ends when the values of the simulated magnetic field matches with the measured values within a tolerance.

The seven parameters employed to search the position of the Hall probe array are:

- The coordinates of the Hall probe HP7 ($HP7_x, HP7_y, HP7_z$).
- The coordinates of the vector perpendicular to the Hall probe plane $\vec{N} = (N_x, N_y, N_z)$.
- The angle Θ. The vector $\vec{M}_p$ is defined to be perpendicular to $\vec{N}$, at an angle Θ from the vector $\vec{M}$.

Figure 6.22 shows the plane, vectors and angle Θ used to calculate the position of the Hall probes. It is further assumed that the distance between probes is d = 0.85 mm and that they are aligned on the same plane (the surface of the Hall probe array).

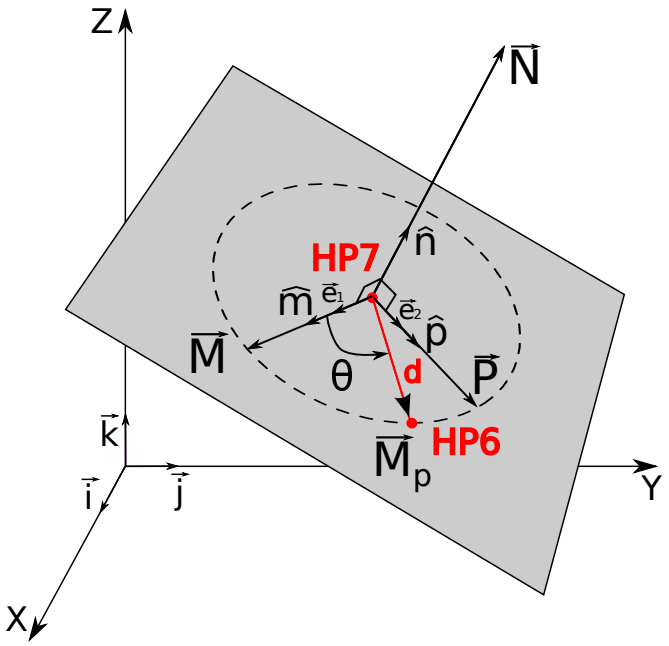

Figure 6.22: Plane, vectors and angle used to search the Hall probe array position. For reasons of clarity, only the Hall probes HP6 and HP7 are shown.

The coordinates of HP6 and the other Hall probes can be calculated with the data of the coordinates HP7, the vector $\vec{N}$ and the angle Θ obtained through the optimization. The unit vector n̂ is given by:

$$\hat{n} = \begin{bmatrix} n_x \\ n_y \\ n_z \end{bmatrix} = \frac{\vec{N}}{N} \tag{6.13}$$

where the magnitude of vector is $N = \sqrt{{N_x}^2 + {N_y}^2 + {N_z}^2}$.

The unit vector m̂ is perpendicular to the unit vector n̂ and is calculated by:

$$\hat{m} = \begin{bmatrix} m_x \\ m_y \\ m_z \end{bmatrix} = \begin{bmatrix} +n_y \\ -n_x \\ 0 \end{bmatrix} \tag{6.14}$$

The unit vector p̂ is orthogonal to the vectors n̂ and m̂ and is calculated through the cross product of these two vectors as:

$$\hat{p} = \hat{n} \times \hat{m} = \begin{vmatrix} \vec{i} & \vec{j} & \vec{k} \\ n_x & n_y & n_z \\ m_x & m_y & m_z \end{vmatrix} = \begin{vmatrix} n_y & n_z \\ m_y & m_z \end{vmatrix} \vec{i} - \begin{vmatrix} n_x & n_z \\ m_x & m_z \end{vmatrix} \vec{j} + \begin{vmatrix} n_x & n_y \\ m_x & m_y \end{vmatrix} \vec{k} \tag{6.15}$$

where $\vec{i}$, $\vec{j}$ and $\vec{k}$ are the standard unit vectors in three dimensions. Then the unit vector $\hat{p}$ is:

$$\hat{p} = \begin{bmatrix} p_x \\ p_y \\ p_z \end{bmatrix} = \begin{bmatrix} +(n_y m_z - n_z m_y) \\ -(n_x m_z - n_z m_x) \\ +(n_x m_y - n_y m_x) \end{bmatrix} \tag{6.16}$$

The unit vector $\vec{e}_1$ and $\vec{e}_2$ are given by:

$$\vec{e}_1 = \begin{bmatrix} e_{1x} \\ e_{1y} \\ e_{1z} \end{bmatrix} = \frac{\hat{m}}{m} \tag{6.17}$$

$$\vec{e}_2 = \begin{bmatrix} e_{2x} \\ e_{2y} \\ e_{2z} \end{bmatrix} = \frac{\hat{p}}{p} \tag{6.18}$$

The last step is to calculate the vector $\vec{M}_p$ between the probes HP7 and HP6. This vector is calculated as:

$$\vec{M}_p = \begin{bmatrix} M_{px} \\ M_{py} \\ M_{pz} \end{bmatrix} = M\cos(\Theta)\ \vec{e}_1 + M\sin(\Theta)\ \vec{e}_2 \tag{6.19}$$

where the vector $\vec{M}$ is:

$$\vec{M} = \begin{bmatrix} M_x \\ M_y \\ M_z \end{bmatrix} = d(7-n)\vec{e}_1 \tag{6.20}$$

with n = 6 (the number of the Hall probe) and the magnitude of vector is $M = \sqrt{{M_x}^2 + {M_y}^2 + {M_z}^2}$.

The coordinates of the Hall probe HP6 are given by:

$$\begin{aligned} \text{HP6}\ (\text{HP6}_x, \text{HP6}_y, \text{HP6}_z) &= \vec{M}_p + \text{HP7} \\ &= (M_{px} + \text{HP7}_x, M_{py} + \text{HP7}_y, M_{pz} + \text{HP7}_z) \end{aligned} \tag{6.21}$$

The problem with the Simplex method is that it does not calculate the parameters' standard deviations directly. It is possible to estimate how widely distributed are the parameters before finding the optimized values. Figure 6.23 shows an example: the values of the parameter HP7_x in the last 100 iterations.

Table 6.9 summarizes the optimization parameter results obtained from three different starting points and the standard deviations calculated from these three

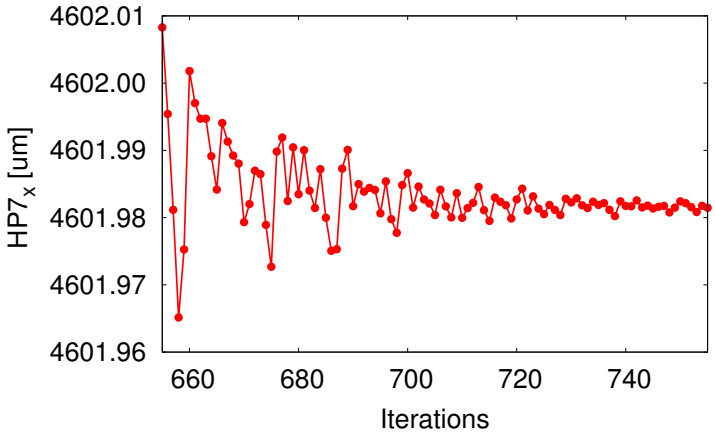

Figure 6.23: Last 100 iterations of the parameter $HP7_x$ optimized through the Simplex Method.

Optimized parameters:	
Coordinates of the Hall probe HP7:	HP7x = (4.62 ± 0.02) mm
	HP7y = (0.459 ± 0.001) mm
	HP7z = (-2.626 ± 0.002) mm
Vector normal to the plane $\vec{N}$:	Nx = (0.009 ± 0.001) mm
	Ny = (0.81 ± 0.06) mm
	Nz) = (-0.33 ± 0.03) mm
Angle between vectors $\vec{M}$ and $\vec{M}_p$	$\Theta = (-3.8 \pm 0.3)$ mrad

Table 6.9: Summary of the results of the Simplex optimization to search the Hall probe positions.

results. The Hall probe array shows an inclination and a displacement of ≈ 0.5 mm in $+x$ direction respect to the ideal position (see data in Figure 6.7). This coincides approximately with the measurement of the position, which was performed manually before inserting the undulator inside the cryostat.

For the other Hall probes position the vector $\vec{M}$ of Equation 6.20 has to be recalculated with a value of n between 1 and 5 to get the new value of the vector $\vec{M}_p$. The coordinates of their positions are calculated then by:

$$\text{HPn } (HP_x, HP_y, HP_z) = \vec{M}_p(n) + \text{HP7} \tag{6.22}$$

The position of rest of the Hall probes was calculated from Equation 6.22 and the optimized values of the coordinates of the Hall probe HP7, the vector normal $\vec{N}$ and the angle Θ. Table 6.10 shows the coordinates of all the Hall probes.

In this thesis, the magnetic measurements were taken only at one fixed longitudinal position z. These measurements were employed to reconstruct the position of the Hall probe array (see Table 6.10), which differs from the ideal position (see Figure 6.7). The reconstructed position is used to simulate in OPERA-3D the magnetic fields produced for the undulator and correction coils, in order to compare

#HP	x[mm]	y[mm]	z[mm]
1	9.72	0.410	-2.608
2	8.87	0.418	-2.611
3	8.02	0.426	-2.614
4	7.17	0.434	-2.617
5	6.32	0.443	-2.620
6	5.47	0.451	-2.623
7	4.62	0.459	-2.626

Table 6.10: Position of the Hall probes after the optimization.

the simulated values with the measured ones. In future measurements in its custom TGU40 cryostat (see Section 6.4) the magnetic field will be measured along the z-axis. In that case different z-positions of the Hall probes can be determined independently (namely at the zero-crossings of the undulator field) and therefore the ambiguity in determining the reconstructed Hall probe position, the vector $\vec{N}$ and angle Θ can be very much reduced.

6.3 TGU40 quench test

As already mentioned, a quench is the transition from the superconducting to the normal-conducting state. Figure 6.12 shows the quench detection wires (Q1-Q3), which are connected to the undulator coils to measure the voltage drop during the undulator coils operation. During the superconducting state this voltage should be close to zero. Only the voltage drops across the non-superconducting solder joints should be measurable. However, after breakdown of the superconductivity, the measurable voltage increases a few millivolts and triggers the quench detector circuit which immediately turns off the power supply and so minimizes the risk of damaging the coils.

In the quench tests performed for this thesis the quench detection system IPE-3420 manufactured by KIT's Institute for Data Processing and Electronics was employed. A threshold voltage between the undulator coils of $\pm 50\,\mathrm{mV}$ was set and the rise time (without filtering) of $< 500\,\mu\mathrm{s}$ was selected.

Half-bridges are inserted in the holes on the solenoid coils, between the racetrack coils, to support the otherwise free superconducting wire. The half-bridges allow the stabilization of the wires, avoiding that the superconducting wire moves and causes a quench. It was shown in a previous experiment with the TGU2 coils [66] that the coil without half-bridges showed a less stable behavior against quench.

The results of the quench tests of the undulator coils in series are shown in Figure 6.24. The Bottura's fit function (see Section 4.1.2) predicts that a quench of the undulator coils in series should occur when the critical current density of $1214\,\mathrm{A/mm^2}$ is reached, which corresponds to a critical current of 891.6 A.

A factor that cause a superconducting coil to quench is for example a mechanical disturbance (wire motion caused by the electromagnetic force), which can occurs

when the current increases rapidly. The first quench tests with the undulator coils in series were made with high ramp rates and therefore the quench currents were lower than expected. In contrast, with a low ramp rates of 20 A/min after 800 A, quench currents of ≈ 898 A were achieved. The time when the quench tests started and ended and the ramp rates for all the quench tests are given in Table 6.11.

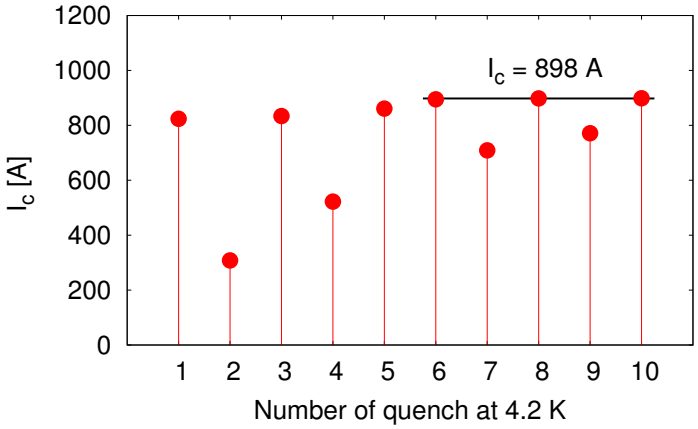

Figure 6.24: Critical current achieved for the TGU40 during the quench tests at 4.2 K.

Quench number	Start to end time	LHe level [cm]	I_c [A]	Ramp rate
1	10:34 to 10:44	90 to 86.9	824.00	0 to 700 A at 100 A/min 700 to 1000 A at 50 A/min
2	10:45 to 10:50	85.9 to 85.4	308.00	0 to 750 A at 200 A/min
3	10:52 to 11:06	84.9 to 80.6	833.82	0 to 700 A at 100 A/min 700 to 1000 A at 20 A/min
4	11:07 to 11:12	79.9 to 79.4	522.31	0 to 800 A at 150 A/min
5	11:13 to 11:23	79.3 to 76	861.13	0 to 800 A at 100 A/min 800 to 1000 A at 20 A/min
6	11:25 to 11:40	75.2 to 71.7	894.74	0 to 800 A at 100 A/min 800 to 1000 A at 20 A/min
7	12:05 to 12:13	97.4 to 94.5	708.92	0 to 800 A at 100 A/min
8	12:15 to 12:28	94.5 to 88.7	898.09	0 to 800 A at 100 A/min 800 to 1000 A at 20 A/min
9	12:30 to 12:38	88 to 86.4	771.18	0 to 800 A at 100 A/min
10	12:47 to 13:00	84.5 to 80.5	898.64	0 to 800 A at 100 A/min 800 to 1000 A at 20 A/min

Table 6.11: Summary of the results of the quench tests of the TGU40 at 4.2 K.

If there are not sufficient helium in the cryostat, the undulator can warm and this make a quench more likely. Furthermore, a quench in the absence of sufficient cooling by the helium can heat the undulator and cause severe damage to it. The helium level during the quench tests was above 70 cm. Table 6.11 gives also the helium level for each quench test.

The operating current will be at 83.5 % of the maximum quench current reached, providing a sufficient safety margin. The maximum quench current value could not be reproduced stably. The instability can be produced because the undulator coils are not impregnated. In future measurements, it is recommended to perform more number of quenchs to study the dependence of the quench current level on the current ramp rates, the helium level and also the time between quenchs.

6.4 Future measurements

In this thesis, the first magnetic measurements of the full-scale undulator TGU40 were performed in the CASPER cryostat (a bad cryostat of KIT). It was measured the vertical component of the magnetic flux density as function of the transverse position at one fixed longitudinal position z in the center of the undulator. The undulator magnetic measurement showed an excellent agreement with the theoretical expectations.

In the near future it is already planned to measure the magnetic field of the TGU40 in its own cryostat (see Section 4.5). This cryostat was not yet available to perform the measurements for this thesis. The magnetic measurement has to be done, before performing the proof-of-principle experiment at the LWFA in Jena with the whole setup, chicane and TGU40. The magnetic measurement system must be removed in order to perform the experiment with the beam passing the undulator.

The measurement will be performed within the horizontal cryostat as is shown in Figure 6.25, at liquid Helium temperature and in high vacuum. The same Hall probe array as described in this thesis will measure the magnetic field, but this time not in a fixed longitudinal position, in the center of the undulator, but scanned along the z-direction.

The Hall probe array will be fixed to the shaft of a transfer rod (VACOM). This shaft will allow a translation without rotation of the Hall probe along the z-axis (see detail in Figure 6.26). The movement of the probe will be controlled with a side mounted stepper motor with a resolution of the probe position of 2 μm. The maximal z-stroke of the linear movement is 609 mm.

With these measurements along the z-direction will be detect field errors due to mechanical deviations or failures in the construction of the undulator coil formers (see Section 4.3), which can not be detect at one fixed longitudinal position z.

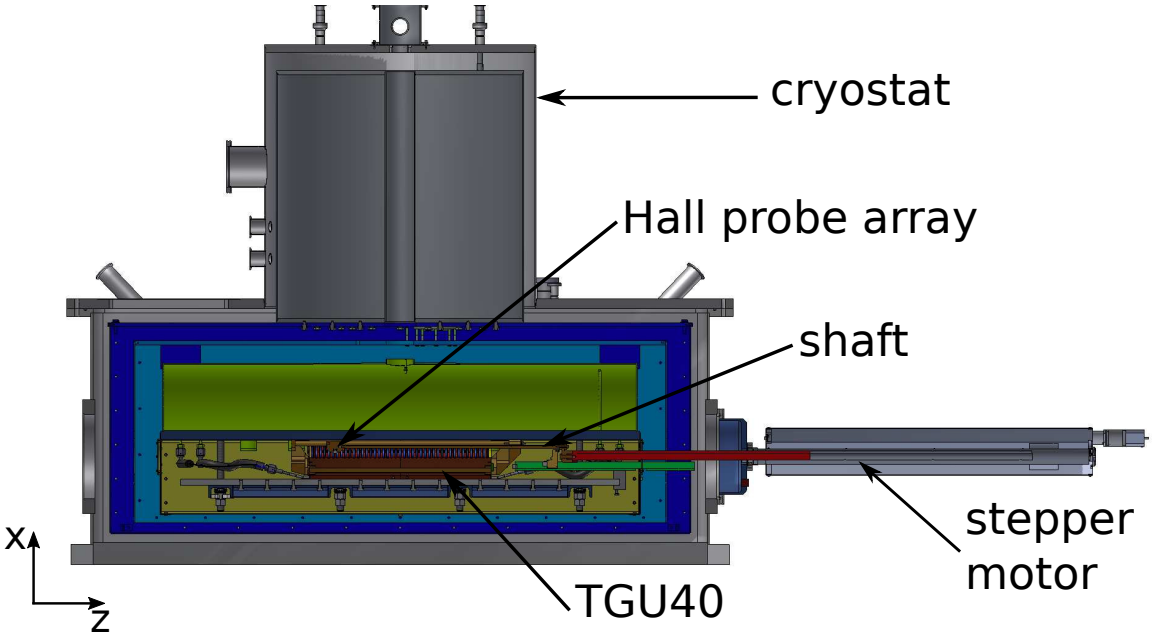

Figure 6.25: Magnetic measurement system tailored for the horizontal cryostat and with an external stepper motor, which moves the Hall probe array along the TGU40 [61].

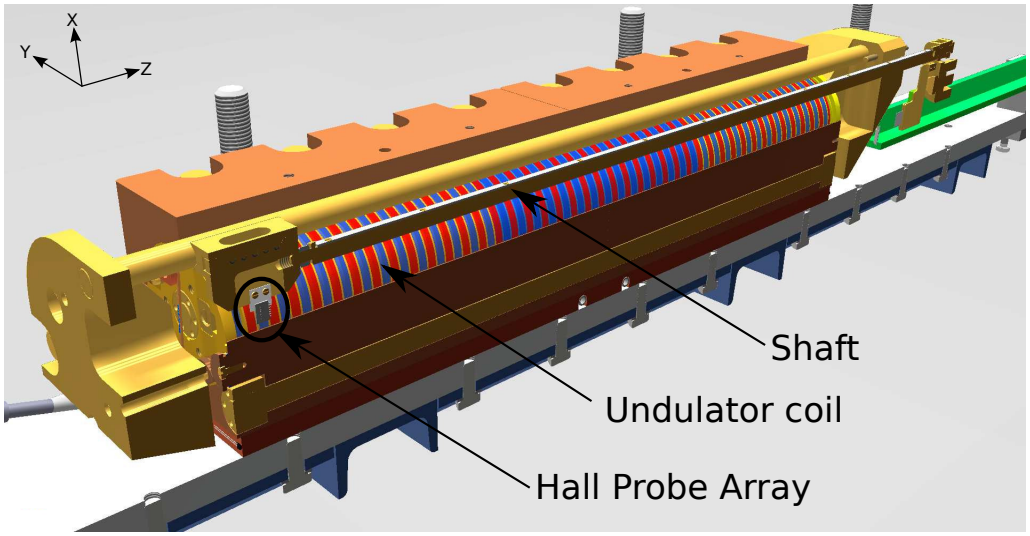

Figure 6.26: Detail of the Hall probe array and the shaft for the magnetic measurement system through the TGU40 with a 1/2 is cut off for better visibility [61].

7. Conclusion

This thesis includes the design, optimization, part of the construction and the characterization of a novel transverse gradient undulator (TGU). The TGU design proposed in this thesis is optimized for an electron energy of $E_0 = 120\,\mathrm{MeV}$ and an energy spread of $\delta = \pm 10\,\%$. These electron beam properties of the laser wakefield accelerator (LWFA) at the University in Jena were conservatively assumed. The relatively high energy spread has to be compensated to achieve a very compact X-ray radiation source combining the LWFA with the short-period TGU. Compact radiation sources based on LWFA have a number of advantages over conventional X-ray sources. Laser-based accelerators imply a large reduction in infrastructure, particularly in size and cost.

A way to perform the compensation of the high energy spread is through a magnetic chicane which spectrally disperses the electron beam in the deflection plane (xz-plane). The electrons with spatial energy distribution travel in z-direction through the TGU which offers a x-dependent flux density amplitude. A constant wavelength of the emitted undulator radiation is achieved when the transversal field gradient matches the spatial energy distribution. Therefore, optimizations were conducted on the TGU and the chicane parameters to achieve a bandwidth of the undulator radiation in the order of the natural bandwidth. For a 100 periods TGU, this condition is $\Delta\lambda/\lambda \approx 1\,\%$.

A summary of the achievements performed during the course of this thesis are the following:

- A TGU with cylindrical pole face geometry was identified using analytical and numerical methods.

  The selection was made by comparing the results between two different TGU geometries, tilted and cylindrical. With the optimization of both TGU models, the main objective of getting a constant wavelength of the undulator radiation $\Delta\lambda/\lambda < 1\,\%$ was highly achieved. In this study different values of the reference electron energy and period length were taken into account. The tilted TGU was discarded because of the total dispersive beam splitting being too large

($> 10\,\mathrm{mm}$). In contrast, the total dispersive beam splitting for the different optimized cylindrical TGU models was around $\pm\ 2\,\mathrm{mm}$.

- Simulations of the TGU magnetic field and the electron trajectories were performed.

  The simulated magnetic field was employed to calculate the undulator radiation and the electron trajectories through the undulator. The results showed that the transversal field gradient of the undulator produces a net deflection of the electrons moving along the axis of the undulator. The resulting transverse drift in the electron position compared with the position before moving into the device was compensated in the simulations by a superposed weak correction field ($\approx -0.5\,\mathrm{mT}$). A couple of long racetrack superconducting (SC) coils installed inside and along the TGU were selected to compensate the electron trajectories drifts.

- Simulations of the iron saturation were performed and the material for the TGU construction was chosen.

  The modulus of the magnetic field of several TGU iron (low carbon steel AISI 1010) models with different pole configurations were simulated. It is necessary to ensure that the weak correction field is not screened by unsaturated soft magnetic material. Only the case of the model with iron pole insets showed the full saturation at $B_{min} = 2.13\,\mathrm{T}$. But this configuration was technically very challenging and therefore an iron-free design was chosen for the cylindrical TGU. The coil formers and their support structure were made of copper (CU OF - DIN 2.0040). Simulations of the copper cylindrical TGUs were performed to obtain the geometrical parameters of the optimized model, including the coil-pole structure and the coil support structure. The main undulator parameters were selected: period length $\lambda_\mathrm{u} = 10.5\,\mathrm{mm}$, pole radius $\mathrm{r} = 30\,\mathrm{mm}$ and gap on axis $\mathrm{g} = 1.1\,\mathrm{mm}$.

- The short TGU models were investigated, including their manufacture, the winding coils and prototypes were characterized.

  Before the construction of the full-scale TGU coil former, a short model with one half period and two short models with two periods (TGU2) were constructed. The short models were employed to prove the undulator geometry and the winding technique that could be scaled up for the longer TGU. The magnetic fields at the TGU2 models along the longitudinal position z and along the transversal position x were measured by a Hall-probe-array of 7 Hall-probes. The measurement showed an excellent agreement with the theoretical expectations. The test of the short models was performed at KIT in a vertical cryostat at KIT called CASPER (Characterization Setup for Field Error Reduction) at $4.2\,\mathrm{K}$.

- The full-scale TGU was described, including its manufacture, the undulator coils winding and its support structure.

  For the proof-of-principle experiment a full-scale prototype of the TGU with 40 periods (TGU40) was built at KIT. A task of this thesis was to perform the winding of the NbTi SC coils of both the TGU40 and the correction coils. This was made in the Laboratory for Application of Synchrotron Radiation

(LAS) at KIT. A bolted clamping structure was selected to support the coil assembly. This structure defines the magnetic gap of the TGU40, applies compressive prestressing to the outer parts of the racetrack coils and takes up the magnetic forces acting on the undulator coils as a whole.

- Characterization of the full-scale TGU.

  A first magnetic field measurement of the full-scale TGU40 was performed. The same Hall-probe-array as used in the short models measurements was employed. This test was also implemented in the liquid helium bath cryostat CASPER at KIT. Therefore, for technical reasons, only the transversal field gradient was measured in the center of the undulator in a fixed z position. The measuring range was adapted within the area of x between 4 mm and 10 mm, which defines the electron beam positions dispersed by the chicane. Both the undulator and the correction coils were tested, first together, then each one separately and finally in series. In the case of the undulator coils, the magnetic field was measured over long periods of time at the operating current 750 A. The magnetic measurements showed an excellent agreement with the simulations. The operating current is 83 % of the measured quench current ($\approx$ 890 A), providing a sufficient safety margin.

In conclusion, the work done in this thesis not only provides simulations and the optimization of a undulator with a transversal magnetic field. Furthermore, it is the first time that a full-scale TGU with a cylindrical geometry and with a short period length of about 1 cm is constructed with the aim to create in a future a very compact high-brilliance radiation source with a laser wakefield accelerator. The first tests with the short models and the full-scale TGU show that the concept is feasible and the designs goals have been reached.

During the technical design of the TGU, the coil geometry form chosen was the antisymmetrical shape with an undesired magnetic flux density component B_x. This results in an extra drift of the electron trajectories in the yz-plane, which did not occur with the cylindrical form. In a future TGU design it might nevertheless be better to avoid these unwanted uncompensated fields, i.e. alternative winding schemes should be evaluated.

The first measurements of the magnetic field exhibit transients with relatively long time constants due to short circuits to ground and between turns of the superconducting coils. The deviation of the measurements of the undulator coils in series are eventually subject to systematic errors. To investigate this, the future measurements should be performed over a longer period of time.

Not all the aspects of the characterization of the TGU40 could be treated in this thesis, mainly because of limited funding and scheduling constraints. It is already planned in the near future some improvements in the next measurements. That includes 2D spatially resolved magnetic measurements as soon as the TGU's own cryostat is available and eventually a proof-of-principle experiment at the LWFA in Jena once all components (particularly beam transport system) are realized.

Appendices

A. Cylindrical undulator C++ code files

A.1 Optimization: Downhill Simplex Method

The downhill simplex algorithm was invented by Nelder and Mead [77]. This algorithm is a method to find the minimum of a function with more than one independent variable. This method only requires function evaluations, no derivatives.

A simplex is a geometrical figure in n-dimensional space with $n+1$ vertices connected by straight lines and bounded by polygonal faces. The number of independent parameters that need to be optimized in order to minimize the value of a function is represented for the dimension of the space. The simplex is a n by $n+1$ matrix, where each column is a vector of size n in n-dimensional space [78].

In this thesis the algorithm is used to minimize the function $\Delta\lambda/\lambda_0$. Section 3.2.1 shows the parameters that need to be optimized according to the geometry of TGU, either tilted or cylindrical. In both cases the final number of the selected parameters was $n = 2$ and the simplex was a triangle. In this case the simplex algorithm was based on the idea of comparing the values of the objective function at the 3 vertices of the triangle in 2-dimensional space. The goal was to minimize the target function $f(X_1) < f(X_2) < f(X_{n+1})$, where $X_{n+1} = X_w$ was the worst point with the highest value and X_1 was the best point with the lowest value. The algorithm iteratively updates the worst point X_w moving the triangle towards the minimum point X_1 [78].

The movement of the triangle towards the minimum point is achieved through four different operations (see Figure A.1), which are listed next:

- Reflection: a reflected point X_r is obtained when the point X_w reflects through the centroid $\bar{X}$. The reflection distance is controlled by the parameter A.
- Expansion: the simplex expands toward the newly found reflected point X_r, if this X_r is better than the existing best point X_1. This expanded point is called X_e and the distance expansion is controlled by the parameter G.

- Contraction: if the reflected point X_r is no better than the existing best point X_1, then the simplex contracts from the worst point X_w towards the centroid $\bar{X}$. This contracted point is called X_c and the distance expansion is controlled by the parameter B.

- Multiple contraction: if the newly found reflected point X_r is worse than the existing worst point X_w, then the simplex contracts along all dimensions toward the existing best point X_1 whose distance is controlled by the parameter H.

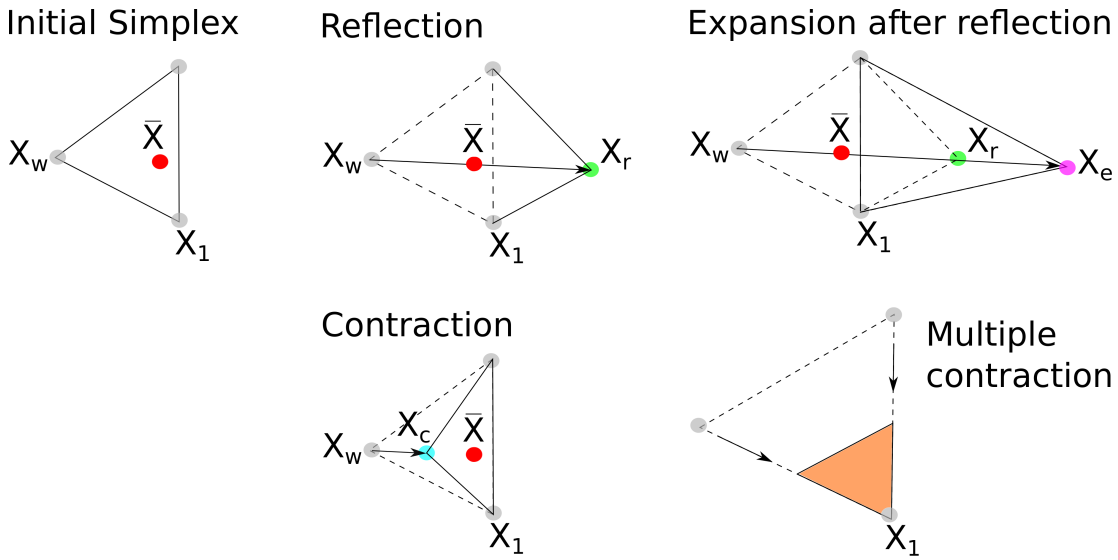

Figure A.1: Allowed moves of a simplex in the 2-dimensional space.

The optimal solution of X_1, and with it the optimal value of the parameters, is found by iterating the above four actions. Figure A.2 shows the simplex algorithm flowchart. The algorithm terminates when it is within a given tolerance ε [77].

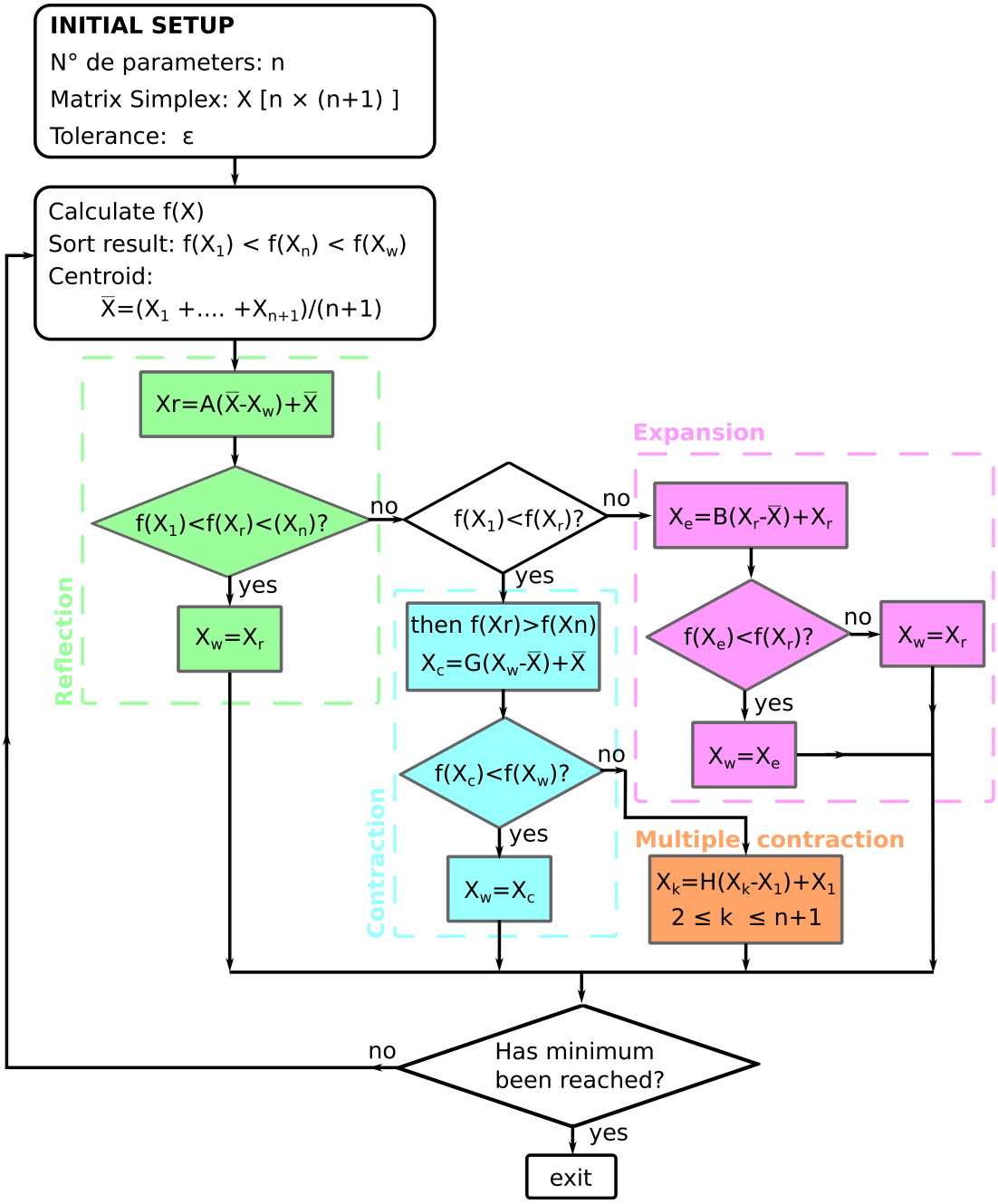

Figure A.2: Simplex algorithm flowchart.

- Main code file: *SCU_tamoeba_optparam_l2_Bymax_vDec*2014*.cpp*

```
/*********************************************************
*   Multidimensional minimization of a function FUNC(X)   *
*  where X is an NDIM-dimensional vector, by the downhill *
*  simplex method of Nelder and Mead.                     *
* ------------------------------------------------------- *
* REFERENCE: "Numerical Recipes, The Art of Scientific    *
*             Computing By W.H. Press, B.P. Flannery,     *
*             S.A. Teukolsky and W.T. Vetterling,         *
*             Cambridge University Press, 1986"           *
*             [BIBLI 08].                                 *
*                                                         *
*                     C++ Release By J-P Moreau, Paris.   *
*********************************************************/
#include <iostream>
#include <fstream>
#include <cstring>
#include <sstream>
#include <iomanip>
#include <cstdio>
#include <cmath>
#include <gsl/gsl_sf_bessel.h>
#include "templates.cpp"
#include "SCU_parameter.cpp"
#include "B_cyl_func.cpp"
#include "B_cyl_proto.cpp"
//Maximum value for NDIM=20
#define   MP  22
#define   NP  21
using namespace std;
typedef   double MAT[MP][NP];
MAT P;
double Y[MP], PT[MP], Pmin[MP], Pmax[MP];
// Function propotypes:
double FUNC1(double *P,ofstream &dataout);
double FUNC2(double *P,ofstream &dataout);
double getx0(float rad,float lund,float kund,float g_2);
double getdeltax(float energy,double l1,double l2,double Bch ) ;
void AMOEBA(MAT P,double *Pmin,double *Pmax,double *Y, int NDIM, double
    FTOL, int *ITER,ofstream &dataout);
double getA ( double B_max, float lund, float rad, float kund, float g_2 ) ;
void getan(int ncoef,string filename,double *an);
void getbn(int ncoef,string filename,double *bn);
double FSR_getx0(float rad,float lund,float kund,float g_2,double *an,int
    ncoef, double Bmax0_rel);

int main(void)  {
  Pmin[1]= Pmin1;
  Pmax[1]= Pmax1;
  Pmin[2]= Pmin2;
  Pmax[2]= Pmax2;
  //define NDIM+1 initial vertices (one by row)
  P[1][1]=P1_1;P[1][2]= P1_2; //V1
  P[2][1]=P2_1;P[2][2]= P2_2; //V2
  P[3][1]=P3_1;P[3][2]= P3_2; //V3
  ofstream dataout(filename_dataopt.c_str() ) ;
  if (!dataout){
    cout << "The file could not open." << endl;
    return 1;
  }
  dataout <<"#####################################################"<< endl;
  dataout <<"# Data from SCU_tamoeba_optparam_l2_Bymax_vDec2014.cpp"<< endl;
  dataout <<"# Period length [mm]: "<< lund*1e3 << endl;
  dataout <<"# Half gap width [mm]: "<<  g_2*1e3 << endl;
  dataout <<"# External pole radius  [mm]: "<< rad*1e3  << endl;
  dataout <<"# Central energy [MeV]: "<< energy0/1e6 << endl;
  dataout <<"#####################################################"<< endl;
  dataout <<"# 1. l2 [m]"<< endl;
  dataout <<"# 2. Bymax [T]"<< endl;
```

```
67    if (FUNCx==1){dataout <<"# 3. Min F1(X):
        sum(By_real-By_ideal)^2/(nep+1)"<< endl;}
68    if (FUNCx==2){dataout <<"# 3. Min F2(X): Δλ / λ 0"<< endl; }
69    //Initialize Y to the values of FUNC evaluated
70    //at the NDIM+1 vertices (rows] of P
71    for (I=1; I<=NDIM+1; I++) {
72      PT[1]=P[I][1]; PT[2]=P[I][2];
73       if (FUNCx==1){Y[I]=FUNC1(PT,dataout);}
74       if (FUNCx==2){Y[I]=FUNC2(PT,dataout);}
75    }
76    //call main function
77    AMOEBA(P,Pmin,Pmax,Y,NDIM,FTOL,&ITER,dataout);
78    //print results
79    printf("\n Number of iterations: %d\n\n", ITER);
80    printf(" Best NDIM+1 points:\n");
81    for (I=1 ; I<=NDIM+1; I++) {
82      for (J=1; J<=NDIM; J++)  printf("  %f", P[I][J]);
83        printf("\n");
84    }
85    printf("\n Best NDIM+1 mimimum values:\n");
86    for (I=1; I<=NDIM+1; I++) printf(" %14.10f\n", Y[I]);
87    printf("\n");
88
89    dataout<<"# Number of iterations:"<< ITER<<endl;
90    dataout<<"# Best NDIM+1 points:"<< endl;
91    for (I=1 ; I<=NDIM+1; I++) {
92      for (J=1; J<=NDIM; J++)  dataout<<"# "<<P[I][J]<< endl;
93    }
94    dataout<<"# Best NDIM+1 mimimum values:"<< endl;
95    for (I=1; I<=NDIM+1; I++) dataout<<"# "<<Y[I]<< endl;
96    dataout.close() ;
97  }
98  //-------------------------------------------------------------
99  // user defined function to minimize
100 double FUNC1(double *P,ofstream &dataout) {
101   double datachi[(nep+1)];
102   x0=getx0(rad,lund,kund,g_2);
103   deltax0=getdeltax(energy0,l1,P[1],Bch);
104   r[0]=x0,r[1]=0,r[2]=-z;
105   A=getA(P[2],lund,rad,kund,g_2);
106   B_E0=By(rad,kund,g_2,A,r);
107   K0=B_E0*abs(e)/(m0*c)/kund;
108   lambda0=(lund/(2*square(gamma0)))*(1+(square(K0)/2));
109
110   for (int i=0;i <=nep;i++){
111     energy = energy0 +(delE - i*2*delE/nep);
112     gammaE=energy/511e3;
113      deltax=getdeltax(energy,l1,P[1],Bch);
114      xund=deltax+(x0-deltax0);
115      K_ideal=sqrt(2*((lambda0*2*square(gammaE)/lund)-1));
116      B_ideal=(K_ideal*m0*c*2*pi)/(abs(e)*lund);
117      r[0]=xund,r[1]=0,r[2]=-z;
118      B_real=By(rad, kund, g_2, A, r);
119      datachi[i]=square(B_real-B_ideal);
120   }// end for energy
121
122   double sum =0;
123   for (int i=0;i<=nep;i++){
124     sum=sum+datachi[i];
125   }
126   cout <<"sum: "<< sum<<endl;
127   double chisquare=sum/(nep+1);
128
129   dataout<<fixed << setprecision(6) << P[1]<< "\t" << P[2]<< "\t" ;
130   dataout<<fixed << setprecision(10) <<chisquare<< endl;
131   return chisquare;
132 }
133
134 double FUNC2(double *P,ofstream &dataout) {
135   double lambda_array[(nep+1)];
136   double an[ncoef];
137   double bn[ncoef];
138   getan(ncoef,filename_fourier,an);
139   getbn(ncoef,filename_fourier,bn);
```

```
140   r[0]=0,r[1]=0,r[2]=-z;
141   Bmax0=FSR_By(rad, kund, g_2, r,an,ncoef);
142   Byrel=FSR_Byrel(rad, kund, g_2, r,an,ncoef,Bmax0);
143   Bmax0_rel=P[2]*Byrel;
144   x0=FSR_getx0(rad,lund,kund,g_2,an,ncoef,Bmax0_rel);
145   deltax0=getdeltax(energy0,l1,P[1],Bch);
146   r[0]=x0,r[1]=0,r[2]=-z;
147   B_E0=P[2]*FSR_Byrel(rad, kund, g_2, r,an,ncoef,Bmax0);
148   K0=B_E0*abs(e)/(m0*c)/kund;
149   lambda0=(lund/(2*square(gamma0)))*(1+(square(K0)/2));
150
151   for (int i=0;i<=nep;i++){
152     energy = energy0 +(delE - i*2*delE/nep);
153     gammaE=energy/511e3;
154     deltax=getdeltax(energy,l1,P[1],Bch);
155     xund=deltax+(x0-deltax0);
156     r[0]=xund,r[1]=0,r[2]=-z;
157     B_real=P[2]*FSR_Byrel(rad, kund, g_2, r,an,ncoef,Bmax0);
158     K_real=B_real*abs(e)/(m0*c)/kund;
159     lambreal=(lund/(2*square(gammaE)))*(1+(square(K_real)/2));
160     lambda_array[i]=lambreal*1e9;
161   }// end for energy
162
163   minL = maxL = lambda_array[0];
164   for (int i=0; i<=nep; i++) {
165     if ( lambda_array[i] < minL ) minL = lambda_array[i];
166     if ( lambda_array[i] > maxL ) maxL = lambda_array[i];
167   }
168
169   dataout<<fixed << setprecision(10) << P[1]<< "\t" << P[2]<< "\t" ;
170   dataout<<fixed << setprecision(10) <<((maxL-minL)/(lambda0*1e9))*100<<
        endl;
171   return ((maxL-minL)/(lambda0*1e9))*100;
172 }
173
174 double getx0(float rad,float lund,float kund,float g_2){
175   double A_i=1;
176   double r0[3]={0,0,z};
177   const double B0=By(rad, kund, g_2, A_i, r0);
178   int nix(0);
179   double nextxu(0),nextBy(0), nextdBy(0);
180   double x0(0);
181   double By_xu(0),dBy_dxu(0);
182
183   for (double ix=0; ix <= rad*1000; ix+=0.000001 ){
184
185     r0[0]=ix/1000;//in Meter
186     By_xu=By(rad, kund, g_2, A_i, r0)/B0; //normiert By_xu
187
188       if (nix>0){
189   dBy_dxu=(By_xu-nextBy)/(r0[0]-nextxu);
190    if (nix>1){
191      if(dBy_dxu < nextdBy) x0 = r0[0];
192    }
193   nextdBy=dBy_dxu;
194       }
195     nextxu=ix/1000;
196     nextBy=By_xu;
197     nix++;
198   }
199   return x0;
200 }
201
202 double getA (double B_max, float lund, float rad, float kund, float g_2 ) {
203   double A_i = 1 ;  // first value
204   double test_r[3] = { 0.0000001, 0, z}  ;
205   double A = B_max / By(rad, kund, g_2, A_i, test_r) ;
206   return A ;
207 }
208
209 double getdeltax ( float energy,double l1,double l2,double Bch ){
210   double gamma = energy/511e3 ;
211   double rhoL = abs(m0*c/(e*Bch));
212   double rL = gamma*rhoL;
```

```
213   double deltax=
        2*rL-(2*sqrt(pow(rL,2)-pow(l1,2)))+(l1*l2/sqrt(pow(rL,2)-pow(l1,2)));
214   return deltax;
215 }
216
217 void getan(int ncoef,string filename,double *an){
218   int row=ncoef;
219   int col=3;
220   double matfourier[row][col];
221   short loop=0;
222   char col0[250],col1[250],col2[250]; //read data from the file
223   string header;
224   ifstream myfile (filename.c_str() ); //opening the file
225   if (myfile.is_open()){
226     getline (myfile,header); //get first line from the file=header
227     while (! myfile.eof() && loop!=ncoef){
228       myfile.getline (col0,256,' '); //get one line from the file
229       myfile.getline (col1,256,' ');
230       myfile.getline (col2,256);
231       matfourier[loop][0]=strtod(col0,NULL);
232       matfourier[loop][1]=strtod(col1,NULL);
233       matfourier[loop][2]=strtod(col2,NULL);
234       loop++;
235     }
236     myfile.close(); //closing the file
237   }else cout << "Unable to open file";
238
239   for (int ian=0;ian<row;ian++){
240     an[ian]=matfourier[ian][1];
241   }
242 }
243
244 void getbn(int ncoef,string filename,double *bn){
245   int row=ncoef;
246   int col=3;
247   double matfourier[row][col];
248   short loop=0;
249   char col0[250],col1[250],col2[250];
250   string header;
251   ifstream myfile (filename.c_str() );
252   if (myfile.is_open()){
253     getline (myfile,header);
254
255     while (! myfile.eof() && loop!=ncoef){
256       myfile.getline (col0,256,' ');
257       myfile.getline (col1,256,' ');
258       myfile.getline (col2,256);
259       matfourier[loop][0]=strtod(col0,NULL);
260       matfourier[loop][1]=strtod(col1,NULL);
261       matfourier[loop][2]=strtod(col2,NULL);
262       loop++;
263     }
264   myfile.close(); //closing the file
265   }else cout << "Unable to open file";
266
267   for (int ibn=0;ibn<row;ibn++){
268     bn[ibn]=matfourier[ibn][2];
269   }
270 }
271
272 double FSR_getx0(float rad,float lund,float kund,float g_2,double *an, int
      ncoef, double Bmax0_rel){
273   const double B0=Bmax0_rel;
274   double r0[3]={0,0,-lund/4};
275   int nix(0);
276   double nextxu(0),nextBy(0), nextdBy(0);
277   double x0(0);
278   double By_xu(0),dBy_dxu(0);
279
280   for (double ix=0; ix <= rad; ix+=0.000001 ){
281     r0[0]=ix;//in Meter
282     By_xu=FSR_By(rad, kund, g_2, r0,an,ncoef)/B0;
283     if (nix>0){
284       dBy_dxu=(By_xu-nextBy)/(r0[0]-nextxu);
```

```
285         if (nix>1){
286     if(dBy_dxu < nextdBy) x0 = r0[0];
287         }
288         nextdBy=dBy_dxu;
289       }
290       nextxu=ix;
291       nextBy=By_xu;
292       nix++;
293     }
294     return x0;
295 }
296
297 void AMOEBA(MAT P, double *Pmin,double *Pmax,double *Y, int NDIM, double
      FTOL, int *ITER,ofstream &dataout) {
298     /*-------------------------------------------------------------------
299     ! Multidimensional minimization of the function FUNC(X) where X is
300     ! an NDIM-dimensional vector, by the downhill simplex method of
301     ! Nelder and Mead. Input is a matrix P whose NDIM+1 rows are NDIM-
302     ! dimensional vectors which are the vertices of the starting simplex
303     ! (Logical dimensions of P are P(NDIM+1,NDIM); physical dimensions
304     ! are input as P(NP,NP)). Also input is the vector Y of length NDIM
305     ! +1, whose components must be pre-initialized to the values of FUNC
306     ! evaluated at the NDIM+1 vertices (rows) of P; and FTOL the fractio-
307     ! nal convergence tolerance to be achieved in the function value. On
308     ! output, P and Y will have been reset to NDIM+1 new points all within
309     ! FTOL of a minimum function value, and ITER gives the number of ite-
310     ! rations taken.
311     !-------------------------------------------------------------------*/
312     // Label: e1
313     const int NMAX=20, ITMAX=5000;
314     //Expected maximum number of dimensions, three parameters which define
315     // the expansions and contractions, and maximum allowed number of
316     //iterations.
317     double PR[MP], PRR[MP], PBAR[MP];
318     double ALPHA=1.0, BETA=0.5, GAMMA=2.0; //H=0.5 for multiple contraction
319     int I,IHI,ILO,INHI,J,MPTS;
320     double RTOL,YPR,YPRR;
321     MPTS=NDIM+1;
322     *ITER=0;
323     e1:ILO=1;
324     if (Y[1] > Y[2]) {
325       IHI=1;
326       INHI=2;
327     }else {
328       IHI=2;
329       INHI=1;
330     }
331     for (I=1; I<=MPTS; I++) {
332       if (Y[I] < Y[ILO])  ILO=I;
333       if (Y[I] > Y[IHI]) {
334         INHI=IHI;
335         IHI=I;
336       }else if (Y[I] > Y[INHI])
337       if (I != IHI)  INHI=I;
338     }
339     //Compute the fractional range from highest to lowest and return if
340     //satisfactory.
341     RTOL=2.0*fabs(Y[IHI]-Y[ILO])/(fabs(Y[IHI])+fabs(Y[ILO]));
342     if (RTOL < FTOL)  return;  //normal exit
343     if (*ITER == ITMAX) {
344       printf(" Amoeba exceeding maximum iterations.\n");
345       return;
346     }
347     *ITER= (*ITER) + 1;
348     // 1.-Reflection:
349     for (J=1; J<=NDIM; J++)  PBAR[J]=0.0;
350       for (I=1; I<=MPTS; I++)
351         if (I != IHI)
352     for (J=1; J<=NDIM; J++)
353       PBAR[J] += P[I][J];
354     for (J=1; J<=NDIM; J++) {
355       PBAR[J] /= 1.0*NDIM;
356       PR[J]=(1.0+ALPHA)*PBAR[J] - ALPHA*P[IHI][J];
357     }
```

```
358   while (PR[1]<Pmin[1]){ for (J=1;J<=NDIM;J++) PR[J]=BETA*PR[J] +
        (1.0-BETA)*PBAR[J];}
359   while (PR[2]<Pmin[2]){ for (J=1;J<=NDIM;J++) PR[J]=BETA*PR[J] +
        (1.0-BETA)*PBAR[J];}
360   while (PR[1]>Pmax[1]){ for (J=1;J<=NDIM;J++) PR[J]=BETA*PR[J] +
        (1.0-BETA)*PBAR[J];}
361   while (PR[2]>Pmax[2]){ for (J=1;J<=NDIM;J++) PR[J]=BETA*PR[J] +
        (1.0-BETA)*PBAR[J];}
362   if (FUNCx==1){YPR=FUNC1(PR,dataout);}
363   if (FUNCx==2){YPR=FUNC2(PR,dataout);}
364   //end of reflexion
365   // 2.-Expansion:
366   if (YPR <= Y[ILO]) {//Is Yr < Ymin ?
367     for (J=1; J<=NDIM; J++)
368       PRR[J]=GAMMA*PR[J] + (1.0-GAMMA)*PBAR[J]; //Calculate Expansion Xe
369     while (PRR[1]<Pmin[1]){ for (J=1;J<=NDIM;J++) PRR[J]=PR[J];}
370     while (PRR[2]<Pmin[2]){ for (J=1;J<=NDIM;J++) PRR[J]=PR[J];}
371     while (PRR[1]>Pmax[1]){ for (J=1;J<=NDIM;J++) PRR[J]=PR[J];}
372     while (PRR[2]>Pmax[2]){ for (J=1;J<=NDIM;J++) PRR[J]=PR[J];}
373     if (FUNCx==1){YPRR=FUNC1(PRR,dataout);}
374     if (FUNCx==2){YPRR=FUNC2(PRR,dataout);}
375     // end of expansion
376     if (YPRR < Y[ILO]) {
377       for (J=1; J<=NDIM; J++) P[IHI][J]=PRR[J]; //Accept Expansion: Xmax = Xe
378       Y[IHI]=YPRR;
379     }else {
380       for (J=1; J<=NDIM; J++) P[IHI][J]=PR[J]; //Accept Reflection: Xmax = Xr
381       Y[IHI]=YPR;
382     }
383   }//end if not Yr < Ymin
384   else if (YPR >= Y[INHI]) {//Is Yr >=Yi? yes
385     if (YPR < Y[IHI]) {// Is Yr < Ymax? yes
386       for (J=1; J<=NDIM; J++)  P[IHI][J]=PR[J]; // Xmax (temp)= Xr
387       Y[IHI]=YPR;
388   }
389   // 3.-Contraction:
390   for (J=1; J<=NDIM; J++)  PRR[J]=BETA*P[IHI][J] + (1.0-BETA)*PBAR[J];
       //Calculate contraction Xc
391     if (FUNCx==1){YPRR=FUNC1(PRR,dataout);} //Calculate Yc
392     if (FUNCx==2){YPRR=FUNC2(PRR,dataout);}
393   if (YPRR < Y[IHI]) { //Is Yc < Ymax? yes
394     for (J=1; J<=NDIM; J++)  P[IHI][J]=PRR[J];//Accept contraction: Xmax = Xc
395       Y[IHI]=YPRR;
396   }
397   // end of Contraction
398   // 4.-Multiple contraction:
399   else //no
400     for (I=1; I<=MPTS; I++)
401       if (I != ILO){cout << "4.-Multiple contraction without bounded
        variables:  "<< endl;
402   for (J=1; J<=NDIM; J++) {PR[J]=0.5*(P[I][J] + P[ILO][J]); }
403   for (I=1; I<=MPTS; I++)
404   for (J=1; J<=NDIM; J++) { P[I][J]=PR[J]; }//corrected
405     if (FUNCx==1){Y[I]=FUNC1(PR,dataout);} //Calculate Yc
406     if (FUNCx==2){Y[I]=FUNC2(PR,dataout);} //Calculate Yc
407       }
408   // end of Multiple contraction
409   }else {//Is Yr >=Yi? No
410     for (J=1; J<=NDIM; J++)  P[IHI][J]=PR[J]; //Accept Reflexion: Xmax=Xr
411       Y[IHI]=YPR;
412     }
413   goto e1;
414 }
```

- Templates file: *templates.cpp*

```
1 template <class T> T square(const T& x) { return x*x ; }
2 template <class T> T abs(T x) { x= x<0 ? -x : x ; return x ; }
3 template <typename T> int sgn(T val){return (val > T(0)) - (val < T(0));}
```

- Declaration of global variables: *SCU_parameter.cpp*

```
//declaration of values (Global variables)
#include "SCU_parameter.h"
#include <cstring>
using namespace std;
//Tamoeba variables:
int I;
int ITER=0;
int J;
int NDIM=2;//number of parameters to optimize: P[1]= l2 and P[2]=ang.
double FTOL=1e-8;//tolerance
//Constants:
const float pi=3.141592653;
const float m0=9.11e-31;
const float e=-1.602e-19;
const float c=299792458;//in m/s
// Choose function to minimize:
// FUNCx=1 ;Min F(X)=sum(By_real-By_ideal)^2/(nep+1)
// FUNCx=2 ;Min F(X)=Deltalambda/lambda0
int FUNCx=2;
//Parameter 1: l2 [m]
double Pmin1= 0;
double Pmax1= 5;
double P1_1=0.2;
double P2_1=1.2;
double P3_1=0.6;
//Parameter 2: Bymax [T]
double Pmin2=0.5;
double Pmax2=4.0;
double P1_2= 1.8;
double P2_2= 1.2;
double P3_2= 0.6;
float energy0 = 120e6;  // Central energy [eV]
double gamma0 = energy0/511e3;
float delE = energy0*10/100; //Energy spread[%]
string filename_dataopt=
    "SCU_120MeV_lper10mm_gap1p5_optparam_l2_Bymax_vDec2014_fmin2.dat";
float energy=0;
double gammaE=0;
int nep=10; //energy points to calculate
//Undulator geometry
float lund = 0.010; // period length[m]
float kund=2*pi/lund;
float g_2=0.0015/2;//half gap-width on axis
float rad=0.030; //external pole-radius
double l1=0.050; // chicane dipole: pole width [m]
double Bch=0.46; // chicane dipole: homogeneous field  [T]
double r[3]={0,0,0};
double z = lund/4; //center of the pole in z-direction
//For the central energy:
double x0=0;
double A=0;
double deltax0=0;
double B_E0=0;
double K0=0;
double lambda0=0;
//For the other energies:
double deltax=0;
double xund=0;
double K_ideal=0;
double B_ideal=0;
double B_real=0;
//Function F2(X)
int ncoef=15;
string filename_fourier = "FSR_rad30_gap1and5_lund10_J800.txt";
double Bmax0=0;
double Byrel=0;
double Bmax0_rel=0;
double minL=0;
double maxL=0;
```

```
69 double K_real=0;
70 double lambreal=0;
71 //End Optimization
72 string filename;
73 //Model_DataBank_Eisen: rad30,g1p5, lper10, Jca800, FSRJ1200
74 // Solution OPtimization:  f2(X)=Δλ/λ0 = 0.5155089%
75 double l2_opt=0.311675;
76 double Bymax_opt=1.743912;
77 string filename_summary =
       "SCU_By_Lambda_vDec2014_120MeV_lper10mm_gap1p5_rad30_summary.dat";
78 string filename_Esigmax  =
       "SCU_By_Lambda_vDec2014_120MeV_lper10mm_gap1p5_rad30_Esigmax.dat";
79 string filename_xByall =
       "SCU_By_Lambda_vDec2014_120MeV_lper10mm_gap1p5_rad30_xByall.dat";
80 string filename_zByall =
       "SCU_By_Lambda_vDec2014_120MeV_lper10mm_gap1p5_rad30_zByall.dat";
81 string filename_xELambda =
       "SCU_By_Lambda_vDec2014_120MeV_lper10mm_gap1p5_rad30_xELambda.dat";
82 double dDxarray[3]={0,0,0};
83 const int n=nep+1;
84 double lambda_array[11];
85 double sigma_array[11];
86 double sigmax_E=0;
87 //Sigma
88 double minsg;
89 double deltxc=0;
90 double xundmin=0;
91 double B_realmin=0;
92 double Krealmin=0;
93 double lambrealmin=0;
94 double xundmax=0;
95 double B_realmax=0;
96 double Krealmax=0;
97 double lambrealmax=0;
98 double xmax=30;
99 double zmax=lund*1e3;
100 //-----------------------------------------------
101 //Trajectories: comment first all the parameters above
102 double l1=50; //in mm
103 double l2=0;
104 double Bch=0.46;
105 //Undulator Geometry:
106 float rad=30; //in mm
107 float  g_2 = 1.5/2;//in mm
108 float lund = 10;//in mm
109 float kund=(2*pi/lund);
110 //Undulator Period:
111 int Nper=100; //number of undulator periods
112 //Cyl_Eisen_Databank_r30_g1p5_lu10_J800
113 double B_max =1.74128007955;
114 int ncoef=15;//Fourier coefficients:
115 double an[15];
116 double bn[15];
117 string filename_fourier= "FSR_rad30_gap1and5_lund10_J800.txt";
118 //Calculate x0:
119 double x0(0);
120 //Calculate l2 optimal:
121 int l2min=0; //Minimum value in mm
122 int l2max=1200;//Maximum value in mm
123 double l2opt(0);
124 //Calculate lambda_E0
125 float energy0 = 120e6; //Electron energy[eV]
126 double gamma0 (energy0/511e3) ;
127 double deltax0(0);
128 double B_E0(0);
129 double K0(0);
130 double lambdal0(0);
131 //Trajectory parameters:
132 int nep=10;//Anzahl der berechneten Energiepunkte
133 float energy(0);
134 double gammaE(0);
135 //Calculate x_E:
136 double deltax(0);
137 double xund(0);
```

```
138 const int n=nep+1; // number of elements in the array
139 double x_array[11];
140 double dDxarray[3]={0,0,0};
141 //Calculate lambda_E:
142 double B_real(0);
143 double Kreal(0);
144 double lambreal(0);
145 double lambda_array[11];
146 double min(0), max(0);
147 double minsg;
148 //Calculate sigma
149 double sigma_array[11];
150 double deltxc(0);
151 double xundmin(0);
152 double B_realmin(0);
153 double Krealmin(0);
154 double lambrealmin(0);
155 double xundmax(0);
156 double B_realmax(0);
157 double Krealmax(0);
158 double lambrealmax(0);
159 float delE = energy0*10/100; //Energy spread[%]
160 float tof =1e-16; //time step[s]
161 double r[3]={0,0,0}; //Point to calculate the field
162 double v[3]={0,0,0};
163 double B[3]={0,0,0};
164 double unitvecB[3]={0,0,0};
165 double F_l[3]={0,0,0};
166 double v_tmax(0), v_p(0);
167 double vec_v_perp[3]={0,0,0};
168 double vec_v_par[3]={0,0,0};
169 double v_perp(0), v_par(0);
170 double omega_c(0), r_l(0); // Cyclotronfrequenz und Larmorradius
171 double guiding_center[3]={0,0,0};
172 double auxiliary_calculation[3]={0,0,0};
173 double e1[3]={0,0,0};
174 double e2[3]={0,0,0};
175 double e3[3]={0,0,0};
176 double r_p_t[3]={0,0,0};
177 double v_p_t[3]={0,0,0};
178 double del_r[3]={0,0,0};
179 float m_e(0);
180 double Bykorr(0);
181 //Cylindrical Iron N10, databank, r30 g1p5, lu10 J800, fit curve: Korrektur
      (mm/T) f r track in c++
182 double coef_a= -1.33994e-06 ; //[T/mm ] +/- 6.297e-08    (4.7%)
183 double coef_b= 3.8944e-05 ; //  [T/mm ] +/- 1.11e-06     (2.849%)
184 double coef_c= -0.000300096  ; // [T/mm]  +/- 6.349e-06    (2.116%)
185 double coef_d= 0.000246456 ;  // [T] +/- 1.177e-05    (4.776%)
186 double x1c(0),x2c(0),Dxc1(0),x2r(0),x2l(0),z2r(0),z2l(0);
187 int non(0);
188 double Dxc100(0);//in mm
189 double Rlc(0);//in m
190 double BRlc(0);//in T
191 //Amplitude:
192 double xamp(0);
193 double aon(0);
194 //Files:
195 string extension = ".dat" ;
196 string filename;
197 string enerprint;
198 // x,y,z,By and dBy in getx0 subroutine
199 string filename_getx0_ohne= "ohne_Korrektur/getx0";
200 string filename_getx0_mit= "mit_Korrektur/getx0";
201 ofstream dataout_getx0;
202 //x, energy, Byreal
203 string filename_xEBy_ohne = "ohne_Korrektur/By_FSRanalytic" ;
204 string filename_xEBy_mit = "mit_Korrektur/By_FSRanalytic" ;
205 ofstream dataout_xEBy;
206 // E,x1c,x2c,Dx1c,Rlc,Brlc,Dxc10 oder Dxc100
207 string filename_Dx_ohne = "ohne_Korrektur/FSRanalytic_Dxcorrectedno" ;
208 string filename_Dx_mit = "mit_Korrektur/FSRanalytic_Dxcorrectedsd" ;
209 ofstream dataout_Dx;
210 //l2,Dlambda/lambda[%]
```

```
211 string filename_l2opt_ohne = "ohne_Korrektur/l2optimal" ;
212 string filename_l2opt_mit = "mit_Korrektur/l2optimal" ;
213 ofstream dataout_l2opt;
214 //Summary
215 string filename_summ_ohne  = "ohne_Korrektur/FSRsummary" ;
216 string filename_summ_mit  = "mit_Korrektur/FSRsummary" ;
217 ofstream dataout_summ;
218 //x,E,lambda
219 string filename_xElambda_ohne = "ohne_Korrektur/FSR_lambda" ;
220 string filename_xElambda_mit = "mit_Korrektur/FSR_lambda" ;
221 ofstream dataout_xElambda;
222 //sigmax
223 string filename_sigmax_ohne  = "ohne_Korrektur/sigmax" ;
224 string filename_sigmax_mit  = "mit_Korrektur/sigmax" ;
225 ofstream dataout_sigmax;
226 //global_sigmax
227 string filename_globalsigmax_ohne = "ohne_Korrektur/global_sigmax" ;
228 string filename_globalsigmax_mit = "mit_Korrektur/global_sigmax" ;
229 ofstream dataout_globalsigmax;
230 //Energy-x-xamplitude(nach der Korrektur)
231 string filename_xEampl_ohne  = "ohne_Korrektur/Energy_x.txt" ;
232 string filename_xEampl_mit  = "mit_Korrektur/Energy_x_sd.txt" ;
233 ofstream dataout_xEampl;
234 //x, y, z, By for every energy
235 string filename_track_ohne = "ohne_Korrektur/FSRtrack_correctedno_EMeV_" ;
236 string filename_track_mit = "mit_Korrektur/FSRtrack_correctedsd_EMeV_" ;
237 ofstream dataout_track;
238 //Graph Byreal x von 0 bis 30mm
239 string filename_xByall_ohne = "ohne_Korrektur/FSR_Byreal_x_analytic" ;
240 string filename_xByall_mit = "mit_Korrektur/FSR_Byreal_x_analytic" ;
241 ofstream dataout_xByall;
242 //Graph Byreal z von 0 bis 100mm
243 string filename_zByall_ohne = "ohne_Korrektur/FSR_Byreal_z_analytic" ;
244 string filename_zByall_mit = "mit_Korrektur/FSR_Byreal_z_analytic" ;
245 ofstream dataout_zByall;
246 //Others:
247 double lamb0(0),lambplus(0),lambminus(0);
248 double deltx0(0),deltxplus(0),deltxminus(0);
249 double B0_ku(0); //Integral sin(nkuz)
```

- Magnetic field function propotypes: *B_cyl_proto.cpp*

```
1 double Bx ( float rad, float kund, float g_2, double A, double *r ) ;
2 double By ( float rad, float kund, float g_2, double A, double *r ) ;
3 double Bz ( float rad, float kund, float g_2, double A, double *r ) ;
4 double FSR_By ( float rad, float kund, float g_2, double *r,double *an,int
      ncoef);
5 double FSR_Byrel ( float rad, float kund, float g_2,  double *r,double
      *an,int ncoef, double Bmax0 );
6 double getB0 ( float rad, float kund, float g_2,  double *r,double *an,int
      ncoef );
```

- Magnetic field functions: *B_cyl_func.cpp*

```
1 double By ( float rad, float kund, float g_2, double A, double *r ) {
2   double &x = r[0] ;
3   double &y = r[1] ;
4   double &z = r[2] ;
5   // o-Field
6         double rhoo = sqrt(square(x) + square(y-(g_2+rad)) ) ;
7   double phio = atan2 ( (y-(g_2+rad)), x) ;
8                 // Vector of direction
9                 double rox = cos(phio) ;
10                double roy = sin(phio) ;
11    // u-Field
```

```
12          double rhou = sqrt(square(x) + square(y + (g_2 + rad)) ) ;
13    double phiu = atan2 ( (y+(g_2+rad)), x) ;
14                  // Vector of direction
15                  double rux = cos(phiu) ;
16                  double ruy = sin(phiu) ;
17    // o-Field
18          double Brhoo= -A*kund*gsl_sf_bessel_Kn(1,kund*rhoo)*sin(kund*z) ;
19          double Byo = Brhoo*roy ;
20    // u-Field
21          double Brhou= A*kund*gsl_sf_bessel_Kn(1,kund*rhou)*sin(kund*z) ;
22          double Byu = Brhou*ruy ;
23          double By = Byu + Byo ;
24    return By ;
25  }
26
27  double FSR_By ( float rad, float kund, float g_2,  double *r,double *an,int
        ncoef ) {
28    double &x = r[0] ;
29    double &y = r[1] ;
30    double &z = r[2] ;
31    double xn = 0 ;
32    double yn = 0 ;
33    // o-Field
34          double rhoo = sqrt(square(x) + square(y-(g_2+rad)) ) ;
35    double phio = atan2 ( (y-(g_2+rad)), x) ;
36                  // Vector of direction
37                  double rox = cos(phio) ;
38                  double roy = sin(phio) ;
39           //Fourier:
40    double rhoo_n = sqrt(square(xn) + square(yn-(g_2+rad)) ) ;
41    double phio_n = atan2 ( (yn-(g_2+rad)), xn) ;
42    double roy_n = sin(phio_n) ;
43     // u-Field
44          double rhou = sqrt(square(x) + square(y + (g_2+rad) ) );
45    double phiu = atan2 ( (y+(g_2+rad)), x) ;
46                  // Vector of direction
47                  double rux = cos(phiu) ;
48                  double ruy = sin(phiu) ;
49          //Fourier:
50    double rhou_n = sqrt(square(xn) + square(yn+(g_2+rad) )) ;
51    double phiu_n = atan2 ( (yn+(g_2+rad)), xn) ;
52    double ruy_n = sin(phiu_n) ;
53
54          double Bytilde_n[ncoef];
55    double By_n[ncoef];
56    double By=0;
57          for (int ian=1;ian<ncoef;ian++){
58      Bytilde_n[ian]=an[ian]/(gsl_sf_bessel_Kn(1,ian*kund*rhoo_n)*
59      roy_n-gsl_sf_bessel_Kn(1,ian*kund*rhou_n)*ruy_n);
60      By_n[ian]=Bytilde_n[ian]*(gsl_sf_bessel_Kn(1,ian*kund*rhoo)*
61      roy-gsl_sf_bessel_Kn(1,ian*kund*rhou)*ruy)*sin(ian*kund*z);
62          }
63           for (int ian=1;ian<ncoef;ian++){
64      By=By+By_n[ian];
65          }
66    return -By; //Minus because Fourier Calculated from -lper/2 and +lper/2
67  }
68
69  double FSR_Byrel ( float rad, float kund, float g_2,  double *r,double
        *an,int ncoef, double Bmax0 ) {
70    double &x = r[0] ;
71    double &y = r[1] ;
72    double &z = r[2] ;
73    double xn = 0 ;
74    double yn = 0 ;
75    // o-Field
76          double rhoo = sqrt(square(x) + square(y-(g_2+rad)) ) ;
77    double phio = atan2 ( (y-(g_2+rad)), x) ;
78                  // Vector of direction
79                  double rox = cos(phio) ;
80                  double roy = sin(phio) ;
81           //Fourier:
82    double rhoo_n = sqrt(square(xn) + square(yn-(g_2+rad)) ) ;
83    double phio_n = atan2 ( (yn-(g_2+rad)), xn) ;
```

```
84   double roy_n = sin(phio_n) ;
85    // u-Field
86         double rhou = sqrt(square(x) + square(y + (g_2+rad) ) );
87   double phiu = atan2 ( (y+(g_2+rad)), x) ;
88                 // Vector of direction
89                 double rux = cos(phiu) ;
90                 double ruy = sin(phiu) ;
91           //Fourier:
92   double rhou_n = sqrt(square(xn) + square(yn+(g_2+rad) )) ;
93   double phiu_n = atan2 ( (yn+(g_2+rad)), xn) ;
94   double ruy_n = sin(phiu_n) ;
95         double Btilde0_n[ncoef];
96   double B0_n[ncoef];
97         double Byrel=0;
98         for (int ian=1;ian<ncoef;ian++){
99     Btilde0_n[ian]=an[ian]/(gsl_sf_bessel_Kn(1,ian*kund*rhoo_n)*
100    roy_n-gsl_sf_bessel_Kn(1,ian*kund*rhou_n)*ruy_n);
101    B0_n[ian]=(Btilde0_n[ian]/Bmax0)*(gsl_sf_bessel_Kn(1,ian*kund*rhoo)*
102    roy-gsl_sf_bessel_Kn(1,ian*kund*rhou)*ruy)*sin(ian*kund*z);
103        }
104     for (int ian=1;ian<ncoef;ian++){
105    Byrel=Byrel+B0_n[ian];
106        }
107   return -Byrel;    //in m
108 }
109
110
111 double getB0 ( float rad, float kund, float g_2,  double *r,double *an,int
      ncoef ) {
112 //Integral By(z)=-B0 sin(2*pi*z/lund) to calculate with fourier the velocity
      parallel, Clarke S.42
113   double &x = r[0] ;
114   double &y = r[1] ;
115   double &z = r[2] ;
116   double xn = 0 ;
117   double yn = 0 ;
118   // o-Field
119         double rhoo = sqrt(square(x) + square(y-(g_2+rad)) ) ;
120   double phio = atan2 ( (y-(g_2+rad)), x) ;
121                 // Vector of direction
122                 double rox = cos(phio) ;
123                 double roy = sin(phio) ;
124          //Fourier:
125   double rhoo_n = sqrt(square(xn) + square(yn-(g_2+rad)) ) ;
126   double phio_n = atan2 ( (yn-(g_2+rad)), xn) ;
127   double roy_n = sin(phio_n) ;
128    // u-Field
129         double rhou = sqrt(square(x) + square(y + (g_2+rad) ) );
130   double phiu = atan2 ( (y+(g_2+rad)), x) ;
131                 // Vector of direction
132                 double rux = cos(phiu) ;
133                 double ruy = sin(phiu) ;
134           //Fourier:
135   double rhou_n = sqrt(square(xn) + square(yn+(g_2+rad) )) ;
136   double phiu_n = atan2 ( (yn+(g_2+rad)), xn) ;
137   double ruy_n = sin(phiu_n) ;
138
139         double Btilde0_n[ncoef];
140   double B0_n[ncoef];
141         double B0_ku=0;
142         for (int ian=1;ian<ncoef;ian++){
143     Btilde0_n[ian]=an[ian]/(gsl_sf_bessel_Kn(1,ian*kund*rhoo_n)*
144     roy_n-gsl_sf_bessel_Kn(1,ian*kund*rhou_n)*ruy_n);
145     B0_n[ian]=Btilde0_n[ian]*(gsl_sf_bessel_Kn(1,ian*kund*rhoo)*
146     roy-gsl_sf_bessel_Kn(1,ian*kund*rhou)*ruy)*(1/(ian*kund));
147         }
148      for (int ian=1;ian<ncoef;ian++){
149     B0_ku=B0_ku+B0_n[ian];
150         }
151    return -B0_ku/1e3;    //in m
152 }
```

A.2 Calculation of $\Delta\lambda/\lambda_0$, Δx_δ and σ_x

- Main code file: *SCU_FieldBy_RadiationLambda_vDec*2014.*cpp*

```
#include <iostream>
#include <fstream>
#include <cstring>
#include <sstream>
#include <iomanip>
#include <cstdio>
#include <cmath>
#include <gsl/gsl_sf_bessel.h>
#include "templates.cpp"
#include "SCU_parameter.cpp"
#include "B_cyl_func.cpp"
#include "B_cyl_proto.cpp"
using namespace std;
// Function propotypes:
void getan(int ncoef,string filename,double *an);
void getbn(int ncoef,string filename,double *bn);
double FSR_getx0(float rad,float lund,float kund,float g_2,double *an,int
    ncoef, double Bmax0_rel);
double getdeltax(float energy,double l1,double l2,double Bch);
double get_sigmax(double *an, int ncoef);
double get_xByall(double *an,int ncoef);
double get_zByall(double *an,int ncoef);
double get_xElambda(double *an,int ncoef);

int main(void){
  //Summary:
  filename = filename_summary;
  ofstream dataout_summ( filename.c_str() ) ;
  if (!dataout_summ){
  cout << "The file "<< filename_summary << " could not be opened." << endl;
  return 1;
  }
  dataout_summ <<"#####################################################"<< endl;
  dataout_summ <<"# Data from SCU_FieldBy_RadiationLambda_vDec2014.cpp"<<
    endl;
  dataout_summ <<"# Period length [mm]: "<< lund*1e3 << endl;
  dataout_summ <<"# Central energy E0 [MeV]: "<< energy0/1e6 << endl;
  dataout_summ <<"#####################################################"<< endl;
  dataout_summ <<"# optimal l2 [mm]: "<< l2_opt*1e3 << endl;
  dataout_summ <<"# optimal Bymax [T]: "<< Bymax_opt << endl;
  dataout_summ <<"#####################################################"<< endl;
  dataout_summ <<"# 1. Energy [MeV]"<< endl;
  dataout_summ <<"# 2. Dx [mm]"<< endl;
  dataout_summ <<"# 3. xund [mm]"<< endl;
  dataout_summ <<"# 4. Byreal [T]"<< endl;
  dataout_summ <<"# 5. Kreal"<< endl;
  dataout_summ <<"# 6. λ real [nm]"<< endl;
  dataout_summ <<"# 7.  σ x [mm]"<< endl;

  filename = filename_Esigmax;
  if( remove(filename.c_str()) != 0 )
  cout << "Error deleting file "<< filename_Esigmax << endl;
  else
  cout << "File "<< filename_Esigmax << " successfully deleted" << endl;
  ofstream dataout_Esigmax( filename.c_str() , std::ios_base::out |
        std::ios_base::app);
  if (!dataout_Esigmax){
  cout << "The file "<< filename_Esigmax << " could not be opened." << endl;
  return 1;
  }

  dataout_Esigmax <<"#############################################"<< endl;
  dataout_Esigmax <<"# Data from SCU_FieldBy_RadiationLambda_vDec2014.cpp"<<
    endl;
  dataout_Esigmax <<"# Period length [mm]: "<< lund*1e3 << endl;
  dataout_Esigmax <<"# Central energy E0 [MeV]: "<< energy0/1e6 << endl;
  dataout_Esigmax <<"#############################################"<< endl;
```

```
65  dataout_Esigmax <<"# optimal l2 [mm]: "<< l2_opt*1e3 << endl;
66  dataout_Esigmax <<"# optimal Bymax [T]: "<< Bymax_opt << endl;
67  dataout_Esigmax <<"##############################################"<< endl;
68
69  double an[ncoef];
70  double bn[ncoef];
71  getan(ncoef,filename_fourier,an);
72  getbn(ncoef,filename_fourier,bn);
73
74  r[0]=0,r[1]=0,r[2]=-z;
75  Bmax0=FSR_By(rad, kund, g_2, r,an,ncoef);
76  Byrel=FSR_Byrel(rad, kund, g_2, r,an,ncoef,Bmax0);
77  Bmax0_rel=Bymax_opt*Byrel;
78  x0=FSR_getx0(rad,lund,kund,g_2,an,ncoef,Bmax0_rel);
79  deltax0=getdeltax(energy0,l1,l2_opt,Bch);
80
81  r[0]=x0,r[1]=0,r[2]=-z;
82  B_E0=Bymax_opt*FSR_Byrel(rad, kund, g_2, r,an,ncoef,Bmax0);
83  K0=B_E0*abs(e)/(m0*c)/kund;
84  lambda0=(lund/(2*square(gamma0)))*(1+(square(K0)/2));
85
86  for( int ienergy = 0; ienergy <= nep; ienergy++ ){
87
88    energy = energy0 +(delE - ienergy*2*delE/nep);
89    gammaE=energy/511e3;
90    deltax=getdeltax(energy,l1,l2_opt,Bch);
91
92    if (energy==energy0){dDxarray[0]=deltax;}
93    if (energy==energy0+delE){dDxarray[1]=deltax; }
94    if (energy==energy0-delE){dDxarray[2]=deltax; }
95
96    xund=deltax+(x0-deltax0);
97    r[0]=xund,r[1]=0,r[2]=-z;
98    B_real=Bymax_opt*FSR_Byrel(rad, kund, g_2, r,an,ncoef,Bmax0);
99    K_real=B_real*abs(e)/(m0*c)/kund;
100   lambreal=(lund/(2*square(gammaE)))*(1+(square(K_real)/2));
101   lambda_array[ienergy]=lambreal*1e9;
102   sigmax_E=get_sigmax(an,ncoef);
103   sigma_array[ienergy]=sigmax_E;
104   dataout_summ << fixed << setprecision(2)<<energy/1e6 << "\t" ;
105   dataout_summ << fixed << setprecision(6);
106   dataout_summ << deltax*1e3 << "\t"<< xund*1e3 << "\t" ;
107   dataout_summ << B_real  << "\t"<< K_real << "\t" << lambreal*1e9<< "\t"
      << sigmax_E<<endl;
108 }// end for energy
109
110 minL = maxL = lambda_array[0];
111 for (int i=0; i<=nep; i++) {
112   if ( lambda_array[i] < minL ) minL = lambda_array[i];
113   if ( lambda_array[i] > maxL ) maxL = lambda_array[i];
114 }// cin.get();//Pause
115
116 dataout_summ << fixed << setprecision(3);
117 dataout_summ <<  "##############################################"<< endl;
118 dataout_summ  << "# λmin [nm] = " << minL << endl;
119 dataout_summ  << "# λmax [nm] = " << maxL << endl;
120 dataout_summ  << "# λ0 [nm] = " << lambda0*1e9 << endl;
121 dataout_summ  << "# Δλ/λ0 = (λmax-λmin)/λ0 [%] = " << ((
      maxL-minL)/(lambda0*1e9))*100 << endl;
122 dataout_summ <<  "##############################################"<< endl;
123 dataout_summ <<  "# Dx(E0+delE)[mm] = "<< dDxarray[1]*1e3<<endl;
124 dataout_summ <<  "# Dx(E0-delE)[mm] = "<< dDxarray[2]*1e3<<endl;
125 dataout_summ <<  "# Dx0(E0)[mm] = "<< dDxarray[0]*1e3<<endl;
126 dataout_summ <<  "# Dx σ [mm] = "<< (dDxarray[2]-dDxarray[1])*1e3<<endl;
127 dataout_summ <<  "##############################################"<< endl;
128
129 minsg = sigma_array[0];
130 for (int isg=0; isg<=nep; isg++) {
131   dataout_Esigmax << fixed << setprecision(3)<< sigma_array[isg]<< endl;
132   if ( sigma_array[isg] < minsg ) minsg = sigma_array[isg];
133 }
134
135 if ((( maxL-minL)/(lambda0*1e9))*100 <= 1){
```

```
136     dataout_Esigmax << fixed << setprecision(3)<< "# Minimum  σ x [mm]: "<<
        minsg << endl;
137     dataout_summ << fixed << setprecision(3)<< "# Minimum  σ x [mm]:
        "<<minsg << endl;
138   }else{
139     dataout_Esigmax << "#  σ x: -, Δλ / λE > 1 %  " <<endl;
140     dataout_summ << "#  σ x: -, Δλ / λE > 1 %   "<< endl;
141   }
142
143   dataout_Esigmax.close();
144   dataout_summ.close() ;
145   get_xByall(an,ncoef);
146   get_zByall(an,ncoef);
147   get_xElambda(an,ncoef);
148 }  //cin.get();//Pause
149 //-------------------------------------------------------------
150 // new user defined functions
151 double  get_xByall(double *an, int ncoef){
152   filename = filename_xByall;
153   ofstream dataout_xByall( filename.c_str() ) ;
154   if (!dataout_xByall){
155     cout << "The file "<< filename_xByall << " could not be opened." << endl;
156     return 1;
157   }
158   dataout_xByall <<"##############################################"<< endl;
159   dataout_xByall <<"# Data from SCU_FieldBy_RadiationLambda_vDec2014.cpp"<<
        endl;
160   dataout_xByall <<"# Period length [mm]: "<< lund*1e3 << endl;
161   dataout_xByall <<"# Central energy E0 [MeV]: "<< energy0/1e6 << endl;
162   dataout_xByall <<"##############################################"<< endl;
163   dataout_xByall <<"# optimal l2 [mm]: "<< l2_opt*1e3 << endl;
164   dataout_xByall <<"# optimal Bymax [T]: "<< Bymax_opt << endl;
165   dataout_xByall <<"##############################################"<< endl;
166   dataout_xByall <<"# 1. x [mm]"<< endl;
167   dataout_xByall <<"# 2. Byreal [T]"<< endl;
168
169   r[0]=0,r[1]=0,r[2]=-z;
170   Bmax0=FSR_By(rad, kund, g_2, r,an,ncoef);
171   for(double ix=0;ix <= xmax; ix+=0.1){
172     double xund2=ix/1e3;
173     r[0]=xund2,r[1]=0,r[2]=-z;
174     double B_realx=Bymax_opt*FSR_Byrel(rad, kund, g_2, r,an,ncoef,Bmax0);
175     dataout_xByall << fixed << setprecision(6) << xund2*1e3 << "\t" ;
176     dataout_xByall << fixed << setprecision(6) << B_realx << endl ;
177   }
178   dataout_xByall.close() ;
179 }
180
181 double get_zByall(double *an, int ncoef){
182   filename = filename_zByall;
183   ofstream dataout_zByall( filename.c_str() ) ;
184   if (!dataout_zByall){
185     cout << "The file "<< filename_zByall << " could not be opened." << endl;
186     return 1;
187   }
188   dataout_zByall <<"##############################################"<< endl;
189   dataout_zByall <<"# Data from SCU_FieldBy_RadiationLambda_vDec2014.cpp"<<
        endl;
190   dataout_zByall <<"# Period length [mm]: "<< lund*1e3 << endl;
191   dataout_zByall <<"# Central energy E0 [MeV]: "<< energy0/1e6 << endl;
192   dataout_zByall <<"##############################################"<< endl;
193   dataout_zByall <<"# optimal l2 [mm]: "<< l2_opt*1e3 << endl;
194   dataout_zByall <<"# optimal Bymax [T]: "<< Bymax_opt << endl;
195   dataout_zByall <<"##############################################"<< endl;
196   dataout_zByall <<"# 1. z [mm]"<< endl;
197   dataout_zByall <<"# 2. Byreal [T]"<< endl;
198
199   r[0]=0,r[1]=0,r[2]=-z;
200   Bmax0=FSR_By(rad, kund, g_2, r,an,ncoef);
201   for(double iz=0;iz <= zmax; iz+=0.1){
202     double zund2=iz/1e3;
203     r[0]=0,r[1]=0,r[2]=-zund2;
204     double B_realz=Bymax_opt*FSR_Byrel(rad, kund, g_2, r,an,ncoef,Bmax0);
205     dataout_zByall<< fixed << setprecision(6) << zund2*1e3 << "\t" ;
```

```
206     dataout_zByall<< fixed << setprecision(6) << B_realz << endl ;
207   }
208   dataout_zByall.close();
209 }
210
211
212 double get_xElambda(double *an, int ncoef){
213   filename =filename_xELambda;
214   ofstream dataout_xElambda( filename.c_str() ) ;
215   if (!dataout_xElambda){
216     cout << "The file "<< filename_xELambda << " could not be opened." <<
      endl;
217     return 1;
218   }
219   dataout_xElambda <<"#############################################"<< endl;
220   dataout_xElambda <<"# Data from
      SCU_FieldBy_RadiationLambda_vDec2014.cpp"<< endl;
221   dataout_xElambda <<"# Period length [mm]: "<< lund*1e3 << endl;
222   dataout_xElambda <<"# Central energy E0 [MeV]: "<< energy0/1e6 << endl;
223   dataout_xElambda <<"#############################################"<< endl;
224   dataout_xElambda <<"# optimal l2 [mm]: "<< l2_opt*1e3 << endl;
225   dataout_xElambda <<"# optimal Bymax [T]: "<< Bymax_opt << endl;
226   dataout_xElambda <<"#############################################"<< endl;
227   dataout_xElambda <<"# 1. x [mm]"<< endl;
228   dataout_xElambda <<"# 2. Energy [MeV]"<< endl;
229   dataout_xElambda <<"# 3. λ [nm]"<< endl;
230
231   r[0]=0,r[1]=0,r[2]=-z;
232   Bmax0=FSR_By(rad, kund, g_2, r,an,ncoef);
233
234   for(double ien=600;ien >=0; ien--){
235     double energy = ien*1e6 ;
236     double gammaE=energy/511e3;
237     double deltax=getdeltax(energy,l1,l2_opt,Bch);
238     double xund=deltax+(x0-deltax0);
239     r[0]=xund,r[1]=0,r[2]=-z;
240     double B_reall=Bymax_opt*FSR_Byrel(rad, kund, g_2, r,an,ncoef,Bmax0);
241     double K_real=B_reall*abs(e)/(m0*c)/kund;
242     double lambreal=(lund/(2*square(gammaE)))*(1+(square(K_real)/2));
243     dataout_xElambda << fixed << setprecision(6) << xund*1e3 << "\t";
244     dataout_xElambda << fixed << setprecision(2) << energy/1e6 <<"\t";
245     dataout_xElambda << fixed << setprecision(6)<<(lambreal*1e9)<< endl ;
246   }
247   dataout_xElambda.close();
248 }
249
250 double get_sigmax(double *an, int ncoef){
251
252     double sigmaxEnd=0;
253     filename = filename_Esigmax;
254     ofstream dataout_Esigmax( filename.c_str() , std::ios_base::out |
255     std::ios_base::app);
256     if (!dataout_Esigmax){
257       cout << "The file "<< filename_Esigmax << " could not be opened." <<
      endl;
258       return 1;
259     }
260     dataout_Esigmax <<"# Calculate sigmax for: "<< endl;
261     dataout_Esigmax <<"# Energy E [MeV]: "<< energy/1e6 << endl;
262     dataout_Esigmax <<"# xE [mm]: "<< xund*1e3 << endl;
263     dataout_Esigmax <<"# λE [nm]: "<< lambreal*1e9 << endl;
264     dataout_Esigmax <<"#################################################"<< endl;
265     dataout_Esigmax <<"# 1. σ x [mm]"<< endl;
266     dataout_Esigmax <<"# 2. Δλ / λE [%] "<< endl;
267     //sigmax:
268     for (int idx=1;idx<=1000;idx++){
269       deltxc=idx/1e6;
270       xundmin=xund-deltxc;
271       r[0]=xundmin,r[1]=0,r[2]=-z;
272       B_realmin=Bymax_opt*FSR_Byrel(rad, kund, g_2, r,an,ncoef,Bmax0);
273       Krealmin=B_realmin*abs(e)/(m0*c)/kund;
274       lambrealmin=(lund/(2*square(gammaE)))*(1+(square(Krealmin)/2));
275
276       xundmax=xund+deltxc;
```

```
277         r[0]=xundmax,r[1]=0,r[2]=-z;
278         B_realmax=Bymax_opt*FSR_Byrel(rad, kund, g_2, r,an,ncoef,Bmax0);
279         Krealmax=B_realmax*abs(e)/(m0*c)/kund;
280         lambrealmax=(lund/(2*square(gammaE)))*(1+(square(Krealmax)/2));
281
282         if ((abs(lambrealmax-lambrealmin)/lambreal)*100 >= 1){
283   break;
284         }else{
285   dataout_Esigmax << fixed << setprecision(3) << 2*deltxc*1e3 << "\t";
286   dataout_Esigmax << fixed << setprecision(6) <<
        (abs(lambrealmax-lambrealmin)/lambreal)*100<< endl;
287   sigmaxEnd=2*deltxc*1e3;
288         }
289     }
290     dataout_Esigmax <<"#########################################"<< endl;
291     return sigmaxEnd;
292 }
```

A.3 Calculation of electron trajectories

- Main code file: *SCU_FSR_tracks.cpp*

```
1 #include <iostream>
2 #include <fstream>
3 #include <cstring>
4 #include <cmath>
5 #include <sstream>
6 #include <iomanip>
7 #include <cstdlib>
8 #include <algorithm>
9 #include "templates.cpp"
10 #include "FSR_B_cyl_proto.cpp"
11 #include "FSR_B_cyl_func.cpp"
12 #include "vector3d.cpp"
13 #include "SCU_parameter.cpp"
14 using namespace std;
15 // Function propotypes:
16 void getan(string filename,double *an);
17 void getbn(string filename,double *bn);
18 double writehead();
19 double getx0(double *an);
20 double getdeltax ( float energy,double l2) ;
21 double get_l2opt(double x0,double *an);
22 double writehead2();
23 int trajectory(float energy,int ienergy);
24 void transform_r ( double r_l, double omega_c, double v_par, float t, double
       *r_p_t ) ;
25 void transform_v ( double r_l, double omega_c, double v_par, float t, double
       *v_p_t ) ;
26 void update_r (double *guiding_center, double *r_p_t, double *e1, double
       *e2, double *e3, double *r) ;
27 void update_v (double *guiding_center, double *v_p_t, double *e1, double
       *e2, double *e3, double *v) ;
28 void writeout ( double *r, ofstream &dataout) ;
29 double get_sigmax(int ienergy);
30 double get_xByall();
31 double get_zByall();
32 double get_xElambda();
33 double get_sigmaglobal();
34
35 int main (void) {
36     //1.-Import an und bn coefficients:
37     getan(filename_fourier,an);
38     getbn(filename_fourier,bn);
39     //2.-Write Header in the files:
40     writehead();
41     //3.-Calculate x0 for E0:
```

```
42      x0=getx0(an);
43      //4.- Calculate l2Optimal:
44      l2opt=get_l2opt(x0,an);
45      //5.- Calculate lambda0:
46      deltax0=getdeltax(energy0,l2opt);
47      r[0]=x0,r[1] = 0 , r[2] = lund/4 ;
48      B_E0=By(rad, kund, g_2, r,an,ncoef);
49      K0 = (B_E0*abs(e)*(lund/1e3))/(m0*c*2*pi) ;
50      lambda10 = ((lund/1e3)/ (2*square(gamma0)))*(1+square(K0)/2) ;
51      writehead2();
52      //6.-Calculate the trajectory for every energy:
53       for( int ienergy = 0; ienergy <= nep; ienergy++ ){
54    if (ienergy==0 || ienergy ==5 || ienergy==10){//Only 132,120 und 108MeV
55      energy = energy0 +(delE - ienergy*2*delE/nep) ;
56      trajectory(energy,ienergy); //equation for the trajectory in mm
57    }
58    //7.- Calculate sigmax:
59    get_sigmax(ienergy);
60      } //end for energy
61       //8.- Calculate Breal x
62       get_xByall();
63       //9.- Calculate Breal z
64       get_zByall();
65       //10.-Calculate lambdareal x
66       get_xElambda();
67       //11.-Calculate Sigma_global
68       get_sigmaglobal();
69  return 0 ;
70  } //end
71  //-------------------------------------------------------------
72  // new user defined functions
73  double get_l2opt(double x0,double *an){
74       if(korrektur==0){
75     filename = filename_l2opt_ohne;//without correction
76    }else if(korrektur==1){
77     filename =filename_l2opt_mit ;//with correction
78    }
79    filename.append(extension) ;
80    ofstream dataout_l2opt( filename.c_str(), std::ios_base::out |
81                    std::ios_base::app);
82    if (!dataout_l2opt){
83        cout << "The file "<< filename << " could not be opened." << endl;
84          return 1;
85    }
86    if(korrektur==0){
87     filename = filename_summ_ohne;//without correction
88    }else if(korrektur==1){
89     filename = filename_summ_mit;//with correction
90    }
91    filename.append(extension) ;
92    ofstream dataout_summ( filename.c_str(), std::ios_base::out |
93                    std::ios_base::app);
94    if (!dataout_summ){
95        cout << "The file "<< filename << " could not be opened." << endl;
96          return 1;
97    }
98    int il2min=l2min*100;
99    int il2max=l2max*100;//2decimals
100   int ni=(il2max-il2min)+1;
101   double l2t_array[ni];
102   double dlam_array[ni];
103   double mindlam,minl2t;
104   double r[3] ;
105     for(int il2=il2min;il2<=il2max;il2++){
106       double l2t=il2/1e2;
107       double lamb0(0);
108       double deltax0t=getdeltax(energy0,l2t);
109       const int n=nep+1; // number of elements in the array
110       double lambda_array[n];
111       double min, max;
112       for( int i = 0; i <= nep; i++ ){
113     double energy = energy0 +(delE - i*2*delE/nep) ;
114     double gammaE=energy/511e3;
115     double deltax=getdeltax(energy,l2t);
```

```
116     double xund=deltax+(x0-deltax0t);
117     r[0]=xund,r[1] = 0 , r[2] = lund/4 ;
118     double B_real=By(rad, kund, g_2, r,an,ncoef);
119     double Kreal= (B_real*abs(e)*(lund/1e3))/(m0*c*2*pi);
120     double lambreal= ((lund/1e3)/ (2*square(gammaE)))*(1+square(Kreal)/2) ;
121     lambda_array[i]=lambreal*1e9;//in nm
122     if (energy==energy0) {
123       lamb0=lambreal;
124     }
125       } //end for energy
126       min = max = lambda_array[0];
127       for (int i=0; i<n; i++) {
128     if ( lambda_array[i] < min ) min = lambda_array[i];
129     if ( lambda_array[i] > max ) max = lambda_array[i];
130       }
131       dataout_l2opt << fixed << setprecision(6) << l2t << "\t";
132       dataout_l2opt <<fixed << setprecision(6)<<((max-min)/(lamb0*1e9))*100
      << endl;
133
134       l2t_array[il2-il2min]=l2t;//in mm
135       dlam_array[il2-il2min]=((max-min)/(lamb0*1e9))*100; //in%
136       }//end for il2
137   //search minimum deltalambda/lambda0 und l2 optimal
138   mindlam = dlam_array[0];
139   minl2t=l2t_array[0];
140   for (int i=0; i<ni; i++) {
141       if ( dlam_array[i] < mindlam )
142       {
143     mindlam = dlam_array[i];
144     minl2t=l2t_array[i];
145       }
146   }
147    dataout_l2opt << "-------------------------------------------------"<<endl;
148   dataout_l2opt << "Solution: "<<endl;
149   dataout_l2opt <<fixed << setprecision(6)<<"Minimum Δλ
      /λ=(λmax-λmin)/λ0[%]: " <<mindlam<< endl;
150   dataout_l2opt <<fixed << setprecision(6)<<"l2 optimal[mm]: " <<minl2t<<
      endl;
151   dataout_l2opt.close() ;
152   double l2opt=minl2t;
153   dataout_summ <<"# Coefficients an: "<< endl;
154     for (int ian=0;ian<=ncoef;ian++){
155       dataout_summ <<fixed << setprecision(16) <<"#
      a["<<ian<<"]:"<<an[ian]<<endl;
156     }
157   dataout_summ <<fixed << setprecision(16) <<"# und B_max[T]: "<<B_max<<
      endl;
158   dataout_summ<<"# Optimal l2[mm]: "<<l2opt<< endl;
159
160   return l2opt;
161 }
162 int trajectory(float energy,int ienergy){
163     gammaE=energy/511e3; //cout <<fixed << setprecision(16)<<"gammaE:
      "<<gammaE<<endl;
164     m_e=m0*gammaE;
165     if(korrektur==0){
166       filename = filename_Dx_ohne;//without correction
167     }else if(korrektur==1){
168       filename = filename_Dx_mit;//with correction
169     }
170     filename.append(extension) ;
171     ofstream dataout_Dx( filename.c_str() , std::ios_base::out |
172   std::ios_base::app);
173     if (!dataout_Dx){
174       cout << "The file "<< filename << " could not be opened." << endl;
175       return 1;
176     }
177     dataout_Dx << fixed << setprecision(2)<< energy/1e6 << "\t" ;
178     dataout_Dx << fixed << setprecision(16);
179     //summary:
180     if(korrektur==0){
181       filename = filename_summ_ohne;//without correction
182     }else if(korrektur==1){
183       filename = filename_summ_mit;//with correction
```

```
184     }
185     filename.append(extension) ;
186     ofstream dataout_summ( filename.c_str(), std::ios_base::out |
187   std::ios_base::app);
188     if (!dataout_summ){
189       cout << "The file "<< filename << " could not be opened." << endl;
190       return 1;
191     }
192     dataout_summ << fixed << setprecision(2)<<energy/1e6 << "\t" ;
193     dataout_summ << fixed << setprecision(16);
194     if(korrektur==0){
195       filename = filename_xEampl_ohne ;//without correction
196     }else if(korrektur==1){
197       filename = filename_xEampl_mit ;//with correction
198     }
199     ofstream dataout_xEampl( filename.c_str() , std::ios_base::out |
200   std::ios_base::app);
201     if (!dataout_xEampl){
202       cout << "The file "<< filename << " could not be opened." << endl;
203       return 1;
204     }
205     if(korrektur==1){
206       dataout_xEampl << fixed << setprecision(2) << energy/1e6 << " " ;
207       dataout_xEampl << fixed << setprecision(16);
208     }
209     if(korrektur==0){
210       filename = filename_xEBy_ohne ;//without correction
211     }else if(korrektur==1){
212       filename = filename_xEBy_mit ;//with correction
213     }
214     filename.append(extension) ;
215     ofstream dataout_xEBy( filename.c_str() , std::ios_base::out |
216   std::ios_base::app);
217     if (!dataout_xEBy){
218       cout << "The file "<< filename << " could not be opened." << endl;
219       return 1;
220     }
221     stringstream eout; //necessary for the name of the energy
222     eout << energy/1e6;
223     int delfile=energy/1e6;
224     enerprint = eout.str();
225     replace(enerprint.begin(), enerprint.end(), '.', 'p');
226     if(korrektur==0){
227       filename = filename_track_ohne ;//without correction
228     }else if(korrektur==1){
229       filename = filename_track_mit ;//with correction
230     }
231     filename.append(enerprint) ;
232     filename.append(extension) ;
233     const char* file_nametest = filename.c_str();
234     ofstream dataout_track( filename.c_str() ) ;
235     if (!dataout_track){
236       cout << "The file "<< filename << " could not be opened." << endl;
237       return 1;
238     }
239     dataout_track <<"# 1.: x [mm]"<< endl;
240     dataout_track <<"# 2.: y [mm]"<< endl;
241     dataout_track <<"# 3.: z [mm]"<< endl;
242     dataout_track <<"# 4.: By [T]"<< endl;
243     //------------------------------
244     deltax=getdeltax(energy,l2opt);
245     xund=deltax+(x0-deltax0);
246     dataout_summ << deltax << "\t"<< xund << "\t" ;
247     //Energy,x,amplitude:
248     if(korrektur==1){dataout_xEampl << xund << " ";}
249     if (energy==energy0){ dDxarray[0]=deltax;cout <<"deltx0: "<<dDxarray[0]
      <<endl;}
250     if (energy==energy0+delE){ dDxarray[1]=deltax; cout <<"deltxplus: "<<
      dDxarray[1] <<endl;}
251     if (energy==energy0-delE){ dDxarray[2]=deltax; cout <<"deltxminus:
      "<<dDxarray[2] <<endl;}
252     r[0]=xund,r[1] = 0 , r[2] = lund/4 ;
253     B_real=By(rad, kund, g_2, r,an,ncoef);
```

```
254     dataout_xEBy << fixed << setprecision(16) << xund << "\t" << energy/1e6
        << "\t" << B_real <<endl ;
255     Kreal= (B_real*abs(e)*(lund/1e3))/(m0*c*2*pi) ;
256     lambreal= ((lund/1e3)/ (2*square(gammaE)))*(1+square(Kreal)/2) ;
257     dataout_summ << B_real << "\t"<<Kreal << "\t" << lambreal*1e9<<endl;
258     lambda_array[ienergy]=lambreal*1e9;//in nm
259     x_array[ienergy]=xund;
260     r[0]=xund,r[1] = 0 , r[2] = 0 ;
261     B0_ku=getB0( rad, kund,g_2, r,an,ncoef);
262     // v_tmax = (B_t*e*(lund/1e3))/(2*pi*m_e) ; // m/s,clarke: 42
263     //It is the Integral sin(nkuz)
264     v_tmax= (e*B0_ku)/(m_e) ;
265     v_p = sqrt( square(c) - square(v_tmax) ) ;// m/s
266     v[0] = v_tmax , v[1] = 0 , v[2] = v_p ;//in m/s
267     r[0] =xund , r[1] = 0 , r[2] = 0 ;//in mm
268     double &x = r[0] , &y = r[1] , &z = r[2] ; //in mm
269     writeout(r,dataout_track) ; // r in mm
270     x1c=r[0];
271     non=0;
272     aon=0;
273     while(z<=Nper*lund){
274       if (korrektur==0){  //cout <<"Ohne Korrektur....." << endl;
275   B[0] = Bx(rad, kund, g_2, 1, r,an,ncoef), B[1]=By(rad, kund, g_2,
        r,an,ncoef), B[2]=Bz(rad, kund, g_2, 1, r,bn,ncoef) ;
276       }else if(korrektur==1){//cout <<"Mit Korrektur....." << endl;
277   Bykorr=coef_a*pow(x,3)+coef_b*pow(x,2)+coef_c*x+coef_d;
278   B[1]=By(rad, kund, g_2,r,an,ncoef)+Bykorr;
279       }
280     dataout_track << fixed << setprecision(16) << B[1] << endl;
281     if  ( z< lund ){
282       if (z> 3*lund/4 ){
283   if (x>=x2l){
284     x2l=x;
285     z2l=z;
286     }}}
287     if (non==0){
288       if (z>lund){
289   x2r=x;
290   z2r=z;
291   non=1;
292     }}
293     //Amplitude:
294     if(korrektur==1){
295       if (aon==0){
296   if (z>lund/4){
297     xamp=x;
298     dataout_xEampl << x1c-xamp<< endl;
299     aon=1;
300     }}}
301     if ( modulo3d(B) != 0){
302   scalarmult3d(r,1/1e3,r); //added r in m
303   unitvec3d(unitvecB,B) ;
304   outerproduct3d(F_l,v,B) ; //corrected v in m/s
305   scalarmult3d(F_l,e,F_l) ;
306   vec_v_par[0] = unitvecB[0],
        vec_v_par[1]=unitvecB[1],vec_v_par[2]=unitvecB[2] ;
307   scalarmult3d(vec_v_par, innerproduct3d(v,unitvecB), vec_v_par ) ;
308   v_par =  modulo3d(vec_v_par) ;
309   substract3d(vec_v_perp, v, vec_v_par) ;
310   v_perp =  modulo3d(vec_v_perp) ;
311   omega_c = abs(e*modulo3d(B)/m_e) ;
312   r_l =  v_perp / omega_c ;    // Larmor radius
313   scalarmult3d(auxiliary_calculation, r_l/modulo3d(F_l), F_l) ;
314   add3d(guiding_center, r , auxiliary_calculation ) ;
315   scalarmult3d(e1,-1/modulo3d(F_l),F_l) ; // F, the minus compensate the
        charge of an electron
316   scalarmult3d(e2, 1/v_perp, vec_v_perp) ;// v_perp
317   unitvec3d(e3, B) ;
318   transform_r(r_l,omega_c,v_par,tof,r_p_t) ;
319   transform_v(r_l,omega_c,v_par,tof,v_p_t) ;
320   update_r (guiding_center, r_p_t, e1, e2, e3, r) ; //in m
321   update_v (guiding_center, v_p_t, e1, e2, e3, v) ; //in m/s
322   scalarmult3d(r,1e3,r); //added r in mm
323   writeout(r,dataout_track) ;
```

```
324     }else{
325   scalarmult3d(r,1/1e3,r); //added r in m
326   del_r[0] = tof*v[0], del_r[1]=tof*v[1], del_r[2]=tof*v[2] ;
327   add3d (r, r, del_r) ;
328   scalarmult3d(r,1e3,r); //added r in mm
329   writeout(r,dataout_track) ;
330     }
331   } //end while z
332     dataout_track.close() ;
333     dataout_xEBy.close() ;
334     dataout_xEampl.close();
335     //Dx-data:
336     x2c=x2r;
337     Dxc1=x2c-x1c;//in mm
338     Dxc100=x-x1c;//in mm
339     Rlc=(((square(lund))+(square(Dxc1)))/(2*Dxc1))/1e3;//in m
340     BRlc=(m0*c*gammaE)/(e*Rlc);//in T
341     dataout_Dx << x1c<< "\t"<< x2c<< "\t";
342     dataout_Dx << Dxc1<< "\t" << Rlc<< "\t"<< BRlc<< "\t"<<Dxc100<<endl;
343     dataout_Dx.close() ;
344 }
345 void transform_r ( double r_l, double omega_c, double v_par, float t, double
      *r_p_t ) {
346        r_p_t[0] = r_l*cos(omega_c*t), r_p_t[1] = r_l*sin(omega_c*t) ,
      r_p_t[2] = v_par*t ;
347 }
348 void transform_v ( double r_l, double omega_c, double v_par, float t, double
      *v_p_t ) {
349   v_p_t[0] = -omega_c*r_l*sin(omega_c*t), v_p_t[1] =
      omega_c*r_l*cos(omega_c*t), v_p_t[2]=v_par ;
350 }
351 void update_r (double *guiding_center, double *r_p_t, double *e1, double
      *e2, double *e3, double *r) {
352   double r1[3], r2[3], r3[3];
353   scalarmult3d(r1,r_p_t[0],e1) ;
354   scalarmult3d(r2,r_p_t[1],e2) ;
355   scalarmult3d(r3,r_p_t[2],e3) ;
356
357   r[0]=guiding_center[0]+r1[0]+r2[0]+r3[0] ;
358   r[1]=guiding_center[1]+r1[1]+r2[1]+r3[1];
359   r[2]=guiding_center[2]+r1[2]+r2[2]+r3[2]  ;
360 }
361 void update_v (double *guiding_center, double *v_p_t, double *e1, double
      *e2, double *e3, double *v) {
362         double v1[3], v2[3], v3[3];
363   scalarmult3d(v1,v_p_t[0],e1) ;
364   scalarmult3d(v2,v_p_t[1],e2) ;
365   scalarmult3d(v3,v_p_t[2],e3) ;
366
367   v[0]=v1[0]+v2[0]+v3[0] ;
368   v[1]=v1[1]+v2[1]+v3[1];
369   v[2]=v1[2]+v2[2]+v3[2]  ;
370 }
371 void writeout ( double *r, ofstream &dataout ){
372   dataout << fixed << setprecision(16) << r[0] << "\t" << r[1] << "\t" <<
      r[2] << "\t" ;
373 }
```

- Vector functions: *vector3d.cpp*

```
1 double modulo3d ( double *r ) ;
2 void unitvec3d ( double *erg, double *r ) ;
3 void outerproduct3d (double *erg, double *a, double *b) ;
4 void scalarmult3d (double *erg, double scalar, double *r) ;
5 double innerproduct (double *a, double *b) ;
6 void add3d (double *erg, double *a, double *b) ;
7 void substract3d (double *erg, double *a, double *b) ;
8 double modulo3d ( double *r ) {
9   double modulo = sqrt( square(r[0]) + square(r[1]) + square(r[2]) ) ;
10  return modulo ;
```

```
11 }
12 void unitvec3d ( double *erg, double *r ) {
13   double modulo = modulo3d ( r ) ;
14   for ( int i = 0 ; i < 3 ; i++ ){
15     erg[i] = r[i]/modulo ;
16   }
17 }
18 void outerproduct3d (double *erg, double *a, double *b) {
19   erg[0] = a[1]*b[2]-a[2]*b[1] ;
20   erg[1] = a[2]*b[0]-a[0]*b[2] ;
21   erg[2] = a[0]*b[1]-a[1]*b[0] ;
22 }
23 void scalarmult3d (double *erg, double scalar, double *r) {
24   for(int i=0; i<3; ++i){
25     erg[i]=r[i]*scalar ;
26   }
27 }
28 double innerproduct3d (double *a, double *b) {
29   double result ;
30   for(int i=0;i<3;i++){
31     result+=a[i]*b[i] ;
32   }
33   return result ;
34 }
35 void add3d (double *erg, double *a, double *b) {
36   for(int i=0;i<3;i++){
37     erg[i] = a[i]+b[i] ;
38   }
39 }
40 void substract3d (double *erg, double *a, double *b) {
41   for(int i=0;i<3;i++){
42     erg[i] = a[i]-b[i] ;
43   }
44 }
```

B. Iron cylindrical undulator database information

As explained in Section 3.4.2 a database with the optimized results for 81 iron cylindrical undulator models was made. The results are summarized in 3 tables according to the external radius values. Cells shaded in light gray show $\Delta\lambda/\lambda_0[\%] < 1\,\%$, and the cell shaded in dark gray shows the minimum $\Delta\lambda/\lambda_0[\%]$ value of the table.

Cylindrical undulator models with r = 25 mm.							
g[mm]	λ_u[mm]	J[A/mm^2]	OPERA B_y^{max}[T]	opt. l_2[mm]	λ_0[nm]	$\Delta\lambda/\lambda_0$[%]	Δx_δ[mm]
1.1	08	0800	1.705	385	102	1.507	5.07
		1000	1.958	299	111	1.274	4.07
		1200	2.209	244	120	1.250	3.43
	10	0800	2.079	206	168	0.852	2.99
		1000	2.426	168	195	1.101	2.54
		1200	2.769	143	225	1.316	2.25
	12	0800	2.443	161	326	2.124	2.46
		1000	2.892	138	404	2.099.	2.19
		1200	3.337	123	492	2.103	2.02
1.3	08	0800	1.531	488	095	1.982	6.27
		1000	1.763	361	102	1.101	4.79
		1200	1.993	291	110	0.986	3.98
	10	0800	1.891	241	153	0.659	3.39
		1000	2.214	192	175	0.907	2.82
		1200	2.534	161	200	1.131	2.46
	12	0800	2.250	172	283	1.835	2.59
		1000	2.672	145	348	1.874	2.27
		1200	3.091	128	422	1.917	2.08
1.5	08	0800	1.379	659	090	3.773	8.27
		1000	1.592	458	096	1.991	5.92
		1200	1.804	351	102	1.070	4.68
	10	0800	1.730	280	142	0.561	3.85
		1000	2.031	221	160	0.707	3.16
		1200	2.328	182	181	0.963	2.71
	12	0800	2.079	188	251	1.598	2.78
		1000	2.476	155	305	1.699	2.39
		1200	2.869	135	368	1.792	2.16

Table B.1: Summary of the optimization results for several iron cylindrical undulator models with r = 25 mm and different values of gap width on axis (g), period length (λ_u) and current density (J).

Cylindrical undulator models with r = 30 mm.							
g[mm]	λ_u[mm]	J[A/mm^2]	OPERA B_y^{max}[T]	opt. l_2[mm]	λ_0[nm]	$\Delta\lambda/\lambda_0$[%]	Δx_δ[mm]
1.1	08	0800	1.716	422	102	1.479	5.50
		1000	1.970	330	111	1.258	4.43
		1200	2.224	270	121	1.248	3.73
	10	0800	2.091	229	169	0.840	3.25
		1000	2.441	188	196	1.097	2.78
		1200	2.787	161	226	1.315	2.46
	12	0800	2.461	180	329	2.129	2.68
		1000	2.914	155	408	2.116.	2.39
		1200	3.363	140	497	2.123	2.22
1.3	08	0800	1.539	536	095	1.989	6.83
		1000	1.772	397	102	1.056	5.21
		1200	2.005	321	110	0.954	4.33
	10	0800	1.903	267	154	0.651	3.70
		1000	2.229	214	176	0.912	3.08
		1200	2.551	180	201	1.156	2.68
	12	0800	2.267	193	285	1.852	2.83
		1000	2.693	163	350	1.874	2.48
		1200	3.115	144	425	1.958	2.26
1.5	08	0800	1.387	718	090	3.733	8.96
		1000	1.602	502	096	1.964	6.44
		1200	1.816	386	102	1.051	5.09
	10	0800	1.741	309	142	0.544	4.19
		1000	2.045	245	161	0.710	3.44
		1200	2.345	202	182	0.990	2.94
	12	0800	2.097	209	253	1.587	3.02
		1000	2.497	173	308	1.736	2.60
		1200	2.894	152	372	1.810	2.36

Table B.2: Summary of the optimization results for several iron cylindrical undulator models with r = 30 mm and different values of gap width on axis (g), period length (λ_u) and current density (J).

Cylindrical undulator models with r = 35 mm.							
g[mm]	λ_u[mm]	J[A/mm^2]	OPERA B_y^{max}[T]	opt. l_2[mm]	λ_0[nm]	$\Delta\lambda/\lambda_0$[%]	Δx_δ[mm]
1.1	08	0800	1.722	457	102	1.451	5.91
		1000	1.977	358	111	1.236	4.76
		1200	2.232	294	121	1.231	4.01
	10	0800	2.098	251	169	0.844	3.51
		1000	2.451	206	196	1.121	2.99
		1200	2.799	178	227	1.290	2.66
	12	0800	2.474	198	331	2.144	2.89
		1000	2.930	172	410	2.117.	2.59
		1200	3.383	155	500	2.115	2.39
1.3	08	0800	1.544	576	096	1.900	7.30
		1000	1.779	430	103	1.089	5.60
		1200	2.013	349	110	0.972	4.65
	10	0800	1.912	291	154	0.658	3.98
		1000	2.241	234	177	0.927	3.31
		1200	2.565	198	202	1.141	2.89
	12	0800	2.279	211	287	1.860	3.04
		1000	2.708	180	353	1.909	2.68
		1200	3.133	160	428	1.932	2.45
1.5	08	0800	1.394	771	090	3.677	9.58
		1000	1.610	542	096	1.936	6.90
		1200	1.824	418	102	1.030	5.46
	10	0800	1.751	336	143	0.553	4.50
		1000	2.057	267	162	0.716	3.70
		1200	2.359	221	183	0.995	3.16
	12	0800	2.110	228	254	1.610	3.24
		1000	2.513	191	310	1.738	2.81
		1200	2.913	167	374	1.799	2.53

Table B.3: Summary of the optimization results for several iron cylindrical undulator models with r = 35 mm and different values of gap width on axis (g), period length (λ_u) and current density (J).

C. Magnetic field Fourier-series expansion of a cylindrical undulator

In cylindrical coordinates, Laplace's equation for a periodic potential in z-direction is given by

$$\Delta\Phi = \frac{1}{\rho}\frac{\partial}{\partial\rho}\left(\rho\frac{\partial\Phi}{\partial\rho}\right) + \frac{1}{\rho^2}\frac{\partial^2\Phi}{\partial\phi^2} + \frac{\partial^2\Phi}{\partial \mathrm{z}^2} = 0. \tag{C.1}$$

The general solution of Equation (C.1) is [40]

$$\Phi\left(\rho,\phi,z\right) = \tilde{\Phi}_\rho(\rho)\tilde{\Phi}_\phi(\phi)\tilde{\Phi}_\mathrm{z}(\mathrm{z}), \tag{C.2}$$

where $\tilde{\Phi}_\mathrm{z}(\mathrm{z}) = \sin(\mathrm{k_u z})$ and for symmetry reasons it applies to a cylindrical coil former $\tilde{\Phi}_\phi(\phi) = \text{constant}$ and then $\partial\tilde{\Phi}_\phi(\phi)/\partial\phi = 0$.

Equation (C.2) can be written in terms of a series Fourier expansion as:

$$\Phi\left(\rho,\phi,z\right) = \sum_{n=0}^{\infty}\tilde{\Phi}_{\rho n}(\rho)\tilde{\Phi}_{\phi n}(\phi)\sin(\mathrm{nk_u z}). \tag{C.3}$$

Substituting Equation (C.3) into Equation (C.1) yields [38]:

$$\begin{aligned}\Delta\Phi &= \sum_{n=0}^{\infty}\sin(\mathrm{nk_u z})\tilde{\Phi}_{\phi n}\left(\frac{\partial^2\tilde{\Phi}_{\rho n}}{\partial\rho^2} + \frac{1}{\rho}\frac{\partial\tilde{\Phi}_{\rho n}}{\partial\rho} - \mathrm{n}^2\mathrm{k_u}^2\tilde{\Phi}_{\rho n}\right)\\ &= \sum_{n=0}^{\infty}\left(\frac{\partial^2\tilde{\Phi}_{\rho n}}{\partial\rho^2} + \frac{1}{\rho}\frac{\partial\tilde{\Phi}_{\rho n}}{\partial\rho} - \mathrm{n}^2\mathrm{k_u}^2\tilde{\Phi}_{\rho n}\right) = 0\end{aligned} \tag{C.4}$$

Equation (C.4) looks like the modified Bessel differential equation of second order:

$$x^2\frac{\partial^2 y}{\partial x^2} + x\frac{\partial y}{\partial x} - \left(x^2 - m^2\right)y = 0 \tag{C.5}$$

where if $m = 0$, $x = \rho$ and $y = \tilde{\Phi}_{\rho n}$, we have:

$$\begin{aligned} \sum_{n=0}^{\infty} \left(\rho^2 \frac{\partial^2 \tilde{\Phi}_{\rho n}}{\partial \rho^2} + \rho \frac{\partial \tilde{\Phi}_{\rho n}}{\partial \rho} - \rho^2 \tilde{\Phi}_{\rho n} \right) = 0 \\ \sum_{n=0}^{\infty} \left(\frac{\partial^2 \tilde{\Phi}_{\rho n}}{\partial \rho^2} + \frac{1}{\rho} \frac{\partial \tilde{\Phi}_{\rho n}}{\partial \rho} - \tilde{\Phi}_{\rho n} \right) = 0 \end{aligned} \tag{C.6}$$

and doing the transformation of the variable ρ to $\mathrm{nk}_u\rho$ yields:

$$\sum_{n=0}^{\infty} \left(\frac{\partial^2 \tilde{\Phi}_{\rho n}(\mathrm{nk}_u\rho)}{\partial(\mathrm{nk}_u\rho)^2} + \frac{1}{(\mathrm{nk}_u\rho)} \frac{\partial \tilde{\Phi}_{\rho n}(\mathrm{nk}_u\rho)}{\partial(\mathrm{nk}_u\rho)} - \tilde{\Phi}_{\rho n}(\mathrm{nk}_u\rho) \right) = 0. \tag{C.7}$$

The solutions of Equation (C.7) are the modified Bessel functions of the first and second kind: $I_0(\mathrm{nk}_u\rho)$ and $K_0(\mathrm{nk}_u\rho)$.

The following conditions are applied to the potential $\tilde{\Phi}_{\rho n}$:

$$\lim_{\rho \to \infty} \tilde{\Phi}_{\rho n} = 0 \tag{C.8}$$

$$\frac{\partial \tilde{\Phi}_{\rho n}}{\partial \rho} < 0 \quad \forall \rho. \tag{C.9}$$

Both conditions are met only with $K_0(\mathrm{nk}_u\rho)$ and therefore it applies:

$$\tilde{\Phi}_{\rho n}(\mathrm{nk}_u\rho) = K_0(\mathrm{nk}_u\rho). \tag{C.10}$$

and the total potential is then:

$$\Phi\left(\rho, \phi, z\right) = \Phi\left(\rho, z\right) = \sum_{n=0}^{\infty} \tilde{B}^* K_0(\mathrm{nk}_u\rho) \sin(\mathrm{nk_u z}), \tag{C.11}$$

where $\tilde{B}^*$ is a constant, which has to be still determined.

The magnetic field is obtained by:

$$\begin{aligned} \vec{B} &= -\vec{\nabla}\Phi(\rho, z) = -\vec{\nabla} \sum_{n=0}^{\infty} \left(\tilde{B}^* K_0(\mathrm{nk}_u\rho) \sin(\mathrm{nk_u z}) \right) \\ &= \sum_{n=0}^{\infty} - \left(\frac{\partial}{\partial \rho}\hat{e}_\rho + \frac{1}{\rho}\frac{\partial}{\partial \phi}\hat{e}_\phi + \frac{\partial}{\partial z}\hat{e}_z \right) \tilde{B}^* K_0(\mathrm{nk}_u\rho) \sin(\mathrm{nk_u z}) \\ &= \sum_{n=0}^{\infty} \left[-\tilde{B}^* \left(\frac{\partial}{\partial \rho} K_0(\mathrm{nk}_u\rho) \right) \sin(\mathrm{nk_u z})\hat{e}_\rho - \tilde{B}^* \mathrm{nk}_u K_0(\mathrm{nk}_u\rho) \cos(\mathrm{nk_u z})\hat{e}_z \right]. \end{aligned} \tag{C.12}$$

Using the following recurrence formula [38]:

$$\frac{\partial}{\partial \rho} K_0(\mathrm{nk}_u\rho) = -\mathrm{nk}_u K_1(\mathrm{nk}_u\rho) \tag{C.13}$$

then the magnetic field in a cylindrical undulator is:

$$\vec{B} = \sum_{n=0}^{\infty} \tilde{B} \left[\sin(\mathrm{nk_u z}) K_1(\mathrm{nk}_u \rho) \hat{e}_\rho + \cos(\mathrm{nk_u z}) K_0(\mathrm{nk}_u \rho) \hat{e}_z \right] \tag{C.14}$$

where $\tilde{B} = -\tilde{B}^* \mathrm{nk_u}$.

The y-component of the magnetic field Fourier-series expansion for the cylindrical undulator results:

$$B_y = \sum_{n=0}^{\infty} \tilde{B} \sin(\mathrm{nk_u} z) K_1 \left(\mathrm{n} k_\mathrm{u} \rho \right) \hat{e}_\rho \tag{C.15}$$

D. TGU40 drawings

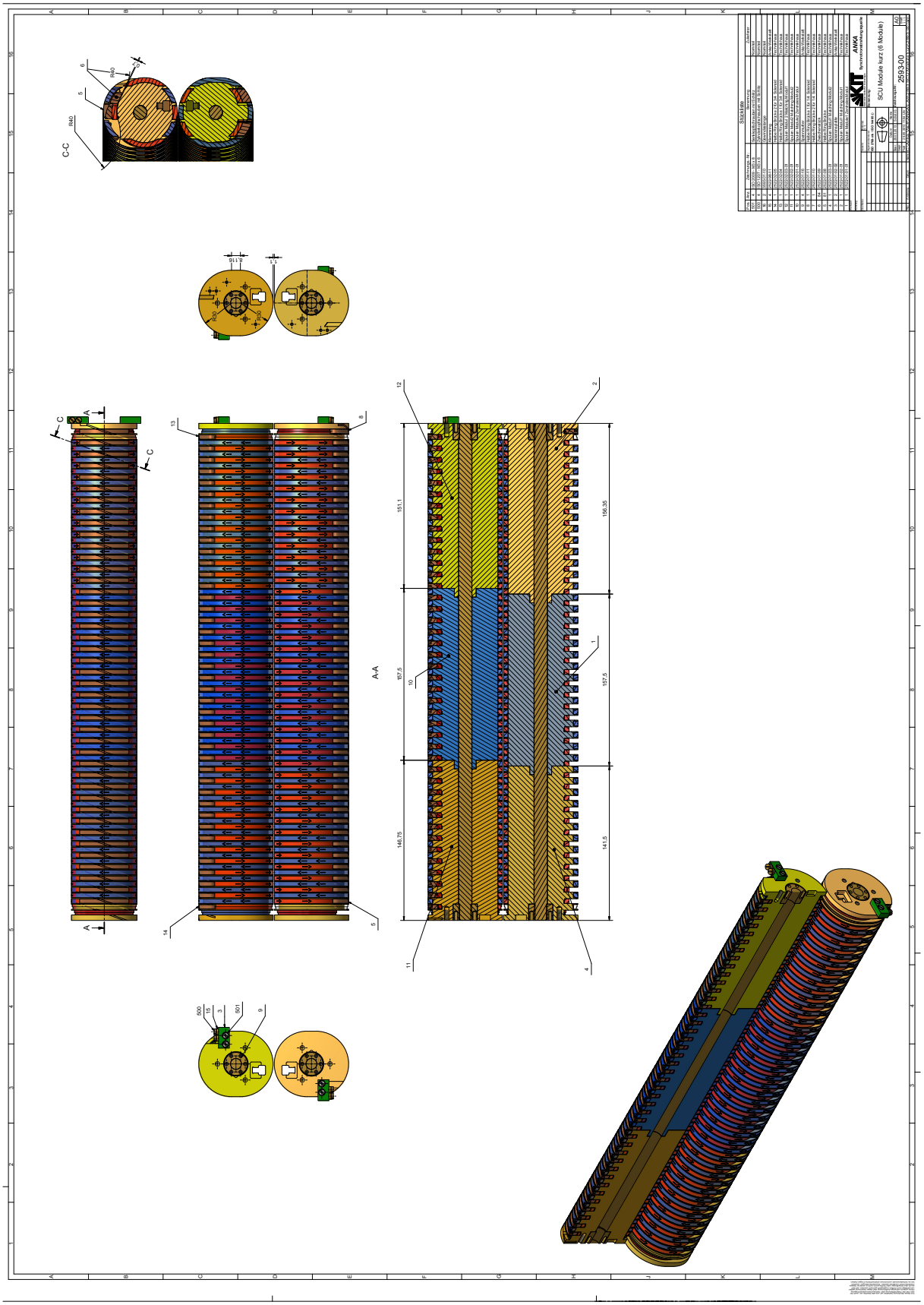
SCU Module kurz (6 Module)
2593-00
C-C
A-A
R40
R20
151.1
156.35
157.5
157.5
146.75
141.5

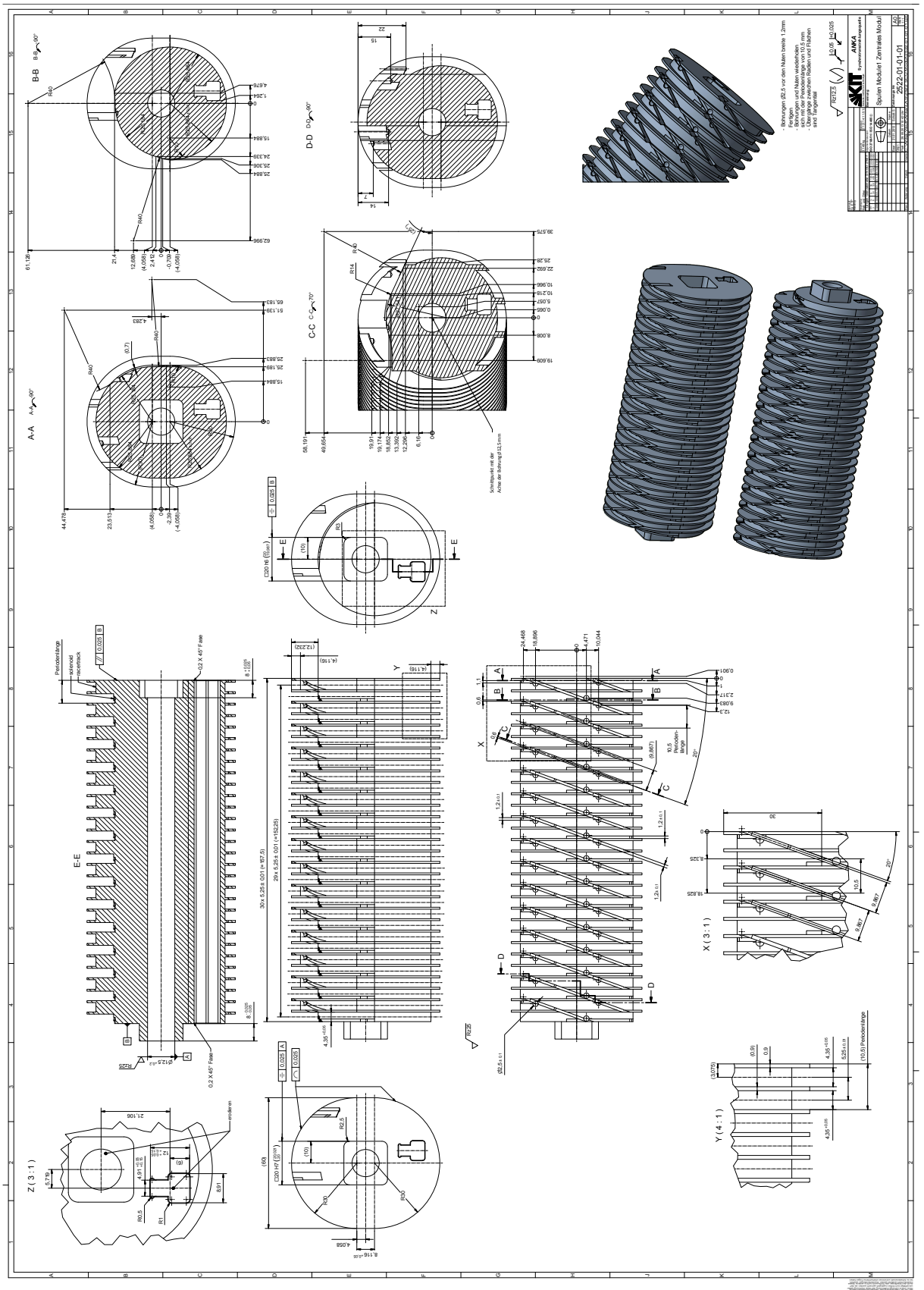
Spulen Modul1 Zentrales Modul
2522-01-01-01
Bohrungen Ø2,5 vor den Nuten breite 1,2mm
Fertigen
Bohrungen und Nuten verdrehen
sich mit der Periodenlänge von 10,5 mm
Übergänge zwischen Radien und Flächen
sind nicht angefast
B-B
A-A
C-C
D-D
E-E
Z (3 : 1)
X (3 : 1)
Y (4 : 1)
Periodenlänge
solenoid
racetrack
Schnittpunkt mit der
Achse der Bohrung ø12,5mm

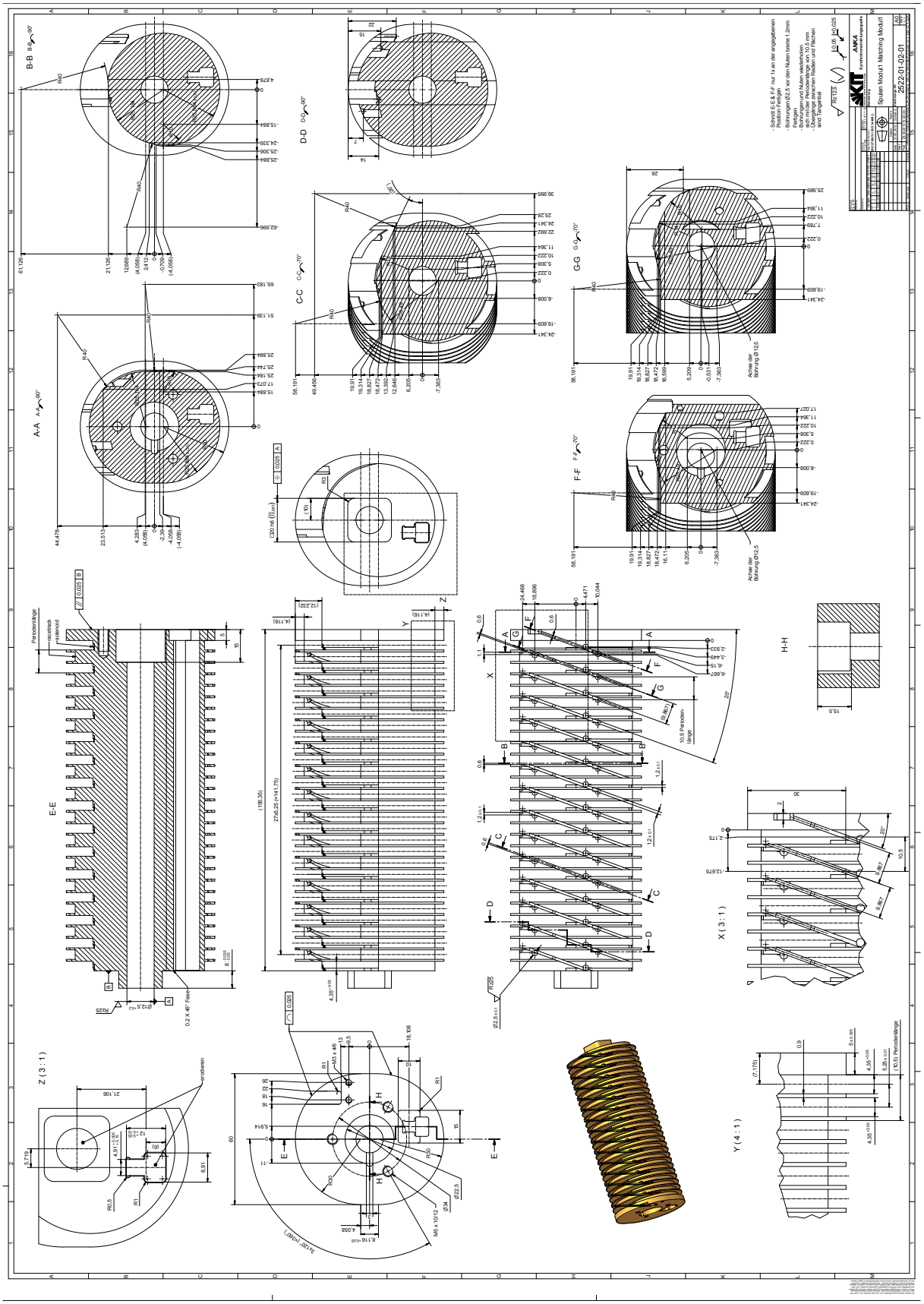
Spulen Modul1 Matching Modul
2522-01-02-01
B-B
A-A
C-C
D-D
E-E
F-F
G-G
H-H
Z (3 : 1)
X (3 : 1)
Y (4 : 1)

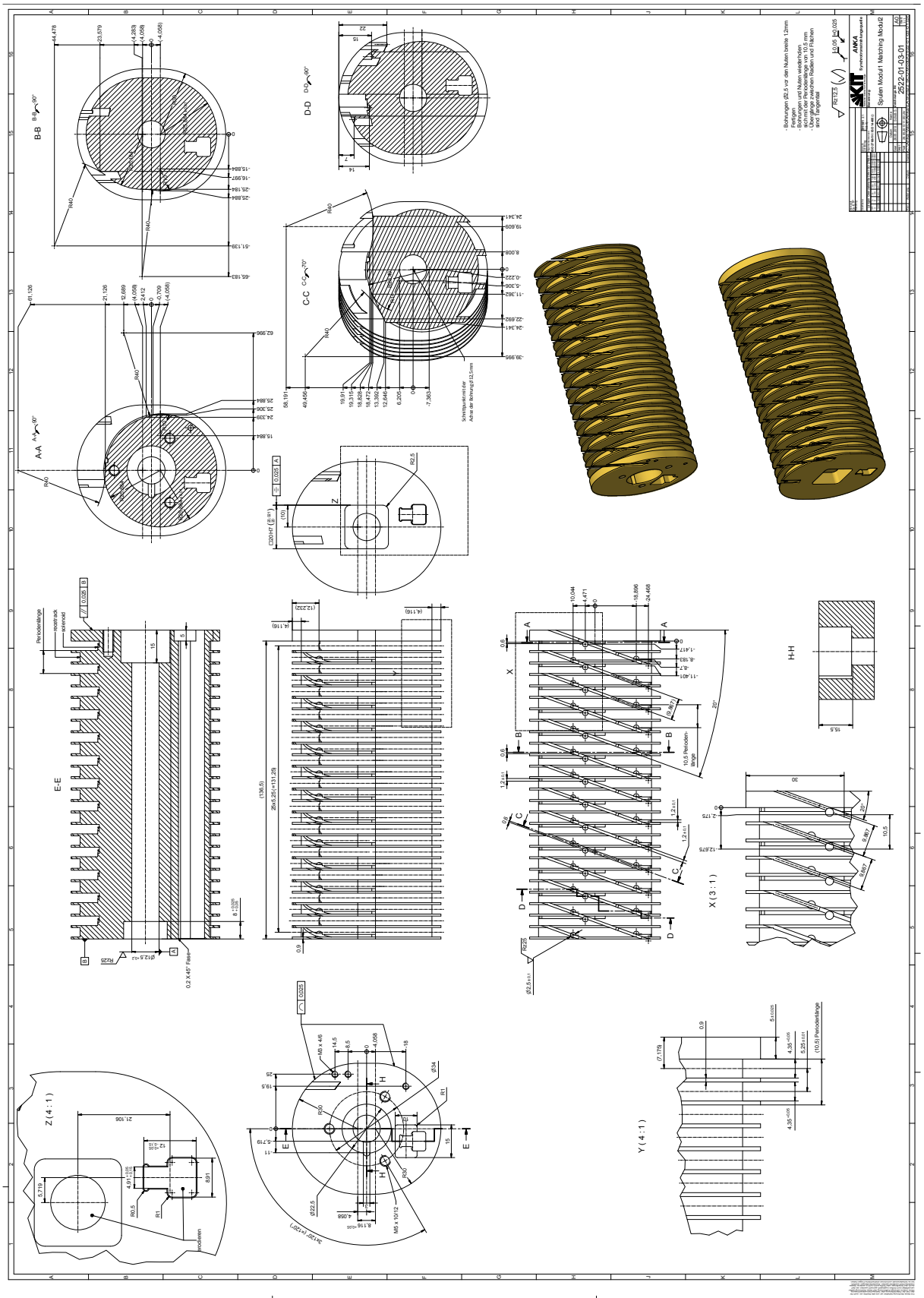
B-B
D-D
C-C
A-A
E-E
H-H
X (3 : 1)
Y (4 : 1)
Z (4 : 1)
Periodenlänge
racetrack
solenoid
Schnittpunkt mit der Achse der Bohrung Ø2,5 mm
10,5 Periodenlänge
(10,5) Periodenlänge
erodieren
0.2 X 45° Fase
25x5,25 (=131,25)
3x120° (=120°)
- Bohrungen Ø2,5 vor den Nuten breite 1.2mm Fertigen
- Bohrungen und Nuten wiederholen sich mit der Periodenlänge von 10.5 mm
- Übergänge zwischen Radien und Flächen sind Tangential
Rz12,5
ANKA
Synchrotronstrahlungsquelle
KIT Karlsruher Institut für Technologie
Benennung:
Spulen Modul1 Matching Modul2
Zeichnungs-Nr:
2522-01-03-01
Werkstoff: Cu-ETP
Gewicht: 2,800 kg
Längen Grenzabmaße DIN ISO 2768-f
ISO 2768-fH / ISO 14405
Bear. 28.05.2013 Schott-S
Plott 29.05.2013 11:05 Uhr
A0
Blatt: 1/1
C:\Anka-Vault\Anka\LAS\2522 SCU Modul\2522-01-03-01.ipt

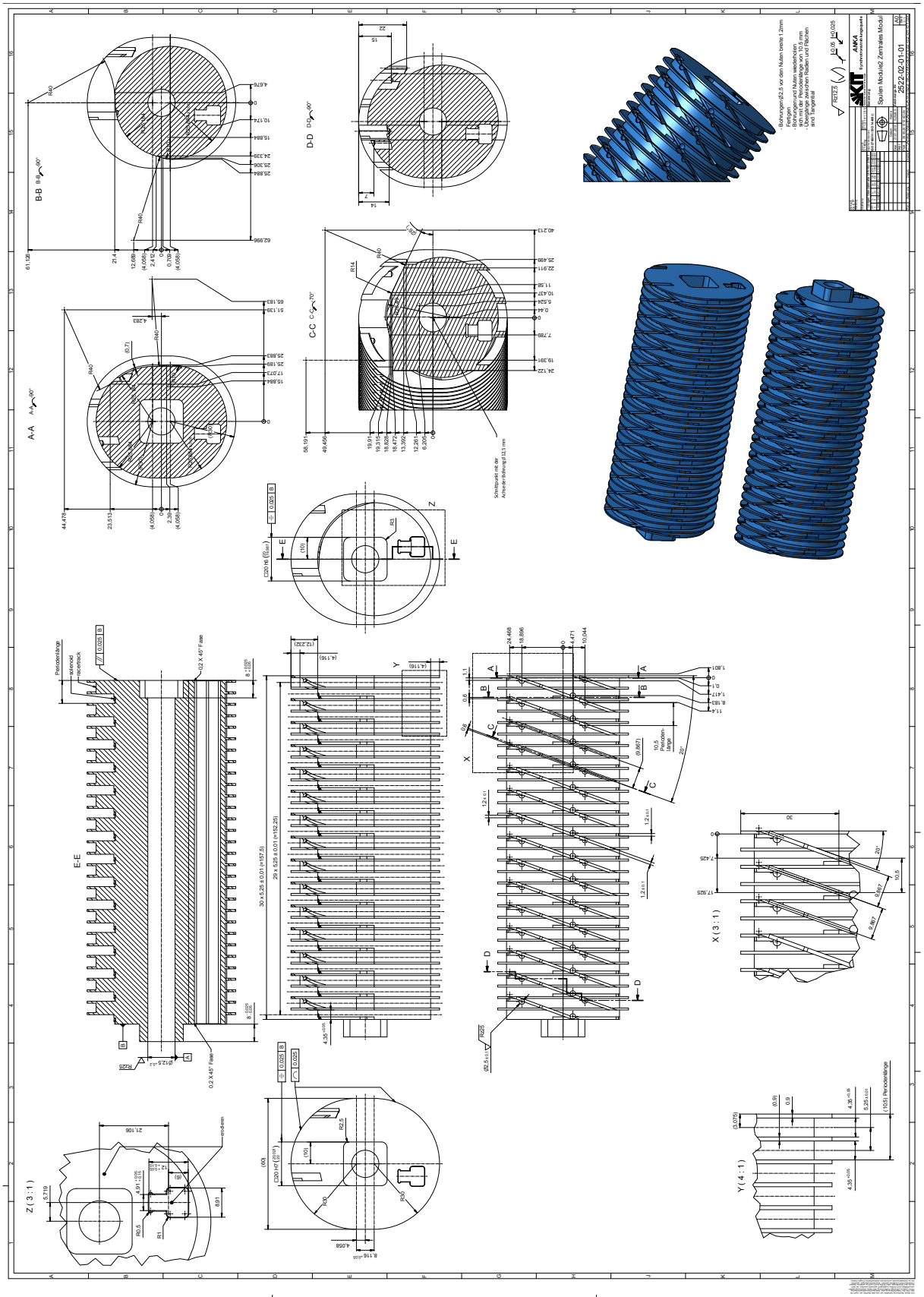
Spulen Modul2 Zentrales Modul
2522-02-01-01
A-A
B-B
C-C
D-D
E-E
Z (3 : 1)
X (3 : 1)
Y (4 : 1)

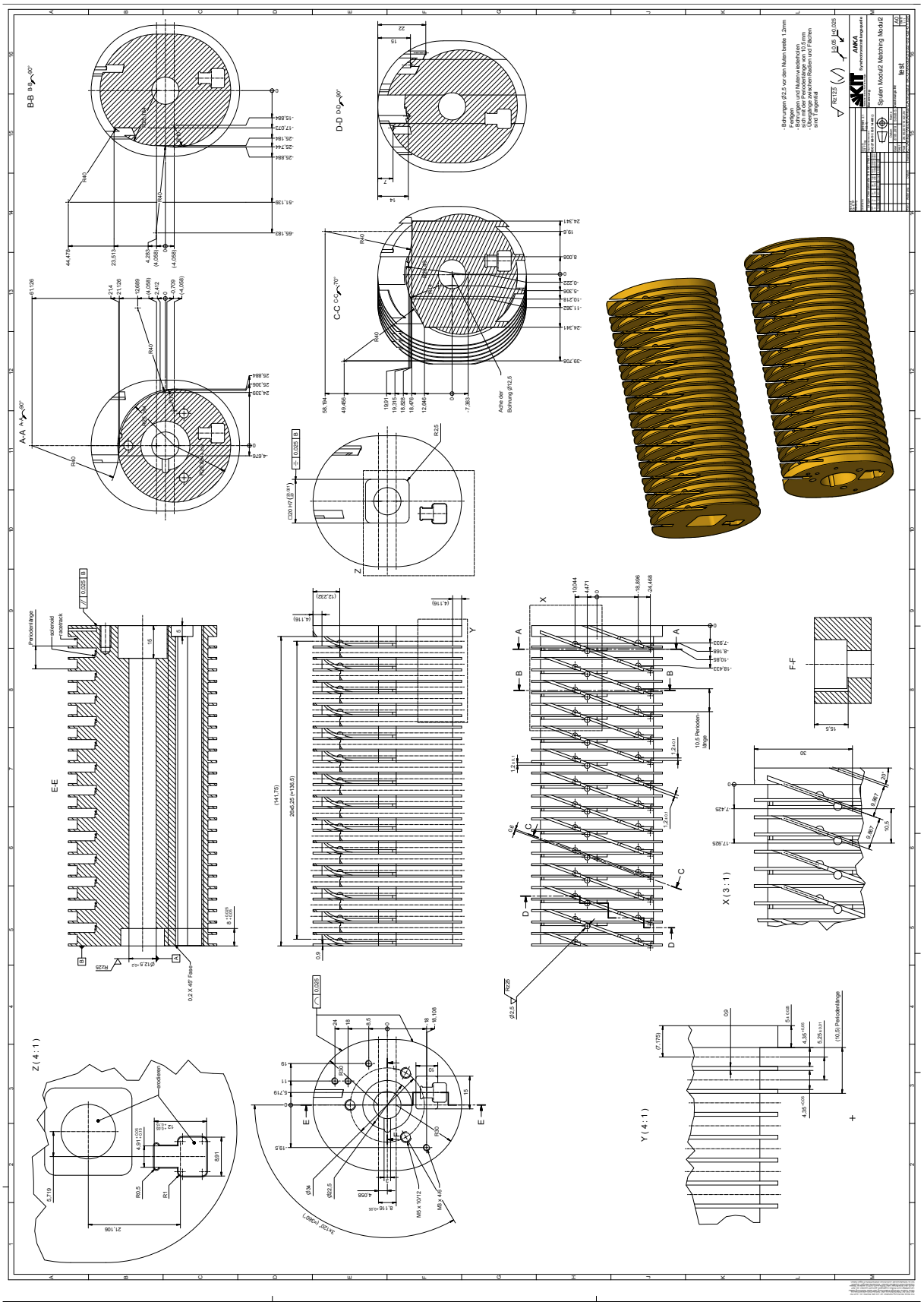
Stylen Modul2 Matching Modul2
test
B-B
D-D
C-C
A-A
E-E
F-F
Z (4 : 1)
X (3 : 1)
Y (4 : 1)

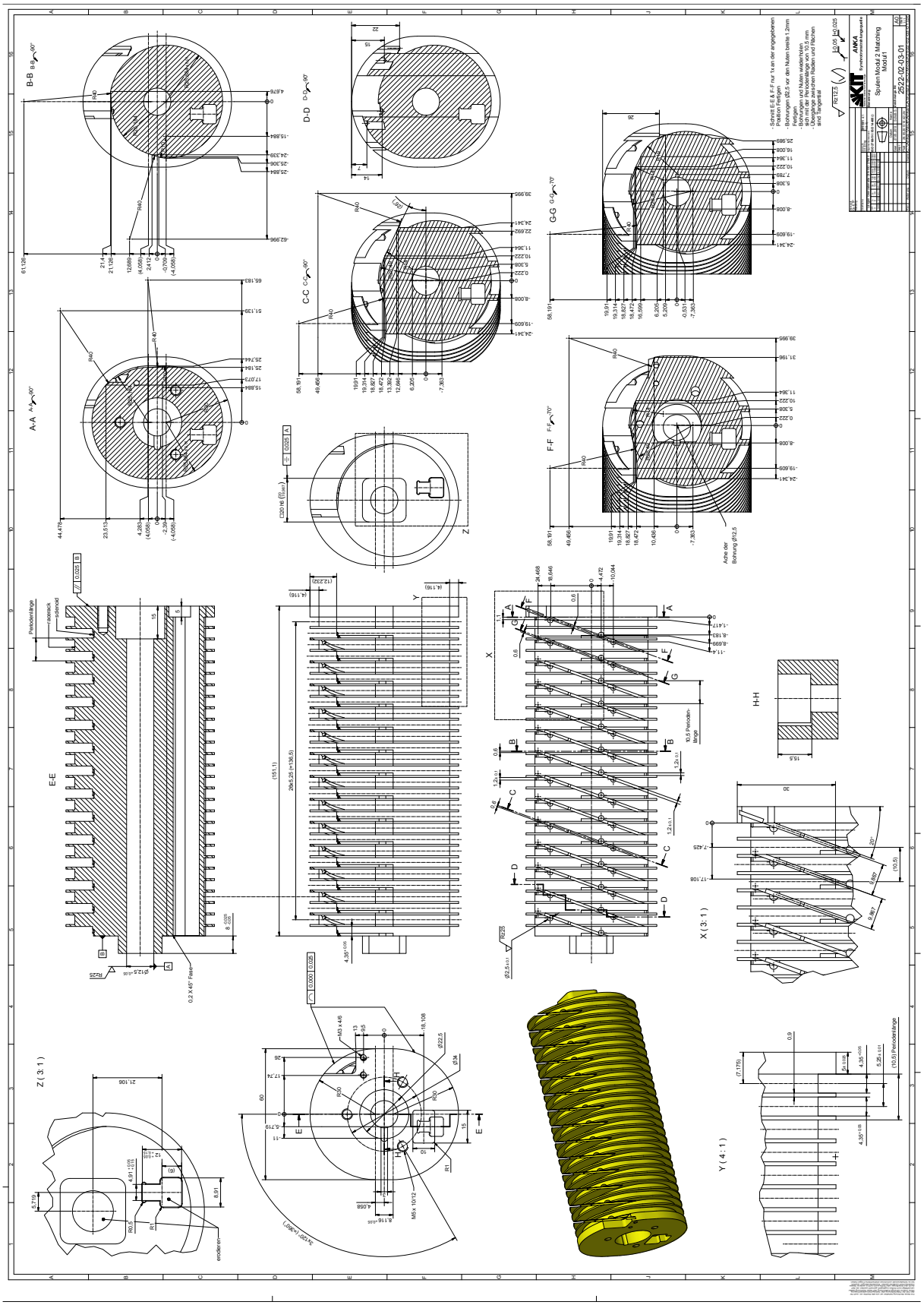
Spulen Modul 2 Matching
Modul
2522-02-03-01
AIKA
Synchrotronstrahlung
B-B
D-D
C-C
G-G
A-A
F-F
E-E
H-H
Z (3:1)
X (3:1)
Y (4:1)

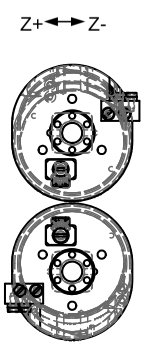

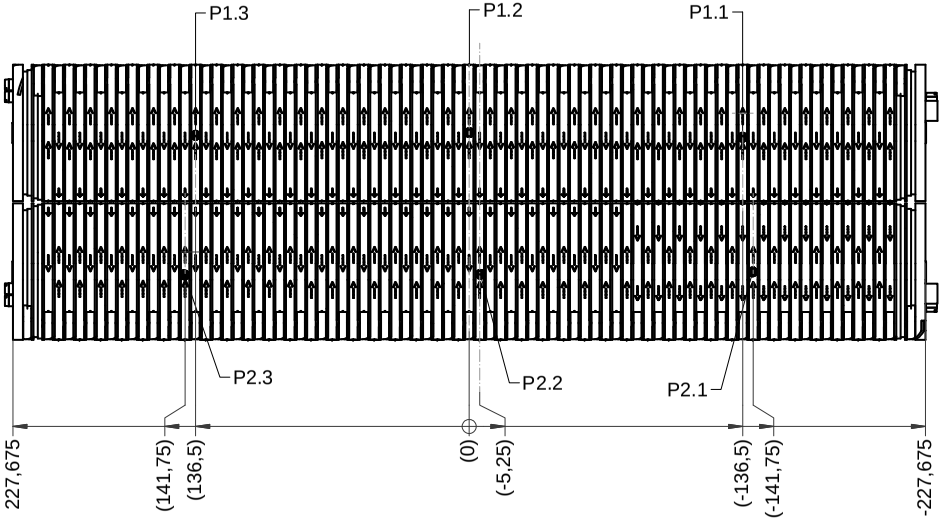

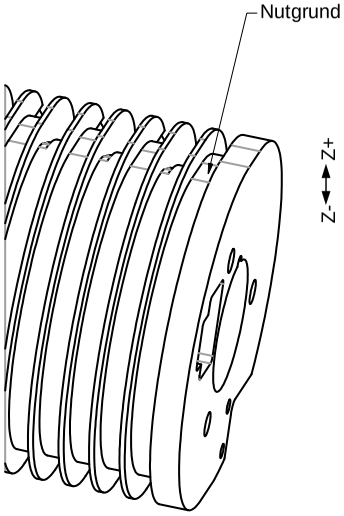

Messpunkt	Messwerte in Z (µ)
P1.1	0
P1.2	+10
P1.3	+25
P2.1	0
P2.2	+10
P2.2	-5

- Gemessen wurde der relative Höhenunterschied des Nutgrundes
- Der Nullpunkt wurde für jede Spule separat bestimmt.

Messmittel:
- Digitaler 3D-Taster mit Tasteinsatz (Ø 4 mm) (Hoffmann 359500)
- Fräsmaschine Deckel FP1

Werkstoff:
Halbzeug:
Oberfläche:
Gewicht: -
Maßstab: 1:2 (1,5:1)
Allgemeintoleranzen: ISO 2768-mk / ISO 14405

KIT Karlsruher Institut für Technologie
ANKA Synchrotronstrahlungsquelle

Benennung: SCU Module kurz (6 Module)

	Datum	Name
Bear.	10.01.2014	Schott-S
Gepr.		
Plott	10.01.2014 09:28 Uhr	

Zeichnungs-Nr: Verm. des Nutgrundes
A3
Blatt: 1 / 1

Rev. | Änderung | Datum | Name
C:\Anka-Vault\ANKA\LAS\2593_SCU Module kurz\2593-00.iam

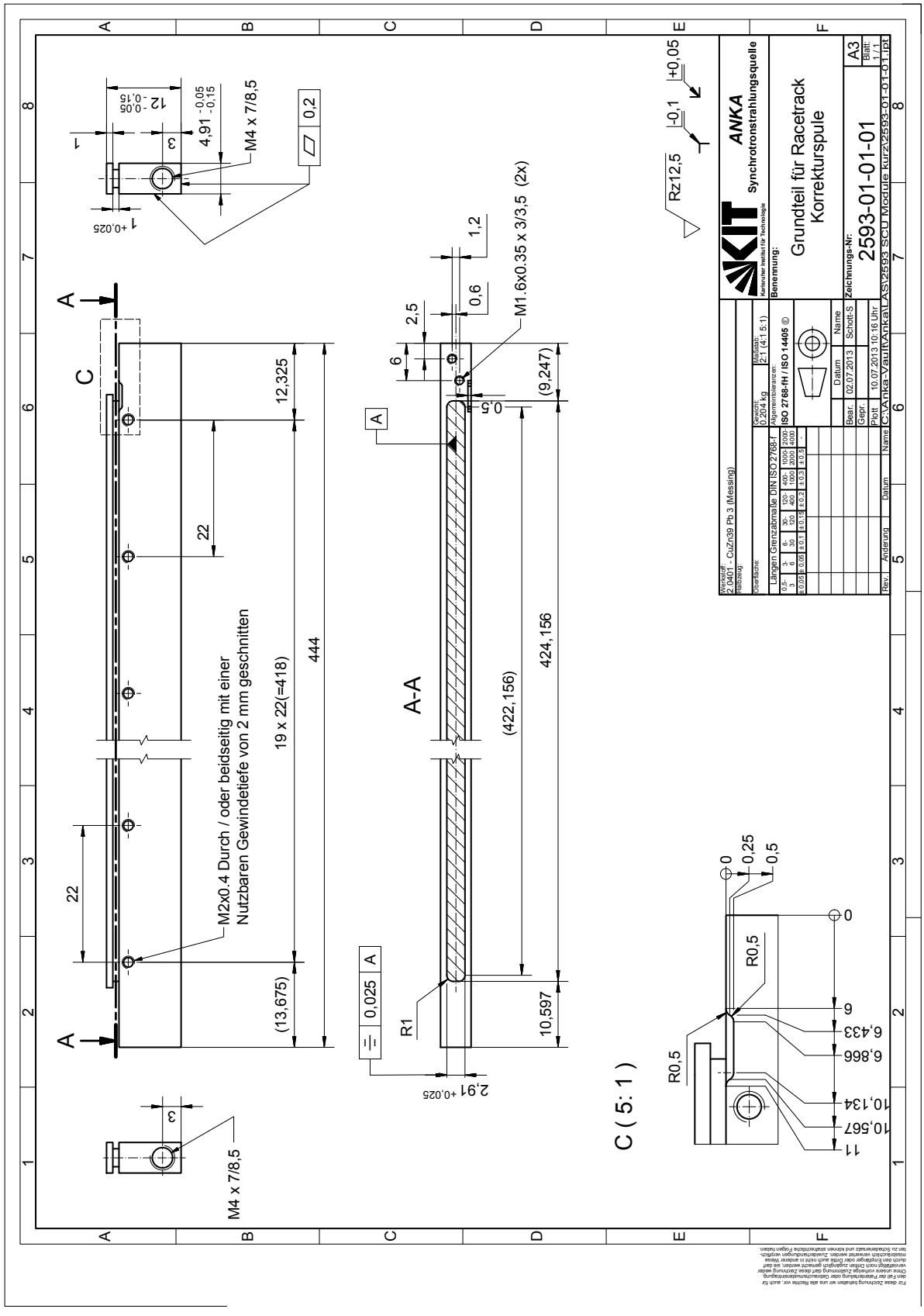
A-A
C (5: 1)
M2x0.4 Durch / oder beidseitig mit einer
Nutzbaren Gewindetiefe von 2 mm geschnitten
19 x 22(=418)
M1.6x0.35 x 3/3,5 (2x)
M4 x 7/8,5
Rz12,5
ANKA
Synchrotronstrahlungsquelle
Grundteil für Racetrack
Korrekturspule
2593-01-01-01
Werkstoff:
2.0401 - CuZn39 Pb 3 (Messing)
Oberfläche:
Gewicht:
0,204 kg
Maßstab:
2:1 (4,1 5:1)
Allgemeintoleranzen:
ISO 2768-fH / ISO 14405
Längen Grenzabmaße DIN ISO 2768-f
Datum
Name
Bear.
02.07.2013
Schott-S
Gepr.
Plott
10.07.2013 10:16 Uhr
Name
C:\Anka-Vault\Anka\LAS\2593 SCU Module kurz\2593-01-01-01.ipt
Rev.
Änderung
Datum
A3
Blatt:
1 / 1

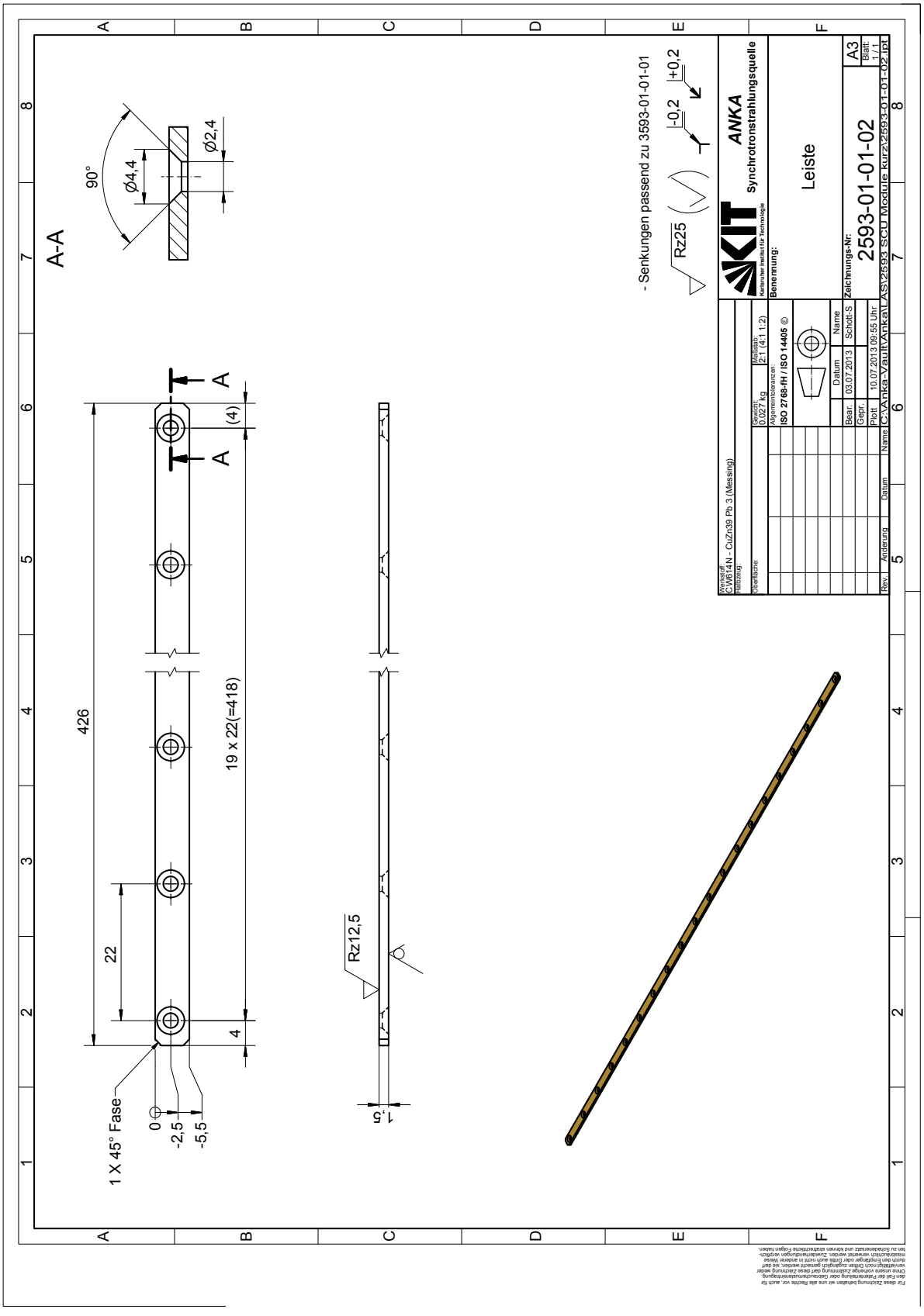
A-A
90°
Ø4,4
Ø2,4
426
22
19 x 22(=418)
(4)
4
1 X 45° Fase
0
-2,5
-5,5
Rz12,5
1,5
- Senkungen passend zu 3593-01-01
Rz25
-0,2
+0,2
ANKA
Synchrotronstrahlungsquelle
Karlsruher Institut für Technologie
Leiste
Zeichnungs-Nr:
2593-01-01-02
A3
Blatt: 1 / 1
Werkstoff: CW614N - CuZn39 Pb 3 (Messing)
Oberfläche:
Gewicht: 0,027 kg
Maßstab: 2:1 (4:1 1:2)
Allgemeintoleranzen: ISO 2768-fH / ISO 14405
Datum
Name
Bear. 03.07.2013 Schott-S
Gepr.
Plott 10.07.2013 09:55 Uhr
Rev. Änderung Datum Name
C:\Anka-Vault\Anka\LAS\2593 SCU Module kurz\2593-01-01-02.ipt

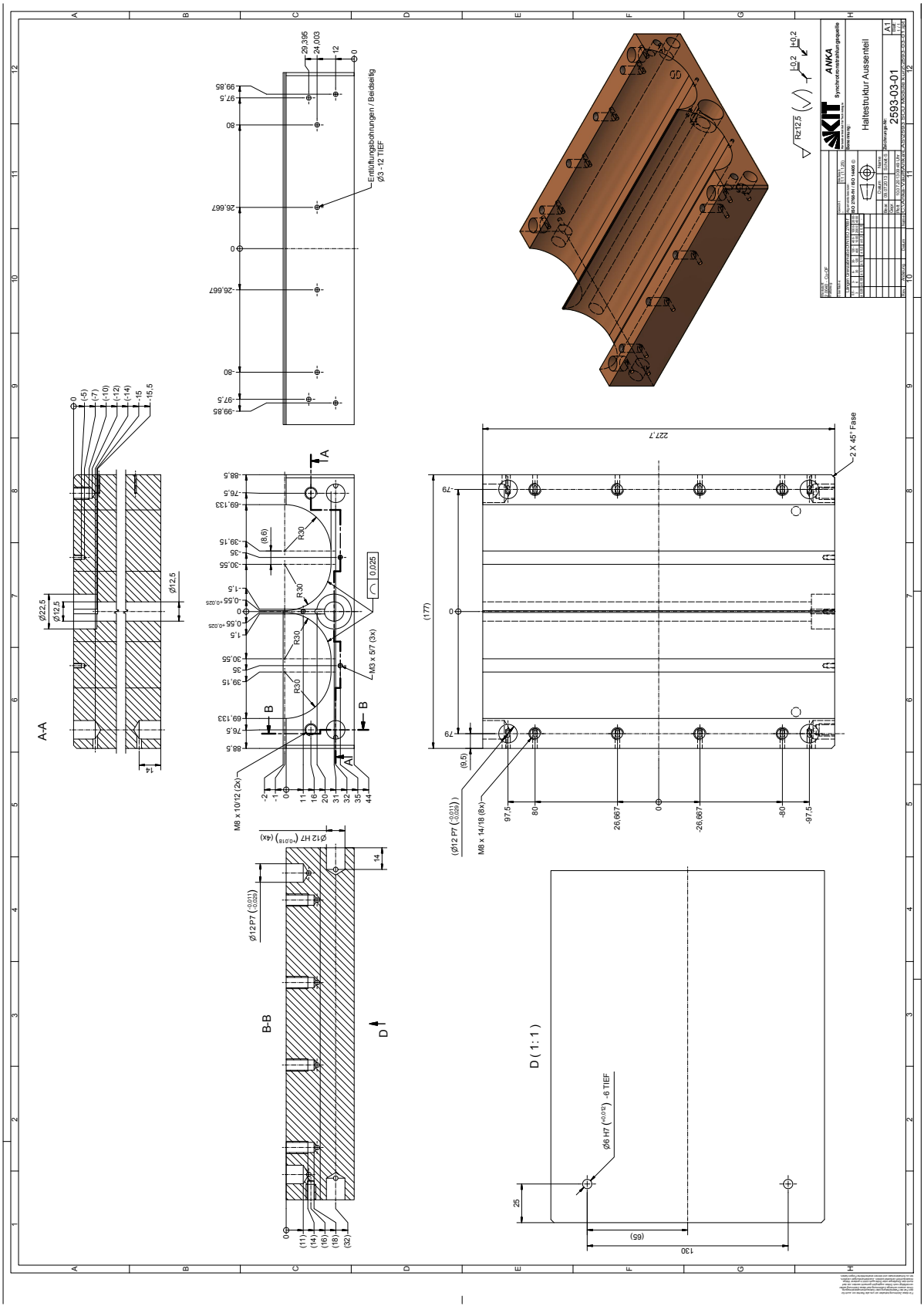
ANKA
Synchrotronstrahlungsquelle
Hallestruktur Aussenteil
2593-03-01
A1
Rz12,5
Entlüftungsbohrungen / Bedseitig
Ø3 -12 TIEF
A-A
B-B
D (1 : 1)
2 X 45° Fase
M8 x 10/12 (2x)
M8 x 14/18 (8x)
M3 x 5/7 (3x)
Ø6 H7 (+0,012 0) -6 TIEF
227,7
130
(65)

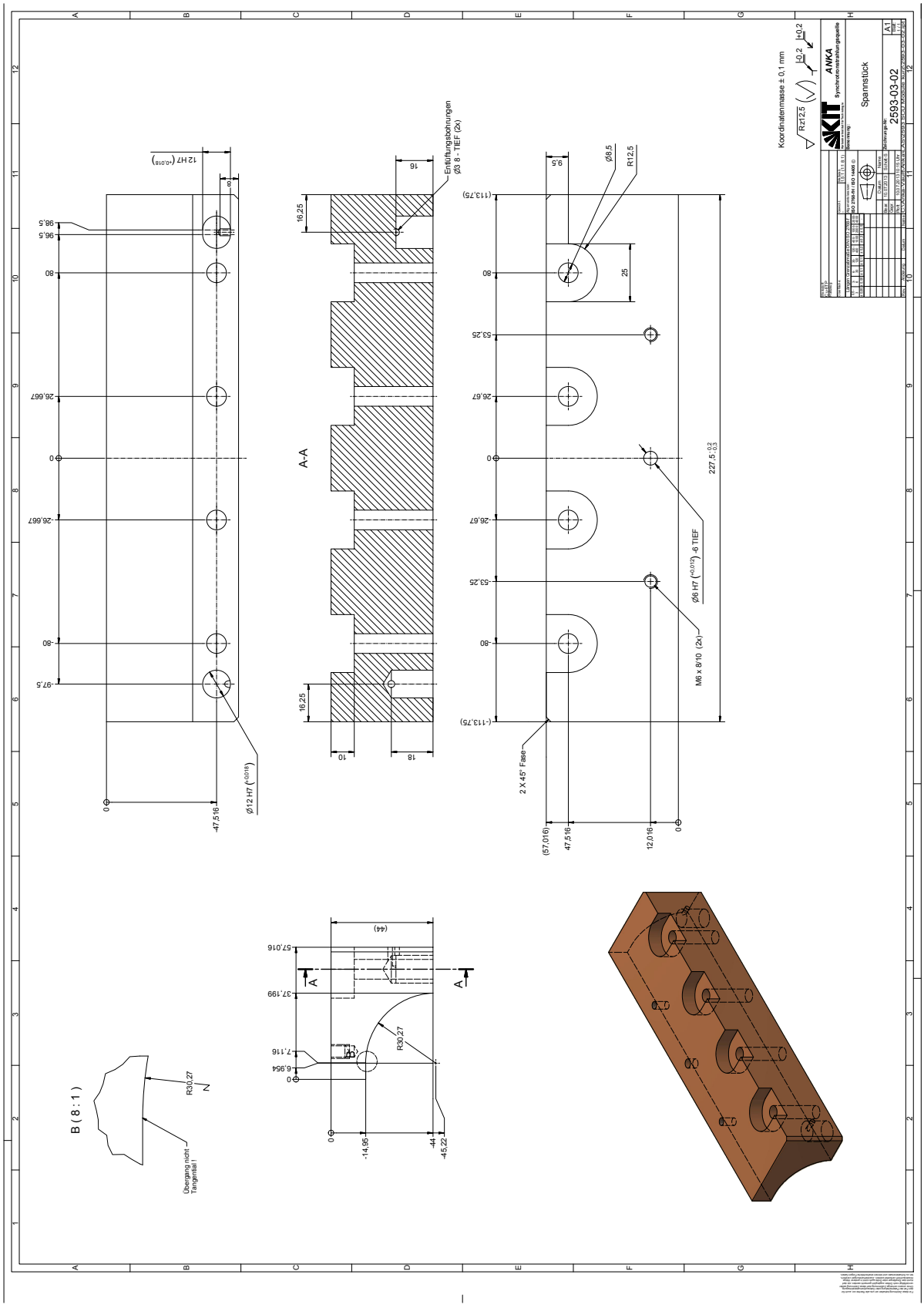
ANKA
Synchrotronstrahlungsquelle
Spannstück
2593-03-02
Koordinatenmasse ± 0,1 mm
Rz12,5
A-A
B (8 : 1)
Übergang nicht fertigmaßt!
Einfüllungsbohrungen Ø3 8 - TIEF (2x)
Ø8,5
R12,5
25
Ø6 H7 (+0,012) -8 TIEF
M8 x 8/10 (2x)
227,5 -0,2 -0,3
2 X 45° Fase
12 H7 (+0,018)
Ø12 H7 (+0,018)
R30,27

List of Figures

List of Tables

Bibliography

[1] F. R. Elder, A. M. Gurewitsch, R. V. Langmuir, and H. C. Pollock. Radiation from Electrons in a Synchrotron. *Phys. Rev.*, 71:829–830, June 1947.

[2] J. A. Clarke. *The science and technology of undulators and wigglers.* Oxford series on synchrotron radiation. OUP Oxford, 2004.

[3] H. D. Nuhn. From storage rings to free electron lasers for hard x-rays. *Journal of Physics: Condensed Matter*, 16(33):S3413–S3421, 2004.

[4] M. Borland. Progress toward an ultimate storage ring light source. *Journal of Physics: Conference Series*, 425(4):042016, 2013.

[5] M. Eriksson, A. Hansson, S. C. Leemann, L. J. Lindgren, L. Rivkin, M. Sjöström, A. Streun, and E. J. Wallen. Using multi-bend achromats in synchrotron radiation sources. Proceedings of EPAC08, WEPC011, 2008.

[6] A. Bernhard. Beschleunigerphysik, Teil 2. Vorlessungsskript WS 2012/2013. Lecture at KIT. 2012.

[7] T. Tajima and J. M. Dawson. Laser electron accelerator. *Phys. Rev. Lett.*, 43:267–270, July 1979.

[8] S. M. Hooker. Developments in laser-driven plasma accelerators. *Nat Photon*, 7(10):775–782, October 2013.

[9] W. P. Leemans, B. Nagler, A. J. Gonsalves, Cs. Tóth, K. Nakamura, C. G. R. Geddes, E. Esarey, C. B. Schroeder, and S. M. Hooker. GeV electron beams from a centimetre-scale accelerator. *Nature Physics*, (10):696–699, 2006.

[10] A. Pukhov and J. Meyer-ter Vehn. Laser wake field acceleration: the highly non-linear broken-wave regime. *Applied Physics B*, 74(4-5):355–361, 2002.

[11] N. Braun. Simulation der Strahlung von Elektronen in einem zylindrischen Undulator. *Bachelor Thesis, KIT*, Juli 2013.

[12] M. Scheer. WAVE - A computer code for the tracking of electrons through magnetic fields and the calculation of spontaneous synchrotron radiation. Proceedings of ICAP2012, TUACC2, 2012.

[13] H. P. Schlenvoigt, K. Haupt, A. Debus, F. Budde, O. Jackel, S. Pfotenhauer, H. Schwoerer, E. Rohwer, J. G. Gallacher, E. Brunetti, R. P. Shanks, S. M. Wiggins, and D. A. Jaroszynski. A compact synchrotron radiation source driven by a laser-plasma wakefield accelerator. *Nature Physics*, 4:130–133, 2008.

[14] M. Fuchs, R. Weingartner, A. Popp, Z. Major, S. Becker, J. Osterhoff, I. Cortrie, B. Zeitler, R. Hoerlein, G. D. Tsakiris, U. Schramm, T. P. Rowlands-Rees, S. M. Hooker, D. Habs, F. Krausz, S. Karsch, and F. Gruener. Laser-driven soft-x-ray undulator source. *Nature Physics*, 5(11):826–829, November 2009.

[15] Drawing realized by C. Widmann, LAS KIT, 2013.

[16] G. Fuchert, A. Bernhard, S. Ehlers, P. Peiffer, R. Rossmanith, and T. Baumbach. A novel undulator concept for electron beams with a large energy spread. *Nuclear Instruments and Methods in Physics Research Section A: Accelerators, Spectrometers, Detectors and Associated Equipment*, 672(0):33–37, 2012.

[17] K. H. Mess, P. Schmüser, and S. Wolff. *Superconducting accelerator magnets*. World Scientific, 1996.

[18] D. Schoerling. Superconducting wiggler magnets for beam-emittance damping rings. *Master's Thesis, TUB*, March 2012.

[19] S. Russenschuck. *Field computation for accelerator magnets: analytical and numerical methods for electromagnetic design and optimization*. Wiley, Weinheim, 2010.

[20] M. N. Wilson. *Superconducting magnets*. Monographs on cryogenics. Oxford University Press on Demand, 1986.

[21] Y. Ivanyushenkov. Advances in superconducting undulators. FRYBB1, 2013.

[22] C. S. Hwang et al. Mini-pole superconducting undulator for X-Ray synchrotron light source. *IEEE Trans. Appl. Supercond.*, 16(2):1855, June 2006.

[23] Y. Ivanyushenkov et al. A design concept for a planar superconducting undulator for the APS. *IEEE Trans. Appl. Supercond.*, 21(3):1717, June 2011.

[24] R. P. Walker. Progress with the Diamond Light Source Project. *Proceedings of the 2003 Particle Accelerator Conference*, pages 232–234, 2003.

[25] Z. C. Zhang et al. Design of a superconducting undulator magnet prototype for SSRF. WEPWA035, 2013.

[26] E. Wallén, J. Chavanne, and P. Elleaume. Status of the development of superconducting undulators at the ESRF. *Proceedings of the EPAC*, pages 378–380, 2004.

[27] S. Casalbuoni, T. Baumbach, S. Gerstl, A. Grau, M. Hagelstein, T. Holubek, D. Saez de Jauregui, C. Boffo, and W. Walter. Development of superconducting undulators at ANKA. *Synchrotron Radiation News*, 24(3):14–19, 2011.

[28] C. B. Schroeder, W. M. Fawley, E. Esarey, W. P. Leemans, et al. A design for an XUV FEL driven by the laser-plasma accelerator at the LBNL LOASIS Facility. https://publications.lbl.gov/islandora/object/ir%3A126995, 2006.

[29] D. A. Jaroszynski, R. Bingham, E. Brunetti, B. Ersfeld, J. Gallacher, B. van der Geer, R. Issac, S. P. Jamison, D. Jones, M. de Loos, A. Lyachev, V. Pavlov, A. Reitsma, Y. Saveliev, G. Vieux, and S. M. Wiggins. Radiation sources based on laser–plasma interactions. *Philosophical Transactions of the Royal Society A: Mathematical, Physical and Engineering Sciences*, 364(1840):689–710, 2006.

[30] F. Gruner, S. Becker, U. Schramm, T. Eichner, D. Habs, et al. Design considerations for table-top, laser-based VUV and X-ray free electron lasers. *Appl.Phys.B*, 2006.

[31] J. Faure et al. A laser-plasma accelerator producing monoenergetic electron beams. *Nature*, 431(7008):541–544, September 2004.

[32] S. P. D. Mangles et al. Monoenergetic beams of relativistic electrons from intense laser-plasma interactions. *Nature*, 431(7008):535–538, September 2004.

[33] C. G. R. Geddes et al. High-quality electron beams from a laser wakefield accelerator using plasma-channel guiding. *Nature*, 431(7008):538–541, September 2004.

[34] F. H. O'Shea, G. Marcus, J. B. Rosenzweig, M. Scheer, J. Bahrdt, R. Weingartner, A. Gaupp, and F. Grüner. Short period, high field cryogenic undulator for extreme performance x-ray free electron lasers. *Phys. Rev. ST Accel. Beams*, 13:070702, July 2010.

[35] R. Walker. Insertion Devices: Undulators and Wigglers. *CERN Accelerator School*, pages 129–190, 1996.

[36] A. Hofmann. *The physics of synchrotron radiation*. Cambridge Monographs on Particle Physics, Nuclear Physics and Cosmology. Cambridge University Press, 2004.

[37] H. Onuki and P. Elleaume. *Undulators, wigglers and their applications*. Taylor & Francis, 2004.

[38] G. Fuchert. Modelle für supraleitende Undulatoren an kompakten Synchrotronstrahlungsquellen mit Laser-Wakefield-Beschleunigern. *Master's Thesis, KIT*, November 2009.

[39] J. D. Jackson. *Classical electrodynamics*. Wiley, 1975.

[40] P. H. Moon and D. E. Spencer. *Field theory handbook: including coordinate systems, differential equations, and their solutions*. Springer-Verlag, 1988.

[41] C. B. Lang and N. Pucker. *Mathematische Methoden in der Physik*. Spektrum Akademischer Verlag, 2005.

[42] G. Fuchert, A. Bernhard, S. Ehlers, P. Peiffer, D. Wollmann, T. Baumbach, and R. Rossmanith. New Superconductive Undulator Design for Use with Laser Wakefield Accelerators. Proceedings of the FEL, WEPC06, 2009.

[43] K. J. Binns, P. J. Lawrenson, and C. W. Trowbridge. *The analytical and numerical solution of electric and magnetic fields*. Wiley, 1995.

[44] ANSYS. http://www.ansys.com/, 2014.

[45] ROXIE, CERN. https://espace.cern.ch/roxie, 2014.

[46] Cobham, OPERA simulation software. http://www.cobham.com/about-cobham/aerospace-and-security/about-us/antenna-systems/specialist-technical-services-and-software/products-and-services/design-simulation-software/opera.aspx, 2014.

[47] U. A. Bakshi and V. U. Bakshi. *Elements of electrical engineering*. Technical Publications, 2010.

[48] Opera-3d reference manual, May 2013.

[49] C. Widmann, V. Afonso Rodriguez, A. Bernhard, P. Peiffer, R. Rossmanith, T. Baumbach, M. Nicolai, and M.C. Kaluza. Design of a dispersive beam transport line for the JETI laser wakefield accelerator. *Proceedings 2nd International Particle Accelerator Conference (IPAC), TUPO006*, 2011.

[50] C. Widmann, V. Afonso Rodriguez, A. Bernhard, T. Baumbach, P. Peiffer, R. Rossmanith, W. Werner, M. Nicolai, M.C. Kaluza, N. Braun, B. Haerer, O. Jaeckel, T. Rinck, A. Saevert, and M. Scheer. Non-Linear beam transport optics for a laser wakefield accelerator. *Proceedings 4th International Particle Accelerator Conference (IPAC), TUPWO013*, 2013.

[51] H. Wiedemann. *Particle Accelerator Physics*. Advanced Texts in Physics. Springer, 2007.

[52] D. Attwood. *Soft X-rays and extreme ultraviolet radiation: principles and applications*. Cambridge University Press, 2007.

[53] M. Koppenhöfer. Design eines Messaufbaus und Charakterisierung von Strahlführungsmagneten für einen Laser-Wakefield-Beschleuniger. *Bachelor Thesis, KIT*, July 2013.

[54] W. H. Press and S. A. Teukolsky. *Numerical recipes in C++: the art of scientific computing*. Cambridge University Press, 2002.

[55] E. Borie et al. Einführung in die Plasmaphysik. *Teil 1. Vorlessungsskript WS 05/06*, 2006.

[56] M. S. Lubell. Empirical scaling formulas for critical current and critical field for commercial NbTi. *Magnetics, IEEE Transactions on*, 19(3):754–757, May 1983.

[57] L. Bottura. A practical fit for the critical surface of NbTi. *Applied Superconductivity, IEEE Transactions on*, 10(1):1054–1057, March 2000.

[58] The measurement was performed by M. Kläser, ITEP KIT, 2012.

[59] P. Peiffer. Korrekturfelder für den JeTi Undulator, LAS-Gruppenseminar, KIT, 2012.

[60] V. Karcher. Simulation und Analyse von Baufehlertoleranzen für einen supraleitenden zylindrischen Undulator. *Bachelor Thesis, KIT*, October 2013.

[61] Technical drawing realized by S. Schott, ANKA KIT, 2013.

[62] The simulations were performed by S. Schott, ANKA KIT, 2013.

[63] Autodesk, Inventor software: 3D CAD software for mechanical design. http://www.autodesk.com/products/inventor/overview, 2015.

[64] W. Younis. *Up and Running with Autodesk Inventor Simulation 2011, Second Edition: A Step-by-step Guide to Engineering Design Solutions*. Butterworth-Heinemann, Newton, MA, USA, 2nd edition, 2010.

[65] B. J. Hamrock, S. R. Schmid, and B. O. Jacobson. *Fundamentals of machine elements*. McGraw-Hill series in mechanical engineering. McGraw-Hill Higher Education, 2004.

[66] Andreas Will. Design eines kryogenen Messaufbaus und dreidimensionale Magnetfeldmessung eines zylindrischen Undulatormodells. *Bachelor Thesis, KIT*, August 2013.

[67] Measurement realized by S. Schott, ANKA KIT, 2013.

[68] Brochure "Stycast 2850 FT Schwarzes Epoxidharz - mit Katalysator 24LV". http://www.cmr-direct.com/de/cmr-2850-cat24lv-1kg.

[69] S. Sanfilippo. Hall probes: physics and application to magnetometry. *CERN Accelerator School CAS 2009: Specialised Course on Magnets*, March 2011.

[70] R.S. Popovic. *Hall effect devices, second edition*. Series in Sensors. CRC Press, 2003.

[71] Brochure "AREPOC s.r.o. high linearity Hall probes for room and cryogenic temperatures". www.arepoc.sk/uploaded/download/HallProbes.PDF, 2008.

[72] Corning. Brochure "MACOR". http://www.precision-ceramics.co.uk/macor-brochure.htm, 2015.

[73] E. Mashkina, A. Grau, T. Schneider, A. Bernhard, S. Casalbuoni, M. Hagelstein, B. Kostka, R. Rossmanith, E. Steffens, D. Wollmann, and T. Baumbach. CASPER - A magnetic measurement facility for superconducting undulators. *Journal of Physics: Conference Series*, 97(1):012020, 2008.

[74] D. Schoerling. Untersuchungen zur zeitlichen Charakteristik von Undulatorstrom und Elektronenstrahllage am supraleitenden Undulator an ANKA. *Projektarbeit, TUB*, December 2007.

[75] S. Ehlers, T. Baumbach, G. Fuchert, P. Peiffer, D. Wollmann, A. Bernhard, R. Rossmanith, and D. Schoerling. Magnetic field transients in superconductive undulators. *Proceedings 23rd Conference Particle accelerator (PAC), WE5RFP085*, May 2009.

[76] T. Williams and C. Kelley. Gnuplot 4.6. http://www.gnuplot.info.

[77] J. A. Nelder and R. Mead. A simplex method for function minimization. *Computer Journal*, 7:308–313, 1965.

[78] B. Jia. Simplex optimization algorithm and implementation in C++ programming. http://www.codeguru.com/, July 2010.

Conference and publications

[ABB+11] V. Afonso Rodriguez, T. Baumbach, A. Bernhard, A. Keilmann, P. Peiffer, R. Rossmanith, C. Widmann, M. Nicolai, M.C. Kaluza, and G. Fuchert. Design optimization for a non-planar undulator for the JETI-laser-wakefield-accelerator in Jena. *Proceedings 2nd International Particle Accelerator Conference (IPAC), TUPO005*, 2011.

[WAB+11] C. Widmann, V. Afonso Rodriguez, A. Bernhard, P. Peiffer, R. Rossmanith, T. Baumbach, M. Nicolai, and M.C. Kaluza. Design of a dispersive beam transport line for the JETI laser wakefield accelerator. *Proceedings 2nd International Particle Accelerator Conference (IPAC), TUPO006*, 2011.

[ABK+13] V. Afonso Rodriguez, A. Bernhard, A. Keilmann, P. Peiffer, R. Rossmanith, C. Widmann, T. Baumbach, M. Nicolai, and M. C. Kaluza. Development of a superconducting transverse-gradient undulator for laser-wakefield-accelerators. *IEEE Transactions on Applied Superconductivity*, 23(3), 2013.

[NSN+12] M. J. Nasse, M. Streichert, N. Niller, E. Huttel, V. Judin, B. Kehrer, M. Klein, S. Marsching, A.-S. Müller, M. Schwarz, N. J. Smale, V. Afonso Rodriguez, A. Bernhard, and C. Meuter. Simulations of fringe fields and multipoles for the ANKA storage ring bending magnets. *Proceedings 3rd International Particle Accelerator Conference (IPAC), TUPPP011*, 2012.

[WAB+12] C. Widmann, V. Afonso Rodriguez, A. Bernhard, P. Peiffer, R. Rossmanith, T. Baumbach, M. Nicolai, and M.C. Kaluza. Setup of a diagnostics beam-line for the JETI laser wakefield accelerator. *Verhandlungen der Deutschen Physikalischen Gesellschaft (DPG)*, 44(37), 2012.

[ABK+12] V. Afonso Rodriguez, A. Bernhard, A. Keilmann, P. Peiffer, R. Rossmanith, C. Widmann, T. Baumbach, M. Nicolai, M.C. Kaluza, and G. Fuchert. Design and optimization of a superconducting cylindrical undulator for the JETI wakefield accelerator in Jena. *Verhandlungen der Deutschen Physikalischen Gesellschaft (DPG)*, 44(37), 2012.

[WAB+13b] C. Widmann, V. Afonso Rodriguez, A. Bernhard, T. Baumbach, P. Peiffer, R. Rossmanith, W. Werner, M. Nicolai, M.C. Kaluza, N. Braun, B. Haerer, O. Jaeckel, T. Rinck, A. Saevert, and M. Scheer. Non-Linear beam transport optics for a laser wakefield accelerator.

Proceedings 4th International Particle Accelerator Conference (IPAC), TUPWO013, 2013.

[ABG+13] V. Afonso Rodriguez, A. Bernhard, A. Grau, B. Härer, P. Peiffer, R. Rossmanith, M. Weber, C. Widmann, M.C. Kaluza, M. Nicolai, R. Thorsten, A. Sävert, O. Jäckel, and M. Reuter. Status of a cylindrical superconducting undulator for the laser wakefield accelerator in Jena. *Verhandlungen der Deutschen Physikalischen Gesellschaft (DPG)*, 45(30), 2013.

[WAB+13c] C. Widmann, V. Afonso Rodriguez, A. Bernhard, B. Härer, P. Peiffer, R. Rossmanith, W. Werner, T. Baumbach, M. Nicolai, M.C. Kaluza, M. Reuter, and O. Jäckel. Design and optimization of an electron-beam guidance for the laser Wakefield accelerator in Jena. Pt. 1. *Verhandlungen der Deutschen Physikalischen Gesellschaft (DPG)*, 45(35), 2013.

[HAB+13] B. Härer, V. Afonso Rodriguez, T. Baumbach, A. Bernhard, P. Peiffer, R. Rossmanith, W. Werner, and C. Widmann. Design and optimization of an electron-beam guidance for the laser Wakefield accelerator in Jena. Pt. 2. *Verhandlungen der Deutschen Physikalischen Gesellschaft (DPG)*, 45(30), 2013.

[WAB+13a] W. Werner, V. Afonso Rodriguez, T. Baumbach, A. Bernhard, B. Härer, P. Peiffer, R. Rossmanith, and C. Widmann. Compact combined-function quadrupole-sextupole magnets for the electron-beam guidance in the JETI wakefield accelerator. *Verhandlungen der Deutschen Physikalischen Gesellschaft (DPG)*, 45(35), 2013.

[ABG+14] V. Afonso Rodriguez, A. Bernhard, A. Grau, P. Peiffer, R. Rossmanith, M. Weber, C. Widmann, A. Will, T. Baumbach, M.C. Kaluza, M. Nicolai, and A. Sävert. Construction and first magnetic field test of a superconducting transversal gradient undulator for the laser wakefield accelerator in Jena. *Proceedings 5th International Particle Accelerator Conference (IPAC), WEPRO036*, 2014.

[WAB+14a] C. Widmann, V. Afonso Rodriguez, A. Bernhard, N. Braun, A. S. Müller, A. Papash, R. Rossmanith, W. Werner, M.C. Kaluza, and M. Reuter. Beam transport system from a laser wakefield accelerator to a transverse gradient undulator. *Proceedings 5th International Particle Accelerator Conference (IPAC),THOBA03*, 2014.

[BAB+14] N. Braun, V. Afonso Rodriguez, A. Bernhard, P. Peiffer, R. Rossmanith, C. Widmann, T. Baumbach, and M. Scheer. Simulation der Strahlung von Elektronen in einem zylindrischen TG-Undulator. *Verhandlungen der Deutschen Physikalischen Gesellschaft (DPG)*, 2014.

[WPA+14] A. Will, P. Peiffer, V. Afonso Rodriguez, A. Bernhard, A. Grau, R. Rossmanith, C. Widmann, and A. S. Müller. Test und Feldmessung eines vollständigen Kurzmodells eines Transversal-Gradient-Undulators. *Verhandlungen der Deutschen Physikalischen Gesellschaft (DPG)*, 2014.

[WAB+14b] C. Widmann, V. Afonso Rodriguez, A. Bernhard, R. Rossmanith, W. Werner, A. S. Müller, M. Nicolai, A. Sävert, M.C. Kaluza, and M. Reuter. Diagnostik-Beamline mit Transversal-Gradient-Undulator am Laser-Wakefield-Beschleuniger in Jena. *Verhandlungen der Deutschen Physikalischen Gesellschaft (DPG)*, 2014.

[WAB+15] C. Widmann, V. Afonso Rodriguez, A. Bernhard, M. C. Kaluza, S. Kuschel, A. S. Müller, M. Nicolai, R. Rossmanith, A. Saevert, M. B. Schwab, and W. Werner. First tests of a beam transport system from a laser wakefield accelerator to a transverse gradient undulator. *Proceedings 6th International Particle Accelerator Conference (IPAC), MOPWA045*, 2015.

[BAB+15] A. Bernhard, V. Afonso Rodriguez, E. Burkard, A. S. Müller, and C. Widmann. Transverse gradient undulator-based high-gain-FELs - a parameter study. *Proceedings 6th International Particle Accelerator Conference (IPAC), TUPWA039*, 2015.

[BAM+15] A. Bernhard, V. Afonso Rodriguez, A. S. Müller, J. Senger, W. Werner, and C. Widmann. Compact In-vacuum Quadrupoles for a Beam Transport System at a Laser Wakefield Accelerator. *Proceedings 6th International Particle Accelerator Conference (IPAC), WEPMA038*, 2015.

[BAG+15] A. Bernhard, V. Afonso Rodriguez, A. Grau, P. Peiffer, S. Schott, W. Werner, C. Widmann, A. Will, A. S. Müller, M. Weber, M. Nicolai, A. Sävert, and M.C. Kaluza. A superconducting transverse gradient undulator for a laser wakefield accelerator: first tests and magnetic field measurements . *Verhandlungen der Deutschen Physikalischen Gesellschaft (DPG)*, 2015.

[WBA+15] C. Widmann, A. Bernhard, V. Afonso Rodriguez, W. Werner, M. Nicolai, S. Kuschel, A. Sävert, M. B. Schwab, M.C. Kaluza, and A. S. Müller. First tests of a beam transport system from a laser wakefield accelerator to a transverse gradient undulator . *Verhandlungen der Deutschen Physikalischen Gesellschaft (DPG)*, 2015.

Supervised Student Theses

[Mor12] M. Morcrette. Particle beam focusing in a non-planar undulator. *Master's Thesis, KIT*, October 2012.

[Kar13] V. Karcher. Simulation und Analyse von Baufehlertoleranzen für einen supraleitenden zylindrischen Undulator. *Bachelor Thesis, KIT*, October 2013.

[Plu15] C. Plusczyk. Ponderomotive electron drift optimization of a transverse gradient undulator. *Master's Thesis, Michigan State University*, 2015.